

THESE DE DOCTORAT DE

L'UNIVERSITE DE NANTES
COMUE UNIVERSITE BRETAGNE LOIRE

ECOLE DOCTORALE N° 602
Sciences pour l'Ingénieur
Spécialité : Génie Civil

Par

Chuheng ZHONG

Study of Soil Behavior Subjected to An Internal Erosion Process

Thèse présentée et soutenue à « Saint-Nazaire », le « 25 octobre 2019 »
Unité de recherche : Institut GeM, UMR CNRS 6183
Thèse N° :

Rapporteurs avant soutenance :

Mahdia HATTAB Professeur, Université de Lorraine
Eric VINCENS Professeur, Ecole Centrale de Lyon

Composition du Jury :

Président : Moulay Saïd EL YOUSOUFI Professeur, Université de Montpellier
Examineurs : Moulay Saïd EL YOUSOUFI Professeur, Université de Montpellier

Dir. de thèse : Didier MAROT Professeur, Université de Nantes
Co-dir. de thèse : Zhenyu YIN MCF-HDR, The Hong Kong Polytechnic University

Résumé

Chap. 1 Introduction

Sur les ouvrages hydrauliques en terre, tels que les barrages et les digues, les phénomènes d'érosion interne sont responsables de nombreux désordres qui peuvent même mener à la rupture desdits ouvrages. Ces phénomènes peuvent également se produire le long des canalisations souterraines fuyardes. Le développement de tels processus peut donc porter préjudice à la sécurité des usagers, des biens et au bon fonctionnement des réseaux de canalisations.

Sur le plan scientifique, l'étude des phénomènes d'érosion interne nécessite une démarche scientifique qui associe plusieurs disciplines, notamment la mécanique des sols et la mécanique des fluides. Selon Fell et Fry (Fell and Fry, 2007), quatre phénomènes d'érosion interne peuvent être distingués : l'érosion de conduit, l'érosion régressive, l'érosion de contact et la suffusion. Cette thèse porte sur la suffusion qui mobilise de manière sélective la fraction fine des grains qui constituent les sols. Sous l'action de l'écoulement interstitiel, certaines particules fines sont détachées, transportées puis éventuellement filtrées au cœur du squelette granulaire constitué principalement par la fraction grossière des grains. Ces mécanismes vont donc modifier la microstructure du sol et entraîner ainsi des modifications de sa conductivité hydraulique et probablement de son comportement mécanique.

Face à la complexité du processus de suffusion et dans le but de caractériser ce processus, notre démarche va consister tout d'abord à mener une étude bibliographique afin d'identifier les différentes phases de l'initiation et du développement de la suffusion. Les différents dispositifs expérimentaux et les critères de sensibilité potentielle à la suffusion qui sont détaillés dans la littérature seront ensuite présentés. L'étude expérimentale menée a pour but de caractériser les processus couplés de filtration et d'érosion sous écoulement vertical descendant. Une étude expérimentale comparative est également réalisée afin d'investiguer l'influence sur la suffusion, de la longueur de l'écoulement. Enfin un modèle numérique de suffusion est développé afin de pouvoir simuler plusieurs essais expérimentaux susmentionnés.

Chap. II Etude bibliographique

Plusieurs études ont souligné l'importance des mécanismes d'érosion interne dans les instabilités des ouvrages hydrauliques en terre et la confrontation des différentes instabilités a permis d'identifier quatre principaux mécanismes qui sont détaillés. Afin d'étudier la suffusion, différents dispositifs ont été développés qui permettent de tester des échantillons de diverses tailles : entre 50 mm et 300 mm de diamètre et de 50 à 600 mm de hauteur. Selon Garner et Fannin (Garner and Fannin, 2010) trois critères doivent être satisfaits pour l'initiation de ce processus : un critère géométrique, un critère de chargement mécanique et un critère de chargement hydraulique. La prise en compte du critère géométrique a permis la proposition de plusieurs critères d'initiation principalement basés sur la distribution granulométrique (Indraratna et al., 2015 ; Kenney and Lau, 1985 ; Kézdi, 1979 ; Lafleur et al., 1989 ; Li and Fannin, 2008 ; Wan and Fell, 2008). Dans la littérature, il convient de noter que la modélisation du chargement hydraulique a été menée suivant différentes approches en utilisant : le gradient hydraulique (Li and Fannin, 2012 ; Skempton and Brogan, 1994), la contrainte de cisaillement hydraulique (Reddi et al., 2000) ou la puissance (Marot et al., 2011 ; Sibille et al., 2015). A partir de l'intégration temporelle de la puissance (i.e. l'énergie dissipée par le fluide interstitiel) et de la masse érodée sèche, une classification de sensibilité à la suffusion a été proposée en distinguant six classes de très résistant à très érodable (Marot et al., 2016). Toutefois, si plusieurs recherches ont d'ores et déjà été menées sur la modélisation de l'écoulement en milieu poreux, très peu de modélisations sur le processus de suffusion sont à ce jour, disponibles dans la littérature.

Chap. III Etude expérimentale sur le couplage érosion et filtration

Cette étude a été réalisée à l'aide d'un perméamètre à paroi rigide, nommé œdoperméamètre qui permet de tester des échantillons de diamètre 280 mm et de hauteur maximale 600 mm. Pour l'application d'une contrainte axiale, la cellule est équipée d'un piston qui contient une couche de gravier afin de diffuser uniformément, sur la section haute de l'échantillon, l'écoulement descendant. L'échantillon repose sur une grille support, dotée d'un tamis d'ouverture choisie. L'embase de la cellule est en forme d'entonnoir pour éviter tout colmatage et le système de drainage est connecté à un réservoir équipé d'un trop plein et d'un système pivotant avec huit béchers pour la récolte des particules érodées. Deux réservoirs de 200 L chacun, avec régulation de la pression sont utilisés alternativement pour générer l'écoulement, sans arrêt de celui-ci. La paroi rigide de la cellule de l'œdoperméamètre est doté de 2 rangés de 6 prises de pression interstitielle chacune. Une prise de pression est présente à la base du piston (c'est-à-dire à l'interface entre l'échantillon et le piston) et une autre est située au niveau de l'entonnoir de l'embase.

Ces quatorze prises de pression sont toutes connectées à un seul capteur de pression, via un connecteur rotatif pour éviter toute dérive entre plusieurs capteurs de pression.

Des essais de filtration sont effectués avec deux matériaux pulvérulents : du sable de Fontainebleau et du gravier G3 (sablère Palvadeau). La couche filtrante située en partie inférieure des échantillons est exclusivement constituée de gravier. Pour étudier l'influence de l'interface, deux configurations sont mises en place pour la partie supérieure : le mélange sable-gravier est placé en partie centrale ou en partie périphérique des échantillons. L'analyse porte sur l'évolution spatiale de la distribution granulométrique et sur les variations temporelles des gradients hydrauliques locaux et de la conductivité hydraulique. Les résultats montrent la décroissance rapide de la quantité de particules filtrées avec la longueur de l'écoulement. Par ailleurs une petite quantité de particules filtrées apparaît suffisante pour modifier significativement la conductivité hydraulique du matériau.

Chap. IV Sensibilité à la suffusion

Pour cette étude, l'œdoperméamètre est utilisé et douze échantillons sont testés, incluant quatre distributions granulométriques continue et discontinue, avec un état initial des échantillons homogènes ou volontairement hétérogènes. L'analyse consiste à caractériser l'évolution spatiale de la distribution granulométrique après suffusion ainsi que les évolutions temporelles : de la distribution granulométrique des particules érodées, du gradient hydraulique local, de la conductivité hydraulique et de la masse sèche érodée. Au fur et à mesure de l'accroissement du gradient hydraulique global appliqué, trois étapes peuvent être distinguées au cours du développement de la suffusion : une étape d'ajustement des particules fines, puis une étape d'écoulement stable et enfin une étape d'évolution de l'écoulement. La suffusion semble d'abord concerner la fraction la plus petite des particules fines puis progressivement des particules plus grossières. En définitive, la suffusion apparaît comme le couplage complexe des phénomènes de : détachement, transport et filtration. Ainsi lorsque pour une couche de sol donnée, la filtration est prépondérante, le gradient hydraulique local est maximum, mais si cette valeur maximale du gradient local apparaît à la base de l'échantillon, une importante érosion de particules fines est aussi mesurée.

Chap. V Effet d'échelle spatiale sur la sensibilité à la suffusion

L'étude bibliographique a permis de souligner la diversité des dispositifs utilisés dans la littérature et donc la diversité des tailles d'échantillons testés. Pourtant l'influence de ces dimensions n'est pas bien établie. Dans ce contexte, l'étude réalisée a consisté à tester des échantillons de six distributions granulométriques distinctes, à l'aide de deux dispositifs de tailles bien diffé-

rentes : l'œdoperméamètre et un érodimètre triaxial de petites dimensions (diamètre échantillon : 50 mm, hauteur maximale d'échantillon : 100 mm) utilisé en conditions œdométriques. Les essais avec l'érodimètre triaxial ont été réalisés par Le Van Thao, doctorant de notre équipe de recherche. Tout d'abord il est noté une perte de particules fines au cours de la phase de saturation. Afin de limiter les écarts de conductivité hydraulique pour les échantillons d'un même sol mais de tailles différentes, la vitesse de saturation est contrôlée pour les deux dispositifs utilisés. Là encore, le couplage des phénomènes de détachement-transport-filtration est mis en évidence par la complexité des évolutions temporelles de conductivité hydraulique et taux d'érosion ainsi que par les évolutions granulométriques.

Pour l'ensemble des essais réalisés, il n'apparaît pas toujours possible d'identifier le gradient hydraulique critique par la méthode proposée par Skempton et Brogan (Skempton and Brogan, 1994) (i.e. par l'accroissement de la conductivité hydraulique). Toutefois lorsque cette détermination est possible, les résultats montrent que la valeur du gradient hydraulique critique diminue avec la longueur de l'écoulement. L'interprétation peut aussi reposer sur la détermination du taux d'érosion et de la contrainte de cisaillement hydraulique. Cependant les résultats indiquent là encore, une influence de la taille des échantillons testés.

L'approche énergétique est utilisée pour interpréter l'ensemble des essais. Lorsque la conductivité hydraulique est constante et que le taux d'érosion diminue, l'indice de résistance à l'érosion est calculé ce qui permet d'identifier la classification de sensibilité à la suffusion. Pour tous les sols testés, l'indice de résistance à l'érosion est du même ordre de grandeur avec les deux dispositifs. L'indice de résistance à l'érosion ne semble donc pas influencé par la longueur de l'écoulement.

Pour le sol argileux testé, sous contrainte effective faible, le développement de la suffusion a induit une érosion régressive qui a mobilisé tous les grains (i.e. pas uniquement la fraction fine). Ces résultats nécessitent une confirmation, notamment par la réalisation d'essais suivant différents états de contrainte. De tels essais nécessitent la possibilité de réaliser les essais en conditions triaxiales et y compris pour des matériaux plus grossiers que ceux qui peuvent être testés avec l'érodimètre triaxial de petites dimensions. Un érodimètre triaxial de grandes dimensions a été développé au sein de notre équipe et la contribution à ce développement effectuée dans le cadre de cette thèse est décrite dans l'annexe A.

Chap. VI Modélisation numérique de l'érosion interne

Pour le développement de ce modèle numérique, quatre phases sont distinguées : la phase solide non érodable, les fines érodables, les fines fluidisées et la phase fluide. Trois lois d'érosion,

inspirées de la littérature sont successivement utilisées. Ce modèle a été codé en 1D, à l'aide de la méthode des différences finies et du logiciel MATLAB.

Huit essais expérimentaux ont été simulés avec les trois lois d'érosion et les résultats des simulations ont été systématiquement confrontés aux mesures réalisées. Les résultats des simulations indiquent la possibilité de reproduire correctement les évolutions temporelles de masse érodée et de conductivité hydraulique. La comparaison de l'ensemble des simulations permet de conclure que la première loi d'érosion apparaît la plus appropriée pour la modélisation de la suffusion.

En utilisant cette première loi d'érosion et pour un sol donné, les influences du maillage, de la longueur de l'échantillon, de la conductivité initiale et du pourcentage initial de fines sont investiguées. Les résultats montrent qu'au-delà de $NS = 300$, le maillage n'a pas d'influence significative sur les résultats. L'influence du pourcentage de fines apparaît aussi limitée. En revanche, la longueur des échantillons influence la masse érodée et le débit. De même, la conductivité hydraulique initiale influence de manière significative les résultats. Enfin quelques conditions initiales peuvent conduire à une oscillation voire une non-convergence de la concentration des particules fluidisées, suivie par une oscillation de la porosité. Par contre la pression interstitielle n'oscille généralement pas.

Chap. VII Conclusion

Les phénomènes d'érosion interne sont complexes et responsables de nombreux désordres sur les ouvrages hydrauliques en terre ou en milieu urbain. Les recherches sur ces processus revêtent donc un important intérêt économique et sociétal. Sur le plan scientifique, ce thème de recherche est particulièrement marqué par son aspect interdisciplinaire entre la mécanique des sols et la mécanique des fluides. La suffusion est l'un des quatre processus d'érosion interne et il mobilise uniquement la fraction fine des sols. L'écoulement interstitiel peut effectivement détacher certaines particules fines qui vont ensuite être transportées dans le milieu poreux, certaines pouvant alors être filtrées. Ces mécanismes vont induire une variation de la microstructure du sol et donc une modification des propriétés hydrauliques et mécaniques du sol considéré. Afin de contribuer à la compréhension et à la caractérisation de la suffusion, des essais de filtration et de suffusion sont réalisés à l'aide d'un prototype expérimental nommé œdoperméamètre.

Les essais de filtration sont menés sur des échantillons constitués : en partie aval par une couche de gravier et en partie amont, par un mélange de sable et de gravier disposé suivant deux configurations. Les résultats mettent en évidence la rapide décroissance de la quantité de particules filtrées avec la longueur de l'écoulement, ainsi que la forte influence de ces particules filtrées sur la conductivité hydraulique du milieu poreux.

Afin de caractériser les variations locales de gradient hydraulique et de distribution granulométrique induites par la suffusion, des essais sont réalisés sur douze échantillons de quatre distributions granulométriques distinctes. Le couplage entre les mécanismes de détachement - transport d'une part et de filtration d'autre part apparaît responsable de la complexité des évolutions temporelles de gradient hydraulique local et de distribution granulométrique des particules érodées. Des essais de suffusion sont également menés sur six distributions granulométriques distinctes à l'aide de deux prototypes avec des échantillons de tailles différentes. La comparaison des résultats ainsi obtenus a permis de mettre en évidence l'influence de la longueur de l'écoulement sur l'approche en gradient hydraulique critique et l'approche en taux d'érosion. L'approche énergétique n'est pas affectée par cet effet d'échelle et permet donc de caractériser la sensibilité à la suffusion des sols.

Enfin un modèle numérique de suffusion est proposé en distinguant quatre phases et en utilisant trois lois d'érosion distinctes. Le modèle est codé avec le logiciel MATLAB en différences finies 1D et huit essais expérimentaux sont simulés. La confrontation des résultats de simulation avec les mesures permet de mettre en évidence la bonne concordance et d'identifier la loi d'érosion la plus appropriée. Par ailleurs, une étude de sensibilité est menée pour identifier l'influence du maillage, du pourcentage initial de fines, de la longueur de l'écoulement et de la conductivité hydraulique initiale.

Contents

- 1 Introduction 1**
 - 1.1 Background 1
 - 1.2 Internal erosion and urban environment 2
 - 1.3 Objective of the research 3
 - 1.4 Thesis layout 3

- II Literature review 5**
 - 2.1 Internal erosion 5
 - 2.2 Mechanisms of internal erosion 7
 - 2.2.1 Concentrated leak erosion 7
 - 2.2.2 Backward erosion 8
 - 2.2.3 Contact erosion 9
 - 2.2.4 Suffusion 10
 - 2.2.5 Control parameters for likelihood of internal erosion 11
 - 2.3 Self-filtration 13
 - 2.3.1 Self-filtration term 13
 - 2.3.2 Models of transport and deposition 13
 - 2.4 Criteria for likelihood of suffusion 14
 - 2.4.1 Geometric criteria to assess soil’s likelihood of suffusion 14
 - 2.4.2 Hydraulic gradient criteria 19
 - 2.4.3 Hydraulic shear stress 20
 - 2.4.4 Flow velocity 21
 - 2.4.5 Approach based on energy 21
 - 2.5 Devices and approaches for assessing soil susceptibility 23

2.5.1	Previously developed testing erodimeters for soil susceptibility experiments	23
2.5.2	Soil susceptibility classification for interface erosion	29
2.5.3	Erosion rate	30
2.6	Numerical simulation of seepage	31
2.6.1	Numerical modeling of internal erosion	31
2.6.2	Application of numerical method in seepage	32
2.7	Summary	34
III Experimental study on coupling of erosion and filtration		35
3.1	Introduction	35
3.2	Fundamental principle of controlling seepage flow by filter layer	36
3.2.1	Fundamental principles of filtration	36
3.2.2	Basic principle of decompression	37
3.3	Downward erosion–filtration test	37
3.3.1	Description of the used device	37
3.3.2	Specimen preparation and testing program	40
3.4	Testing results and discussion	43
3.4.1	Post-test sand filtering effect of filter layer of specimens	43
3.4.2	Hydraulic gradient	47
3.4.3	Analysis of the decompression effect of the filter during the test	49
3.4.4	Hydraulic conductivity	53
3.4.5	Comparison of experimental results and filtration law	55
3.4.6	Expended energy	57
3.5	Conclusion	58
IV Suffusion susceptibility		59
4.1	Introduction	59
4.2	Testing equipment and materials	59
4.2.1	Oedo-permeameter	59
4.2.2	Tested gradations	60
4.3	Downward seepage tests	62
4.3.1	Tested specimens	62
4.3.2	Experimental procedures	65
4.4	Analysis of experimental results	67

4.4.1	Post-test particle size distributions of specimens	67
4.4.2	Grain size distribution of eroded particles	69
4.4.3	Influence of fine particles in soil on the permeability	70
4.4.4	Hydraulic conductivity	77
4.5	Discussion	79
4.5.1	Hydraulic gradient ratio	79
4.5.2	Position of the maximum local hydraulic gradient	81
4.6	Qualitative analysis of seepage test	82
4.6.1	The three stages of the seepage process	82
4.6.2	Study of the permeation deformation mechanism	90
4.7	Conclusion	93
V	Spatial scale effects on suffusion susceptibility	95
5.1	Introduction	95
5.2	Laboratory experiments	95
5.2.1	Main characteristics of testing devices	95
5.2.2	Testing materials	97
5.2.3	Specimen preparation and testing program	99
5.3	Results	101
5.3.1	Post-test particle size distributions of specimens	101
5.3.2	Grain size distribution of eroded particles	103
5.3.3	Rate of erosion and hydraulic conductivity	104
5.4	Discussion	107
5.4.1	Onset of suffusion	107
5.4.2	Erosion coefficient	111
5.5	Method based on energy	113
5.6	Conclusion	115
VI	Numerical modeling of the internal erosion	117
6.1	Introduction	117
6.2	Model formulations	119
6.2.1	Mass exchange and mass balance equations	119
6.2.2	Constitutive equation for seepage erosion	122
6.2.3	One dimensional suffusion process	124
6.3	Finite difference based numerical solution	125

6.4	Numeric simulations of laboratory tests	126
6.4.1	Analysis of parameters affecting simulation results	126
6.4.2	Comparison of three erosion laws	137
6.5	Conclusions	141
6.5.1	FEM in the future	142
VII Conclusion and perspectives		149
7.1	Conclusion	149
7.2	Perspectives	152
Appendix A Contribution to the development of a new triaxial device		167
A.1	Introduction	167
A.2	Validation tests	168
A.2.1	Main characteristics of testing device	168
A.2.2	Specimen preparation and testing program	170
A.2.3	Testing materials	171
A.3	Test results and discussion	173
A.3.1	Post-test particle size distributions of specimens	173
A.3.2	Hydraulic conductivity and rate of erosion	174
A.3.3	Influence of suffusion on the mechanical strength	176
A.3.4	Suffusion susceptibility characterization	176
A.4	Conclusion	177
Appendix B Finite difference solution for 1D suffusion process		179

List of Figures

II.1	Timeline of the number of dam failures and the number of dam failures involving fatalities in the U.S. (NPDP, 2017)	6
II.2	Failure mechanism caused by through flow (Bartsch and Nilsson, 2007)	6
II.3	Illustration of initiation of internal erosion by four modes: backward erosion, concentrated leak erosion, soil contact erosion and suffusion (Zhang et al., 2016)	7
II.4	Dam failure caused by concentrated leak erosion (Fell and Fry, 2013)	8
II.5	Backward erosion piping mechanism (Sellmeijer et al., 2011)	9
II.6	Global backward erosion mechanism (Fell and Fry, 2013)	9
II.7	Contact erosion model (Fell and Fry, 2013)	10
II.8	Classification of broadly graded soils (Lafleur et al., 1989)	11
II.9	Factors affecting the initiation of internal erosion (Garner and Fannin, 2010) . .	12
II.10	Grain size distributions of some broadly graded soils without self-filtration (Sherard, 1979)	13
II.11	Main factors that influence the transportation of suspended particles (Yao et al., 1971)	14
II.12	H/F curve to assess instability by Kenney and Lau (Kenney and Lau, 1985) .	16
II.13	Method for assessing internal instability of broadly graded silt-sand-gravel soils (Wan and Fell, 2008)	17
II.14	Method for assessing internal instability of soils (Li and Fannin, 2008)	17
II.15	Method for assessing internal instability of soils (Indraratna et al., 2015)	19
II.16	Test arrangement of seepage test using permeameter cell (a) 245 mm, (b) 580 mm (Kenney and Lau, 1985)	26
II.17	Permeameter for screen tests (Lafleur et al., 1989)	26
II.18	Apparatus of seepage test (Skempton and Brogan, 1994)	27
II.19	Schematic diagram of downward flow seepage test apparatus (Wan and Fell, 2008)	27

II.20 Schematic of testing apparatus (Chang and Zhang, 2013a)	28
II.21 Seepage test apparatus (Marot et al., 2012): (a) General view of the IFSTTAR centrifuge bench, (b) schematic diagram of downward seepage flow test apparatus	28
II.22 Seepage test apparatus (Indraratna et al., 2015)	28
III.1 The type of filter layer and working mechanism	36
III.2 Real view of oedo-permeameter	38
III.3 Schematic diagram of oedo-permeameter	38
III.4 Erosion cell: (a) rigid cylindrical cell; (b) specimen supports; (c) wire mesh and grid	39
III.5 Soil collecting system: (a) effluent tank; (b) rotating sampling system	40
III.6 Grain size distribution of soils for filtration tests	41
III.7 Schematics and pictures of the filtration tests performed with the oedo-ermeameter	42
III.8 Profile of sand percentage after test for specimen Filtration-C	44
III.9 Profile of sand percentage after test for specimen Filtration-G-1	44
III.10 Profile of sand percentage after test for specimen Filtration-G-2	45
III.11 Influence of the saturation phase on the initial state of the specimen	45
III.12 Relative local hydraulic gradient versus time for specimen Filtration-C	48
III.13 Relative local hydraulic gradient versus time for specimen Filtration-G-1	48
III.14 Relative local hydraulic gradient versus time for specimen Filtration-G-2	49
III.15 The variation of hydraulic gradient ratio with the increasing time for specimen Filtration-C (“2”: layer L2R2-L3R3; “3”: layer L3R3-L4R4; “4”: layer L4R4-L5R5)	50
III.16 The variation of hydraulic conductivity ratio with the increasing time for specimen Filtration-C (“2”: layer L2R2-L3R3; “3”: layer L3R3-L4R4; “4”: layer L4R4-L5R5)	50
III.17 The variation of hydraulic gradient ratio with the increasing time for specimen Filtration-G-1 (“2”: layer L2R2-L3R3; “3”: layer L3R3-L4R4; “4”: layer L4R4-L5R5)	51
III.18 The variation of hydraulic conductivity ratio with the increasing time for specimen Filtration-G-1 (“2”: layer L2R2-L3R3; “3”: layer L3R3-L4R4; “4”: layer L4R4-L5R5)	51
III.19 The variation of hydraulic gradient ratio with the increasing time for specimen Filtration-G-2 (“2”: layer L2R2-L3R3; “3”: layer L3R3-L4R4; “4”: layer L4R4-L5R5)	52

III.20	The variation of hydraulic conductivity ratio with the increasing time for specimens Filtration-G-2 (“2”: layer L2R2-L3R3; “3”: layer L3R3-L4R4; “4”: layer L4R4-L5R5)	52
III.21	Variations of hydraulic conductivity in each layer for Filtration-C	53
III.22	Variations of hydraulic conductivity in each layer for Filtration-G-1	53
III.23	Variations of hydraulic conductivity in each layer for Filtration-G-2	54
III.24	The relationship between percentage of filtered particles and seepage length for three specimens	56
III.25	The relationship between percentage of filtered particles and seepage length for two experimental configurations	56
III.26	The relationship between cumulative expended energy and percentage of filtered particles	57
IV.1	Permeameter apparatus: the oedo-permeameter	60
IV.2	Tested grain size distributions	61
IV.3	Cumulative eroded dry mass versus cumulative energy of W-a	63
IV.4	Different types of homogeneity of specimens	64
IV.5	The electric mixer for production of specimens	66
IV.6	Grain size distribution after suffusion: (a) W-c-I (Zoom fine content), (b) W-c-II (Zoom fine content), (c) G-b-I	68
IV.7	Grain size distribution of detached particles for G-b-I	69
IV.8	Seepage judgment conditions	70
IV.9	The relationship between the hydraulic gradient and time for W-b-I	72
IV.10	The relationship between the hydraulic gradient ratio and time for W-b-I	72
IV.11	The variation of the global hydraulic conductivity and flow rate with the increasing time for W-b-I	73
IV.12	The relationship between the hydraulic conductivity of each layer and time for W-b-I	73
IV.13	Grain size distribution after test for W-b-I	74
IV.14	Grain size distribution before test for W-b-I	74
IV.15	Grain size distribution of eroded particles for W-b-I	75
IV.16	Time evolutions of hydraulic conductivity: (a) W-b-I, (b) W-d, (c) W-e-I	78
IV.17	Time evolutions of hydraulic gradient ratio: (a) W-b-I, (b) W-d, (c) W-e-I	80
IV.18	Cumulative eroded mass versus the position of maximum local hydraulic gradient for each step	81

IV.19 Schematic diagram for seepage extrusion	83
IV.20 Hydraulic conductivity and hydraulic gradient versus time curve of the whole soil layer (W-b-I)	84
IV.21 Hydraulic gradient of third and fourth layers versus time curve (W-b-I)	84
IV.22 Hydraulic conductivity and hydraulic gradient versus time curve of the whole soil layer (W-b-III)	85
IV.23 Hydraulic gradient of third and fourth layers versus time curve (W-b-III)	85
IV.24 Hydraulic conductivity and hydraulic gradient versus time curve of the whole soil layer (W-c-I)	86
IV.25 Hydraulic gradient of third and fourth layers versus time curve (W-c-I)	86
IV.26 Hydraulic conductivity and hydraulic gradient versus time curve of the whole soil layer (W-c-II)	87
IV.27 Hydraulic gradient of third and fourth layers versus time curve (W-c-II)	87
IV.28 Hydraulic conductivity and hydraulic gradient versus time curve of the whole soil layer (W-d)	88
IV.29 Hydraulic gradient of third and fourth layers versus time curve (W-d)	88
IV.30 Hydraulic conductivity and hydraulic gradient versus time curve of the whole soil layer (W-e-I)	89
IV.31 Hydraulic gradient of third and fourth layers versus time curve (W-e-I)	89
IV.32 Force diagram of particles in laryngeal tube	92
V.1 Permeameter apparatus (a) oedo-permeameter, and (b) triaxial erodimeter	96
V.2 Grain size distribution of tested soils	98
V.3 Influence of loss particles during saturation on initial hydraulic conductivity on soil 6	101
V.4 Initial soil gradation and post-suffusion gradations of (a) specimen 1-O; and (b) specimen 4-O	102
V.5 Grain size distribution of eroded particles for test 1-O	103
V.6 Time evolution of (a) the hydraulic conductivity; and (b) the erosion rate per unit pore area for soil 3	105
V.7 Time evolution of (a) the hydraulic conductivity; and (b) the erosion rate per unit pore area for soil 2	106
V.8 Flow velocity versus hydraulic gradient, critical hydraulic gradients for (a) soil 1; and (b) soil 3	108
V.9 Critical hydraulic gradient versus specimen length	110

V.10 Erosion rate per unit pore area versus hydraulic shear stress for (a) soil 1; and (b) soil 3	112
V.11 Cumulative loss mass versus cumulative expended energy	114
VI.1 REV of a fully saturated soil mixture and the four-constituent continuum model	119
VI.2 Geometry and finite difference grid in space-time of analyzed 1D internal erosion	126
VI.3 Variations in the cumulative eroded mass per cross-sectional area with time for different nodes	127
VI.4 Variations in the hydraulic conductivity with time for different nodes	127
VI.5 Variations in the cumulative eroded mass per cross-sectional area with time for different specimen heights	128
VI.6 Variations in the hydraulic conductivity with time for different specimen heights	129
VI.7 Variations in the concentration with depth at different times (a) $H = 0.225$ m, (b) $H = 0.325$ m, and (c) $H = 0.42$ m	129
VI.8 Variations in the concentration with time for different specimen heights	130
VI.9 Variations in the porosity with time for different specimen heights	130
VI.10 Variations in the flow rate with time for different specimen heights	131
VI.11 Variations in the cumulative eroded mass per cross-sectional area with time for different initial permeabilities	132
VI.12 Variations in the porosity with time for different initial permeabilities	133
VI.13 Variations in the concentration with time for different initial permeabilities	133
VI.14 Variations in the flow rate with time for different initial permeabilities	134
VI.15 Variations in the cumulative eroded mass per cross-sectional area with time for different fine content	135
VI.16 Variations in the hydraulic conductivity with time for different fine content	135
VI.17 Variations in the concentration with time for different fine content	136
VI.18 Variations in the porosity with time for different fine content	136
VI.19 Variations in the flow rate with time for different fine content	137
VI.20 Comparison of the calculated results of the cumulative eroded mass per cross- sectional area among three models (including experimental results) (a) specimen 1-O (b) specimen 4-O	143
VI.21 Comparison of the calculated results of the cumulative eroded mass per cross- sectional area among three models (including experimental results) (a) specimen 5-O (b) specimens 6-O-1 and 6-O-2	144

VI.22	Comparison of the calculated results of of the cumulative eroded mass per cross-sectional area among three models (including experimental results) (a) specimens 2-O-1 and 2-O-2 (b) specimen 3-O	145
VI.23	Comparison of the calculated results of the hydraulic conductivity among three models (including experimental results) (a) specimen 4-O (b) specimen 6-O-2 .	146
VI.24	Comparison of the calculated results of the hydraulic conductivity among three models (including experimental results) (a) specimen 2-O-1 (b) specimen 2-O-2	147
A.1	Schematic diagram of the large triaxial erodimeter	168
A.2	General view of the large triaxial erodimeter	169
A.3	Picture of the soil in site	171
A.4	Grain size distribution before test	172
A.5	Grain size distribution after suffusion test	173
A.6	Time series of the applied hydraulic gradient (a) and the computed hydraulic conductivity (b) during the suffusion test	174
A.7	Time series of the erosion rate per unit cross section	175
A.8	Deviatoric stress vs axial strain, with and without a full suffusion process . . .	176
A.9	Cumulative eroded mass vs cumulative expanded energy for the full suffusion test	177
B.1	Geometry and finite difference grid in space-time of analyzed 1D internal erosion	180

List of Tables

II.1	Erosion rate index, I_{HET} (Wan and Fell, 2004)	29
II.2	Erosion resistance index I_{α} for suffusion (Marot et al., 2011)	29
III.1	Specification of test materials	41
III.2	Types of each specimen	43
III.3	The average percentage of sand at each point within each layer	46
IV.1	Properties of tested gradations	61
IV.2	Potential susceptibility classifications based on recent geometric criteria	62
IV.3	Characteristics of the specimens	63
IV.4	Characteristics of hydraulic parameters	65
V.1	Properties of tested gradations	98
V.2	Properties of tested specimens and summary of testing program	100
V.3	Critical hydraulic gradient and erosion coefficient	109
V.4	Cumulative loss dry mass, cumulative expended energy, erosion resistance index and suffusion susceptibility classification	114
VI.1	Experimental results of computational specimen	139
VI.2	Model parameters	141
A.1	Properties of tested soil	172

List of Symbols

c	Particle mass concentration (%)
c_0	Initial particle mass concentration (%)
C_e	Coefficient of soil erosion
C_u	Uniformity coefficient
d_0	Smallest grain size (mm)
$d_{pore,c}$	Effective pore diameter of the coarse fraction (mm)
d_k	Control particle size (mm)
d_x	Sieve size for which $x\%$ of the sample by weight passes (mm)
$D_{x,f}$	Diameter of the $x\%$ mass passing in the fine part (mm)
$D_{x,c}$	Diameter of the $x\%$ mass passing in the coarse part (mm)
D_h^c	Kozeny effective diameter of the coarse fraction (mm)
D_i^c	Average diameter of grains in the i^{th} interval of the particle size distribution curve of the coarse fraction (mm)
$D(H/F)_{min}$	Corresponding diameter with the minimum value of ratio H/F (mm)
D_{c35}^c	Controlling constriction size for coarser fraction from constriction size distribution by surface area technique (mm)
$D_{85,SA}^f$	representative size for finer fraction by surface area technique (mm)
e	Void ratio
E_{flow}	Cumulative energy expended by the seepage (J)
f_c	Amount of erodible fines (%)
f_{c0}	Initial value of $f_c(x, t)$ (%)
$f_{c\infty}$	Ultimate fine content fraction after a long seepage period (%)
F^f	Mass percentage of the finer fraction (%)
g	Gravity acceleration (m/s^2)
G_r	Ratio of the maximal and minimal particle size of the missing interval

G_s	Specific gravity of the material
H/F	Ratio of H and F , where H is mass fraction between D and $4D$, and F is mass fraction smaller than particle diameter D
i	Hydraulic gradient
i_c	Critical hydraulic gradient
i'	Relative local hydraulic gradient
i_{local}	Local hydraulic gradient
i_{global}	Global hydraulic gradient
I_α	Erosion resistance index for surface erosion
I_{HET}	Erosion index for the hole erosion test
K	Intrinsic permeability (m^2)
k	Hydraulic conductivity (m/s)
k_d	Erodibility coefficient ($kg \cdot N^{-1} \cdot s^{-1}$)
k_n	Permeability coefficients of n^{th} layer of soil (m/s)
L	Specimen length (m)
$L_{non-saturated}$	Length of the specimen before saturation (mm)
$L_{saturated}$	Length of the specimen after saturation (mm)
m	Eroded dry mass (kg)
\dot{m}	Soil erosion rate ($kg \cdot s^{-1} \cdot m^{-2}$)
N_p	Average number of pore
O'_F	Actual opening size of voids (mm)
P	Percentage of particles finer than 0.063 mm (%)
P_{flow}	Seepage flow power (W)
p_w	Pore fluid pressure (Pa)
Q	Fluid flow rate (m^3/s)
q_w	1D volume discharge rate (the volume of flow through the unit cross-sectional area in unit time) (m/s)
r_p	Average radius of pores (m)
S	Cross section of the specimen (m^2)
S_p	Average pore area (m^2)
t	Duration (s)
T	Tortuosity which means the ratio between the shortest distance of two points in flow direction and the effective length of the flow path following the winding pore channels

T_n	Thickness of n^{th} layer of soil (m)
v	Velocity of the seepage (m/s)
\bar{v}_p	Mean pore velocity (m/s)
ΔF_i^c	Fraction of grains in the i^{th} interval of the particle size distribution curve of the coarse fraction (%)
Δh	Hydraulic head drop (m)
ΔL	Seepage length between two sections (m)
ΔP	Pressure drop (Pa)
Δz	Altitude change for a one dimensional flow between two sections (m)
α'	Arch coefficient, the number of particles with which the controlled particle size of the foundation soil may form an arch at the pore entrance of the filter layer and prevent other particles from entering
α_1	Stress reduction factor
α_D	Shape coefficient
α_t	Stress transformation coefficient
β_1	Material parameter
β_2	Material parameter
γ'	Submerged unit weight of soil (kN/m ³)
γ_d	Unit weight of dry soil (kN/m ³)
γ_w	Unit weight of water (kN/m ³)
λ	Filter coefficient
λ_e	Material parameter
μ	Dynamic viscosity (Pa·s)
ω	Specific volume of filtered fraction and filter fraction
ϕ	Porosity of soil
ϕ_0	Initial porosity of soil
$\phi_{0,c}$	Initial porosity of the coarse fraction
ϕ_c	Porosity of the coarse fraction
ρ_f	Water density (kg/m ³)
ρ_s	Soil density (kg/m ³)
$\bar{\rho}(c)$	Density of the mixture (kg/m ³)
$\bar{\sigma}'_{vm}$	Mean effective vertical stress of the soil (kPa)
τ	Hydraulic shear stress at the soil-water interface (Pa)
τ_c	Critical hydraulic shear stress at initiation of erosion (Pa)

INTRODUCTION

1.1 Background

Barriers, which are used to prevent flooding, provide hydropower, or store water for consumption or irrigation, are built in streams, rivers, and estuaries. Human beings have a long history of dam construction, with such structures dating back to 3,000 BC in Mesopotamia, the Middle East, and Ancient Egypt. With the development of science and technology, construction in this area has also made considerable progress. Thanks to the building of dams, water resources can be fully used to solve energy problems and fossil fuel pollution. As such, in the last century, dams have been widely constructed all over the world. Meanwhile, increasing numbers of investigators have been noticing, and then focusing on, the risks that may be associated with dams, particularly the internal erosion problem.

Internal erosion is an intricate phenomenon that is one of the most common reasons for failure of levees and soil dams. In a study by Foster et al. (Foster et al., 2000), among 11,192 surveyed dams, 136 revealed dysfunctions, around 46 % showed internal erosion, 48 % displayed overtopping, and 5.5 % exhibited sliding. These statistics confirm that internal erosion is a significant cause of failure. Today, many questions remain over internal erosion, specifically the influence on mechanical properties of soils, especially dynamic properties. Consequently, studies on internal erosion are highly influential in the industry and science area.

Internal erosion is highly difficult to detect because it has no apparent features; alternatively, while some subtle traces may be evident, they are often covered by water and therefore easily ignored. This means that internal erosion is very hazardous for dams and levees. If we are unable to discover and prevent internal erosion in a timely fashion, it will lead to failure in an extremely short time when the presence of erosion becomes obvious. As a matter of fact, because of the difficulty of observing internal erosion, an important process is considering and reducing the

possibility of such erosion during the construction of the dam. For instance, waterproof clay soil can be added to the surface of the dam to prevent seepage, or an impervious layer with smaller permeability can be built within the structure. In addition to all these actions, the mechanism of internal erosion research is also key to controlling the risk for the dams when internal erosion is not taken into account during the building process.

Past failure cases indicate that the potential for the loss of life in the event of a dam failure depends on the warning time available to evacuate the population at risk downstream of the dam (DeKay and McClelland, 1993; Jonkman et al., 2008). The warning time depends on the failure mode and the erosion resistance of the dam materials. Therefore, it is important to investigate the failure mechanisms of embankment dams and landslide dams and simulate the dam breaching process.

Because internal erosion is an interdisciplinary research field involving soil mechanics, fluid mechanics, environmental science, and so on, the investigation of this phenomenon will do much to deepen our understanding of these subjects. After years of research, we have already attained some knowledge of internal erosion. The internal erosion process can be divided into four phases: initiation, continuation, progression to form a pipe, and formation of a breach. Internal erosion in soil can be initiated by concentrated leak erosion, backward erosion, contact erosion, or suffusion (Fell and Fry, 2007). This research focuses on suffusion. Suffusion involves selective erosion of fine particles within the matrix of coarse soil particles under seepage flow. For a soil susceptible to suffusion, once some fine particles are washed away, the microstructure of the soil will change accordingly, which may induce a mutation of hydraulic and mechanical conditions in the soil (Schuler, 1995). In severe cases, the loss of fine particles could induce concentrated flow and lead to piping failure eventually. As such, security risk control of dams and levees is a complex issue. Meanwhile, the prevailing view of internal erosion is that it is worthy of study. Ever since Karl von Terzaghi (1883-1963) founded that the field of soil mechanics, internal erosion has consistently been one of the discipline's focal points. Although we already have an improved understanding of internal erosion, more efforts need to be made if we are to discover its deepest intricacies.

1.2 Internal erosion and urban environment

Internal erosion and urban environment are closely related. Coastal erosion and riparian erosion are common natural urban disasters. They will lead to the retreat and disappearance of the shore while transporting eroded sediment to harbors to damage waterways.

The aging and recession of urban underground pipeline systems are widespread problems. A variety of damage on the tube wall seriously affects the structural stability of a pipeline. Seepage from the cracked pipe will cause internal erosion in the city's underground, resulting in soil erosion and desertification.

Dams and levees are often built in the upper reaches of cities. If internal erosion is present in the embankment, it will pose a huge threat to urban safety. As such, research on internal erosion of the dam will help protect lives and property.

A coupling relationship exists between soil erosion and climate change. Soil erosion can affect soil carbon accumulation because of the vegetation, before influencing climate change. Conversely, the impact of global climate change on soil erosion is increasingly evident because of more heavy rain and strong winds. Internal erosion represents the intersection of environmental science and soil mechanics, and as such its study is of great urgency for urban life.

1.3 Objective of the research

As we know, the process of filtration is an important part of suffusion. A series of specially designed experiments will be realized for the filtration research. Thereafter, the soil susceptibility to internal erosion will also require investigation, especially the influence of heterogeneity on internal erosion. Considering that laboratory results are usually used in engineering directly, the scale effect of the specimen will be evaluated. To investigate the consequences of internal erosion, the mechanical properties of the given soil need to be analyzed, and the coupling of erosion and filtration will be studied. However, most triaxial instruments do not support large specimens, so some early work on a new large triaxial device will be conducted. Finally, we will attempt to apply numerical methods to the internal erosion research.

1.4 Thesis layout

This thesis comprises eight chapters.

In Chapter 1, we describe the background of internal erosion, its relationship with other fields, the objective of this research, and the thesis layout.

Chapter II is the literature review. Here, we describe the definition and phases of internal erosion, suffusion, and the instability of hydraulic structures as a result of suffusion. We also cover some widely used methods of assessing the potential of internal instability based on soil geometrics and controlling constriction size. Finally, the soil susceptibility discovered in previous work on

internal instability is presented.

Chapter III, the study concerns the coupling of erosion and filtration. The process of filtration is an important part of suffusion, and the coupling of erosion and filtration is always accompanied in the process of the suffusion. Considering that few experimental studies have been conducted on the coupling of erosion and filtration, a series of specially designed experiments will be undertaken for the coupling of erosion and filtration process research. From the two aspects of filtration and decompression, the filter mechanism in the coupling test of erosion and filtration is studied, and the relevant factors affecting filtration are discussed. At the same time, the filtering effect of the coupling test of erosion and filtration is analyzed.

In Chapter IV, we describe the suffusion susceptibility. We present the susceptibilities of soils, with a range of size distributions, to internal erosion, with a focus on the influence of heterogeneity on the latter.

The title of Chapter V is “Spatial Scale Effects on Suffusion Susceptibility”. Considering that the results from the laboratory are usually used in engineering directly, the scale effect of the specimen will be investigated to assess the risk of this method. The suffusion susceptibility experiments will be carried out on the large scale seepage instrument designed by our team. The experimental results are compared with those of small samples (cylinders of 50 mm or 100 mm in length and 50 mm in diameter), and they verify each other. The size effect of the specimens is discussed.

Chapter VI is entitled “Simulation of Homogeneous Specimens”. Here, we will endeavor to apply the numerical methods to the suffusion research. Firstly, four-constituent based mass exchange formulations are proposed to describe the detachment and transportation of finer particles. The coupling formulations are solved numerically by a finite difference method. Then, the model is validated by simulating 1D internal erosion tests by demonstrating that it can reproduce the main features of erosion during the suffusion process. Coefficients solution of the difference equation are given in the Appendix B.

Some early work on large triaxial devices is introduced in Appendix A. Because most triaxial instruments do not support large specimens, some early work is required to realize a new large triaxial device.

Finally, a general conclusion is offered for the whole study. Experimental and numerical works presented in this thesis are summarized, and recommendations for further research are indicated.

LITERATURE REVIEW

2.1 Internal erosion

Over the years, dams and dikes have played a significant role in irrigation, preventing floods, electricity generation, water supply, and so on. However, because of the flooding caused by dam or dike breach, earth structures also bring areas of potential risk to the downstream. In the 21st century, with the rapid social and economic development, the potential threat of dams to said development is also growing. Therefore, earth structure safety is not just an engineering security issue that only concerns administrative departments and earth structure managers but also a public safety issue that affects the populace at large. To study the laws of earth structure breakage and reduce the risk of breach, many countries and organizations have collated a huge amount of failure cases for analysis. In 1974, the International Commission on Large Dams (ICOLD) counted 202 cases of dam failure in 43 countries before 1965 (ICOLD, 1974). In 1995, ICOLD analyzed again the statistical data of 176 dam failure cases around the world (ICOLD, 1995). The United States Committee on Large Dams (USCOLD) also conducted two dam accident investigations in 1970s (USCOLD, 1975) and 1980s (USCOLD, 1988). The first survey saw the collection of 349 cases of serious accidents before the end of 1972, 74 of which involved dam failure. In the second investigation, 521 dam accident cases from 1973 to the end of 1985 were collected, of which 125 were dam failure cases. As shown in Figure II.1 (NPDP, 2017), the National Performance of Dams Program (NPDP), which was founded in 1994 at Stanford University, concluded that about 4% of dam failures in the United States involve fatalities. Many researchers have also collected dam accident cases and used them to perform analysis. Vogel (Vogel, 1981) collected hundreds of dam failure cases. In addition, Blind (Blind, 1983) and Foster et al. (Foster et al., 2000) performed statistical analyses based on these cases. In Foster et al.'s study, among 11,192 surveyed dams, 136 revealed dysfunctions, of which around

46 % were caused by internal erosion, 48 % were a result of overtopping, and 5.5 % were down to sliding. According to the statistic result of failure cases and distresses of embankment dams (Fell et al., 2003; Foster et al., 2000; Zhang et al., 2009), internal erosion has historically resulted in about 37 % embankment dam failures.

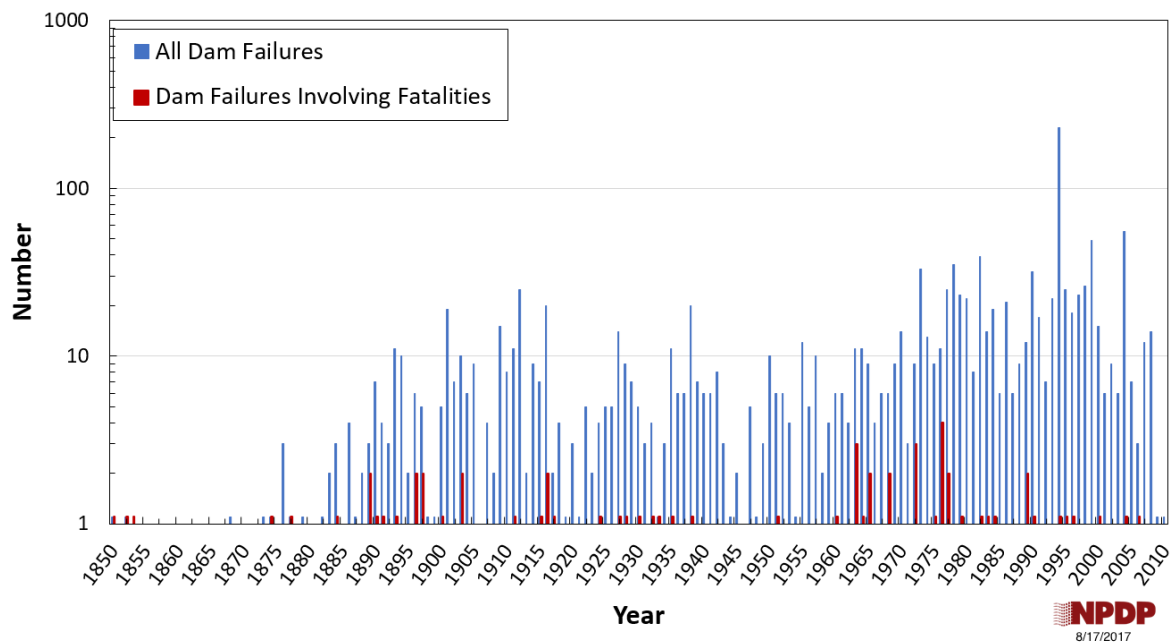


Figure II.1 – Timeline of the number of dam failures and the number of dam failures involving fatalities in the U.S. (NPDP, 2017)

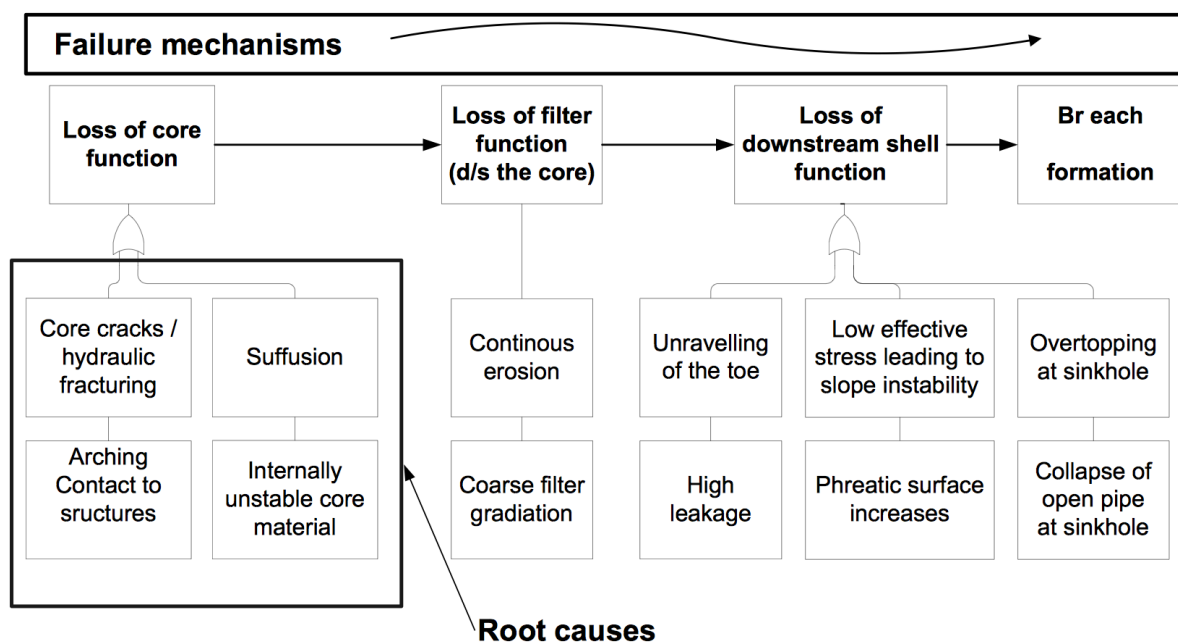


Figure II.2 – Failure mechanism caused by through flow (Bartsch and Nilsson, 2007)

Initiating root causes of internal erosion and resulting failure mechanisms caused by through flow are illustrated in Figure II.2. Four processes occur in the event of dam failure: initiation, continuation, progression and breach (Fell and Fry, 2007). Correspondingly, in Figure II.2, the

four steps are loss of core function, loss of filter function, loss of downstream shell function and breach formation. Therefore, it is crucial to gain fundamental understandings of the triggering mechanism and process of internal erosion. Today, many questions remain over internal erosion, such as the influence of spatial scale on soil susceptibility and the influence of erosion on soil's mechanical properties.

In summary, it is essential to investigate the internal erosion of embankment dams to better understand the mechanisms and to suggest possible improvement of the engineering practice.

2.2 Mechanisms of internal erosion

Internal erosion is one of the most common failure modes of embankment dams. It refers to the loss of soil particles within an embankment dam or its foundation by seepage forces. Nowadays, there are usually four types of internal erosion that are considered (Fell and Fry, 2007): (i) concentrated leak erosion, (ii) backward erosion, (iii) contact erosion and (iv) suffusion. Figure II.3 illustrates these four initiation modes for internal erosion (Zhang et al., 2016). Seepage exists without exception, the varying extent of which is shown by the different orders of magnitude. This seepage is safe unless the seepage rate is out of control, which will lead to failure. Next, four different internal erosion processes will be introduced.

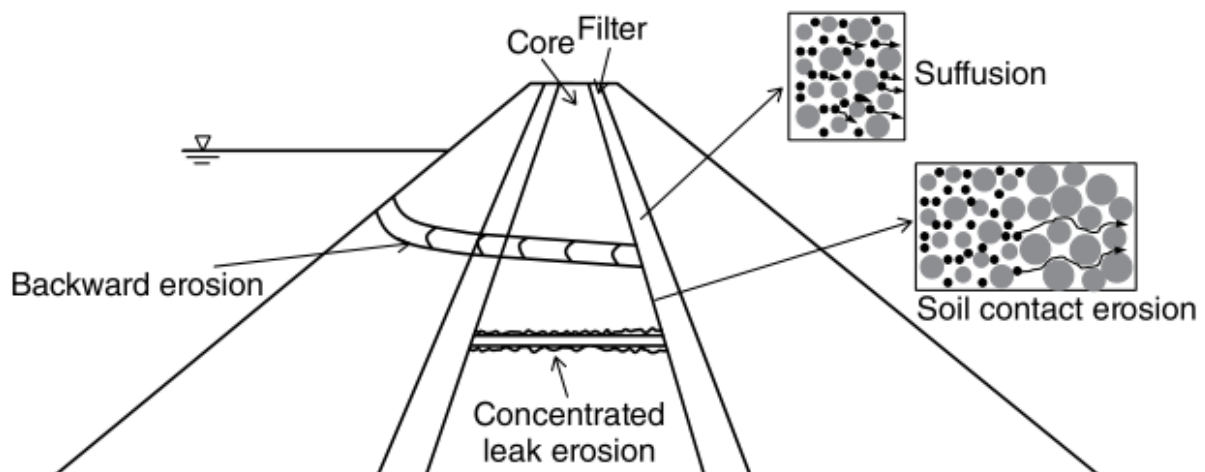


Figure II.3 – Illustration of initiation of internal erosion by four modes: backward erosion, concentrated leak erosion, soil contact erosion and suffusion (Zhang et al., 2016)

2.2.1 Concentrated leak erosion

Water seepage within earth structures, such as embankments, dams, or dikes, can generate the detachment and transport of particles from the soil constituting their structure or foundation.

Moreover, the seepage force will cause the particles to detach from the surface of the soil structures, and if a concentrated leakage exists in these cracks, this will result in their deterioration and the formation of a tunnel connecting the upstream and downstream (Benahmed and Bonelli, 2012). This process is named concentrated leak erosion because the water erodes a crack, a hole, or a hollow. Concentrated leakage may enlarge pre-existing cracks or holes by seepage forces. Along pipes within embankments, soil particles are detached from dams or core materials. When a concentrated leak affects a levee, the walls will be eroded or scoured.

Cracks may exist within an embankment core as a result of differential settlement, hydraulic fracture, or desiccation (Fell et al., 2005). In continuous and permeable zones, the concentrated leak erosion will emerge with a high probability because this type of soil is prone to creating an interconnecting void system (Hunter, 2012). Figure II.4 presents a dam failure caused by concentrated leak erosion. The case is the “Saint-Julien des Landes dam”. During first filling, the concentrated leak erosion appeared at: (a) the upstream slope and (b) the pipe.



Figure II.4 – Dam failure caused by concentrated leak erosion (Fell and Fry, 2013)

2.2.2 Backward erosion

Researchers such as Terzaghi (Terzaghi, 1939) and Sherard (Sherard et al., 1963) have described backward erosion, which has two different types: backward erosion piping and global backward erosion (Fell and Fry, 2013).

Backward erosion piping will lead to regression of eroded particles from downstream. A penetrating pipe is created by the eroded particles when moving along the upstream line toward the external environment. Figure II.5 reveals the processes of backward erosion piping.

Backward erosion piping begins on the free surface, which is formed with the erosion of non-cohesive soils. Furthermore, if heave occurs, backward erosion is apt to be initiated (Cyganiewicz et al., 2008). This piping can be recognized by the sand boils at the downstream side. Figure II.6 shows how global backward erosion will result in a near vertical pipe in the

core of a dam.

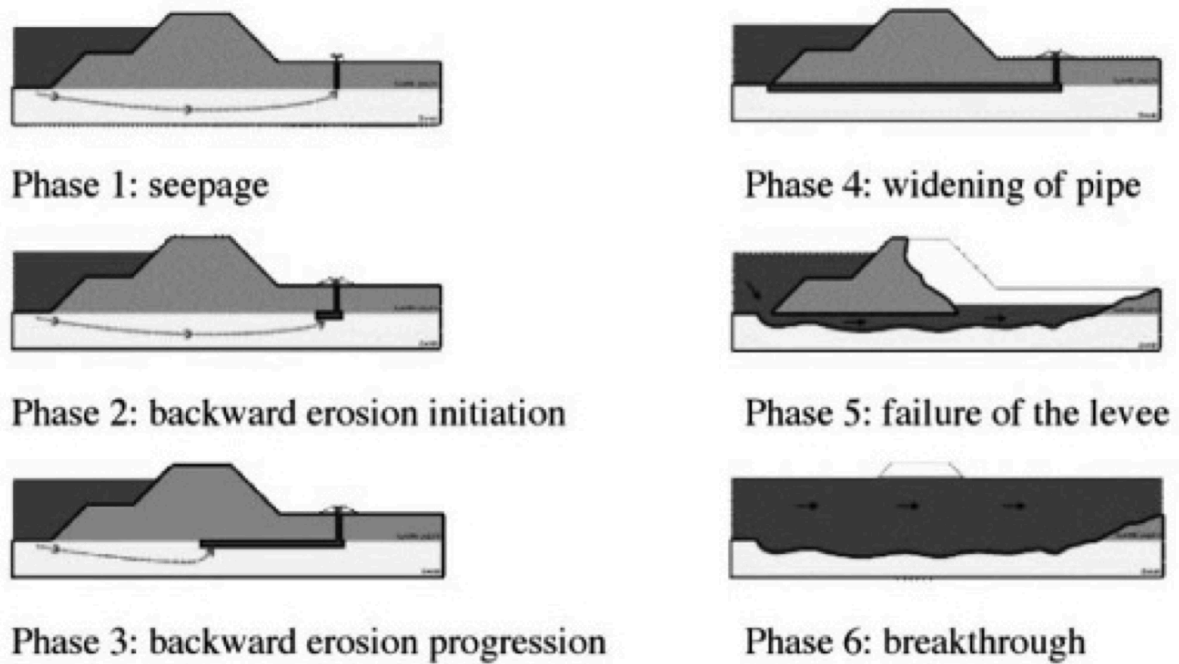


Figure II.5 – Backward erosion piping mechanism (Sellmeijer et al., 2011)

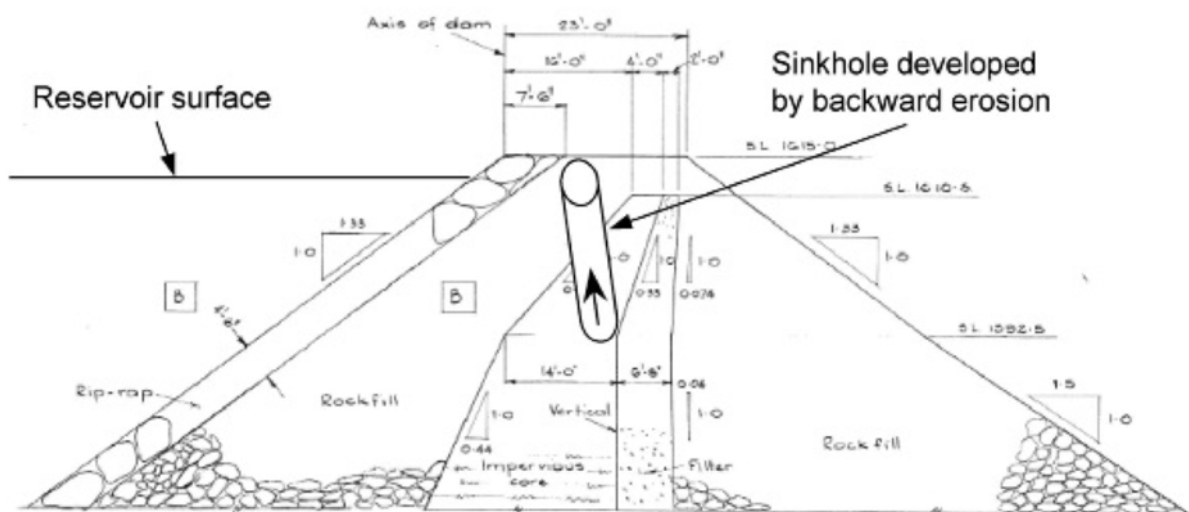


Figure II.6 – Global backward erosion mechanism (Fell and Fry, 2013)

2.2.3 Contact erosion

Contact erosion is a type of internal erosion in which fine particles are selectively eroded from the place where a coarser layer is in contact with a fine soil, when the flow is parallel through the coarser layer (Hoffmans, 2012). In the foundations of a dam or a levee, the flow through the gravel layer will lead to erosion of the fine particle layer, or the fine particles at the core will move into the coarser layer because of the segregation during the soil structure, as displayed in

Figure II.7.

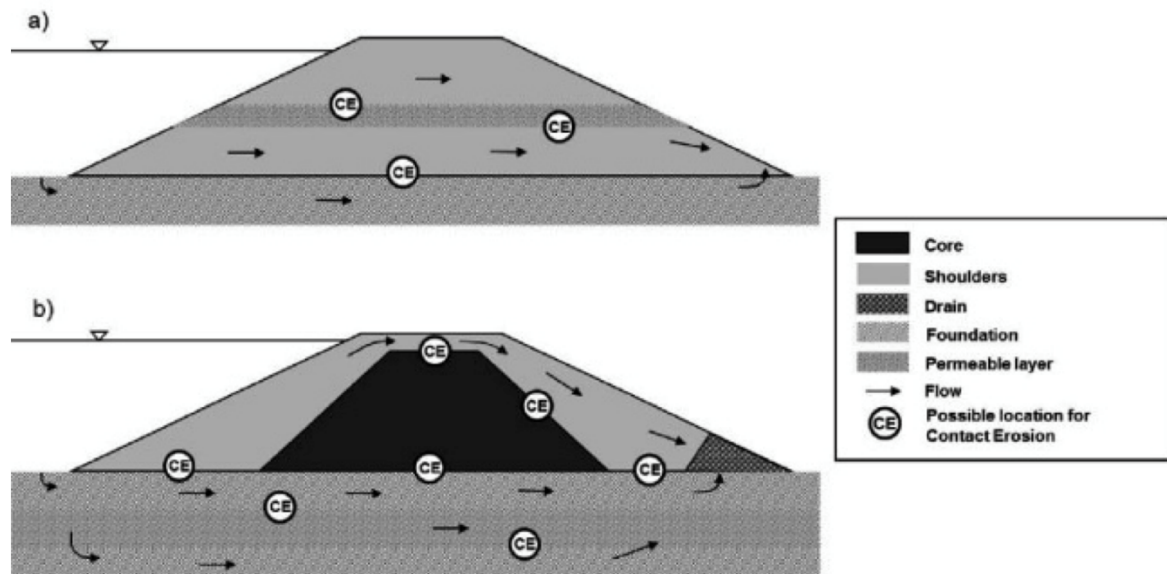


Figure II.7 – Contact erosion model (Fell and Fry, 2013)

2.2.4 Suffusion

In suffusion, the fine particles are selectively eroded from the matrix of coarser particles. Suffusion may occur when the soil is gap-graded materials and presents internal instability (Kézdi, 1979). The potential for suffusion and instability is based on the grain size distributions (Kenney and Lau, 1985). Research has shown that the critical hydraulic gradient for unstable materials is much lower than the value calculated by Terzaghi's theory, at almost one third the critical gradient for heaving (Skempton and Brogan, 1994). The fine particles move through the voids between the coarser particles, which remain stationary. Particles move through the entire soil, not just from the downstream surface along the upstream line as in backward erosion (Fell and Fry, 2013). Because effective stresses load the coarser particles, little or no volume change or loss of matrix integrity occurs. Three criteria must be satisfied for suffusion: geometric criterion, stress criterion, and hydraulic criterion (Wan and Fell, 2008).

1. The size of fine particles must be smaller than the size of the voids between the coarser particles, which compose the matrix of the soil.
2. The fine particles are not enough to cram the space between the coarser particles. If the fine particles are enough to fill the voids, they will be loaded by the effective stresses. We need to allow some fine particles to move freely.
3. The rate of flow through the soil must be able to apply sufficient stress to conquer the resistance to the fine particles' movement through the constrictions between the rough

particles.

Gradation and particle size are important for suffusion. With the increase in particle size, higher velocity (more energy) of flow is required to move the soil particles. In addition, the potential for internal instability is the linchpin gradation element for the process of suffusion. This is a problem for broadly graded soils (particle sizes with extensive range), especially gap-graded soil (absence of medium sized particles). Lafleur et al. (Lafleur et al., 1989) categorized the broadly graded soils into three types, as shown in Figure II.8.

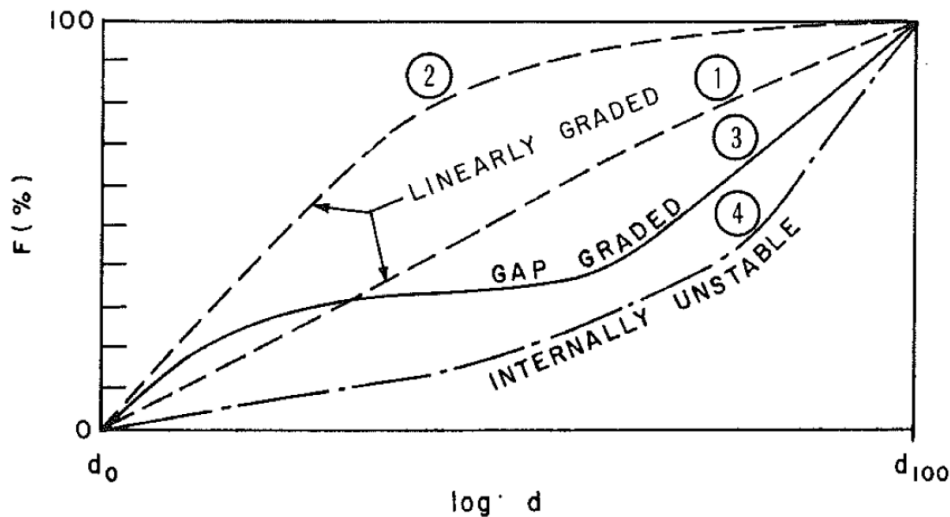


Figure II.8 – Classification of broadly graded soils (Lafleur et al., 1989)

2.2.5 Control parameters for likelihood of internal erosion

Internal erosion of a soil is influenced by geometric conditions of soil, hydraulic conditions, and mechanical conditions (Garner and Fannin, 2010; Indraratna et al., 2011; Kenney and Lau, 1985; Richards and Reddy, 2007; Schuler, 1995; Wan and Fell, 2004). However, the control variables for different modes of internal erosion are not exactly the same. For backward erosion, the most important factors are hydraulic gradient, seepage exit location, relative density of the soil, and grain size distribution. Once a pipe forms within a dam or its foundation, the hydraulic shear stress induced by the pipe flow and the erodibility of the soil are the two most critical parameters influencing the enlargement of the pipe and its stability. For concentrated leak erosion, the soil property (i.e., fines content, dispersivity, degree of compaction, water content, and plasticity index), hydraulic gradient, hydraulic shear stress within the crack, crack orientation and diameter, and chemical property of the fluid are the most important parameters.

Currently, a typical measure of hydraulic conditions that control the onset of internal erosion in dams is critical hydraulic gradient. When the hydraulic gradient reaches a critical value, the fine

particles in the dam body or its foundation may erode. The mechanical conditions of the dam material (i.e. stress state, relative compaction) also influence the initiation of internal erosion.

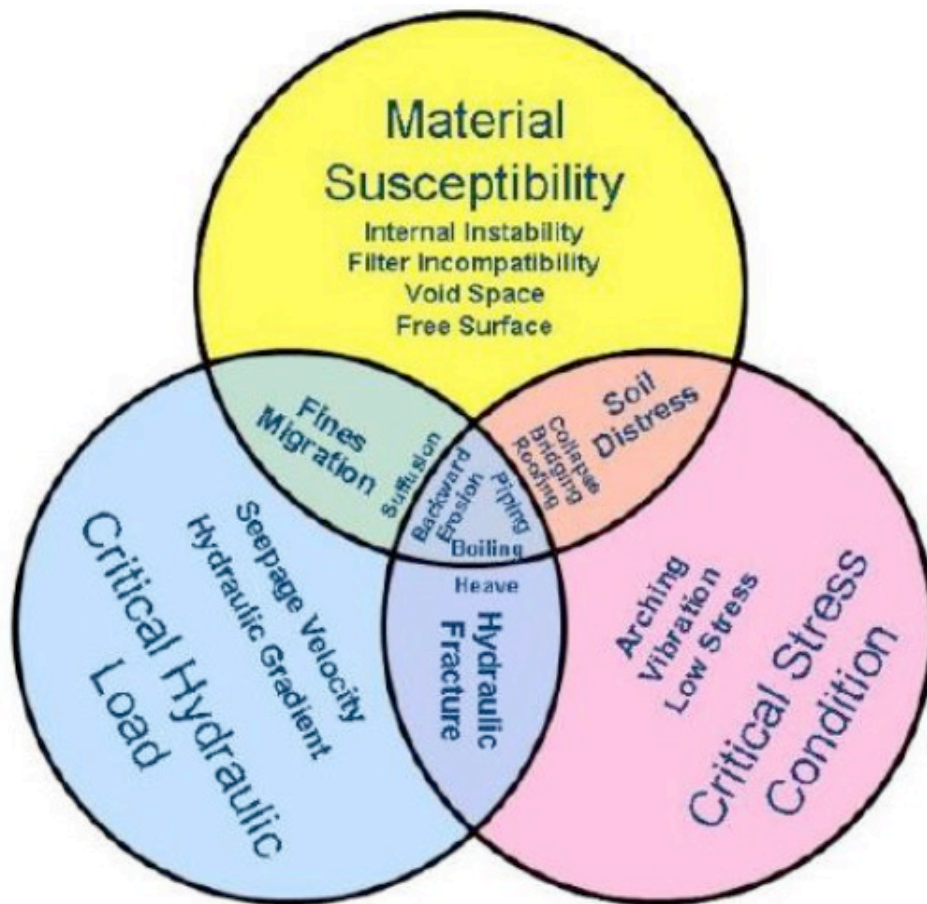


Figure II.9 – Factors affecting the initiation of internal erosion (Garner and Fannin, 2010)

There are three conditions as shown in Figure II.9 for internal erosion initiation and progression (Garner and Fannin, 2010):

- (a) Material susceptibility. The material susceptibility to internal erosion is associated with the possibility of fine fraction being removed from its parent matrix. The detachment and migration are related to grain size distribution, shape of the grains and pores. And for cohesive soil, it can be affected by the physicochemical characteristics of solid medium such as dispersiveness.
- (b) Critical hydraulic load. This factor can refer to the hydraulic gradient, the seepage velocity and the hydraulic shear stress which exist in the embankment and foundation. The critical hydraulic load is associated with the action of seepage flow that is enough to trigger the initiation of internal erosion.
- (c) Critical stress conditions. The critical stress condition is related to the ability against internal erosion due to the magnitude of effective stress within the earth structure.

2.3 Self-filtration

2.3.1 Self-filtration term

This mechanism is a part of suffusion. It will lead to the end of particles' migration at the base soil-filter interface. Medium sized particles are carried by the seepage from the core material into the filter, where they become trapped by the coarse particles as they keep in contact with each other. The retained medium sized particles then in turn prevent erosion of, or filtrate, finer particles, which in turn filtrate even finer particles. This process will recur until no more particles can move. The area within the filter where the self-filtration mechanism occurs is normally known as the "self-filtration zone". Kezdi (Kézdi, 1979) and Sherard (Sherard, 1979) both proposed a method to evaluate the potential of self-filtration. This is realized by plotting the grain size distribution and checking the compatibility of fine and coarse fractions. Figure II.10 shows some grain size distributions without self-filtration, as tested by Sherard (Sherard, 1979). Lafleur et al. (Lafleur et al., 1989) detailed the self-filtration mechanism and found that for broadly graded soils, the process of self-filtration is mainly related to the coefficient of broadness, defined as O'_F/d_0 , where O'_F means the actual opening size of voids and d_0 is the smallest grain size, to the profile of their gradation curve.

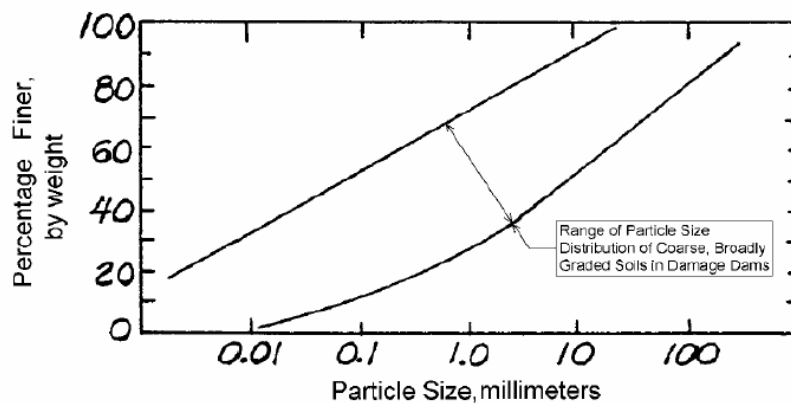


Figure II.10 – Grain size distributions of some broadly graded soils without self-filtration (Sherard, 1979)

2.3.2 Models of transport and deposition

In 1937, Iwasaki (Iwasaki et al., 1937) proposed the basic empirical filtration equation and recognized that particle removal from solution was the first order in particle concentration:

$$c(\Delta L) = c_0 e^{-\lambda \Delta L} \quad \text{II.1}$$

Where c_0 is the initial particle mass concentration, $c(\Delta L)$ is the particle concentration after flow through a filter with seepage length ΔL , and λ is the filter coefficient.

Stein (Stein, 1940) assumed that the suspended particles were carried by the flow surrounding the collector. According to this hypothesis, the main factors as shown in Figure II.11 that influence the transportation of suspended particles are the interception, the sedimentation, and the diffusion (Yao et al., 1971).

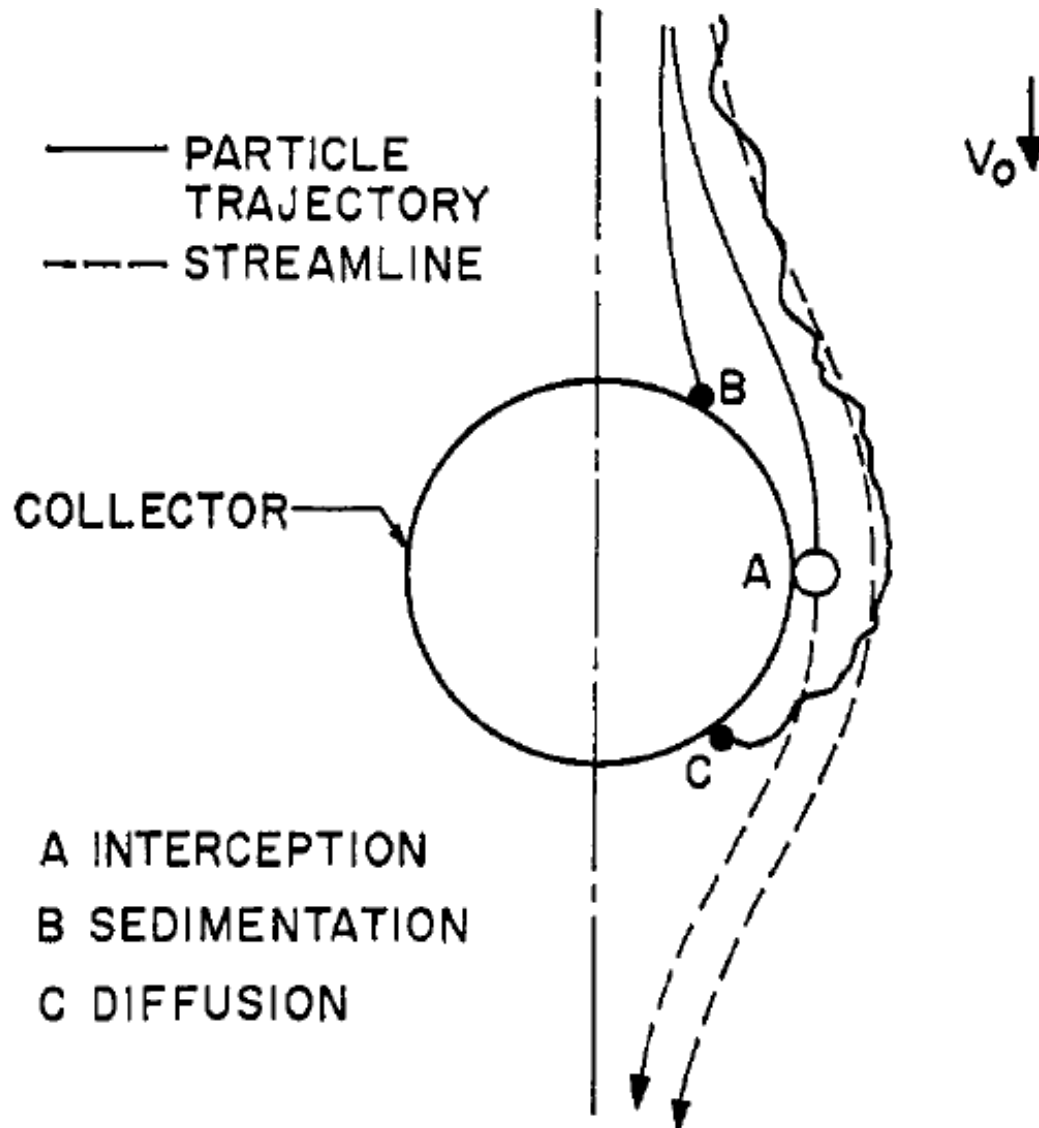


Figure II.11 – Main factors that influence the transportation of suspended particles (Yao et al., 1971)

2.4 Criteria for likelihood of suffusion

2.4.1 Geometric criteria to assess soil's likelihood of suffusion

The geometric condition of a soil may control the potential of internal erosion. Proposals for various geometric assessment methods exist in the literature. Geometric criteria can be divided

into two types: (a) based on the particle size distribution; (b) based on constriction size distribution.

Kézdi and Sherard criteria

As mentioned before, Kezdi (Kézdi, 1979) and Sherard (Sherard, 1979) both proposed a method of splitting a curve into its coarse and fine components. According to Terzaghi's idea of filtration criterion, self-filtering is the process whereby the coarse particles of a cohesionless soil prevent erosion of the fine particles, which is considered by this method. The soil is internally unstable if the maximum value of $D_{15,c}/D_{85,f}$ is greater than 4 where $D_{15,c}$ is the diameter of the 15% mass passing in the coarse fraction; $D_{85,f}$ is the diameter of the 85% mass passing in the fine fraction. Furthermore, Moffat and Fannin (Moffat and Fannin, 2006) indicated that a soil is stable if $(D_{15,c}/D_{85,f})_{max} \leq 4$ and unstable if $(D_{15,c}/D_{85,f})_{max} \geq 7$. However, in the case of a continuous grain size distribution (as opposed to gap-graded distribution), for this method the main difficulty is related to the selection of the point at which to precisely split the grain size distribution between fine and coarse fractions.

Kovács method

Kovács (Kovács, 1981) proposed an average pore diameter based on the capillary tube model to assess internal stability. The average pore diameter of the coarse fraction $d_{pore,c}$ is computed as the following expression:

$$d_{pore,c} = 4 \frac{\phi_c}{1 - \phi_c} \frac{D_h^c}{\alpha_D} \quad \text{II.2}$$

Where ϕ_c is the porosity of the coarse fraction. The Kozeny effective diameter of the coarse fraction is D_h^c , and α_D is the shape coefficient (for rounded particles this is 6, for angular particles it is 7 to 9).

The porosity of the coarse fraction ϕ_c is:

$$\phi_c = \phi + F^f(1 - \phi) \quad \text{II.3}$$

Where ϕ is the porosity of the soil, and F^f is the mass percentage of the finer fraction.

D_h^c can be computed by:

$$D_h^c = \frac{1}{\sum \frac{\Delta F_i^c}{D_i^c}} \quad \text{II.4}$$

Where ΔF_i^c and D_i^c are the weight and average diameter of grains in the interval of i according to the particle size distribution curve of the coarse fraction.

Kenney and Lau method

For this method, the boundary between unstable and stable soil is based on the shape of the particle size grading curve. Kenney and Lau (Kenney and Lau, 1985) defined the ratio of F and H , where F denotes a mass fraction smaller than particle diameter D , and H measures the mass fraction between D and $4D$ (as shown in Figure II.12(a)). Soils with a ratio $H/F < 1$, as shown in Figure II.12(b) are defined as internally unstable. They chose a size interval with a ratio equal to four times because the size of predominant constrictions in the void network of a filter is approximately equal to one quarter the size of particles making up the filter, meaning particles of size D can pass through a filter composed of particles of size $4D$ or larger. With the aim of determining the boundary of coarser and finer fractions, Li and Fannin (Li and Fannin, 2008) later indicated that the limit corresponds to the minimum value of ratio H/F .

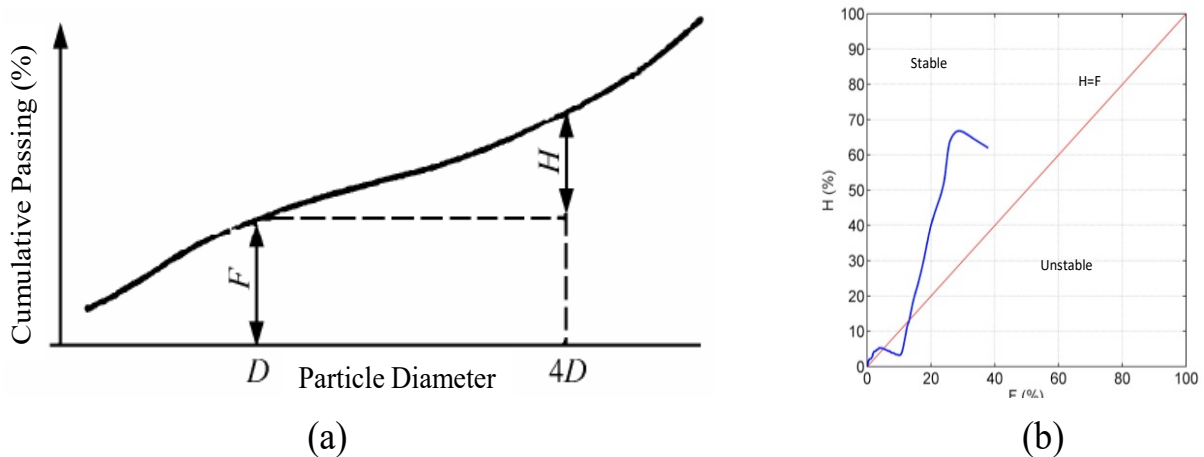
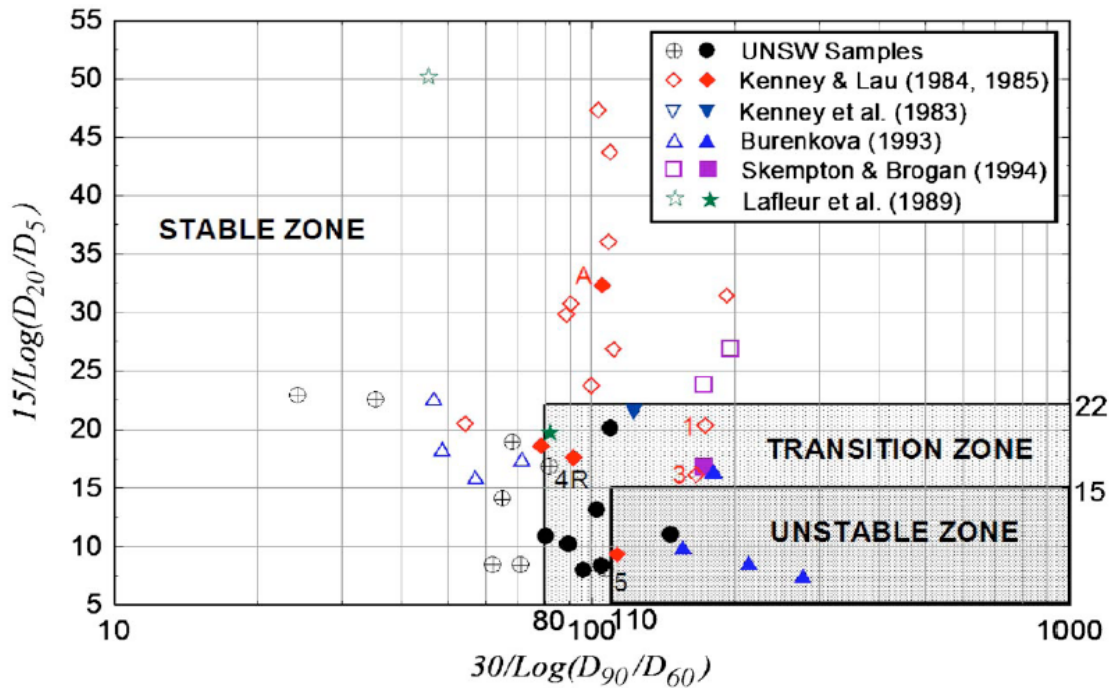


Figure II.12 – H/F curve to assess instability by Kenney and Lau (Kenney and Lau, 1985)

Wan and Fell method

After testing 20 soil samples, Wan and Fell (Wan and Fell, 2008) proposed the hypothesis that soils with a steep slope on the coarse fraction and a shallow slope on the finer fraction are likely to be internally unstable. Through trials, they found that these gradations could be represented by defining couple ratios between d_{90}/d_{60} and d_{20}/d_5 . Figure II.13 plots these values and defines two boundaries to assess the internal instability of broadly graded silt-sand-gravel soils. Take note that this method is not able to identify the internal instability of gap-graded soils or soils having a finer fraction less than 15%.



- Notes:
 1. Hollow symbol represents internally stable sample.
 2. Solid symbol represents internally unstable sample.

Figure II.13 – Method for assessing internal instability of broadly graded silt-sand-gravel soils (Wan and Fell, 2008)

Li and Fannin method

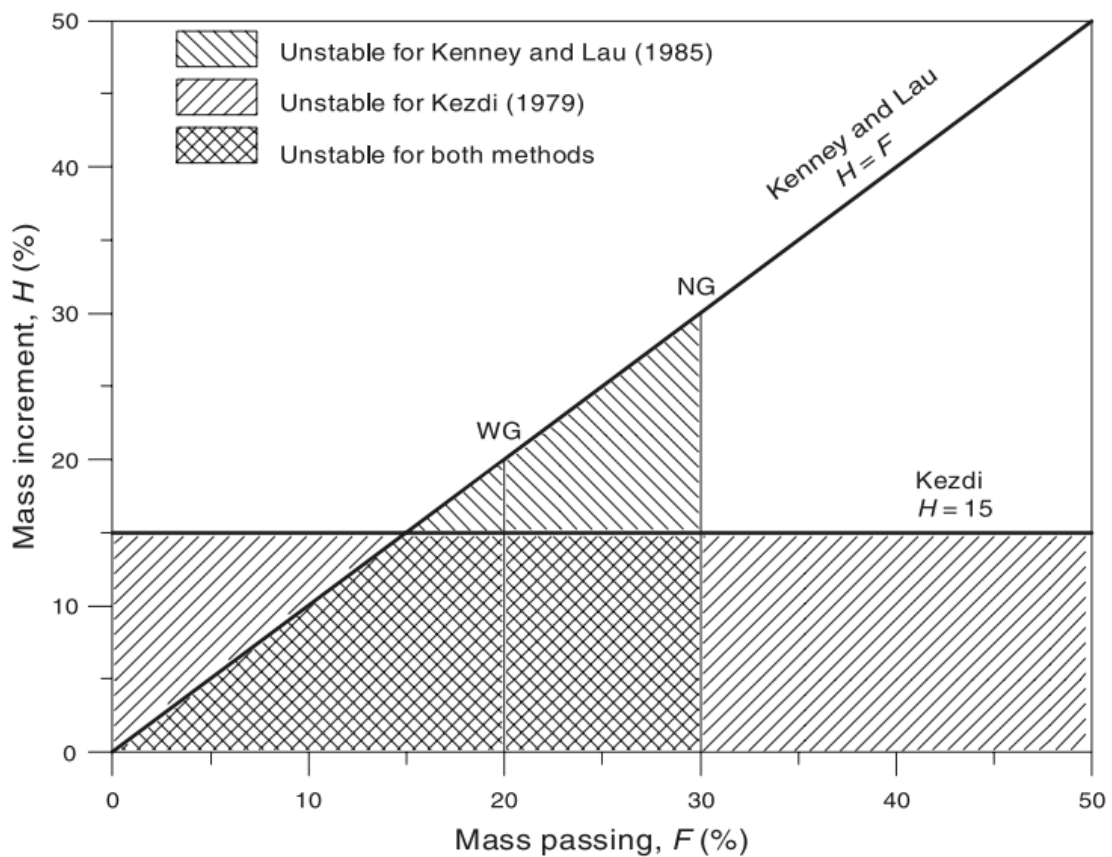


Figure II.14 – Method for assessing internal instability of soils (Li and Fannin, 2008)

Using a database of 25 gap-graded soils and 32 widely graded soils, Li and Fannin (Li and Fannin, 2008) set out to compare the subtle differences between the Kenney and Lau (Kenney and Lau, 1985) and Kézdi (Kézdi, 1979) methods and proposed a strategy for assessing internal stability based on the filtering capacity of the coarse to the fine particles. The result of the comparison was that the filter ratio $D_{15,c}/d_{85,f}$ of the Kézdi's method is more conservative for $F^f < 15\%$, and the stability index $(H/F)_{min}$ of the Kenney and Lau's method is more conservative for $F^f > 15\%$. The method is shown in Figure II.14.

Chang and Zhang method

According to the content of particles finer than 0.063 mm (named P), three geometric criteria for well-graded soils and gap-graded soils were proposed by Chang and Zhang (Chang and Zhang, 2013b), which are only applicable to low plasticity soils. Kenney and Lau's criterion (Kenney and Lau, 1985) $(H/F)_{min}$ is used for well-graded soils. The soil is stable if $P < 5\%$ and $(H/F)_{min} > 1.0$. With $5\% \leq P \leq 20\%$, soil is stable if $(H/F)_{min} > 4/3 - P/15$ and a soil with $P > 20\%$ is stable. For gap-graded soils, the stability is assessed with gap ratio $G_r = d_{max}/d_{min}$ (d_{max} and d_{min} are the maximal and minimal particle size, respectively, of the missing interval). With $P < 10\%$, a soil is stable if $G_r < 3$. A soil with $10\% \leq P \leq 35\%$ is stable if $G_r < 0.3P$, and with $P > 35\%$, the soil is considered stable.

Indraratna et al. method

Detached particles can be moved by seepage flow when the size of the controlling constriction in the pore network is larger than the maximum diameter of the loose particles. Indraratna et al. (Indraratna et al., 2015) proposed a criterion based on a probabilistic method using a broadly graded soil. The grading information and relative density of the soil are necessary for plotting the constriction size distribution curve. By dividing a soil into a coarse and a fine component, according to the $(H/F)_{min}$ ratio (Kenney and Lau, 1985) for $F^f \leq 30\%$ and adopting the method of surface area technique, two curves can be obtained, namely the particle size distribution of the finer fraction and the constriction size distribution of the coarser fraction by the surface area technique for a given relative density. $D_{c35}^c/d_{85,SA}^f$, the ratio between the controlling constriction size of coarse particles and the fine fraction component, was deduced to distinguish stable from unstable soils. D_{c35}^c is defined as the controlling constriction size of the coarse component, and $d_{85,SA}^f$ is the representative size for the finer fraction. If a soil satisfies $D_{c35}^c/d_{85,SA}^f \leq 1$, it is considered internally stable as shown in Figure II.15. For this method, it was assumed that the coarse particles contact each other in that the pore formed by the coarse

particles is filled by the fine particles. However, even in soil specimens compacted by moisture tamping, some fine particles could also form the matrix.

Kovács (Kovács, 1981) recognized that even if the geometrical conditions allow particle movements, the hydraulic conditions have to be studied. To take the hydraulic loading into account, different approaches have already been described in the literature.

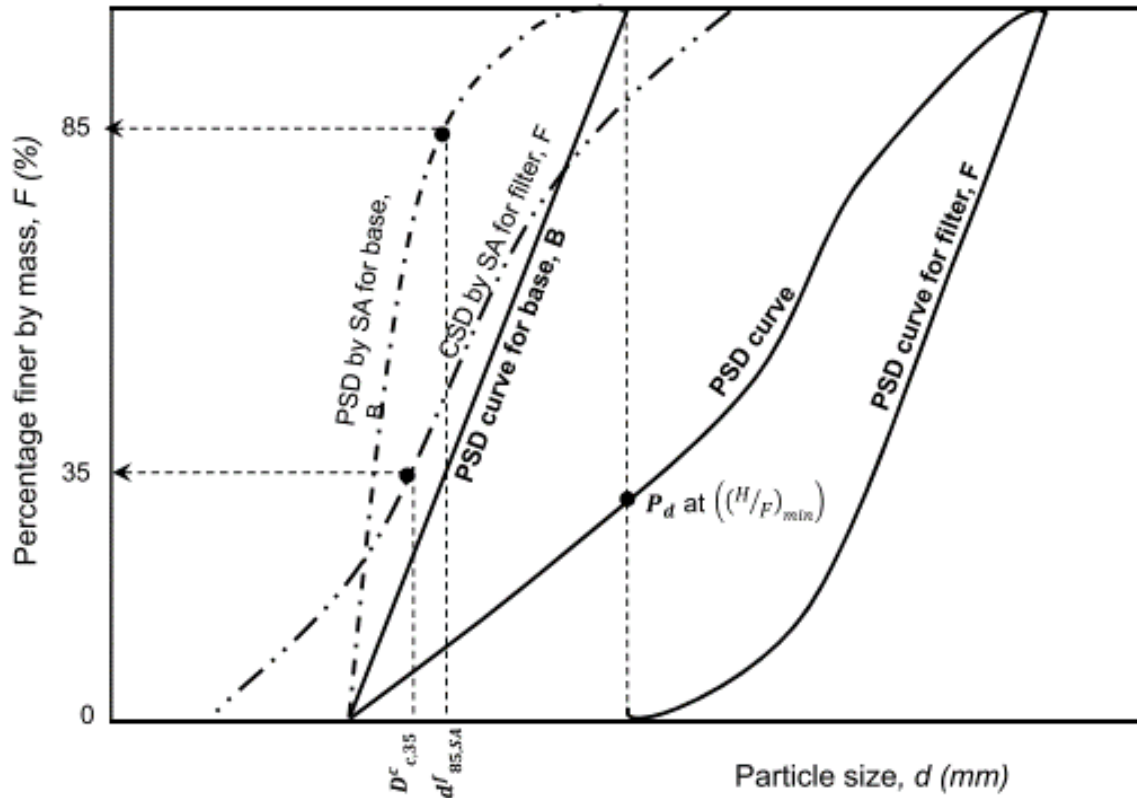


Figure II.15 – Method for assessing internal instability of soils (Indraratna et al., 2015)

2.4.2 Hydraulic gradient criteria

Terzaghi approach

Terzaghi (Terzaghi, 1939) proposed that the vertical effective stress becomes zero within the soil if the upward hydraulic gradient reaches the critical hydraulic gradient. Therefore the critical hydraulic gradient for heaving $i_c (= \gamma' / \gamma_w)$ equal to 1.0, where γ' is the submerged unit weight of soil and γ_w is the unit weight of water. This criterion is used for initiation of hydraulic heave, which is not an erosion process. As such, caution must be exercised when using this criterion in the case of suffusion.

Skempton and Brogan method

Skempton and Brogan (Skempton and Brogan, 1994) performed tests under upward seepage on internally unstable sandy gravels. After comparing the theoretical value of the critical hydraulic

gradient by Terzaghi (Terzaghi, 1939) with the actual hydraulic gradient, the result indicated that the real critical hydraulic gradient could be much lower. This can be explained by the overburden load being carried entirely by the coarse fraction, leaving the finer fraction under relatively small stress. Thus the critical gradient required to initiate suffusion is expressed by:

$$i_c = \alpha_1 \left(\frac{\gamma'}{\gamma_w} \right) \quad \text{II.5}$$

Where α_1 is the stress reduction factor. This relationship describes how a larger α_1 will yield greater resistance to the onset of instability induced by seepage, and its value needs to be determined by internal erosion tests. Because it is modified from Terzaghi's criterion for initiation of hydraulic heave, caution must still be exercised when using in the suffusion.

Li and Fannin method

For the critical hydraulic gradient of a soil under overburden stress, a theoretical hydromechanical equation was proposed by Li and Fannin (Li and Fannin, 2012), which can be expressed as:

$$i_c = \frac{\alpha_t}{1 - 0.5\alpha_t} \left(\bar{\sigma}'_{vm} + \frac{0.5(G_s - 1)}{(1 + e)} \right) \quad \text{II.6}$$

Where α_t is the stress transformation coefficient, G_s is the specific gravity of the material, e is the void ratio, and $\bar{\sigma}'_{vm}$ is the effective vertical stress of the soil.

2.4.3 Hydraulic shear stress

Reddi et al. (Reddi et al., 2000) proposed a system comprising an ensemble of uniform capillary tubes with a constant radius r_p to evaluate shear stress. The hydraulic shear stress relates to pressure gradients for a horizontal seepage from inlet section 1 to outlet section 2, which can be expressed by Equation II.7:

$$\tau = 1.414 \left(\frac{\Delta P}{\Delta L} \right) \left(\frac{r_p}{2} \right) \quad \text{II.7}$$

Where $\Delta P = P_1 - P_2$ is the pressure drop between sections 1 and 2. ΔL is the seepage length between these two sections.

Equation II.7 also can be reformulated as follows for a vertical flow:

$$\tau = \left(\frac{\Delta h \gamma_w}{\Delta z} \right) \sqrt{\frac{2k\mu}{\gamma_w \phi}} \quad \text{II.8}$$

Where Δh is the hydraulic head drop, and Δz is the altitude variation for the 1D flow entering upstream section 1 and downstream section 2. k is the hydraulic conductivity, μ is the dynamic viscosity, and ϕ is the porosity.

2.4.4 Flow velocity

Considering the unsuitability of the hydraulic gradient for describing the transport of particles along the flow path, Perzmaier (Perzmaier, 2007) proposed a hydraulic criterion based on the critical pore velocity. The average pore speed \bar{v}_p can be derived from the Darcian flow velocity v , the porosity ϕ and the tortuosity T as shown in Equation II.9. The Darcian flow velocity may be just one quarter or even one eighth of the value of mean pore velocity.

$$\bar{v}_p = \frac{v}{T\phi} \quad \text{II.9}$$

2.4.5 Approach based on energy

Marot et al. (Marot et al., 2011) proposed a new method of linking the energy dissipated by the fluid and the loss mass of the soil. The variations of seepage flow and the soil lead to the loss of the energy and mass. To illustrate this approach, V is a given volume of fluid that comprises a mass M and density ρ_f , and mass M has a contact surface S with its environment (soil and wall).

The external surface of the volume is defined by its normal vector \vec{n} from fluid to environment. The temporal variation of the energy of seeping fluid expressed as Equation II.10 is equal to the sum of the variation of its thermal energy and the variation of the mechanical work of external forces to the volume:

$$\frac{dE}{dt} = \frac{d}{dt} \iiint_{Mass} \left(e_{int} + \frac{\vec{w}^2}{2} + \vec{g}\vec{z} \right) dM \quad \text{II.10}$$

Which is equivalent to:

$$\frac{dE}{dt} = \frac{\partial}{\partial t} \iiint_{Volume} \left(e_{int} + \frac{\vec{w}^2}{2} + \vec{g}\vec{z} \right) \rho_f dV + \iint_S \left(e_{int} + \frac{\vec{w}^2}{2} + \vec{g}\vec{z} \right) \rho_f (\vec{U}\vec{n}) dS \quad \text{II.11}$$

And:

$$\frac{dE}{dt} = \frac{dE_{ther}}{dt} + \frac{dW}{dt} \quad \text{II.12}$$

Where t is the time; E_{ther} is the thermal energy exchange between the system of the specimen and the environment; W is the mechanical work from upstream to downstream; e_{int} is the internal energy of the fluid; \vec{U} is the velocity of the fluid (it components \vec{u} , \vec{v} , \vec{w}); \vec{g} is gravity; \vec{n} is normal vector of external surface oriented from fluid to environment; and \vec{z} indicates coordinates.

For this method, three assumptions are made: a) it is an adiabatic system and only the mechanical work between the upstream and the downstream is considered; b) the temperature and the internal energy with time are assumed to be constant for the volume; c) with a constant density and without the temporal variation of kinetic energy, the flow is in steady state condition. After using the given assumptions, the equations may be simplified as:

$$\frac{dW}{dt} = \iint_S \left(\frac{\vec{w}^2}{2} + \vec{g}\vec{z} \right) \rho_f (\vec{U}\vec{n}) dS \quad \text{II.13}$$

The mechanical work W is defined as the sum of mechanical work by pressure $W_{pressure}$, by erosion at the fluid-solid interface $W_{erosion}$, and by viscosity and turbulence in the fluid $W_{intrafluid}$. For this closed system, the dissipation of total energy can be written as:

$$\frac{dW}{dt} = \frac{dW_{pressure}}{dt} + \frac{dW_{intrafluid}}{dt} + \frac{dW_{erosion}}{dt} \quad \text{II.14}$$

The temporal derivative of work is done by pressure P , which is presented by:

$$\frac{dW_{pressure}}{dt} = - \iint_S P (\vec{U}\vec{n}) dS \quad \text{II.15}$$

Substituting Equations II.13 and II.15 for II.14, the new equation is:

$$\frac{dW_{intrafluid}}{dt} + \frac{dW_{erosion}}{dt} = \iint_S \left(\frac{\vec{w}^2}{2} + \vec{g}\vec{z} + \frac{P}{\rho_f} \right) \rho_f (\vec{U}\vec{n}) dS \quad \text{II.16}$$

Based on flow conservation with the same specimen section on the whole length, from the upstream section A to downstream section B, the average velocity remains constant. Equation II.16 becomes:

$$\frac{dW_{intrafluid}}{dt} + \frac{dW_{erosion}}{dt} = \iint_S \left(\vec{g}\vec{z} + \frac{P}{\rho_f} \right) \rho_f (\vec{U}\vec{n}) dS = \rho_f g \Delta z Q + Q \Delta P \quad \text{II.17}$$

Where $\Delta P = P_A - P_B$, $\Delta z = z_A - z_B$, and Q is the fluid flow rate. Specific to the suffusion process, we can assume that the energy dissipation by viscosity is mainly transformed into erosion, and the erosion dissipation representing the transfer of energy from the fluid to the solid phase is neglected with a small Reynolds number (Sibille et al., 2014). In consequence, the temporal derivative of mechanical work through erosion can be expressed by:

$$\frac{dW_{erosion}}{dt} = \rho_f g \Delta z Q + Q \Delta P \quad \text{II.18}$$

For downward flow, $\Delta z > 0$, and $\Delta z < 0$ if the flow is upward. Furthermore, $\Delta z = 0$ if the flow is horizontal. The total energy dissipation for the entire test duration is the temporal integration of the instantaneous erosion power.

2.5 Devices and approaches for assessing soil susceptibility

2.5.1 Previously developed testing erodimeters for soil susceptibility experiments

To obtain a better understanding of the mechanisms of initiation and progression of erosion that occur in hydraulic structures subjected to seepage flow, numerous laboratory testing apparatuses and methods have been designed. Many experimental studies have been carried out by researchers and engineers based on these new devices since the early 1940s. The aim of these studies was to provide the tools to evaluate the compatibility of materials in earth structures. Such methods involved packing the material into the device cylinder cell through which water was then allowed to seep. The response of the particles to the seepage was then recorded and the suitability of the specimen to the suffusion was investigated. In this subsection, we describe a selection of testing apparatuses and methods that have been used to assess the internal stability of specimens. The principal findings of each are also summarized.

Kenney and Lau

Kenney and Lau (Kenney and Lau, 1985) carried out a study on the effect of disturbing forces such as seepage and vibration on cohesionless soils. The permeameter cells used for two constant head tests had the following dimensions: 245 mm in diameter and 450 mm in height, and 580 mm in diameter and 860 mm in height. The coarse particles were selected as the drainage layer for the base soil placed at the bottom of cells, as shown in Figure II.16, while the top surface was stressed with a 10 kPa perforated plate. To move loose particles toward the bottom of the samples, a light

vibration was applied throughout the tests, which was found to have a significant influence on some of the soils.

Lafleur et al.

Based on the difference of the filtration mechanisms between broadly graded soils and uniform soils, Lafleur et al. (Lafleur et al., 1989) conducted tests on an artificial material (spherical glass beads) that had three different grain size distribution curves: linear, broadly graded, and gap-graded. The tests were performed using a cylindrical permeameter cell of 197 mm in diameter and 230 mm in length, as presented in Figure II.17. All specimens were subjected to a downward direction flow by imposing hydraulic gradients between 2.5 and 6.5. Four piezometer tubes were installed to monitor local pore water pressure. During these tests, the detached particles were separated by a metal wire mesh placed at the bottom of the test soils.

Skempton and Brogan

These authors conducted infiltration tests on internally unstable sandy gravels that were subjected to a upward seepage flow in a rigid cell of 139 mm in diameter and about 155 mm in length, as shown in Figure II.18. After being fully mixed and moistened, the soil was placed into the cell in four layers, each about 40 mm thick, and then tamped by the hand. To ensure uniform flow across the area of the sample, the specimen was rested on a screen formed by the gravel and coarse sand. The specimen was saturated by slowly raising the water level to the top edge of the cell. Four standpipe piezometers measured the piezometric response as the upward flow of water was increased in small steps, and overflow was captured by the lower basin to measure the discharge. Hydraulic gradients were imposed by the upward vertical flow and increased until the failure of the sample or the opening of a horizontal crack, which would then work its way to the surface. After the test, the washed out fine particles were collected, dried, and weighed.

Wan and Fell

The schematic diagram of the downward flow seepage test apparatus used by Wan and Fell (Wan and Fell, 2008) is shown in Figure II.19. In the cylindrical cell with a 300 mm internal diameter, the 300 mm thick tested soil was placed between the top filter layer of 25 mm single sized aggregates and the bottom filter layer of 20 mm single sized aggregates. A constant head tank located 2.5 m above the seepage cell supplied a downward direction flow, and the seepage cell was placed inside a transparent overflow tank to maintain a constant water head at the downstream. Thus a seepage gradient $i \approx 8$ was maintained across the specimen during the

test. The loss particles and overflow were collected to capture the loss mass and flow rate. The water pore pressure was measured by the piezometers located at different depths of the soil sample and recorded by the transducers, an electronic data logger, and a computer.

Chang and Zhang

Chang and Zhang (Chang and Zhang, 2013a) conducted the suffusion test on the gap-graded sand-gravel soil subjected to a downward seepage. The apparatus, as shown in Figure II.20, was a modified triaxial device controlled by a computer composed of a triaxial system, a pressurized water supply system, a soil collection system, and a water collection system. The soil specimen, measuring 100 mm both in diameter and height, was wrapped in the flexible membrane to minimize the probable interface leakage. During the erosion process, an LVDT and a digital camera were used to measure the soil specimen deformation. Three transparent water tanks, 200 mm in diameter and 400 mm in height, were used to pour the sufficient water into the soil specimen. The collection system included a transparent funnel-shaped tube, eroded mass containers, and water containers. A T-fitting was used to separate the outflow water and the eroded soil by putting a steel wire mesh of 0.064 mm in the inlet of the outflow drainage tube. The collected mass in the container was then dried and measured, while the outflow was measured by an electronic balance to compute the flow rate.

Marot et al.

Marot et al. (Marot et al., 2012) carried out suffusion tests on broadly graded clayey sand using a centrifuge machine, which was compatible with specimens of 73 mm in diameter and 60 mm-120 mm in height. To reproduce the full scale stress state, the entire device was placed in the IFSTTAR (Institut Français des Sciences et Technologies des Transports) centrifuge swinging basket as shown in Figure II.21. The small scale model was subjected to a downward seepage flow supplied by a tank of 245 mm inner diameter under a constant hydraulic head. To diffuse the fluid across the soil specimen uniformly, a glass bead layer was placed in the top of the specimen. For the collecting system, the bottom of the funnel-shaped draining system was equipped to avoid the clogging of eroded particles. A wire mesh with a 0.1 mm pore opening size was placed under the specimen to prevent coarse particles from detaching. A drainage pipe and needle valve were used to connect the cell outlet and effluent sampling system. When the selected centrifuge acceleration was reached, the upstream and downstream valves became open. A rotating effluent system composed of several beakers was developed to perform a sampling of the effluent during the test duration, which was controlled remotely from the centrifuge operator's room.

Indraratna et al.

The test apparatus, as shown in Figure II.22 used by Indraratna et al. (Indraratna et al., 2015), consisted of a specially manufactured smooth plates with an internal diameter of 150 mm and a height of 250 mm, which was compatible with 200 mm long specimens. Before placing them into the cell over a wire mesh with a nominal opening of 80 μm , the soil samples were mixed and then compacted to the target height in five uniform layers within the test hydraulic cell. The specimens were saturated by de-aired water with a downward flow under a relatively small constant head of 50 mm applied at the top of the specimen to avoid a slight internal disturbance. To ensure full saturation, the specimens were left for a minimum of 24 hours. During tests, they were subjected to an upward flow applied by an electro-pneumatic pump at a predetermined pressure. The differential head causing upward flow through the specimen was measured by a pressure transducer located at the outflow. Through the circulation system of effluent, the loss particles were collected in sampling chambers for post-test forensic analysis.

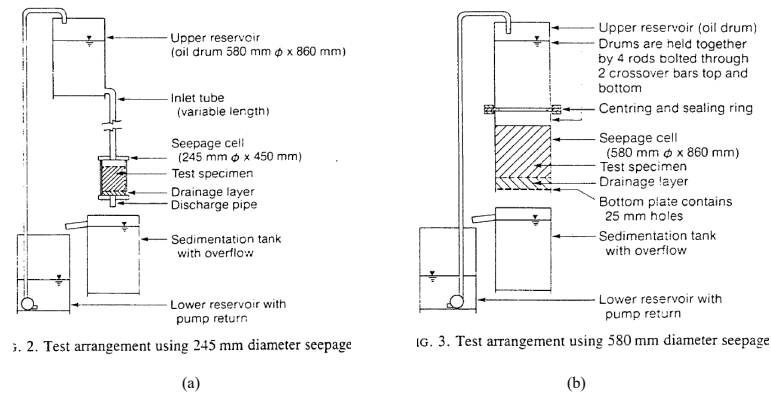


Figure II.16 – Test arrangement of seepage test using permeameter cell (a) 245 mm, (b) 580 mm (Kenney and Lau, 1985)

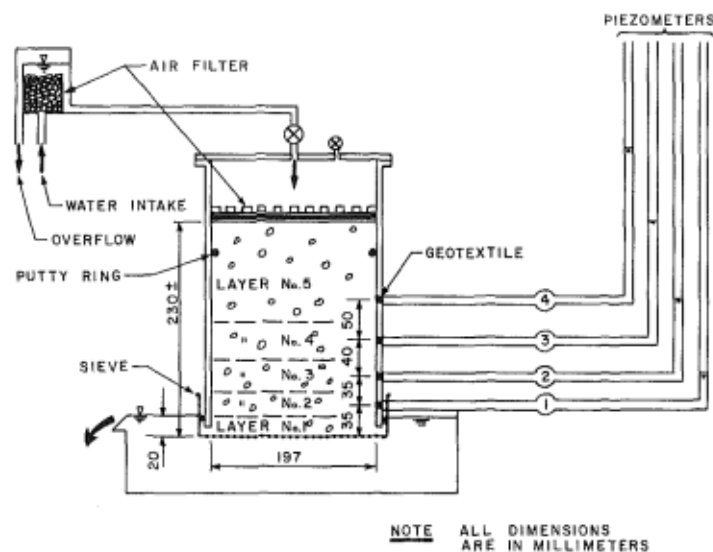


Figure II.17 – Permeameter for screen tests (Lafleur et al., 1989)

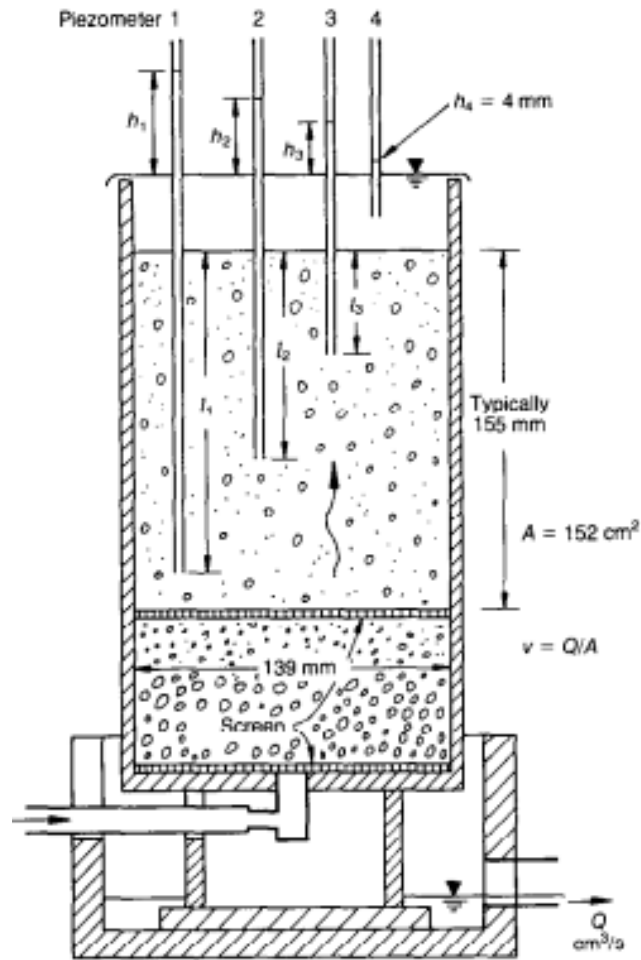


Figure II.18 – Apparatus of seepage test (Skempton and Brogan, 1994)

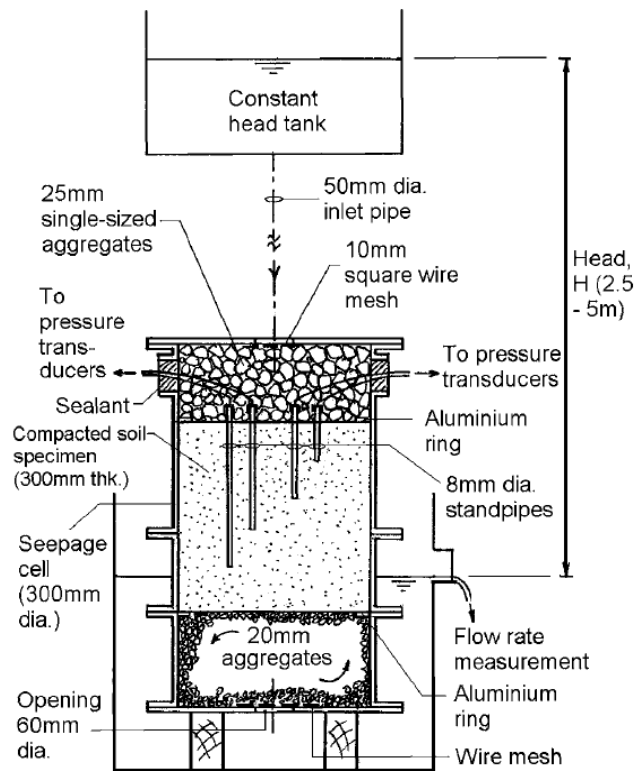


Figure II.19 – Schematic diagram of downward flow seepage test apparatus (Wan and Fell, 2008)

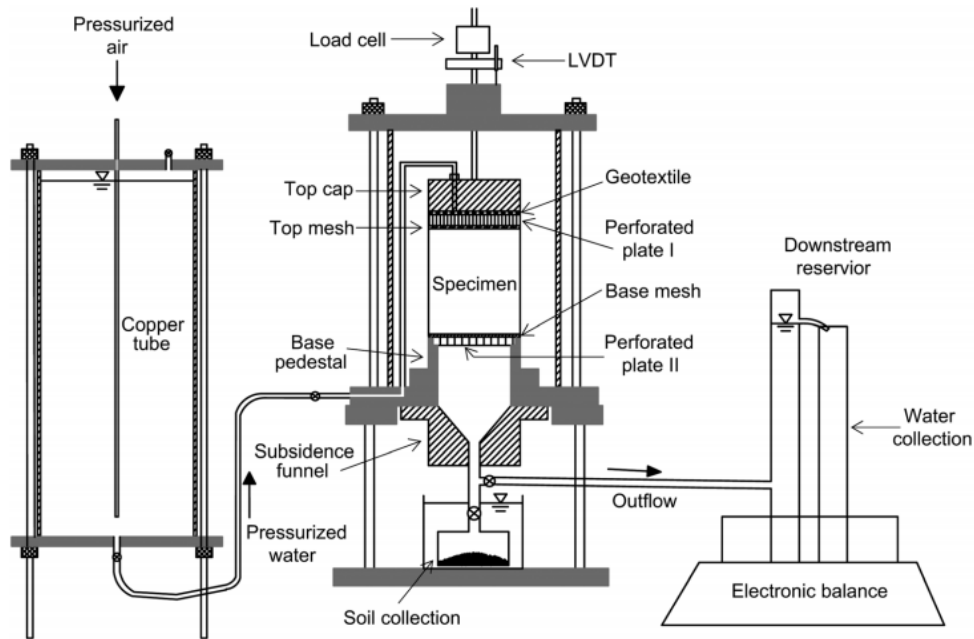


Figure II.20 – Schematic of testing apparatus (Chang and Zhang, 2013a)

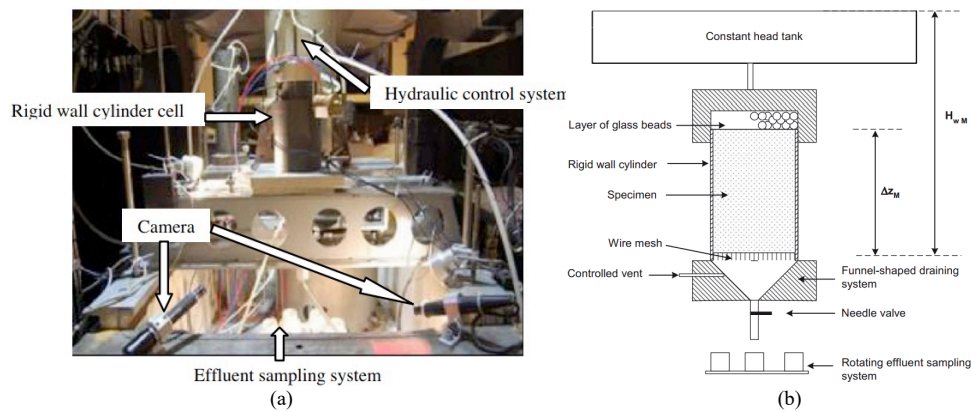


Figure II.21 – Seepage test apparatus (Marot et al., 2012): (a) General view of the IFSTTAR centrifuge bench, (b) schematic diagram of downward seepage flow test apparatus

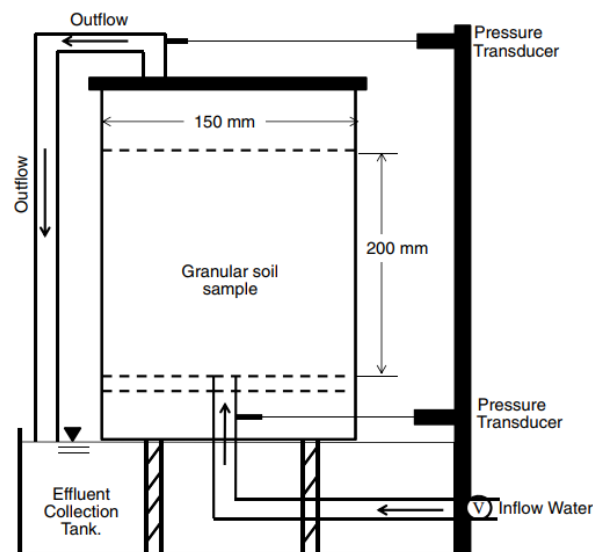


Figure II.22 – Seepage test apparatus (Indraratna et al., 2015)

2.5.2 Soil susceptibility classification for interface erosion

According to Wan and Fell (Wan and Fell, 2004), the erodibility of a soil can be characterized in two aspects: (i) the rate of erosion when a given hydraulic shear stress is applied to the soil, and (ii) the ease of initiating erosion in the soil.

Using the hole erosion test (HET), Wan and Fell (Wan and Fell, 2004) determined that the erosion rate index I_{HET} ranged from 1 to 6, as shown in Table II.1. I_{HET} is expressed as a function of C_e . C_e means the coefficient of soil erosion corresponding to the ratio of erosion rate per unit surface area of the slot or hole at time to hydraulic shear stress along the hole at time.

$$I_{HET} = -\log(C_e) \quad \text{II.19}$$

Table II.1 – Erosion rate index, I_{HET} (Wan and Fell, 2004)

Index of erosion rate, I_{HET}	Description of erosion rate	Ranking of erosion
<2	Very highly fast	1
2-3	Very fast	2
3-4	Moderately fast	3
4-5	Moderately slow	4
5-6	Slow	5
>6	Very slow	6

Using the approach based on energy, Marot et al. (Marot et al., 2011) firstly proposed an equation of erosion resistance index I_α for the interface erosion process, as in Equation II.20, and ranged soils from highly erodible to highly resistant (see Table II.2).

$$I_\alpha = -\log_{10}\left(\frac{\text{dry eroded mass}}{\text{total dissipated flow energy}}\right) \quad \text{II.20}$$

Table II.2 – Erosion resistance index I_α for suffusion (Marot et al., 2011)

Index of erosion resistance, I_α	Description of erosion rate	Ranking of erosion
$I_\alpha < 1$	Highly erodible	1
$1 \leq I_\alpha < 2$	Erodible	2
$2 \leq I_\alpha < 3$	Moderately erodible	3
$3 \leq I_\alpha < 4$	Moderately resistant	4
$4 \leq I_\alpha < 5$	Resistant	5

$I_\alpha \geq 5$	Highly resistant	6
-------------------	------------------	---

For the suffusion process, Marot et al. (Marot et al., 2016) gave a dedicated expression of expended energy (Equation II.20), and the corresponding susceptibility categories are: highly erodible for $I_\alpha < 2$; erodible for $2 \leq I_\alpha < 3$; moderately erodible for $3 \leq I_\alpha < 4$; moderately resistant for $4 \leq I_\alpha < 5$; resistant for $5 \leq I_\alpha < 6$; and highly resistant for $I_\alpha \geq 6$.

2.5.3 Erosion rate

Erodibility means the resistance of a soil to erosion caused by water flow. The hydraulic shear stress on the soil at the water-soil interface induced by hydraulic loading detaches the fine particles from the soil skeleton. Wan and Fell (Wan and Fell, 2004) proposed an expression, shown as Equation II.21, to describe the rate of erosion when a given hydraulic shear stress was applied to the soil for the cases of hole erosion or concentrated leak erosion:

$$\dot{m} = k_d(\tau - \tau_c) \quad \text{II.21}$$

Where \dot{m} is the soil erosion rate; k_d is the erodibility coefficient; τ is the actual hydraulic shear stress at the soil-water interface; and τ_c is the critical hydraulic shear stress to initiate the erosion. Based on the equation, a linear relationship exists between the rate of erosion and the applied hydraulic shear stress. Critical hydraulic shear stress refers to the minimum value of hydraulic shear stress to trigger the erosion. For a given shear stress, a greater erodibility coefficient leads to more eroded particles at an interval time. In short, the critical erosive shear stress characterizes the ease of initiation of erosion in the soil, while the erodibility coefficient represents the velocity of the soil erosion.

The value of erosion rate per unit of surface area depends largely on the definition of the surface area. Specific to the suffusion process, the surface of pores is more representative than the surface of the specimen's cross section. The erosion rate of soils per unit of pore area \dot{m} was defined by Reddi et al. (Reddi et al., 2000) through use of a series of capillary tubes to present the pores. The calculation process of this method is presented from Equations II.22-II.26:

$$\dot{m}(t) = \frac{m(t)}{N_p S_p t} \quad \text{II.22}$$

Where m is total eroded dry mass, N_p means the average number of pores, S_p is the average

pore area, and t is test duration;

$$N_p = \frac{S\phi}{\pi r_p^2} \quad \text{II.23}$$

Where S is the cross-sectional area of the specimen, ϕ means the porosity and r_p is the average radius of pores;

$$S_p = 2\pi r_p L \quad \text{II.24}$$

Where L is the length of the specimen;

$$r_p = \sqrt{\frac{8K}{\phi}} \quad \text{II.25}$$

Where K is the intrinsic permeability;

$$K = k \frac{\mu}{\gamma_w} \quad \text{II.26}$$

Where k is the hydraulic conductivity, and μ is the dynamic viscosity.

2.6 Numerical simulation of seepage

2.6.1 Numerical modeling of internal erosion

With the rapid development of modern computers, the application of numerical methods is becoming increasingly extensive, and their calculation accuracy has greatly improved. The numerical methods of piping include the finite difference method, finite element method, discrete element method, and free element method. In 1941, Biot derived a relatively perfect three dimensional consolidation theory directly from the elastic theory, considering the equilibrium conditions of soil, elastic stress-strain relationship, deformation compatibility conditions, and seepage continuity conditions. The theory successfully reveals the Mandel-Cryer effect that the excess pore water pressure does not decrease and rise in a certain area of the soil at the initial stage of loading. Due to the complexity of the Biot consolidation equation, only a few special problems have been solved analytically (Cryer, 1963; McNamee and Gibson, 1960).

Javandel and Witherspoon (Javandel and Witherspoon, 1968) were the first to study the transient flow in porous media using the finite element method. Sandhu and Wilson (Sandhu and Wilson, 1969), meanwhile, were first to obtain the finite element equation of Biot consolidation theory

based on the variational principle. However, in the initial stage of consolidation calculation, pore pressure calculation often shows greater numerical instability than displacement, especially for the low permeability foundation. To ensure the stability of pore pressure calculation in finite element analysis, Vermeer and Verruijt (Vermeer and Verruijt, 1981) set the lower limit of the time step. Murad and Loula (Murad and Loula, 1992) introduced Galerkin Petrov-Galerkin post-processing technology, mixed finite element method, and incompatible finite element method, respectively.

At present, many fitting equations describe non-Darcy seepage. Among them, the most discussed in recent years is the formula composed of two parts: the power function of the low speed seepage section and the linear function of the high speed seepage section, as proposed by Hansbo (Hansbo, 1960):

$$v = \begin{cases} \frac{K_1 i^{m_c}}{m_c i_1^{m_c-1}}, & i \leq i_1 \\ K \left(i - \frac{i_1(m_c - 1)}{m_c} \right), & i > i_1 \end{cases} \quad \text{II.27}$$

Where v is the seepage velocity, i is the hydraulic gradient, m_c is the constant determined by the test, K_1 is the permeability coefficient of the linear section, and i_1 is the initial hydraulic gradient of the linear seepage.

Teh and Nie (Teh and Xiaoyan, 2002), considering Hansbo seepage and based on the principle of virtual work, derived the governing equation of finite element analysis for Biot consolidation theory under the axisymmetric condition. They also offered the range of non-Darcy seepage, which must be considered by parameter analysis.

2.6.2 Application of numerical method in seepage

The numerical simulation of seepage is focused mainly on the following directions: (i) seepage evolution process simulation; (ii) the ease of initiating erosion in the soil; (iii) simulation of the soil failure due to seepage. The numerical methods of piping research include the finite element method, finite difference method, discrete element method, and free element method. In this paper, the finite element method is used.

Desai (Desai, 1976) had introduced the method to unsteady seepage, and Neuman (Neuman, 1973) was the first to use it to solve saturated and unsaturated seepage problems. He used the Galerkin method to discretize the Richards equation in the space domain and the Crank-Nicolson finite difference scheme to discretize the time domain. In 1973, the finite element method for one dimensional unsaturated seepage was proposed. Later, the same method for solving the two

dimensional saturated-unsaturated seepage problem was proposed.

Lam and Fredlund (Lam and Fredlund, 1984) proposed a finite element analysis model for unsaturated soils. Sterpi (Sterpi, 2003) considered the stress redistribution of the surrounding soil caused by the loss of fine particles. The finite difference method was used to study the loss process of fine particles, and an empirical formula for the loss of said particles and the hydraulic gradient was obtained. Cividini and Gioda (Cividini and Gioda, 2004) used the finite element method to study 1D and 2D piping problems. The failure process of piping is actually a multi-field coupling process. The seepage flow takes away the fine particles in the soil, changes the structure of the soil, and affects its stress distribution. That said, the change of soil stress will also affect the permeability coefficient and thus the seepage field. Although the influence of said field on the loss of fine particles in soil was taken into account in the aforementioned three papers, real multi-field coupling was not realized.

Fredlund and Hasan (Fredlund and Hasan, 1979) assumed that the gas phase is continuous and that Fick's law and Darcy's law are appropriate. For the flow of gas and liquid phases, the permeability coefficients of said phases are the volume and mass of soil. A partial differential equation for solving pore pressure and pore water pressure in the consolidation process of unsaturated soils was proposed. The finite element form of two dimensional steady seepage was derived from Galerkin's principle of adding buckling allowance.

Rank and Werner (Rank and Werner, 1986) firstly introduced the adaptive theory into seepage analysis and extended the linear error estimation method to solve two dimensional nonlinear seepage problems with free surface. Chung and Kikuchi (Chung and Kikuchi, 1987) discussed the problem of mesh adaptation for a two dimensional inhomogeneous jet. Through iterative calculation, a method of optimizing mesh and determining the position of free surface was proposed.

Lam and Fredlund (Lam and Fredlund, 1984) comprehensively discussed the saturated and unsaturated seepage problem. Some seepage problems are solved by using the saturated-unsaturated seepage analysis program trace. Combining the theory of unsaturated soil water movement with the theory of unsaturated soil consolidation, the governing equation of saturated and unsaturated seepage was obtained. Several seepage problems of the complex groundwater flow system were simulated by the two dimensional finite element method. Fredlund and Xing (Fredlund and Xing, 1994) deduced the finite element scheme of two dimensional steady seepage by using the principle of weighted residual, while Freeze (Freeze, 1971) studied the saturated and unsaturated unsteady flow of a three dimensional groundwater aquifer and obtained a numerical solution. Abrahamsen et al. (Abrahamsen and Hansen, 2000) used the finite difference method

to solve Richards equation in the famous Daisy software.

Lee and Abriola (Lee and Abriola, 1999) used the finite element method and dynamic wave method to compare with the Integral Richards Equation method (IRE), the results showing that the simulation results of the IRE method are similar to those of the finite element method. In the soil layer near the upper boundary, the method overestimates the soil water content. In the lower boundary layer, the method underestimates the drainage.

Meanwhile, to improve the computational efficiency, Miller et al. (Miller et al., 2006) proposed an adaptive strategy based on error control, which was applied to both spatial discretization and temporal difference of the Richards equation. Juncu et al. (Juncu et al., 2009), combining multi-grid technology with the finite difference method, designed the nonlinearity of the spatial two dimensional Richards equation. The multi-grid method can effectively improve the convergence speed of the solution.

Frias et al. (de Frias Lopez et al., 2016) applied the PFC^{3D} discrete element program to study the gradation of coarse and fine particles, grain skeleton structure, and stress transfer. They also applied the software to study the contact relationship between soil particles under stress conditions.

2.7 Summary

The suffusion is one of the most complex types of internal erosion due to the filtration process. The grain size distribution is a key parameter to describe the suffusion susceptibility. In the past few decades, the research on soil gradation has earned much attention to characterize the potential of suffusion. But other properties of the material, such as density and grain shape, are also important to describe the process of suffusion. All of these geometric assessment methods can only divide the material into stable or unstable, which is not enough. Suffusion is caused by seepage but these criteria don't consider the hydraulic load.

The suffusion susceptibility is one of the properties of the soil and should be independent from the spatial scale and hydraulic load history. The classification method based on energy considers both the cumulative eroded mass and the cumulative expand energy at the steady state and can divide the soil into six levels (from highly erodible to highly resistant). Taking account of the entire specimen and suffusion process, the erodibility index is independent from the hydraulic load history and can avoid the spatial scale effect. Only the erodibility index at the steady state is not enough to describe the suffusion development, so an erosion law based on energy is necessary to further study the suffusion process with the time but not only at the steady state.

EXPERIMENTAL STUDY ON COUPLING OF EROSION AND FILTRATION

3.1 Introduction

As mentioned before in the Chapter II, the process of filtration is an important part of suffusion. More and more researchers are interested in the role of filtration process in suffusion because the decrease of the hydraulic conductivity is visible, and it is resulted from the clogging caused by the filtration of some detached particles. In the Chapter II, the basic filtration equation (Iwasaki et al., 1937) has been already introduced, which is expressed as follow:

$$c(\Delta L) = c_0 e^{-\lambda \Delta L} \tag{III.1}$$

Where c_0 is the initial particle mass concentration, $c(\Delta L)$ is the particle concentration after flow through a filter with seepage length ΔL and λ is the filter coefficient.

Taking into account that few experimental studies have been conducted on the entire process of erosion–filtration, a complete set of experimental schemes for said process has been designed. Two types of specimens can be discerned, and the interlayer coefficient between the binary mixture and filter layer was kept unchanged at $D_{15,c}/D_{85,f} = 4$, this chapter aims to analyze the post-test particle size distribution and the influence of the filtration on hydraulic parameters with a new experimental method. At last, the results of the filtration tests and Equation III.1 are compared. The effect of the unequal contact area between the binary mixture and filter layer on the efficiency of the filter system was studied. The influence of the particle concentration of the binary mixture on the permeability of the filtration system is discussed. At the same time, the influence of the particle size of the filter aggregate and binary mixture on sand filtration’s

efficiency is also analyzed.

3.2 Fundamental principle of controlling seepage flow by filter layer

The two basic requirements propounded by Terzaghi (Terzaghi, 1922) for the filter layer are the soil filtration and pressure reduction. These two requirements also constitute the basic principle that the filter layer can play the role of seepage control.

3.2.1 Fundamental principles of filtration

An important function of the filter layer is to filter soil. In terms of filtration, including the Terzaghi benchmark, the following principles are followed: not many particles of the base soil are allowed to pass through the pore of the filter layer, because this leads to clogging.

$$\frac{d_{pore,c}}{d_k} = \alpha' \quad \text{III.2}$$

In the formula: $d_{pore,c}$ is the effective pore diameter of the filter layer; d_k is the control particle size, i.e., the control particle size of the foundation soil without seepage damage; α' is the number of particles with which the controlled particle size of the foundation soil may form an arch at the pore entrance of the filter layer and prevent other particles from entering, also known as the arch coefficient.

In the downward seepage test, the filter layer is located at the lower part of the foundation soil. The process of specimen installation necessitates the installation of the filter layer firstly followed by the foundation soil. In this way, the large particles controlling the seepage stability in the foundation soil will enter the pore of the filter layer at the same time under the action of gravity, facilitating the formation of a stable arch structure composed of three particles at the entrance of the filter layer. As shown in Figure III.1, here α' is not greater than 3.

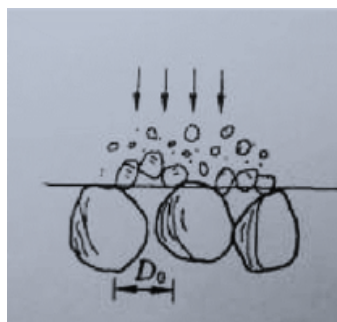


Figure III.1 – The type of filter layer and working mechanism

3.2.2 Basic principle of decompression

Decompression is another primary function of the filter layer. According to the decompression criterion of the Terzaghi filter layer, said layer can only consist of the finest particles allowed. After the erosion of base soil particles into the filter layer, if the pressure basically disappears, the permeability coefficient of the filter layer must be significantly greater than that of the base soil. According to the seepage calculation theory of double layers medium, from one layer of soil to the filter layer, the hydraulic parameters ratio of seepage in two layers shows the following relationship:

$$\frac{i_1}{i_2} = \frac{k_2}{k_1} \quad \text{III.3}$$

Where k_1 and i_1 are the permeability coefficient of the filter layer and the actual hydraulic gradient; and k_2 and i_2 are the permeability coefficient of the base soil and its actual hydraulic gradient. Hydraulic gradient is inversely proportional to the permeability coefficient in two layers of soil.

Kézdi (Kézdi, 1979) divided the particles into two groups at any particle size based on the theory of filter layer design. Coarse particles were regarded as the filter layer and fine particles as base soil. The author considered that when the $D_{15,c}/D_{85,f} < 4 < D_{15,c}/D_{15,f}$ relationship is satisfied, and subscripts c and f indicate that the amount corresponds to the filter layer and the base soil, respectively, then the fine particles will not move out to stabilize the graded soil; otherwise, the soil is unstable and piping may occur. In 1957, through the analysis of a large number of experiments, Istornina proposed that the failure mode of seepage depends mainly on the non-uniformity coefficient $C_u = d_{60}/d_{10}$. When $C_u < 10$, piping will not occur, and flowing soil will occur; when $10 < C_u < 20$, transition type will occur; when $C_u > 20$, piping will occur easily.

3.3 Downward erosion–filtration test

3.3.1 Description of the used device

The device used for this study is named as “oedo-permeameter”, as shown in Figure III.2. The main bench characteristics of the prototype are described in Figure III.3 (Sail et al., 2011). It consists of a rigid wall cylindrical cell, a water supply system, a soil collection system, an axial stress control system, and a data acquisition system.



Figure III.2 – Real view of oedo-permeameter

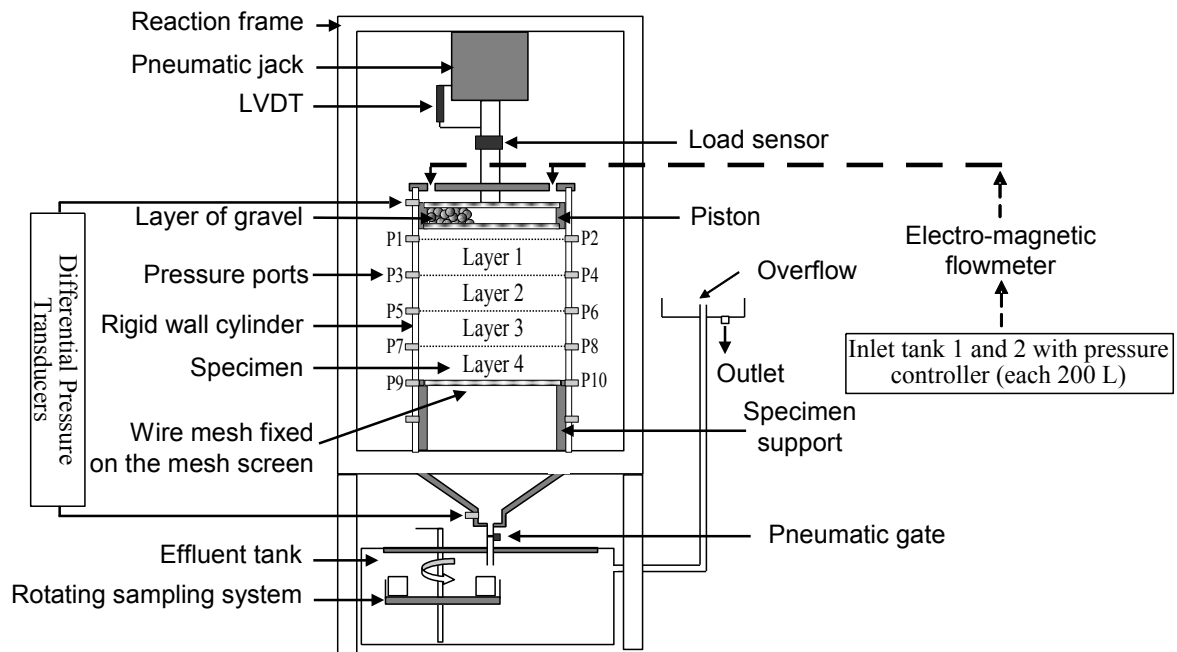


Figure III.3 – Schematic diagram of oedo-permeameter

Figure III.4(a) shows that the cell diameter is 280 mm and that the maximum height can reach 600 mm. It is transparent and equipped with a funnel-shaped draining system connecting the rigid tubular cell and the rotary sampling system to avoid clogging. A valve at the bottom of the funnel controls the drainage. A total of 12 pressure ports are symmetrically installed on the

outside of the rigid cylindrical cell, and the vertical distance between each set is 100 mm. The local pressure ports are connected to a multiplex unit, which is linked to a manometer to avoid discrepancy, and a differential pressure transducer is used to measure the water head difference between the top and base of the specimen. With the different supports shown in Figure III.4(b), specimens of variable heights can be tested. Figure III.4(c) demonstrates that a wire mesh with changeable pore opening size is fixed on the grid to allow the migration of fine content while limiting the coarse part. A geotextile is placed between the mesh edge and the wall of the rigid cylindrical cell to eliminate any particle migration from the slit.



Figure III.4 – Erosion cell: (a) rigid cylindrical cell; (b) specimen supports; (c) wire mesh and grid

Hydraulic load during the filtration phase is provided by a 200 L tank, which is equipped with a pressure controller to regulate flow. In fact, two tanks are working in parallel because one is so small that it potentially cannot supply the full flow. Only one container is used at a time, but the other one will be turned on when the currently used cistern only has a little water. Take note that before changing, a necessary step is to keep these two reservoirs open for a while before closing the empty one. This is because turning off the empty tank and then directly opening its counterpart will result in sharp fluctuations in the term of hydraulic head. The seepage through the specimen is measured by one of two flowmeters with different scales of measurement. The process of switching to the other flowmeter is similar to adjusting the reservoirs.

The collecting system is composed of an effluent container, shown in Figure III.5(a), which is equipped with a pallet. The pallet is divided into eight areas, and a beaker protected by

a triangular steel container is found in each of these sections, as presented in Figure III.5(b). Meanwhile, an external handle is also present with which to manipulate the rotatable pallet to switch to a different beaker to catch the eroded fine particles of different steps during a test. The effluent tank is filled with water to maintain a constant hydraulic head by connecting an overflow outlet that possesses a constant height.

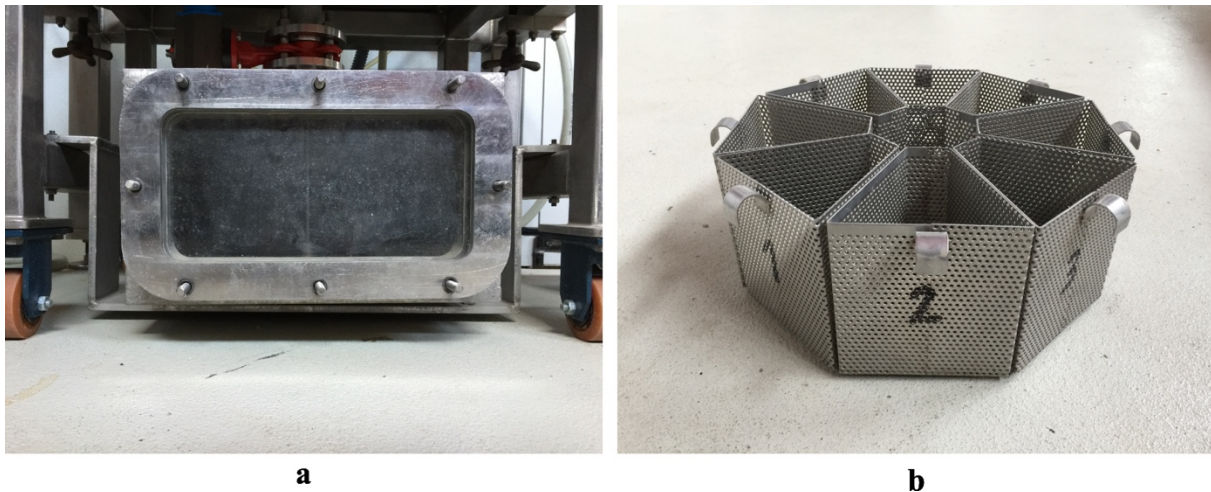


Figure III.5 – Soil collecting system: (a) effluent tank; (b) rotating sampling system

The axial loading system is made up of a piston, a pneumatic cylinder, and a reaction frame. Air pressure controls the piston, and the pneumatic cylinder has a range of movement over 200 mm to provide the axial stress even in the case of significant settlement of the specimen. We can load the required axial stress on the tested specimen by the system, which enables the study of the internal erosion in the complex stress condition.

The data acquisition system of the oedo-permeameter oversees the acquisition of flow rate, specimen settlement, and hydraulic head along the specimen and axial stress. The apparatus is joined to a computer so that throughout the experiment, all the obtained data are automatically recorded. The computer control system can be modified for various experiments. During the experiment, the curves of the main parameters are displayed on the screen, allowing the relevant results to be promptly observed.

3.3.2 Specimen preparation and testing program

Properties of tested materials

A cohesionless soil is selected, because the suffusion very concerns the cohesionless material. The diameter of the device is 280 mm, which is a limitation for the maximum grain size of the soil. Thence, the very coarse material cannot be used. For filtration tests, Palvadeau Gravel G3, which is classified as angular to the sub-angular material, is selected as the filter (named

as Filtration-1), and Fontainebleau Sand (named as Filtration-2) plays the role of suspended particles. The grain size distribution of tested materials is shown in Figure III.6. Filtration-3 shows the grain size distribution of the tested soil consisting of sand and gravel. The soil is identified as a gap-graded distribution with 50 % fine content. With a larger particle size, gravel works as the coarse particle, while sand soil acts as detachable fine particles. According to the criteria of particle size, the mixture is unstable, which permits the fine particles to move. Therefore, we can analyze the filtered particles in the downstream part. The specification of test materials is shown in Table III.1.

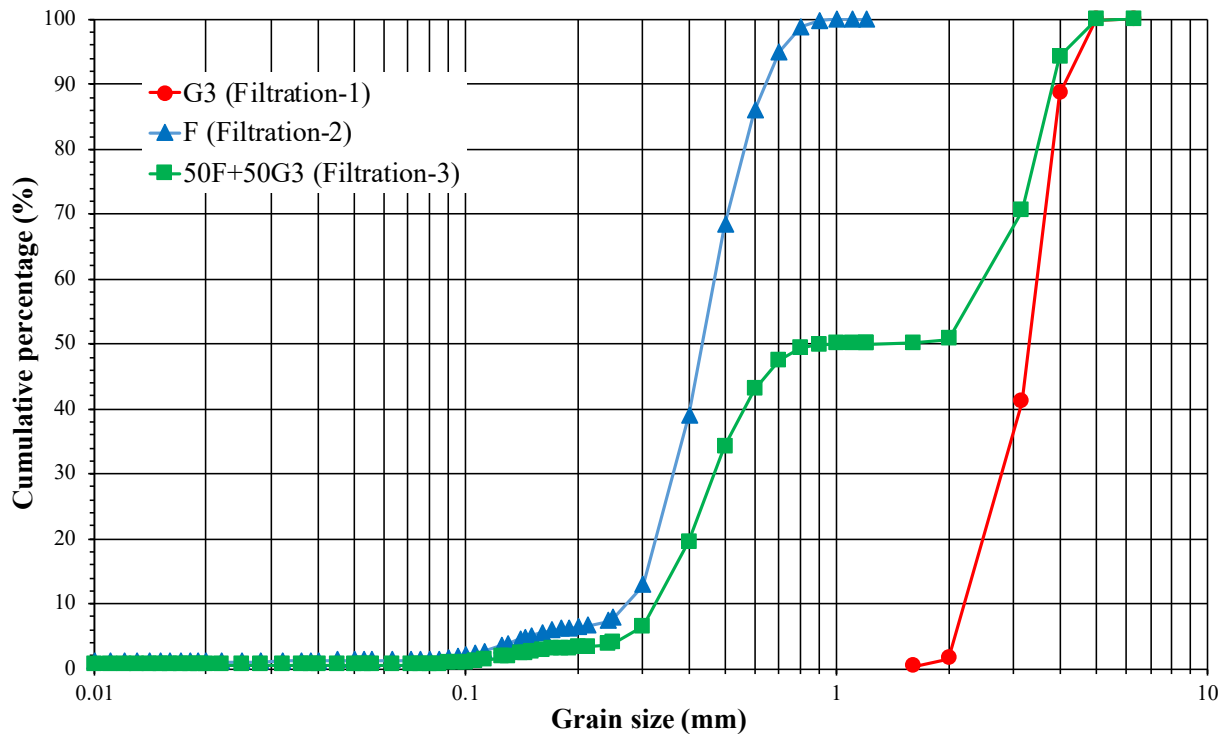


Figure III.6 – Grain size distribution of soils for filtration tests

Table III.1 – Specification of test materials

Characteristic particle size	G3	F	F+G3
d_{15} (mm)	2.39	0.31	0.37
d_{85} (mm)	3.94	0.59	3.67
C_u	1.55	1.74	7.70

Specimen preparation and testing program

There are two different testing configurations in the filtration process study:

1. With the purpose of limiting the influence of interface flow between the rigid wall of the cylinder cell and the specimen, the binary mixture with a diameter of 98 mm is in

the center of the upper part and surrounded by Palvadeau Gravel G3. An impervious membrane separates them (depicted in Figure III.7(a)). The cross-sectional area of the mixture is not equal to the filter layer, which allows us to observe the possible movement of the particles perpendicular to the direction of seepage.

2. The binary mixture is located in the gap between the oedo-permeameter cylinder and an impervious internal plastic bucket with an average diameter of 210 mm in order to follow the variation of particles through the transparent rigid wall of the cylinder cell (depicted in Figure III.7(b)). It is easier than last configuration to determine whether the test duration is sufficient and the sand particles move.

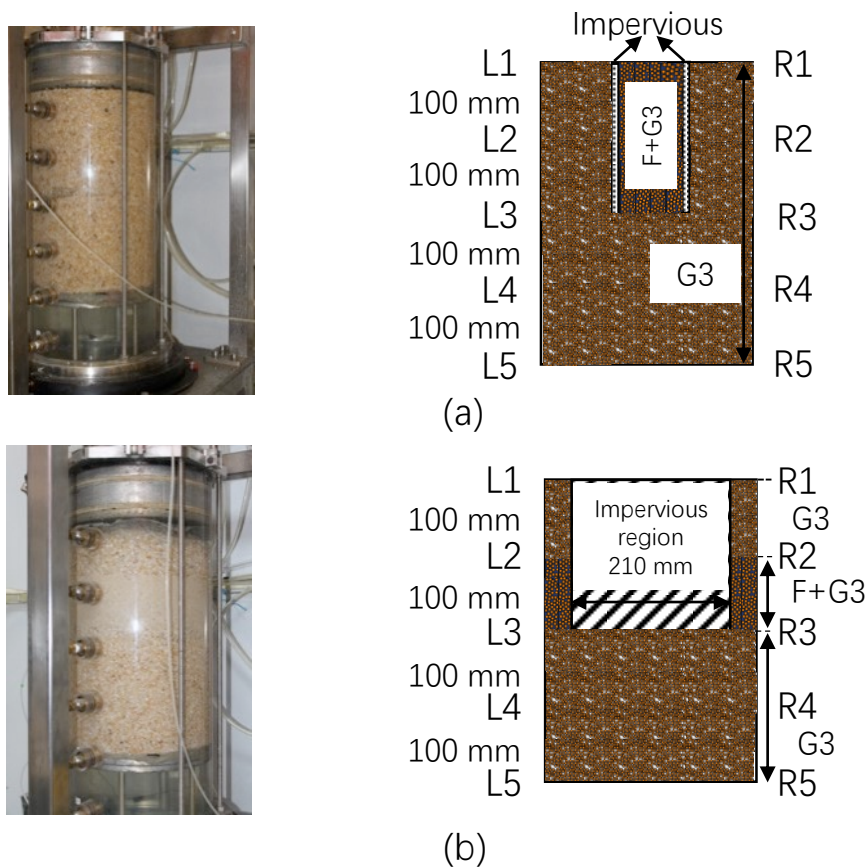


Figure III.7 – Schematics and pictures of the filtration tests performed with the oedo-permeameter

To perform a filtration test, a binary mixture of sand and gravel (Filtration-3), prepared with a water content of 3 %, was placed over a 200 mm high bed of gravel. All samples were saturated firstly with CO_2 and then with upward water seepage. Specimens were saturated under the same moistening velocity, and a beaker was used to catch the loss of particles during the saturation phase. Based on the evidence of Rochim et al. (Rochim et al., 2017) that the history of hydraulic loading has a significant influence on the development of suffusion, the specimens were systematically tested under a multistage hydraulic gradient, each stage lasting 30 minutes.

A beaker was used to catch the eroded particles during each hydraulic gradient stage, and the corresponding dry mass was measured.

To study the influence of the contact area between the piping soil layer and filter material layer on the hydraulic characteristics, three specimens were prepared: Filtration-C, Filtration-G-1, and Filtration-G-2. With the objective of improving the readability of filtration tests, C and G relate to the tests with the binary mixture in the center (Figure III.7(a)) and in the gap (Figure III.7(b)), respectively, and the number is the specimen number. The label of each sample is shown in Table III.2. In sample Filtration-C, no water permeability occurs between F+G3 and its surrounding part G3.

Table III.2 – Types of each specimen

Specimen name	Filtration-C	Filtration-G-1	Filtration-G-2
Specimen view	Figure III.7(a)	Figure III.7(b)	Figure III.7(b)

3.4 Testing results and discussion

For the analysis and discussion of the results to be described below, the letters L and R represent the left and right sides of the specimen, respectively. The numbers after the letters L and R represent the vertical position on the specimen.

3.4.1 Post-test sand filtering effect of filter layer of specimens

Post-test particle distributions in each layer

For the filtration part of the test, we focused on the area between pressure ports L3-R3 and L5-R5 because the filtration process existed in the downstream part of the specimen. Figures III.8, III.9, and III.10 show the fine fraction distribution along the seepage length after filtration tests in this area. The tested specimens were divided into several layers, and several positions (detailed in figures) were selected to measure the sand percentage for each layer. The circle in each figure is the top view of the cross section of the specimen, and the letters in the circle represent the sampling points for the measurement of gradation.

In order to get a more general conclusion, specimens Filtration-G-1 and Filtration-G-2 were designed as a set of repeated experiments. These two specimens were placed in the device with the same procedure and reached the same target density. Unfortunately, even using the same very low seepage velocity to saturate, the two specimens still became different. Figure III.11 displays the influence of the saturation phase on the initial state of the specimen. After saturation,

more particles move from upstream to downstream in the specimen Filtration-G-1. Therefore, Filtration-G-1 and Filtration-G-2 are no longer a set of repeated experiments. From these three figures, the reader may note that finer particles were filtered in areas that were closer to the binary mixture. Within the area between L3-R3 and L4-R4, the sand percentage was more than 10% at some positions near the binary mixture. In contrast, within the area between L4-R4 and L5-R5, the sand percentage rapidly dropped to zero.

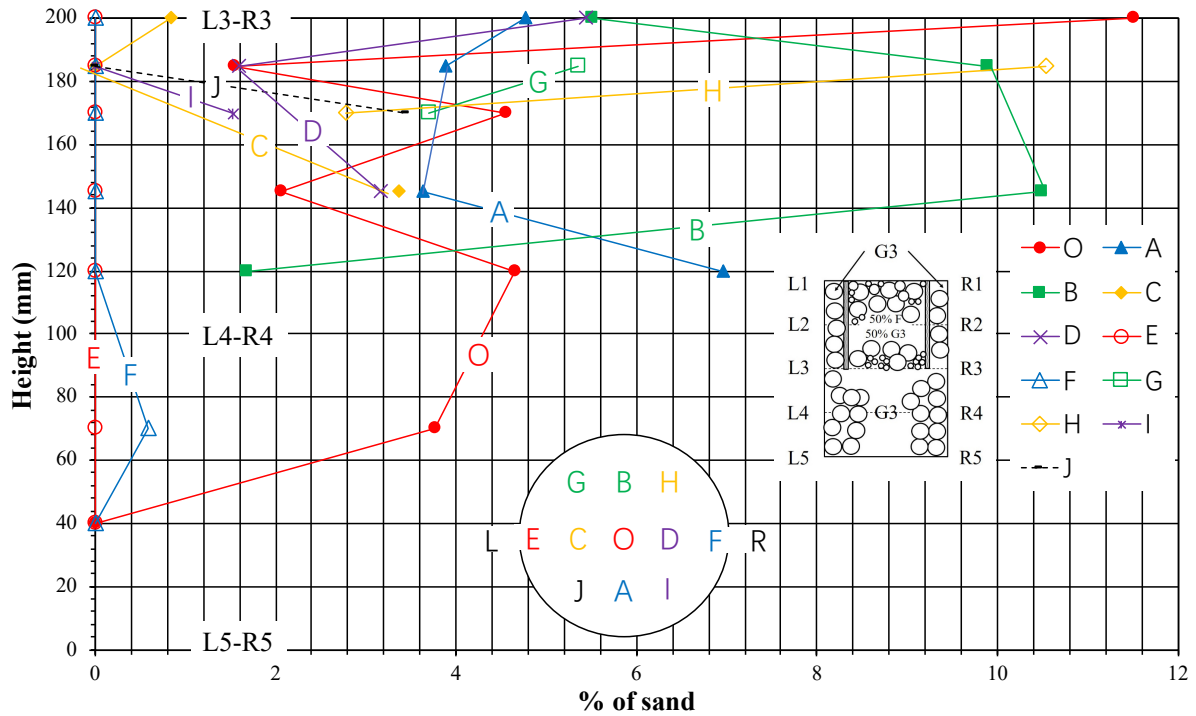


Figure III.8 – Profile of sand percentage after test for specimen Filtration-C

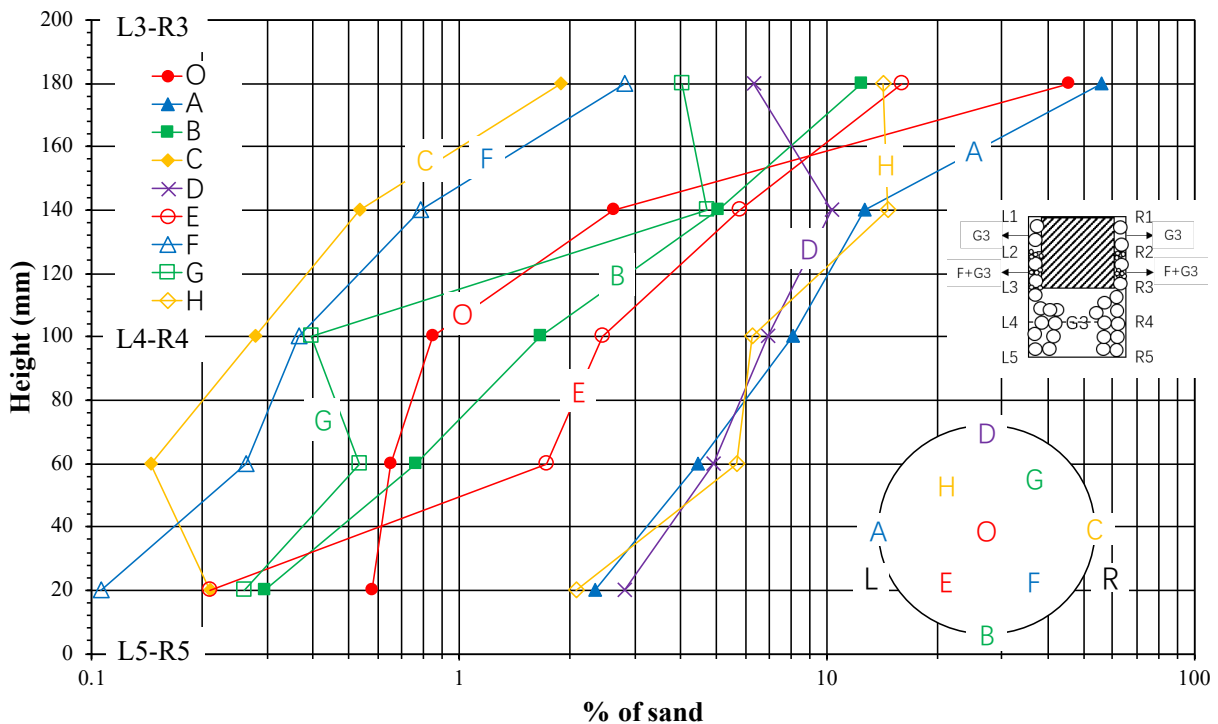


Figure III.9 – Profile of sand percentage after test for specimen Filtration-G-1

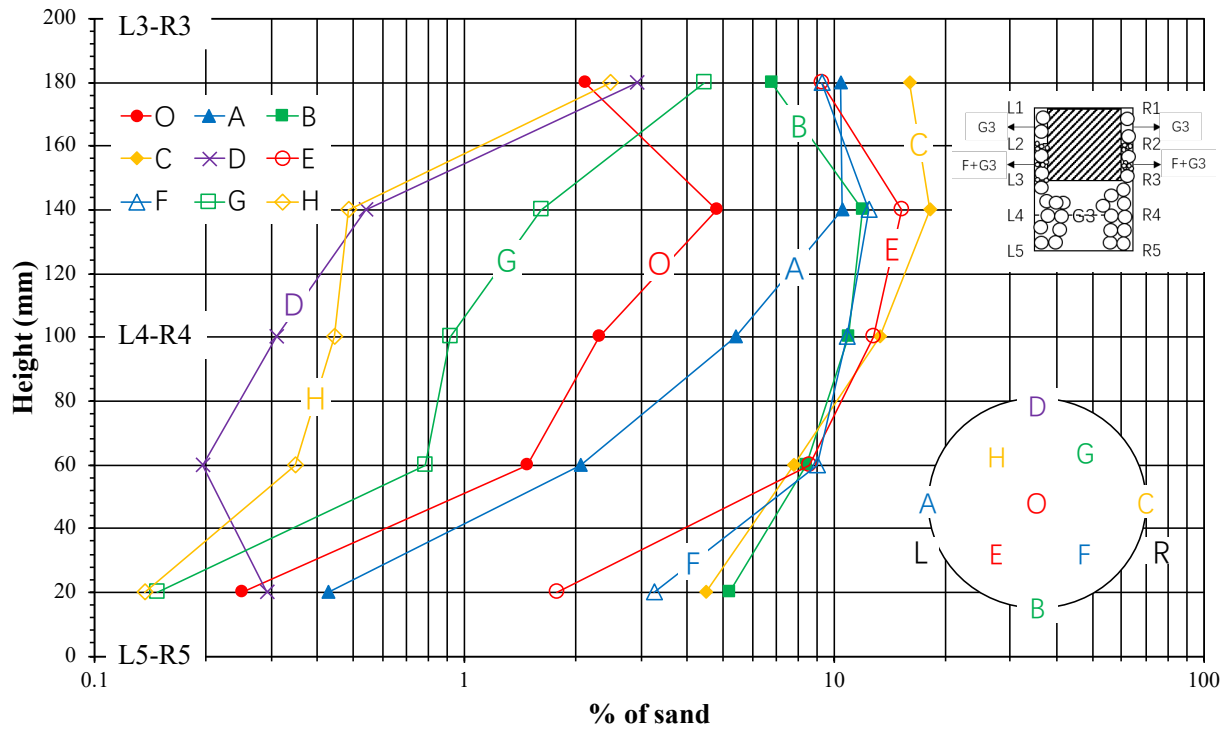


Figure III.10 – Profile of sand percentage after test for specimen Filtration-G-2

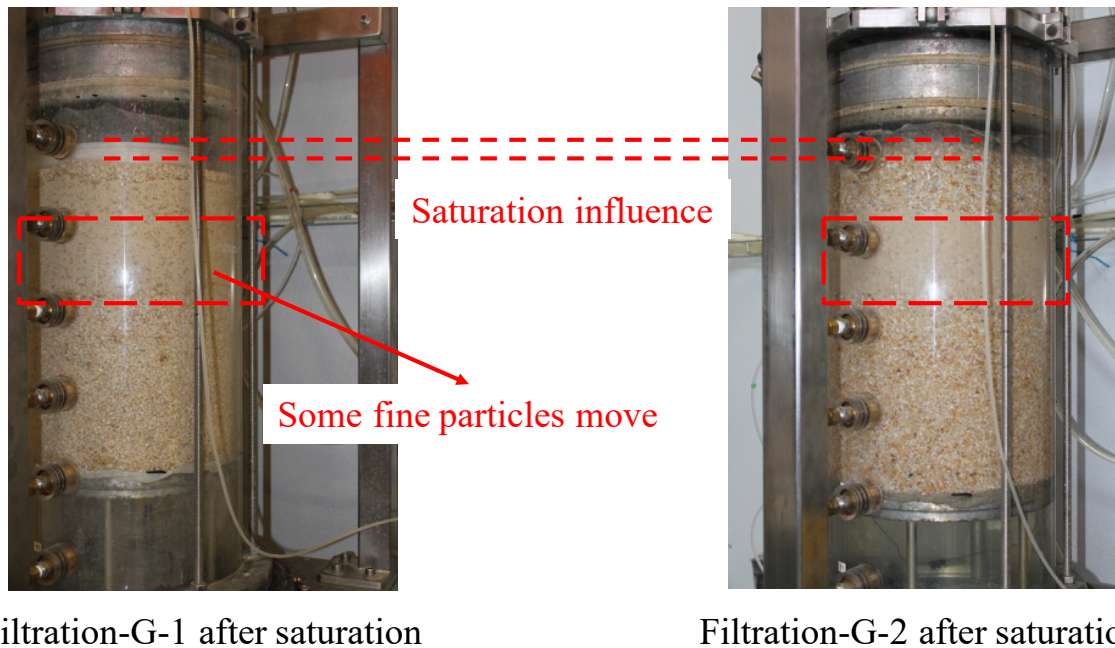


Figure III.11 – Influence of the saturation phase on the initial state of the specimen

Specific to the specimen Filtration-C, the phenomenon of filtration was more obvious at positions O, B, and H within the area between L3-R3 and L4-R4, and the greatest number of filtered particles could be seen on the border of L3-R3 at position O because the binary mixture was in the center. The positions with more filtered fine particles were O, A, E, and H in the case of specimen Filtration-G-1, and the percentage of sand on the boundary of L3-R3 was maximum because the binary mixture was next to the rigid wall. Similarly, more particles were blocked

at points B, C, E, and F for specimen Filtration-G-2, and the most obvious blockage existed at point C after the filtration's initialization. The point D is at the similar position as point B in the configuration Filtration-G, however, there is a significant difference in the sand content between point B and point D, which means that the filtration process in suffusion is heterogeneous. The average percentage of sand at each measuring point within each layer is displayed in Table III.3. Compared with the area between L3-R3 and L4-R4, the sand percentage within the area between L4-R4 and L5-R5 was much smaller. Thence, the sand percent rapidly decreases along the seepage length.

Table III.3 – The average percentage of sand at each point within each layer

Name		Filtration-C		Filtration-G-1		Filtration-G-2	
Area		L3R3-L4R4	L4R4-L5R5	L3R3-L4R4	L4R4-L5R5	L3R3-L4R4	
% of sand	O	5	1.9	24.1	0.7	3.1	0.9
	A	4.8	/	34.1	4.9	8.8	1.2
	B	6.9	/	8.7	0.9	10	6.8
	C	1.4	/	1.2	0.2	15.8	6.1
	D	3.4	/	8.3	4.9	1.3	0.2
	E	0	0	10.9	1.5	12.4	5.2
	F	0	0.3	1.8	0.2	10.8	6.1
	G	4.5	/	4.4	0.4	2.3	0.5
	H	6.7	/	14.4	4.7	1.1	0.2
	I	0.8	/	/	/	/	/
	J	1.7	/	/	/	/	/
	Total	35.2	2.2	107.9	18.4	65.6	27.2
	Two layers	37.4		126.3		92.8	

Note: / means no measured value is available.

Analysis of filtration mechanism

Because the permeability coefficients of the binary mixing layer and reverse filter layer are quite different, when seepage flows perpendicular to the contact surface of two adjacent middle layers with a large difference in the permeability coefficient, the fine particles of the soil layer with a smaller coefficient are brought into another layer with a larger coefficient, and the phenomenon of contact sand boiling occurs. When seepage flows along two contact surfaces with different permeability coefficients, fine particles are transported along the interface, and contact scouring

occurs. The instability coefficient of binary mixing in the sample was $C_u = 7.70 < 10$, and the interlayer coefficient between the binary mixing layer and the filter layer was $D_{15,c}/D_{85,f} = 4$. These two parameters indicated that piping would not occur in the binary mixing. For the specimens Filtration-G-1 and Filtration-G-2, because the contact area of binary mixing and filter layer were equal, the former may have been subjected to contact sand boiling on the boundary of L3-R3; because of the existence of the stable arch structure on the boundary of L3-R3, in the post-test the fine particles accumulated mainly on the boundary of L3-R3 and L4-R4, and the distribution was not uniform. For the specimen Filtration-C, because the contact area of the binary mixing was smaller than that of the filter layer, and the hydraulic gradient of the binary mixture was larger than that of its peripheral filter layer, the binary mixing may have been subjected to contact scouring on the boundary of L3-R3. That is, the fine particles would flow along the interface, post-test fine particles accumulated on the boundary of L3-R3 only and diffused from the center to the surrounding area, and fewer fine particles were deposited, which was different from the situation for the specimens Filtration G-1 and Filtration G-2 on the boundary of L3-R3 and L4-R4.

When the fine particles in the binary mixture enter the filter layer, they are free in the pore as a result of the small number and low concentration of fine particles. Under the action of a small seepage gradient, the fine particles are lost along with the seepage flow. For the specimens Filtration-G-1 and Filtration-G-2, the number of fine particles deposited on the boundary of L4-R4 was small, but the corresponding distribution on the boundary of L3-R3 was basically the same. Because the concentration of fine particles in layer L3R3–L4R4 was relatively low for the specimen Filtration-C, no accumulation of fine particles occurred in layer L4-R4, as shown in Figures III.8, III.9, III.10 and Table III.3.

Based on the analysis of the preceding results, the experimental scheme designed in this test achieved the effect of filtration. At the same time, the experimental results show that at the filter interface, the interface area of the binary mixing and the filter layer had an effect on the permeability function of the infiltration system, leading to a change in the direction of seepage.

3.4.2 Hydraulic gradient

The variation of relative local hydraulic gradient during test

The difference between local hydraulic gradient i_{local} and global hydraulic gradient i_{global} was computed. In order to characterize the influence of filtration on the hydraulic gradient, the ratio of this difference and global hydraulic gradient i_{global} was defined as the relative local hydraulic

gradient and expressed as Equation III.4:

$$i' = \frac{i_{local} - i_{global}}{i_{global}} \quad \text{III.4}$$

Figures III.12, III.13 and III.14 display the variations in the relative local hydraulic gradient.

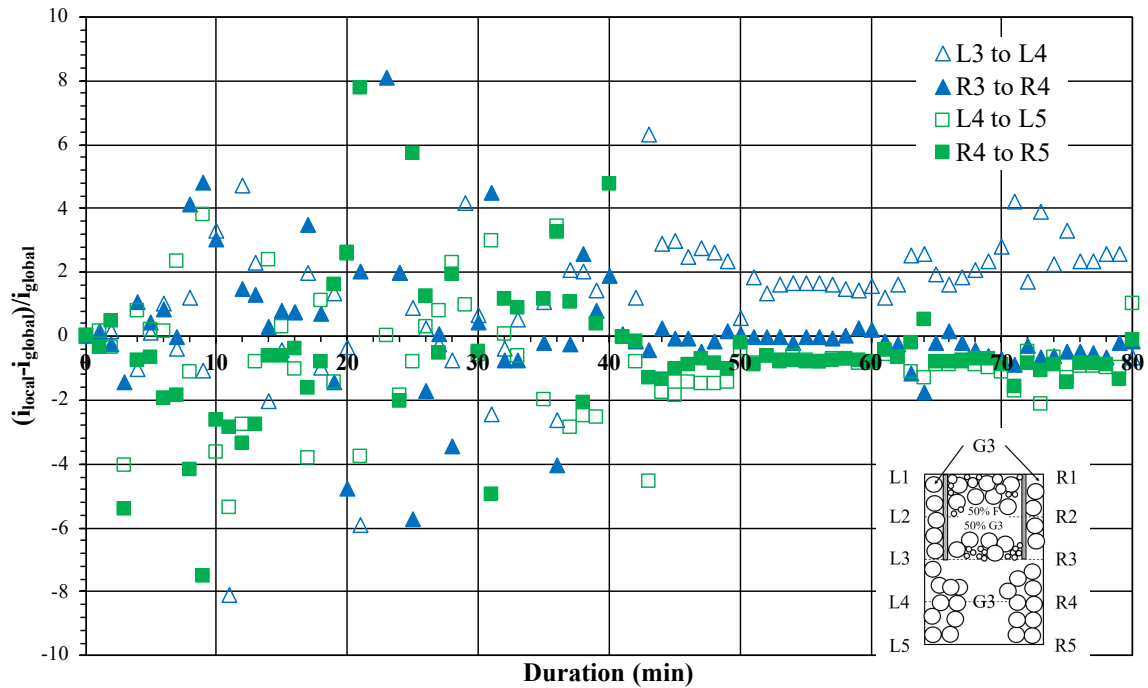


Figure III.12 – Relative local hydraulic gradient versus time for specimen Filtration-C

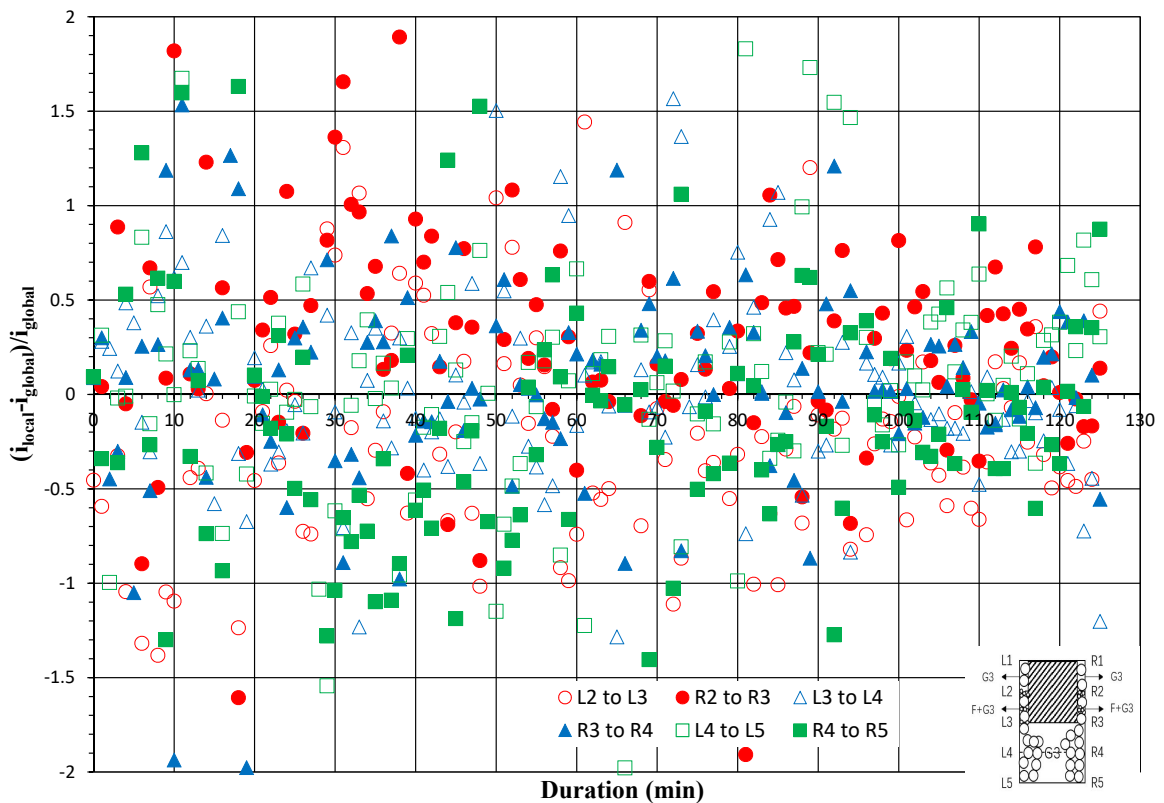


Figure III.13 – Relative local hydraulic gradient versus time for specimen Filtration-G-1

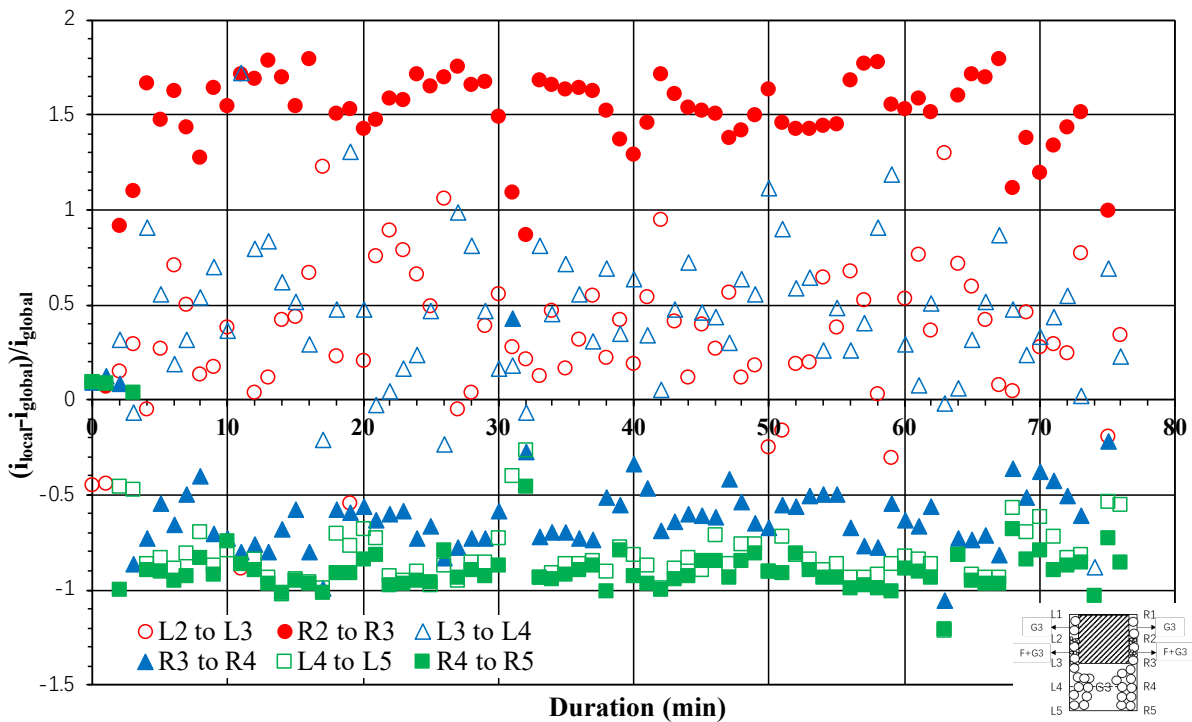


Figure III.14 – Relative local hydraulic gradient versus time for specimen Filtration-G-2

For specimen Filtration-C, only the area between L3-R3 and L5-R5 is demonstrated because the hydraulic parameters could not be measured in the binary mixture. From these three figures, the reader can find that the local hydraulic gradient was higher in areas that were closer to the binary mixture, which is consistent with the previous post-test particle size distributions.

Another concern was the inconsistency of the local hydraulic gradient on the left and right sides of the same level. For specimen Filtration-C, starting from 40 minutes, the local hydraulic gradient of L3 to L4 was greater than that of R3 to R4. Compared with Figure III.8 and Table III.3, the sand percentages at the two most important points, E and F, within the area L3R3-L4R4 were zero. However, a small amount of filtered fine particles can be seen around E and F. Consequently, a small number of fine particles also have a large impact on hydraulic parameters.

As presented by Figure III.14, taking the layer L2R2-L3R3 as an example, during the whole experiment, the local hydraulic gradients on the left and right sides are different. The local hydraulic gradient on the left is close to the global hydraulic gradient, while the local hydraulic gradient on the right is greater than the global hydraulic gradient. Therefore, the overpressure depends on the position due to the heterogeneity of filtration process.

3.4.3 Analysis of the decompression effect of the filter during the test

Figures III.15; III.17 and III.19 show the variation of hydraulic gradient ratio with the increasing time, Figures III.16; III.18 and III.20 show the variation of hydraulic conductivity ratio with the

increasing time for specimens Filtration-C, Filtration-G-1 and Filtration-G2, respectively.

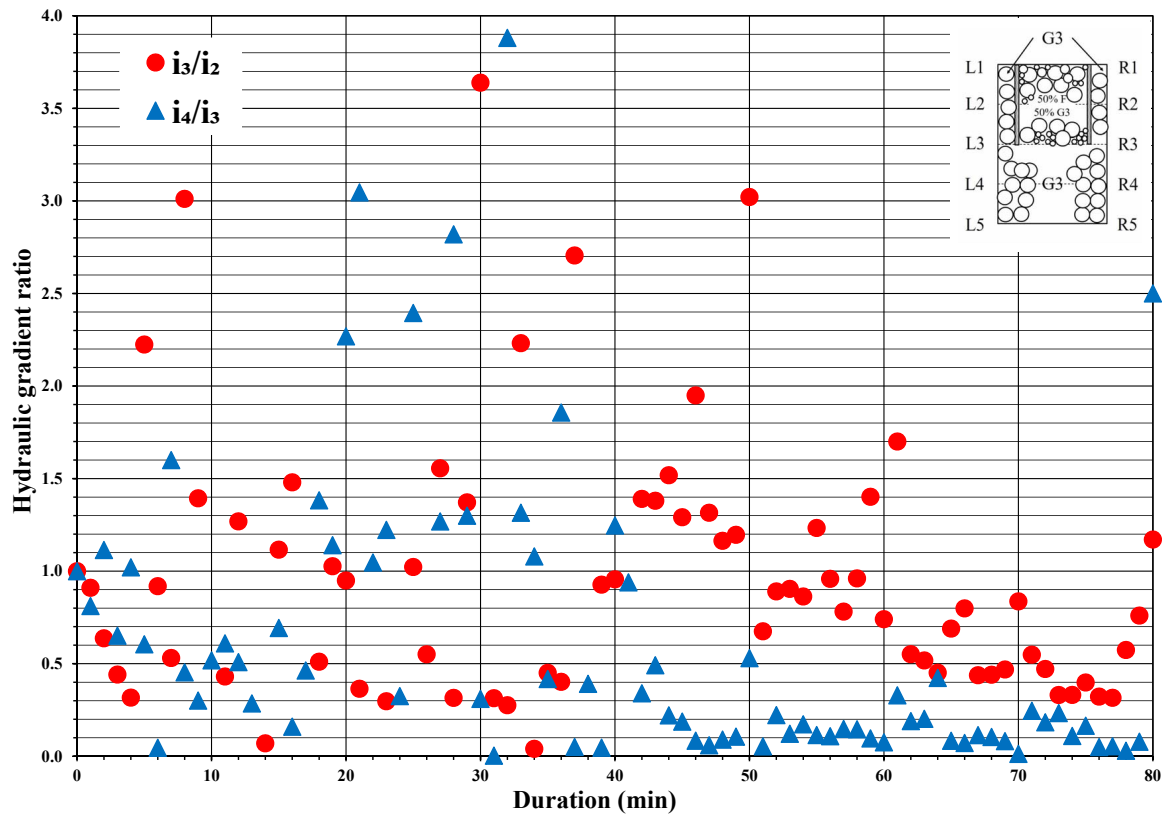


Figure III.15 – The variation of hydraulic gradient ratio with the increasing time for specimen Filtration-C (“2”: layer L2R2-L3R3; “3”: layer L3R3-L4R4; “4”: layer L4R4-L5R5)

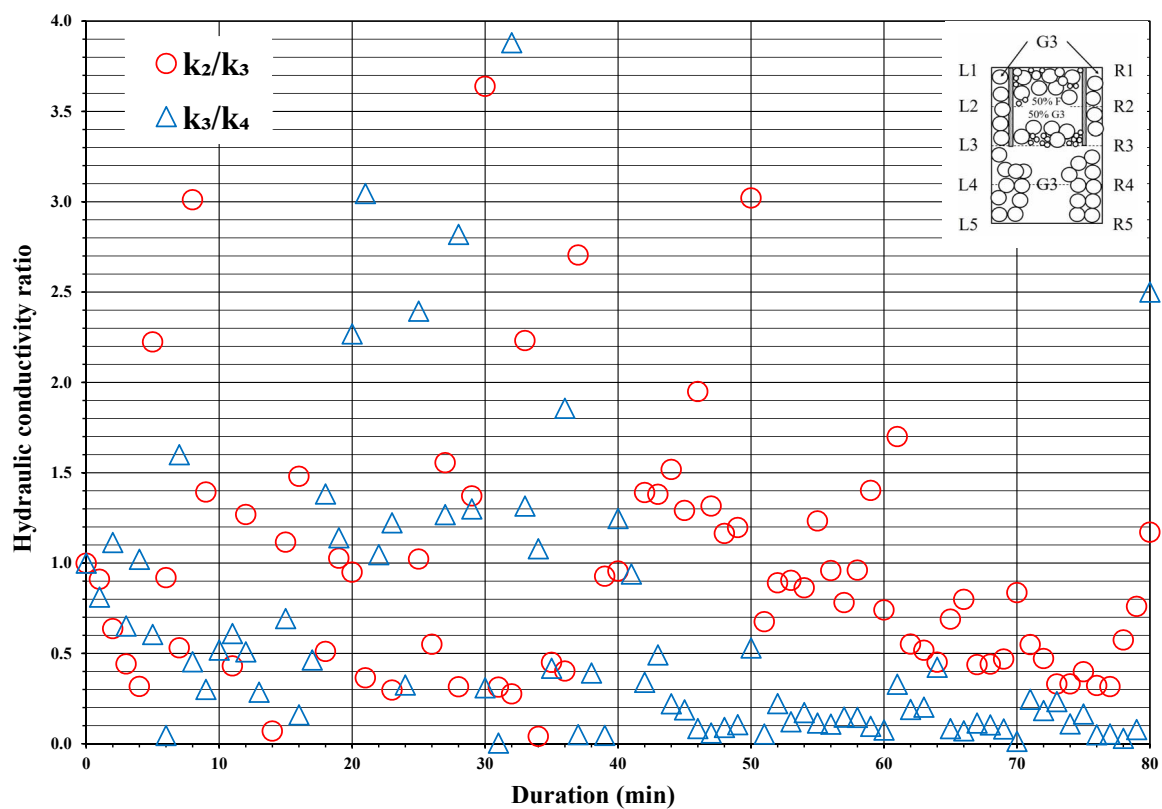


Figure III.16 – The variation of hydraulic conductivity ratio with the increasing time for specimen Filtration-C (“2”: layer L2R2-L3R3; “3”: layer L3R3-L4R4; “4”: layer L4R4-L5R5)

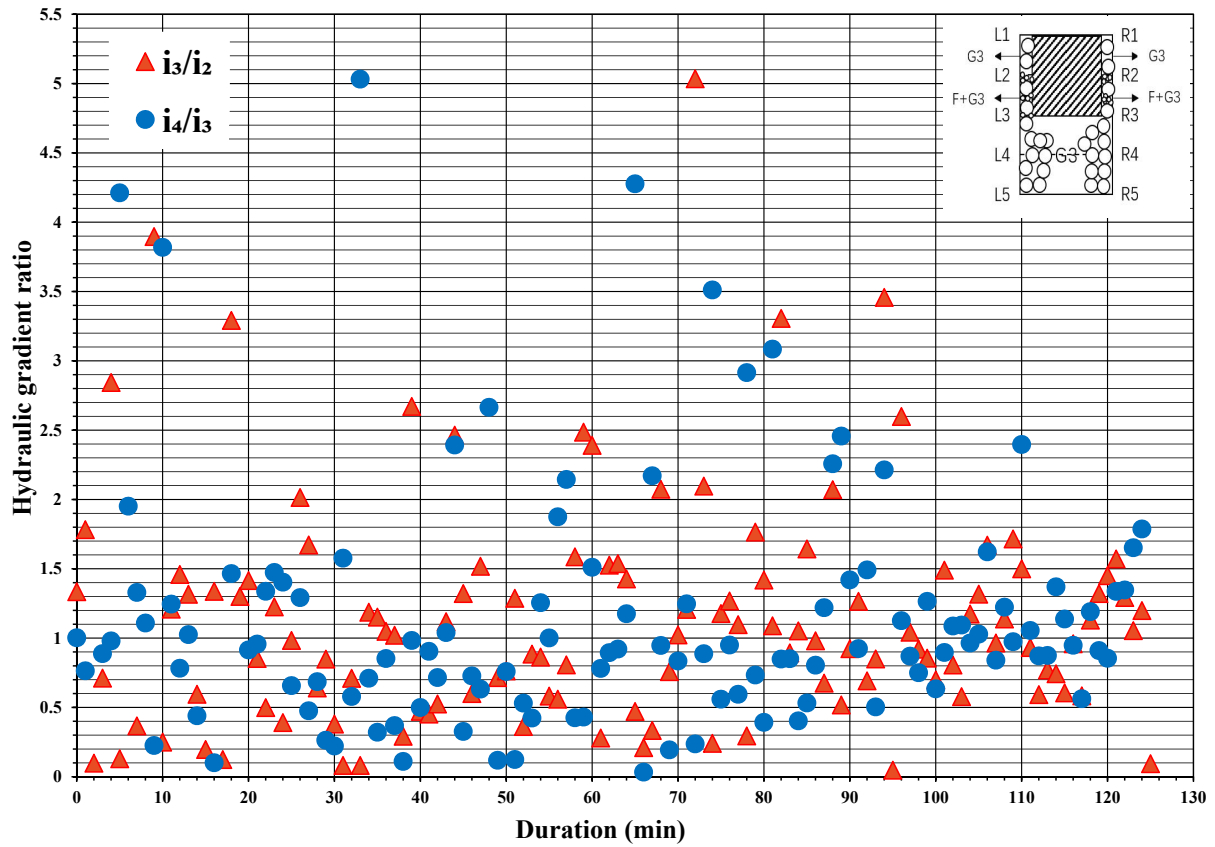


Figure III.17 – The variation of hydraulic gradient ratio with the increasing time for specimen Filtration-G-1 (“2”: layer L2R2-L3R3; “3”: layer L3R3-L4R4; “4”: layer L4R4-L5R5)

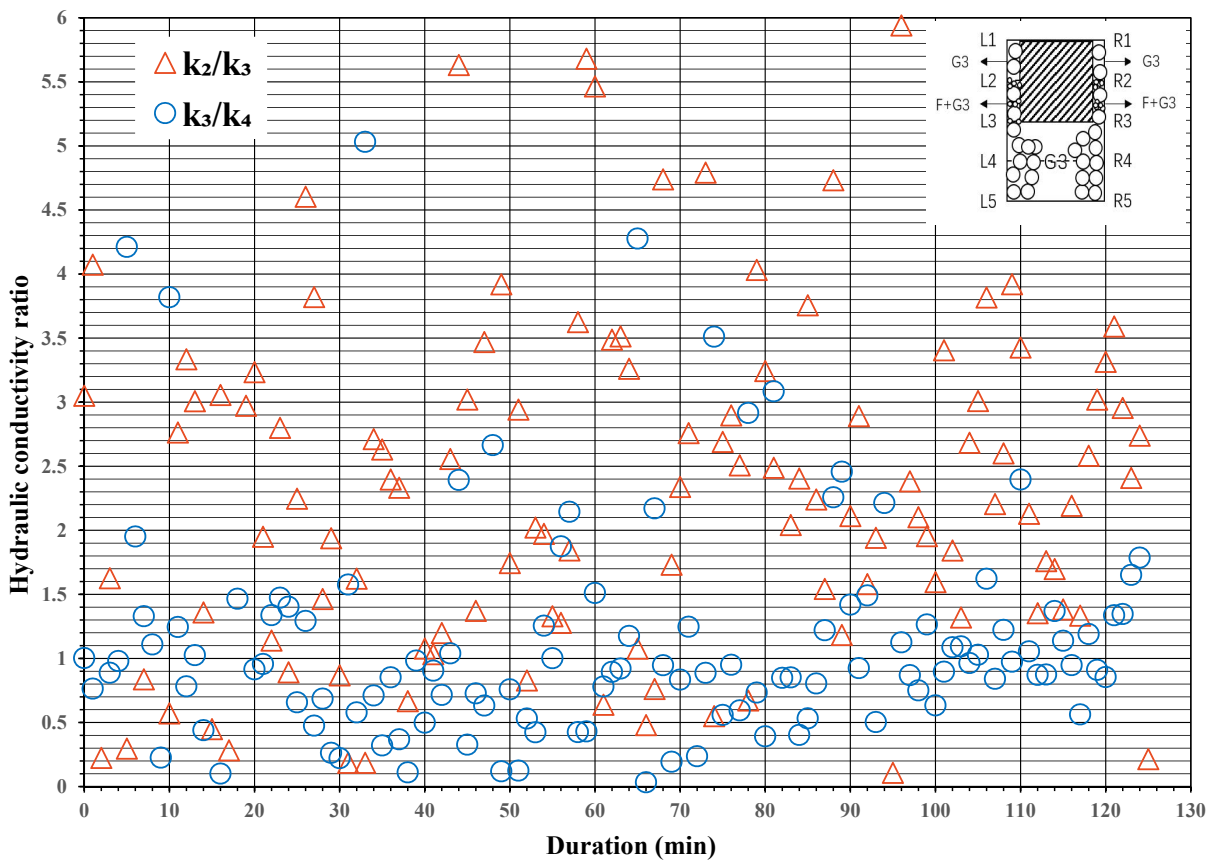


Figure III.18 – The variation of hydraulic conductivity ratio with the increasing time for specimen Filtration-G-1 (“2”: layer L2R2-L3R3; “3”: layer L3R3-L4R4; “4”: layer L4R4-L5R5)

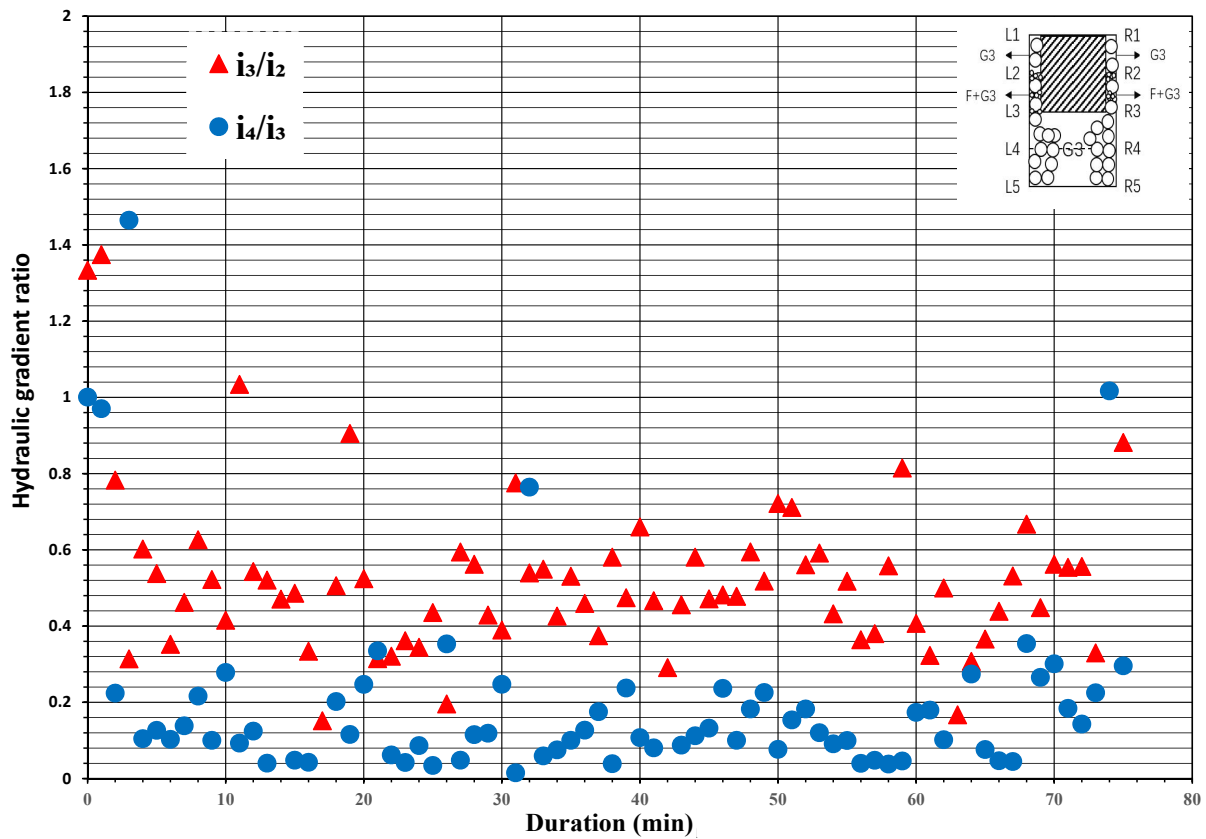


Figure III.19 – The variation of hydraulic gradient ratio with the increasing time for specimen Filtration-G-2 (“2”: layer L2R2-L3R3; “3”: layer L3R3-L4R4; “4”: layer L4R4-L5R5)

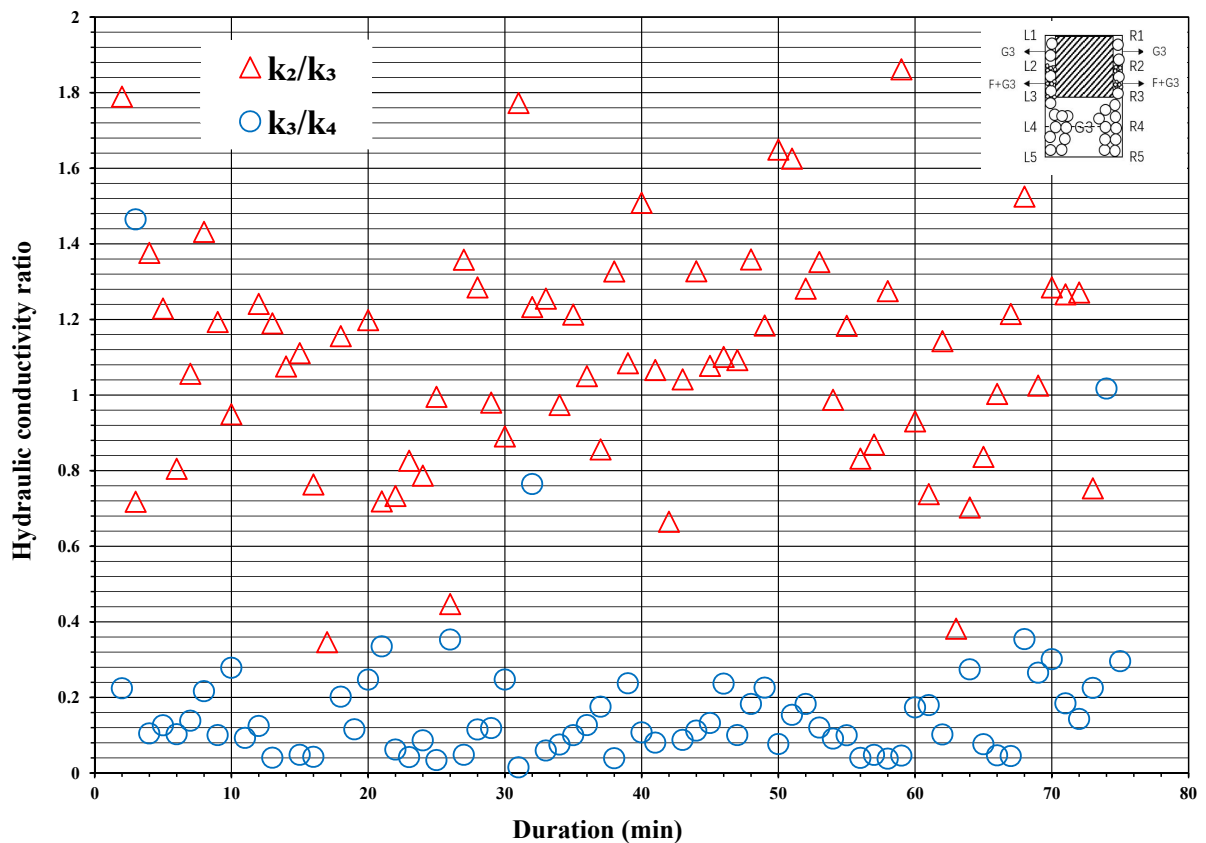


Figure III.20 – The variation of hydraulic conductivity ratio with the increasing time for specimen Filtration-G-2 (“2”: layer L2R2-L3R3; “3”: layer L3R3-L4R4; “4”: layer L4R4-L5R5)

From the preceding graph analysis, the reader can see that the test results of the three specimens show the same filtering characteristics. This shows that the design of filters for the three experiments satisfies the decompression principle of filters.

3.4.4 Hydraulic conductivity

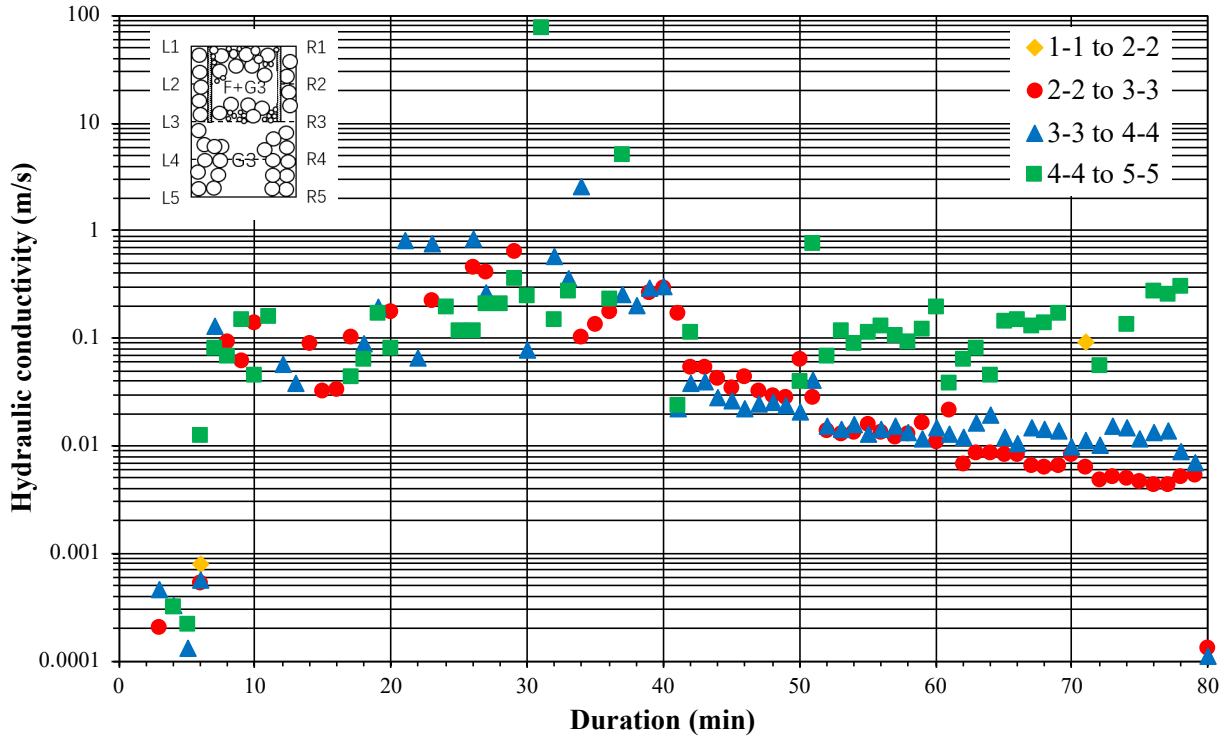


Figure III.21 – Variations of hydraulic conductivity in each layer for Filtration-C

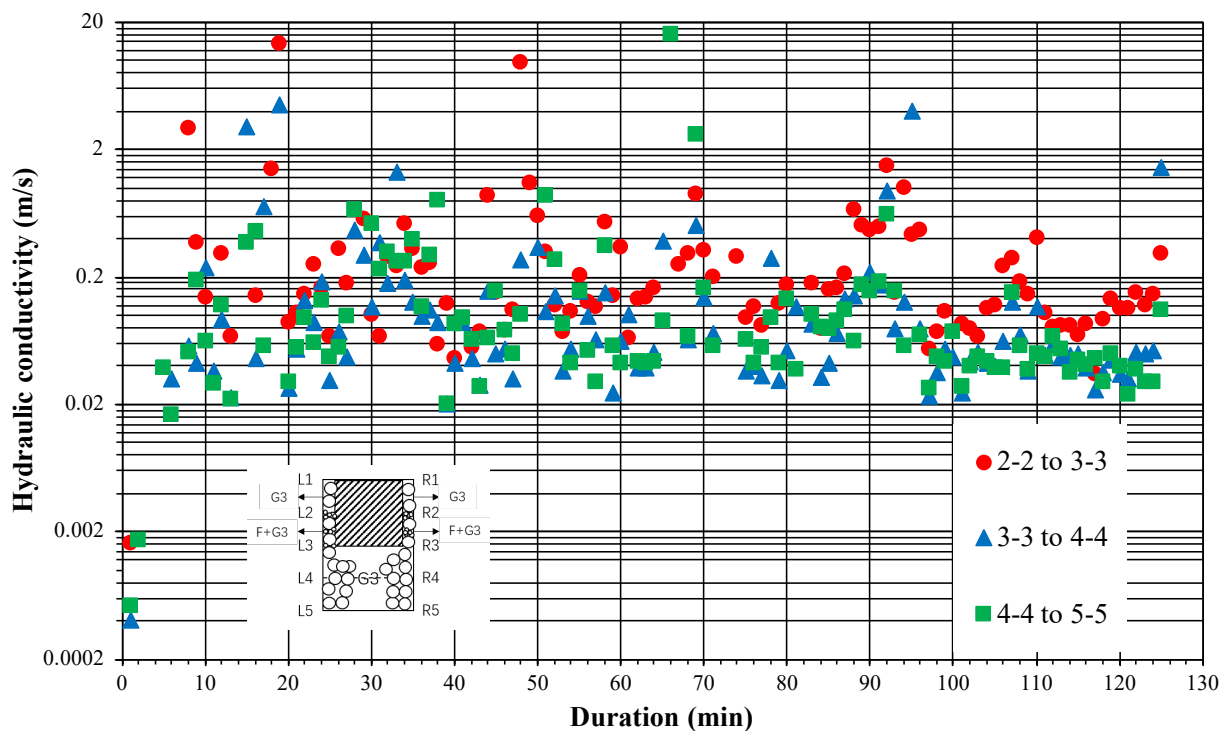


Figure III.22 – Variations of hydraulic conductivity in each layer for Filtration-G-1

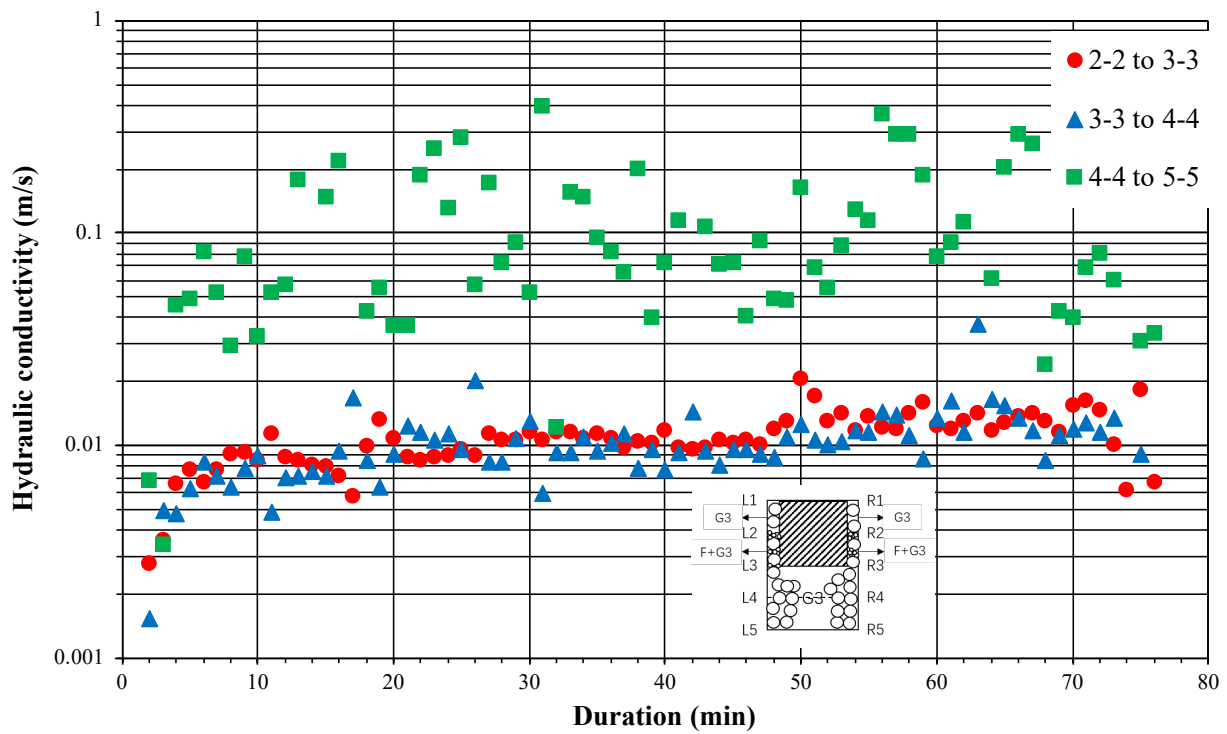


Figure III.23 – Variations of hydraulic conductivity in each layer for Filtration-G-2

Figures III.21, III.22 and III.23 present the variations of hydraulic conductivity in each layer for these three specimens. Figure III.23 indicates that the hydraulic conductivity of Filtration-G-2 was more stable than that of Filtration-C; in other words, the filtration process in Filtration-G-2 was closer to complete, leading to constant hydraulic conductivity. For Filtration-C, the hydraulic conductivity decreased as a result of the existence of seepage along the interface and downward directions.

The curves of hydraulic conductivity for L2R2-L3R3 and L3R3-L4R4 are very closed, but the sand content in these two layers was very different (initial sand content was 50 % in L2R2-L3R3). Therefore a small amount of fine content has a great impact on hydraulic conductivity, but the influence cannot increase infinitely.

Considering the entire specimen from layers L2R2 to L5R5, the hydraulic conductivity of Filtration-G-1 was higher than that of Filtration-G-2 based on a comparison of Figure III.22 and Figure III.23. The average fine content in the downstream (L3R3 to L5R5) was 7.02 % for Filtration-G-1 but 5.16 % for Filtration-G-2. This means that more fine particles moved from the binary mixture to the downstream for Filtration-G-1, which made the whole specimen more homogeneous than Filtration-G-2. Therefore, if more particles move, the specimen shows more permeable. In Filtration-G-2, the fine particles were more concentrated in the layer L2R2 to L3R3. The results show that clogging occurred on the boundary of L3-R3 for Filtration G-1. As for specimen Filtration-C, its overall permeability was also larger than that of Filtration-G-2. For Filtration-C, although the number of fine particles entering the downstream was small, the periphery was

the material with high permeability that fine particles could not enter because of the impervious tube. This also increased the average permeability of the entire specimen. As a result of the small amount of fine particles in the downstream, the conductivity of the downstream (L3R3 to L5R5) maintained considerable consistency with the upstream (L1R1 to L3R3) in Filtration-C. Because of greater homogeneity, the permeability of each layer was much closer in Filtration-G-1 than in Filtration-G-2. Moreover, the conductivity of the bottom was higher than the other layers because of its small fine particle content in Filtration-G-2, which was closed to Filtration-G-1.

3.4.5 Comparison of experimental results and filtration law

Because multilayer soil has varying permeability and thickness, the same layer of soil is isotropic while the multilayer soil is anisotropic. To determine the permeability coefficient of multilayer soil, it is assumed to be a plane problem firstly, and the seepage is calculated in two directions: parallel to the layer and perpendicular to the layer.

The equivalent average permeability coefficient K_x parallel to the layers is:

$$K_x = \frac{k_1 T_1 + k_2 T_2 + \cdots + k_n T_n}{T} = \frac{1}{T} \sum_{i=1}^n k_i T_i \quad \text{III.5}$$

The equivalent average permeability coefficient K_y perpendicular to the layers is:

$$K_y = \frac{T}{\frac{T_1}{k_1} + \frac{T_2}{k_2} + \cdots + \frac{T_n}{k_n}} = \frac{T}{\sum_{i=1}^n \frac{T_i}{k_i}} \quad \text{III.6}$$

Where k_1 , k_2 , and k_n are the permeability coefficients of each layer of soil. T_1 , T_2 , and T_n are the thickness of each layer of soil. Total thickness: $T = T_1 + T_2 + \cdots + T_n$.

On that basis, K_x can be approximately controlled by the permeability coefficient and thickness of the most permeable layer. K_y can be approximately controlled by the permeability coefficient and thickness of the most impermeable soil layer. Thus the horizontal permeability coefficient K_x is always greater than the vertical permeability coefficient K_y for multilayer soil. Therefore, along the seepage path, the content of fine particles drops rapidly, because the fine particles that are detached from the binary mixture are distributed to the entire cross section.

For all specimens, we can note that the sand content decreases along the seepage length in Figure III.24. If we use the sand content to present the particle mass concentration, this result agrees with Equation III.1 but is not a complete exponential decrease. The reason is that the filter coefficient λ is not constant in the suffusion.

Yang et al. (Yang et al., 2000) presented the filter coefficient λ as follows:

$$\lambda = \frac{\phi_{0,c} - \omega}{vt} \quad \text{III.7}$$

Where $\phi_{0,c}$ is the initial filter layer porosity, v is the seepage velocity, t is the time, and ω is the specific volume of filtered fraction and filter fraction.

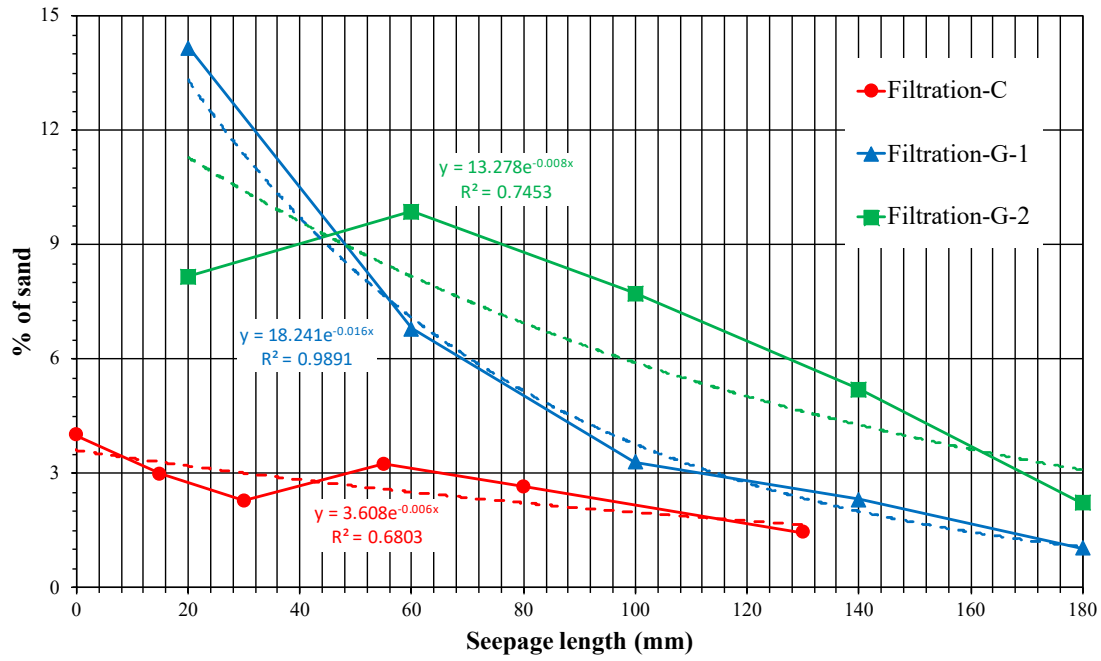


Figure III.24 – The relationship between percentage of filtered particles and seepage length for three specimens

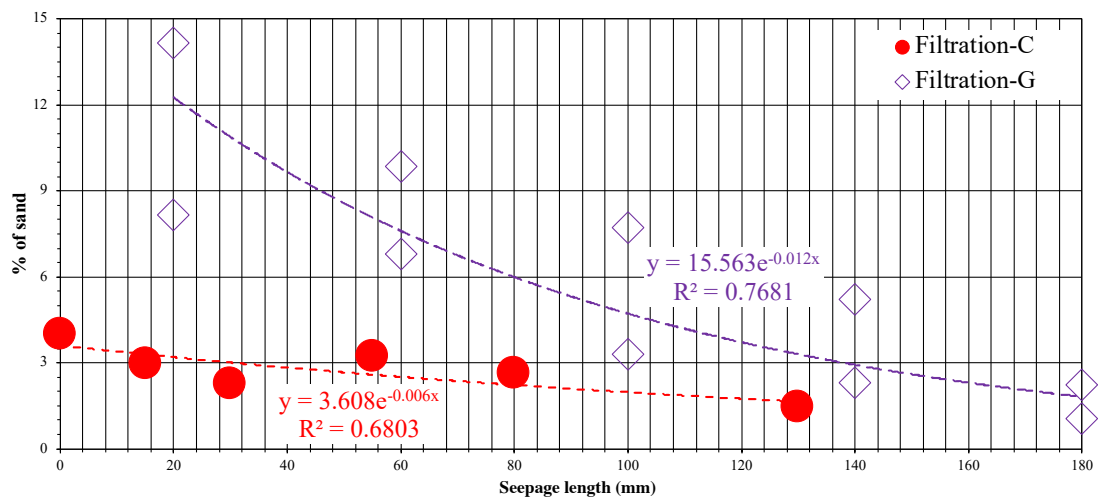


Figure III.25 – The relationship between percentage of filtered particles and seepage length for two experimental configurations

Ideally, the filtration process ends when the result reaches the state described as Equation III.1. For all specimens, no particles are pushed out at the outline, therefore, the filtration process may not finish. The λ is related to the sand content in the downstream part. Due to the influence of

saturation phase, the C_0 is different for Filtration-G-1 and Filtration-G-2. If we consider all ten values together in order to reduce the discrepancy of λ , the curve of configuration Filtration-G is shown as Figure III.25. For the entire specimen, the configuration Filtration-G had a higher sand content than Filtration-C and was more consistent with Equation III.1. Consequently, Equation III.1's results and the experimental results appear to have a better consistency, with more fine particles within specimens.

3.4.6 Expended energy

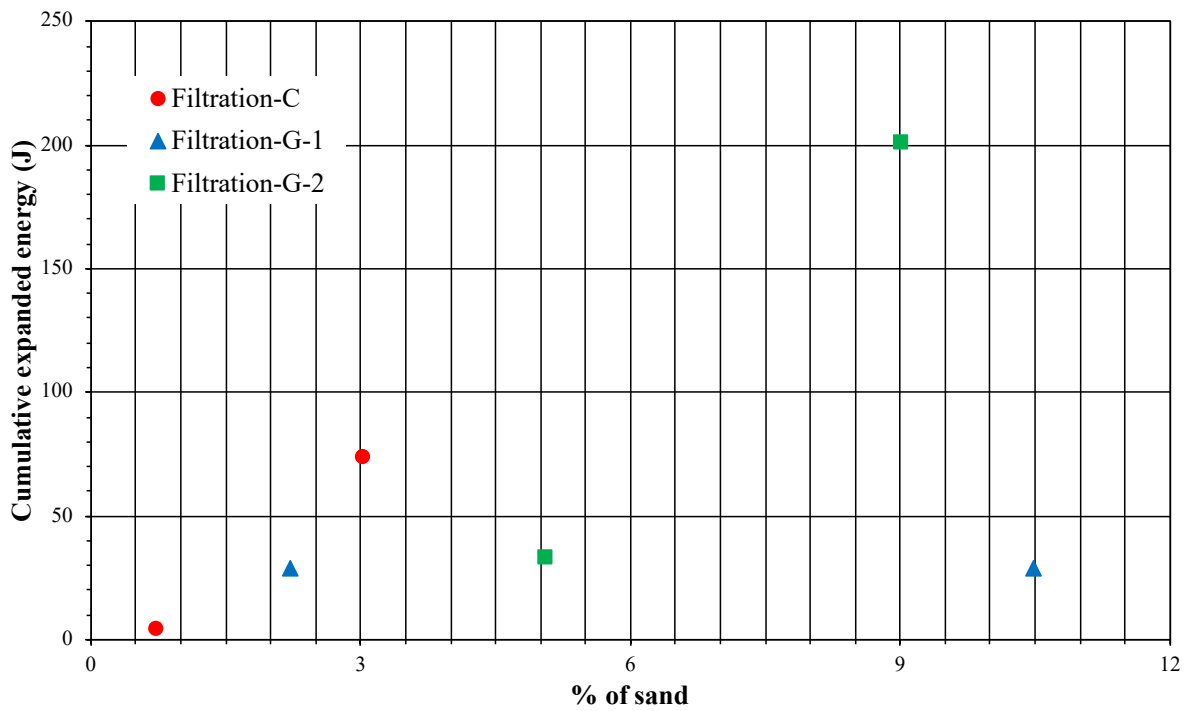


Figure III.26 – The relationship between cumulative expended energy and percentage of filtered particles

As already mentioned in Chapter II, the power expended by the seepage flow P_{flow} and the erosion resistance index I_α were expressed by Marot et al. (Marot et al., 2016):

$$P_{flow} = Q\gamma_w\Delta h \tag{III.8}$$

Where Q is the fluid flow rate and Δh is the drop of hydraulic head.

$$I_\alpha = -\log_{10} \frac{\text{dry eroded mass}}{\text{total dissipated flow energy}} \tag{III.9}$$

Figure III.26 displayed the relationship between cumulative expended energy and percentage of filtered particles. The hydraulic load detaches the fine particles, which move with the flow.

Therefore more filtered particles need more expanded energy.

3.5 Conclusion

According to the erosion-filtration tests performed with two different programs, the content of filtered fine particles decreases along the seepage length. The basic filtration equation indicates the final state of the filtration process. In the suffusion process, the filtration process ends when the fine content is closed to the value computed by the basic filtration equation. Only a small account of fine particles is needed to change the fabric of the soil, thereby affecting its hydraulic responses. The interface area between the binary mixture and filter layer has a certain influence on the permeability function of the filtration system. Because said area is not equal, the seepage direction of the binary mixture at the interface will change. The particle size of the aggregate and fine particles of said mixture have a significant influence on the sand filtering effect of the filter. The filters designed in the three samples had the effect of filtering soil and reducing pressure.

SUFFUSION SUSCEPTIBILITY

4.1 Introduction

Suffusion is a combination of three processes: detachment, transport, and possible filtration of the finer fraction, meaning that the local process plays an important role in suffusion and highlights its complexity. Moreover, in Chapter III, the filtration tests showed that a small amount of fine content has a great impact on hydraulic conductivity. However, the local process has not been paid sufficient attention. Thanks to the special design of the oedo-permeameter, we can study the local process of suffusion. For this study, both gap-graded and well-graded gradations were selected and divided into seven groups. According to the different experimental purposes, the number of samples in each group was different; details are given in Table IV.3. The experimental process control parameters are shown in Table IV.4. For each tested soil, the post-test grain size distribution of each layer and eroded particle are discussed. By analyzing the local hydraulic gradient, we find that the position of maximum local hydraulic gradient is important for suffusion and that suffusion is a gradual process from the upstream to the downstream part. At the same time, the influence of fine particles in soil on the hydraulic conductivity is discussed, the judgment method of silting up in the seepage process is dissected, and the seepage process is qualitatively analyzed.

4.2 Testing equipment and materials

4.2.1 Oedo-permeameter

The device selected to study suffusion susceptibility was the oedo-permeameter, which was introduced in Chapter III. As such, it will only be described briefly here. It is composed of a 280 mm inner diameter rigid wall cylinder cell, and the specimen height can reach 600 mm (see

Figure IV.1). A detailed description was provided by Sail et al. (Sail et al., 2011). The fluid circulates into the top cap, which contains a layer of gravel to diffuse the fluid uniformly on the specimen's top surface. A vertical funnel-shaped draining system is connected to the device base, which is specially designed to avoid clogging. Furthermore, the draining system includes a collecting system composed of an effluent tank containing a rotating support with eight beakers to catch the particles lost during the test. Two 200 L tanks with a pressure controller, are used as the hydraulic control system. The differential pore water pressure across the specimen is measured by using a differential pressure transducer connected to the top cap and base pedestal. The rigid wall of the cell is equipped with 12 pressure ports, another pressure port is placed on the piston base plate (i.e., at the specimen–piston interface), and a 14th port is located below the specimen on the funnel-shaped draining system. All these pressure ports are connected to a multiplex unit, which is linked to a manometer to avoid discrepancy.

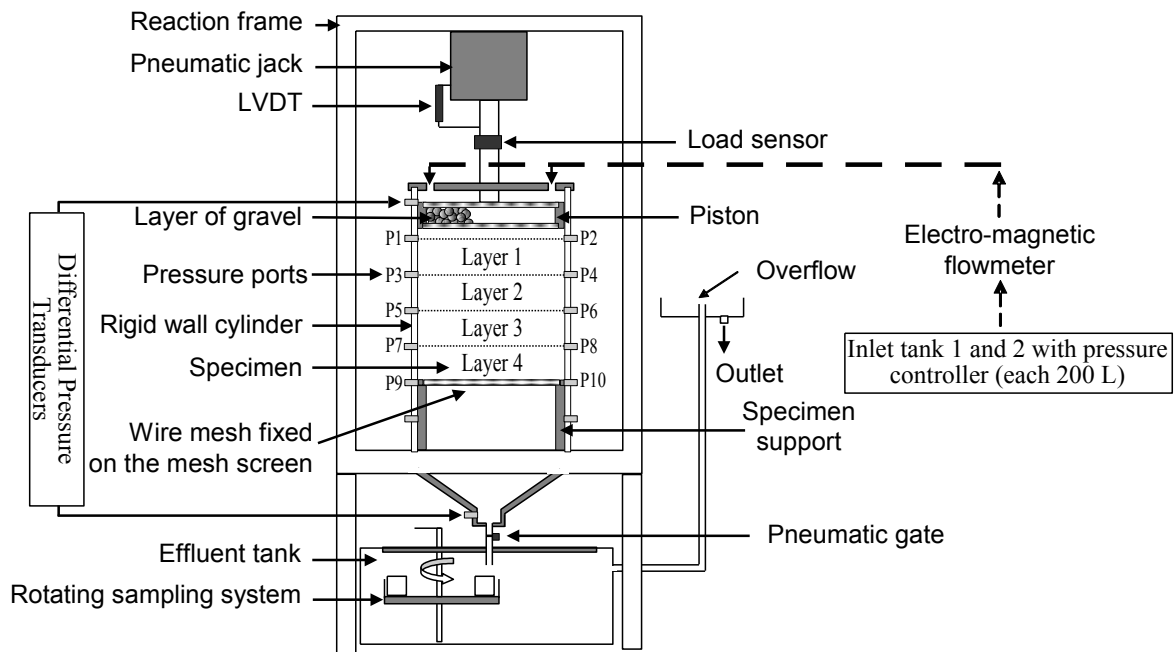


Figure IV.1 – Permeameter apparatus: the oedo-permeameter

4.2.2 Tested gradations

The gradations used in this study can be identified as gap-graded and widely graded distributions. Figure IV.2 displays the grain size distribution of the tested soils. Four types of grain size distribution were selected to realize the tests. Soil Chavanay is a real soil from a French dike. F means the Fontainebleau Sand, and G3 refers to the Palvadeau Gravel G3. Grain size distributions W1 and W2 are well-graded soils, and the others are gap-graded soils. For the given gradations, the properties and result of the assessment of suffusion susceptibility are shown in

Table IV.1 and Table IV.2.

All the grain size distributions were considered poorly graded soils based on Lafleur et al. (Lafleur et al., 1989). Soils with discontinuous or gap-graded distribution were considered internally unstable. Wan and Fell's criterion (Wan and Fell, 2008) indicates that W1 and W2 had identically stable behavior. For the other criteria, except Chang and Zhang's criterion (Chang and Zhang, 2013b), all gradations qualified as unstable, but in the case of gap-graded soils, G1 and G2 were stable based on Chang and Zhang's criterion.

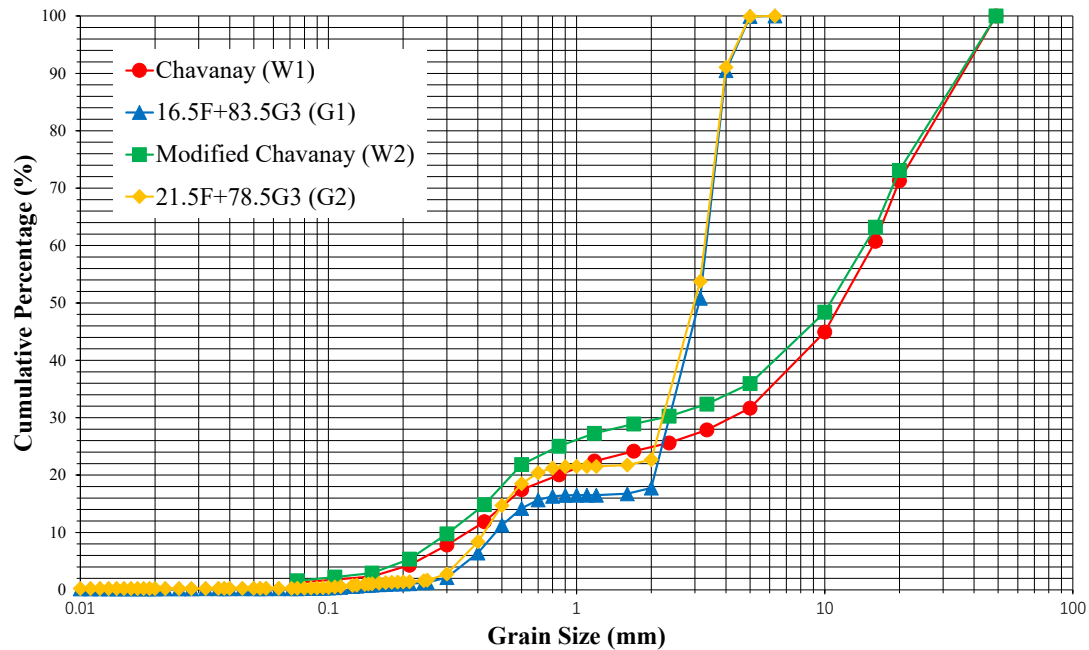


Figure IV.2 – Tested grain size distributions

The fine particle content of W1 and G1 were 5% smaller than W2 and G2, respectively. The choice was to investigate the effect of inhomogeneity and further study the influence of the local process on suffusion. Six recent criteria based on gradation distribution were chosen to assess the potential susceptibility to suffusion of soils (see Table IV.2). In these criteria, certain other parameters that could not be ignored were not considered, such as grain shape, soil density (except the criterion of Indraratna et al. (Indraratna et al., 2011, 2015)), and stress state.

Table IV.1 – Properties of tested gradations

	C_u	G_r	P (%)	d_5 (mm)	d_{10} (mm)	d_{20} (mm)	d_{60} (mm)	d_{90} (mm)	$\frac{H}{F_{min}}$	$D_{\frac{H}{F_{min}}}$ (mm)	$\frac{D_{15,c}}{D_{85,f}}$
W1	42.49	WG	1.07	0.23	0.37	0.85	15.72	38.90	0.37	1.18	7.79
W2	47.42	WG	1.34	0.20	0.31	0.55	14.70	38.22	0.29	1.19	8.24
G1	7.13	2.29	0.21	0.37	0.47	2.08	3.35	3.99	0.60	0.49	4.02

G2	7.65	2.29	0.27	0.34	0.43	0.68	3.29	3.98	0.56	0.51	4.02
----	------	------	------	------	------	------	------	------	------	------	------

Note: C_u = uniformity coefficient; $G_r = d_{\max}/d_{\min}$ (d_{\max} and d_{\min} : maximal and minimal particle sizes, respectively, characterizing the gap in the grading curve); P = percentage of particles smaller than 0.063 mm; d_x = the sieve size for which $x\%$ of the weighed soil is finer; F and H = the mass percentages of the grains with a size lower than a given particle diameter d and between d and $4d$, respectively; $D(H/F)_{\min}$ = the corresponding diameter with the minimum value of ratio H/F ; $D_{15,c}$ is the diameter of the 15 % mass passing in the coarse fraction; $D_{85,f}$ is the diameter of the 85 % mass passing in the fine fraction; WG = widely graded soil.

Table IV.2 – Potential susceptibility classifications based on recent geometric criteria

	W1	W2	G1	G2
Kézdi (Kézdi, 1979)	U	U	U	U
Kenney and Lau (Kenney and Lau, 1985)	U	U	U	U
Li and Fannin (Li and Fannin, 2008)	U	U	U	U
Wan and Fell (Wan and Fell, 2008)	S	S	/	/
Chang and Zhang (Chang and Zhang, 2013b)	U	U	S	S
Indraratna et al. (Indraratna et al., 2015)	U	U	U	U

U = unstable; S = stable; / = method not relevant for considered soil.

4.3 Downward seepage tests

4.3.1 Tested specimens

W1 is a real soil in the natural environment, and its optimum water content is 6.75 % based on the proctor test (NF P94-093 (10/99)) conducted on the part finer than 20 mm. The maximum dry density was 2,100 kg/m³ at the optimum water content.

Considering the use of the multistage hydraulic gradient, the duration of each step had to be determined. To follow the process of suffusion, a suitable water content and dry density also needed to be decided. Initially, a specimen named W-a, with 8 % water content and 2,085 kg/m³ dry density before saturation, was made to verify the experimental conditions.

The variation of sensitivity to suffusion of specimen W-a is shown in Figure IV.3 (Marot et al., 2016). Difficulties were involved in following the process of suffusion because the specimen appeared to be resistant from the beginning of the test. Thus the experimental conditions had

to be modified. To observe the suffusion more clearly and approach the natural water content (4.2%), the water content of specimens was decreased from 8% to 2%. The duration of every step of hydraulic loading was also reduced from 60 to 30 minutes because suffusion mainly existed at the beginning of each step. Bleu Methylene was used to color the part with more fine fraction.

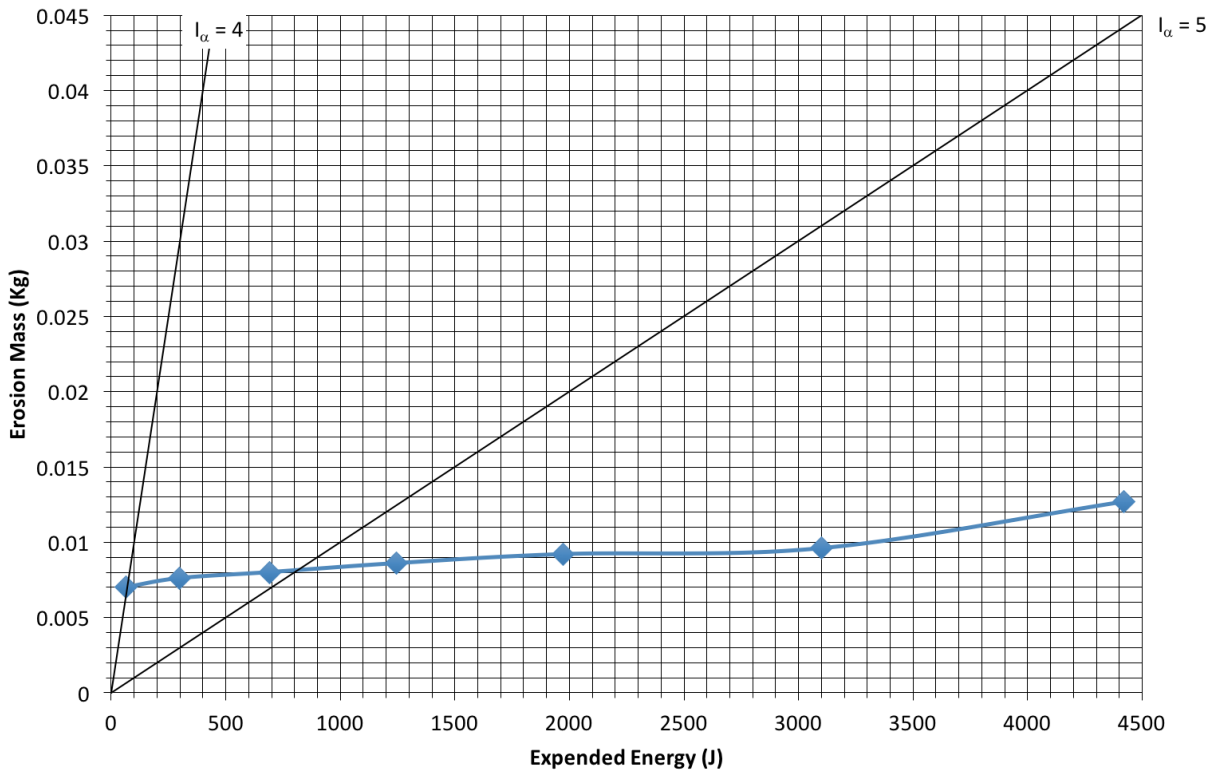


Figure IV.3 – Cumulative eroded dry mass versus cumulative energy of W-a

Table IV.3 summarizes selected specimens with descriptions of their defining characteristics. Based on homogeneity, the 12 specimens used for the study could be divided into two groups. All types of specimens are shown in Figure IV.4(a–e).

With respect to hydraulic history, only two specimens were subjected to a continuously changing hydraulic loading (W-c-I and W-c-II), whereas the others were tested with a growing hydraulic loading step by step.

Table IV.3 – Characteristics of the specimens

Tested gradations	Tested specimens	Water content (%)	Homogeneity	Axial stress (kPa)	$L_{non-saturated}$ (mm)	$L_{saturated}$ (mm)
W1	W-a	8	Figure IV.4(a)	21	415	415
W1	W-b-I	2	Figure IV.4(a)	21	375	370
W1	W-b-II	2	Figure IV.4(a)	21	380	380

W1	W-b-III	2	Figure IV.4(a)	21	355	355
W1	W-c-I	2	Figure IV.4(a)	21	370	370
W1	W-c-II	2	Figure IV.4(a)	21	370	370
W1+W2	W-d	2	Figure IV.4(b)	21	430	378
W1+W2	W-e-I	2	Figure IV.4(c)	21	405	359
W1+W2	W-e-II	2	Figure IV.4(c)	21	440	380
G1	G-a	2	Figure IV.4(d)	21	440	437
G1+G2	G-b-I	2	Figure IV.4(e)	21	440	440
G1+G2	G-b-II	2	Figure IV.4(e)	21	440	425

$L_{non-saturated}$ is the specimen length before saturation, $L_{saturated}$ is the specimen length after saturation.

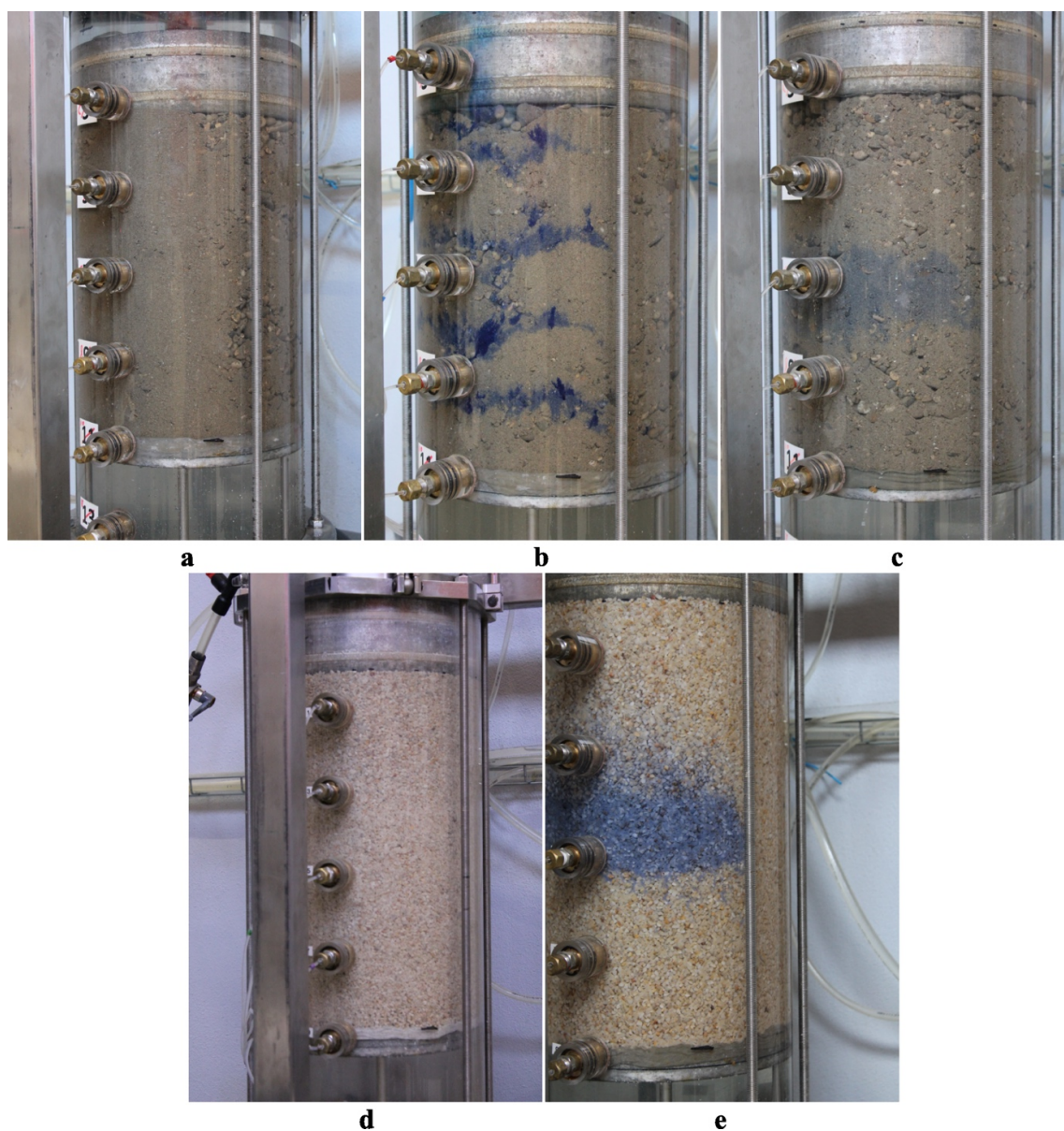


Figure IV.4 – Different types of homogeneity of specimens

Table IV.4 – Characteristics of hydraulic parameters

Tested gradations	Tested specimens	Applied hydraulic gradient	Step duration (min)
W1	W-a		60
W1	W-b-I	0.1 - 0.2 - 0.3 - 0.6 - 1 - 2 - 5	30
W1	W-b-II	0.1 - 0.2 - 0.3 - 0.6 - 1 - 2 - 5	30
W1	W-b-III	0.1 - 0.2 - 0.3 - 0.6 - 1 - 2 - 5	30
W1	W-c-I	0.06 - 0.16 - 0.34 - 0.47 - 0.63 - 0.86 - 1.04 - 1.23 - 1.38 - 1.54 - 1.85 - 2 - 2.18 - 2.32	6
W1	W-c-II	0.02 - 0.08 - 0.27 - 0.41 - 0.57 - 0.79 - 1.01 - 1.12 - 1.30 - 1.44 - 1.93 - 2.01 - 2.45	6
W1+W2	W-d	0.16 - 0.32 - 0.42 - 0.71 - 1.22 - 2.23 - 5.3	30
W1+W2	W-e-I	0.13 - 0.2 - 0.26 - 0.59 - 0.83 - 1.99 - (5 - 8.52 - 9.95) one step	30
W1+W2	W-e-II	0.08 - 0.18 - 0.35 - 0.63 - 0.99 - 2.52 - 5.46	30
G1	G-a	0.05 - 0.07 - 0.1 - 0.13 - 0.15 - 0.17	30
G1+G2	G-b-I	0.03 - 0.0675 - 0.07 - 0.13 - 0.2 - 0.33	30
G1+G2	G-b-II	0.05 - 0.07 - 0.1 - 0.13 - 0.15 - 0.17	30

4.3.2 Experimental procedures

A series of suffusion tests was realized in the following order: specimen production, saturation, downward flow suffusion test, and post-suffusion gradation.

In the specimen production phase, different components of G1 and G2 were mixed with water, based on a certain water content, for three minutes by an electric mixer as presented in Figure IV.5. In the case of W1 and W2, because of the maximum grain size permitted by the mixer, only the particles smaller than 5 mm were mixed with water according to a certain water content in the device. Thereafter, they were mixed manually with particles greater than 5 mm (except the largest grains greater than 20 mm). In addition, the coarsest grains were directly distributed evenly in the cell as the core material. The specimen was installed in three layers, each of which was compacted to reach the target density. Firstly, the specimen was saturated by using CO_2 for half an hour. Secondly, it was saturated by water under vertical upward flow and kept in the water for 24 hours.

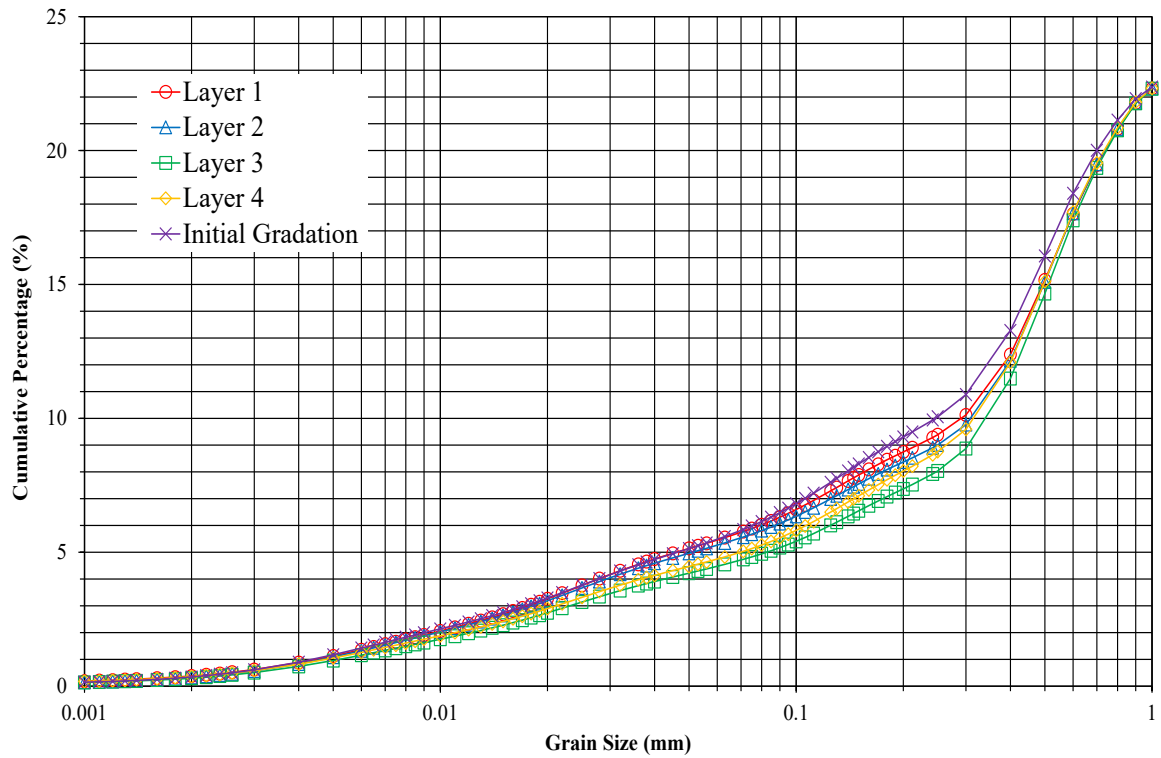
The specimen was subjected to a downward seepage during the suffusion test. A multistage hydraulic gradient was applied to the specimens. We changed the hydraulic gradient in the oedo-permeameter through the pressure controller of the water tanks. A beaker was present to catch the eroded particles for each step, and the dry eroded mass was obtained by placing the beakers containing water and the eroded particles in an oven for 24 hours at a temperature of 105 °C. After the test, the specimen was divided into four layers to measure the post-test grain size distribution. The layer numbered 1 corresponded to the upstream part of the specimen (see Figure IV.1), whereas layer 4 corresponded to the downstream part.



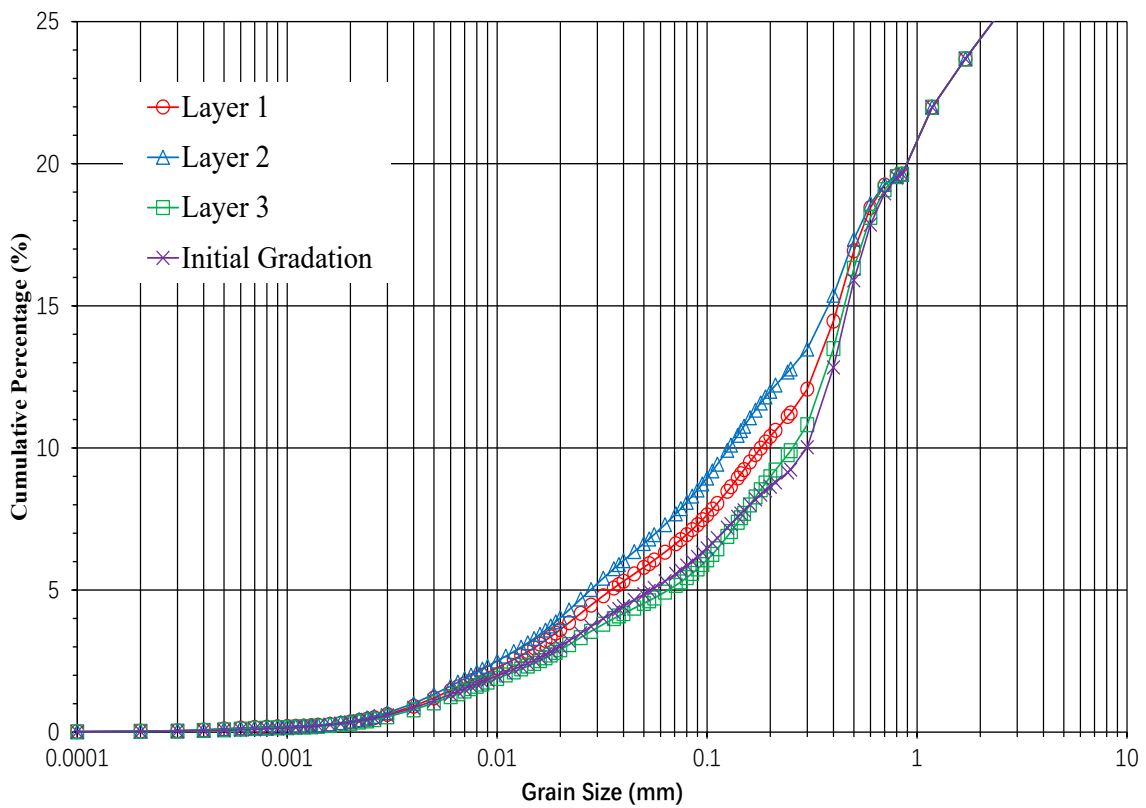
Figure IV.5 – The electric mixer for production of specimens

4.4 Analysis of experimental results

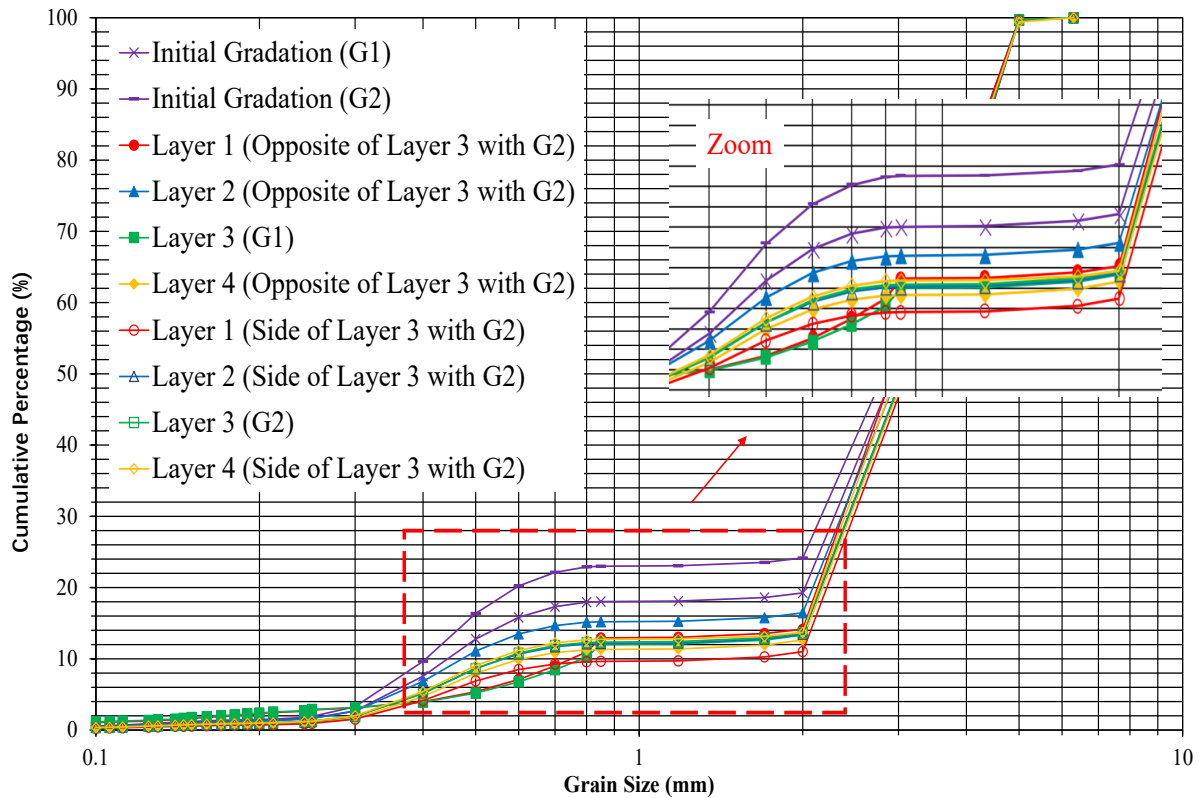
4.4.1 Post-test particle size distributions of specimens



(a)



(b)



(c)

Figure IV.6 – Grain size distribution after suffusion: (a) W-c-I (Zoom fine content), (b) W-c-II (Zoom fine content), (c) G-b-I

Figure IV.6(a–c) show the initial gradation and the gradation of post-suffusion specimens divided into four layers for specimens W-c-I and G-b-I and three layers for specimen W-c-II. For both specimens W-c-II and G-b-I, the reader may note that the loss of fine particles is slightly higher in the upstream part of the specimen in comparison with the middle part. This result agrees with the results of Chapter III. However, for the specimen W-c-I, the conclusion is exactly the opposite. Moreover, the difference of fine content after suffusion between the upstream and middle parts is minute (within 1%) for both specimens W-c-I and W-c-II. Because the step duration of the hydraulic loading was just 6 minutes for these specimens, the process of suffusion may have just been triggered.

The final percentage of fine particles for layer 2 exceeded the initial percentage for specimen W-c-II because the transport of detached particles from the upstream to downstream parts could partly offset the loss of particles in the downstream region. At the same time, as a result of the selection of the post-test grain size distribution measurement position, the layer 1 of the specimen W-c-II also exceeded the initial percentage.

For layers 1 and 2 (upstream part), the loss of fine particles was slightly higher on the side with the gradation G2 in layer 3 in comparison with the side without said gradation, which resulted in

more fine particles being filtered in the part with this gradation. Therefore local inhomogeneity is more likely to cause suffusion for gap-graded soil.

4.4.2 Grain size distribution of eroded particles

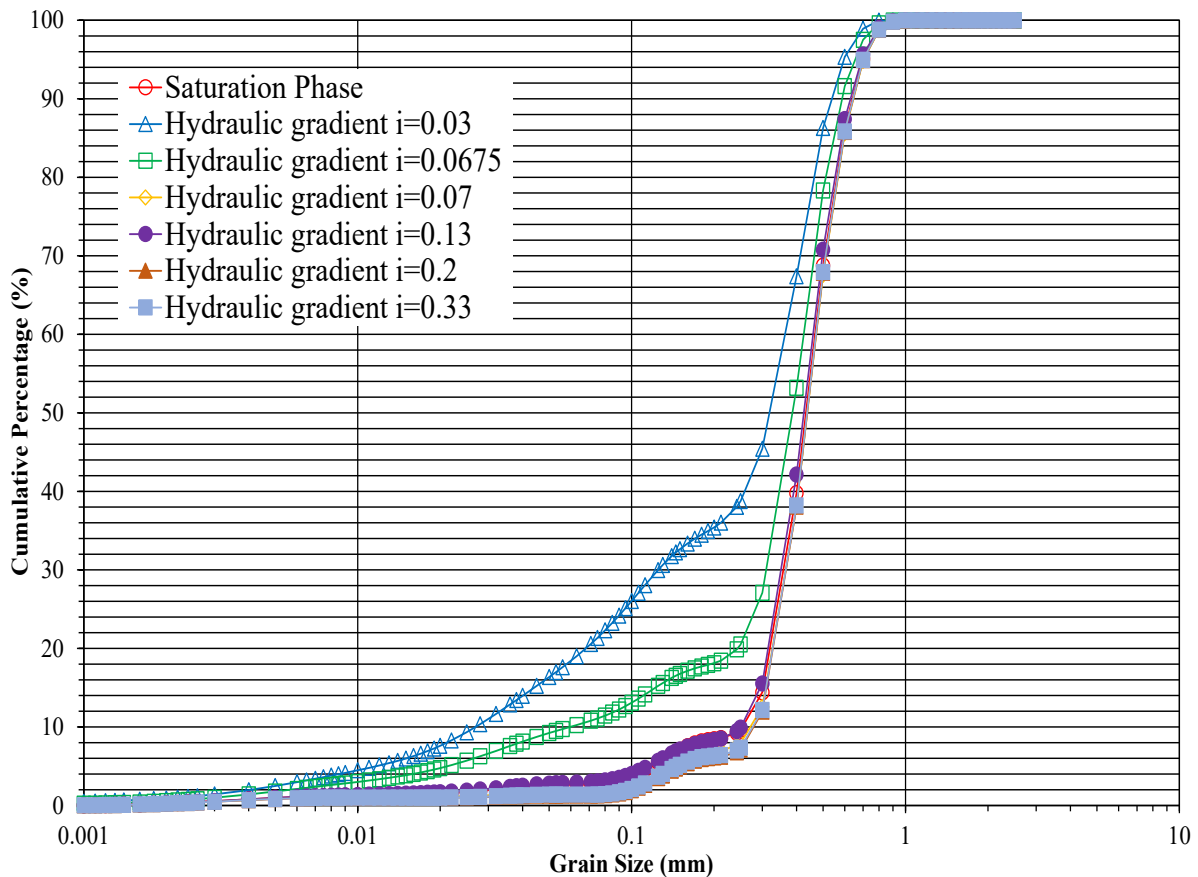


Figure IV.7 – Grain size distribution of detached particles for G-b-I

Considering that just a few data exist in the literature concerning the grain size distribution of eroded particles during the suffusion process, the variation of eroded particles' size was also analyzed. Figure IV.7 displays the grain size distribution of eroded particles in the case of test G-b-I for each stage of the hydraulic gradient (i.e., between two applied hydraulic gradients). From the first stage of the gradient ($i = 0.03$) to the third one ($i = 0.07$), the grain size became greater and greater, because the suffusion process initially concerns only the finest particles of the finer fraction and, progressively, all sizes of said fraction. However, the variation of the last three phases is different from that in the previous hydraulic gradients. From $i = 0.07$ to $i = 0.13$, the grain size of eroded particles became smaller but enlarged again from $i = 0.13$ to 0.33 . Consequently, the cyclical variation of grain size distribution of detached particles reflected the complexity of the suffusion process, which appears as a combination of three processes: (1) particle adjustment stage, (2) stable seepage stage, and (3) seepage change stage.

4.4.3 Influence of fine particles in soil on the permeability

For soil without seepage, erodible or fluidized particles may migrate or enter the pore under the action of gravity. Because of the change of geometric size and stress conditions, the pore is then blocked or occupied. For soils with seepage (hydrostatic or hydrodynamic), static pore water pressure or seepage force is more likely to accelerate such effects. That is to say, erosion of unstable particles inside soil or entry of fluidized particles into the pore may result in the blockage of the said pore by particles moving with seepage, changes in the pore structure, and the weakened permeability of the soil. Another possibility is that the soil pore will become larger, and the permeability will increase as a result of the complete loss.

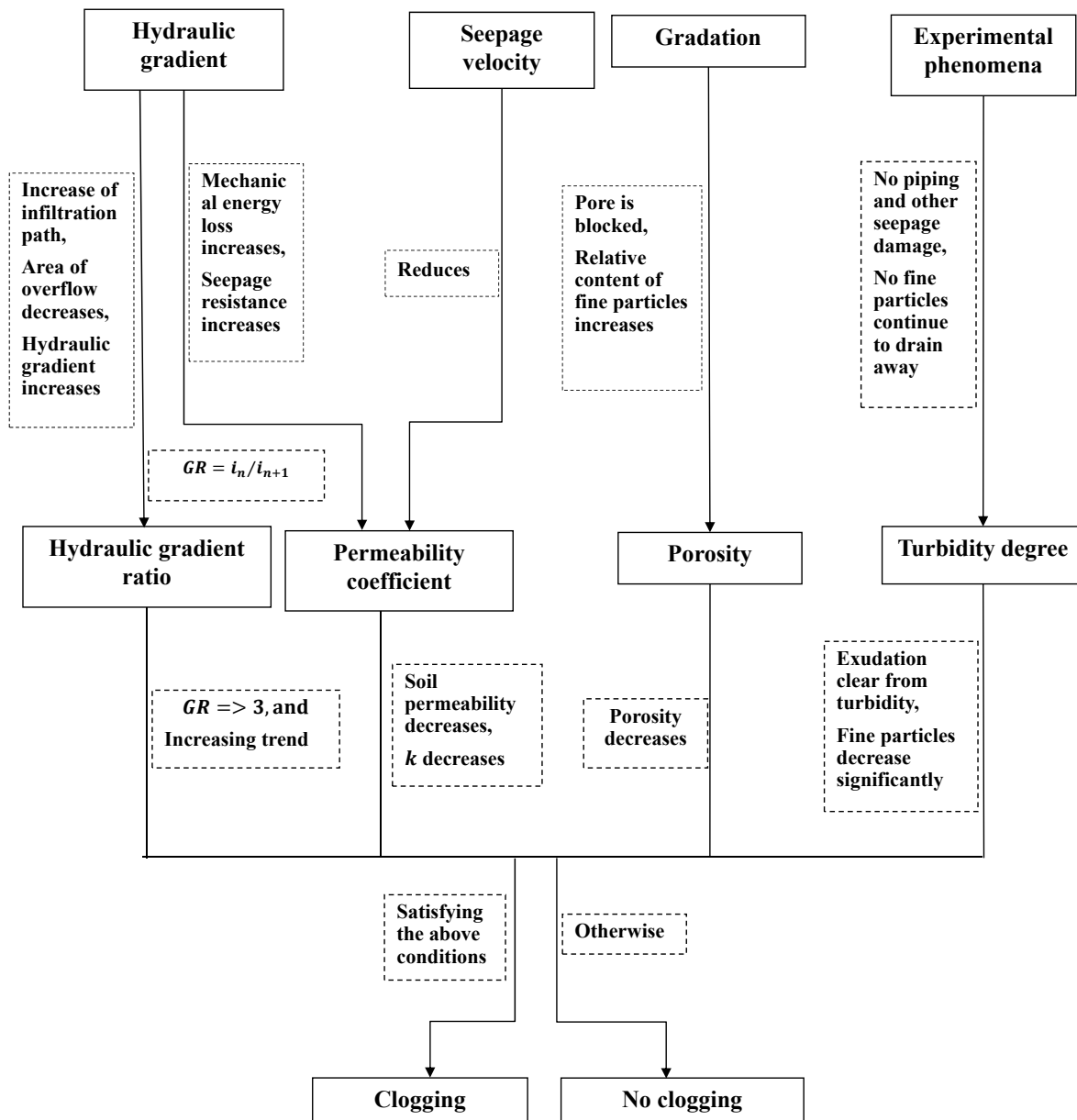


Figure IV.8 – Seepage judgment conditions

The hydraulic gradient, seepage velocity, change of gradation, and experimental phenomena should be considered comprehensively to determine whether the siltation occurs by conducting

seepage tests on soil. Seepage judgment conditions are shown in Figure IV.8.

Next, we will analyze the experimental results of W-b-I to determine whether silting occurred in the experimental process. The experimental results of specimen W-b-I are shown in Figures IV.9 - IV.15.

Global permeability parameters

During the entire test, the flow rate of soil sample fluctuated with time and increased as a whole, as shown in Figure IV.11. The growth rate of each step was more than 50% compared with the initial state. The hydraulic gradient of the whole specimen rose gradually and reached a relatively stable state, as shown in Figure IV.9. The global hydraulic conductivity tended to decrease, meaning that we could provisionally judge that the permeability of the whole specimen would also decrease, as shown in Figure IV.11.

Permeability parameters of each layer

From the hydraulic gradient of each layer of the specimen shown in Figure IV.9, we may deduce that the loss of mechanical energy of the seepage in the initial stage of the experiment was relatively uniform; that is, the soil was in a more ideal uniform state. After 100 minutes, the hydraulic gradient of the third and fourth layers began to increase gradually, especially in the fourth layer. And at last, the hydraulic gradient of the fourth layer increased to more than 15. Late in the experiment, the seepage gradient relationship of each layer was $i_4 > i_3 > i_2 \approx i_1$. The loss of mechanical energy of the seepage caused by the impermeability of the specimen was concentrated in the third and fourth layers. The increasing trend of the local hydraulic gradient in each layer showed that the resistance of the soil to the seepage increased, as did the seepage path.

The hydraulic gradient ratio GR_n is defined as the ratio of the local hydraulic gradients of the layers $n + 1$ and n , expressed as:

$$GR_n = \frac{i_{n+1}}{i_n} \quad \text{IV.1}$$

Figure IV.10 shows that GR_1 fluctuated between 0.9 and 1.5 and that GR_2 fluctuated slightly between 0.7 and 1 during the entire experimental period, and neither had a significant upward nor downward trend. The fluctuation of GR_3 between 3 and 6 also did not show a significant upward or downward trend, but at the end of the experiment, the sharp decrease was close to zero. Figure IV.12 shows that the hydraulic conductivity of each layer decreased gradually and

tended to stop decreasing at the end.

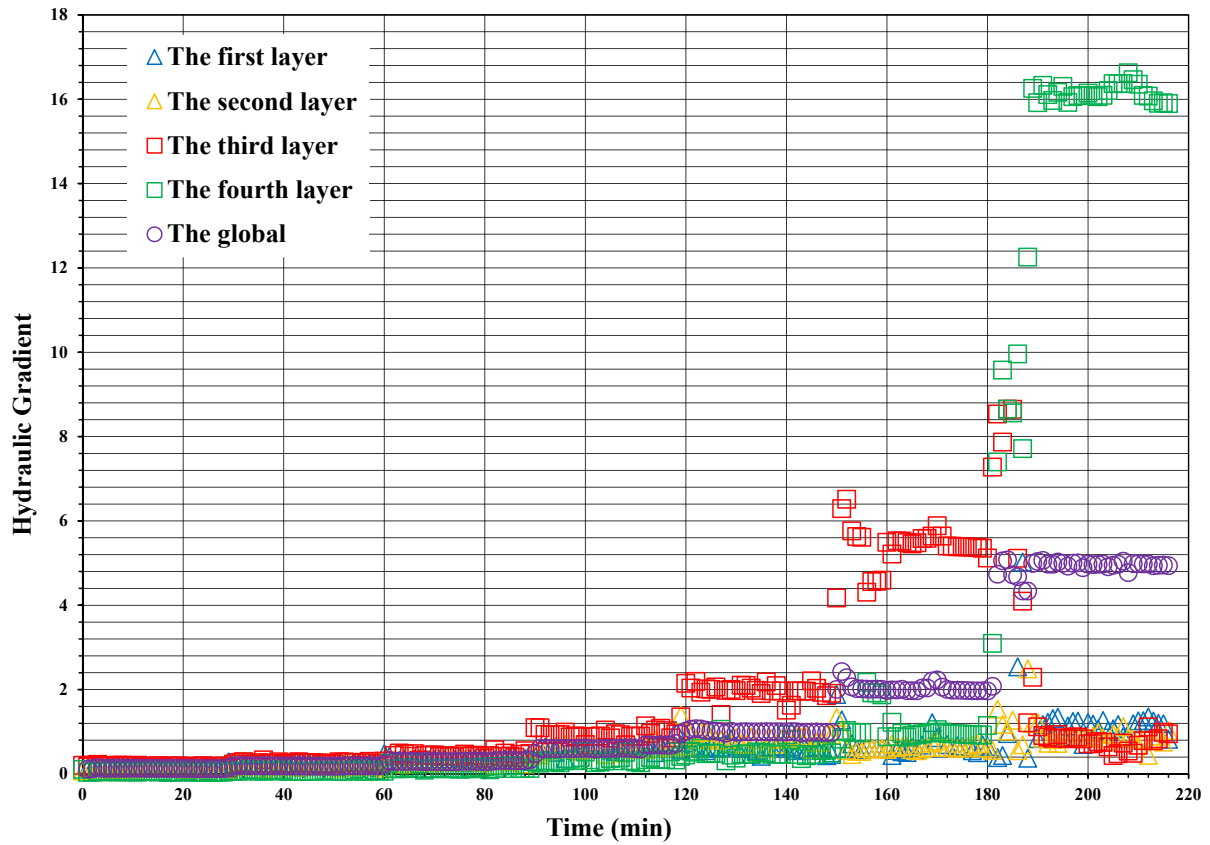


Figure IV.9 – The relationship between the hydraulic gradient and time for W-b-I

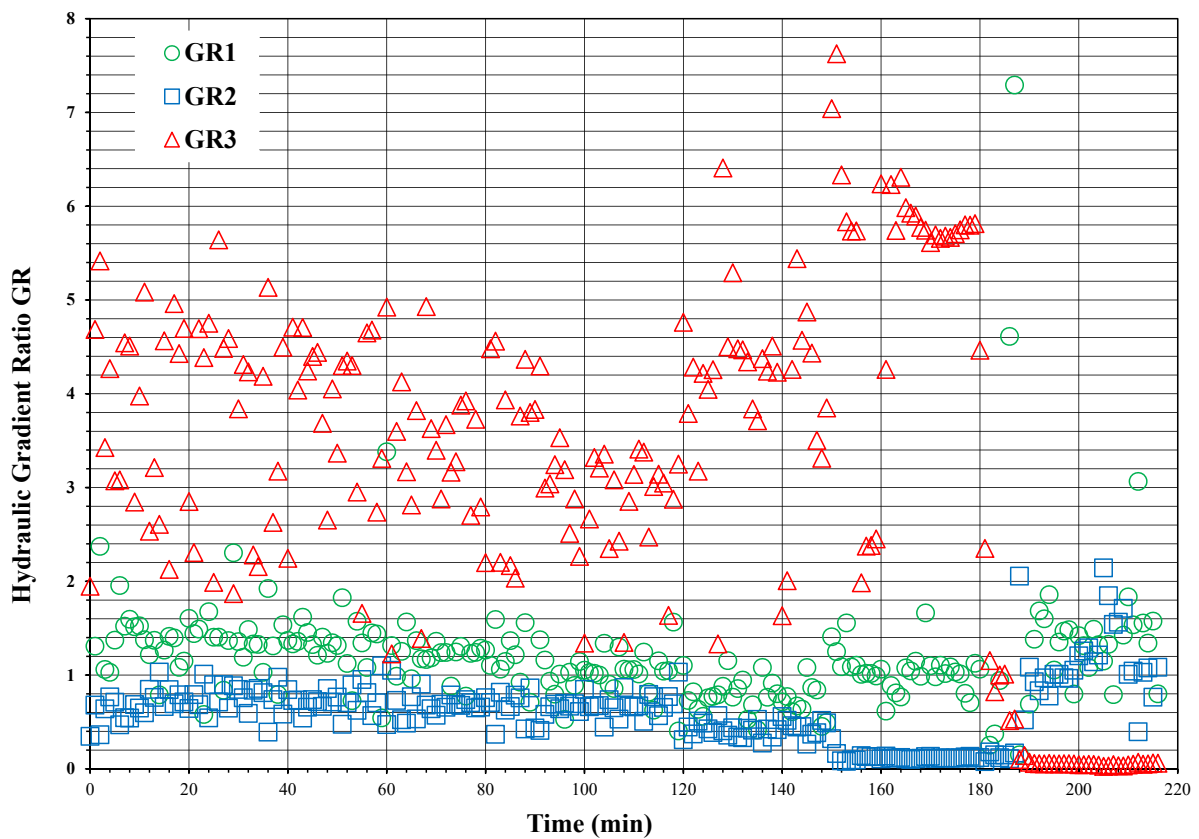


Figure IV.10 – The relationship between the hydraulic gradient ratio and time for W-b-I

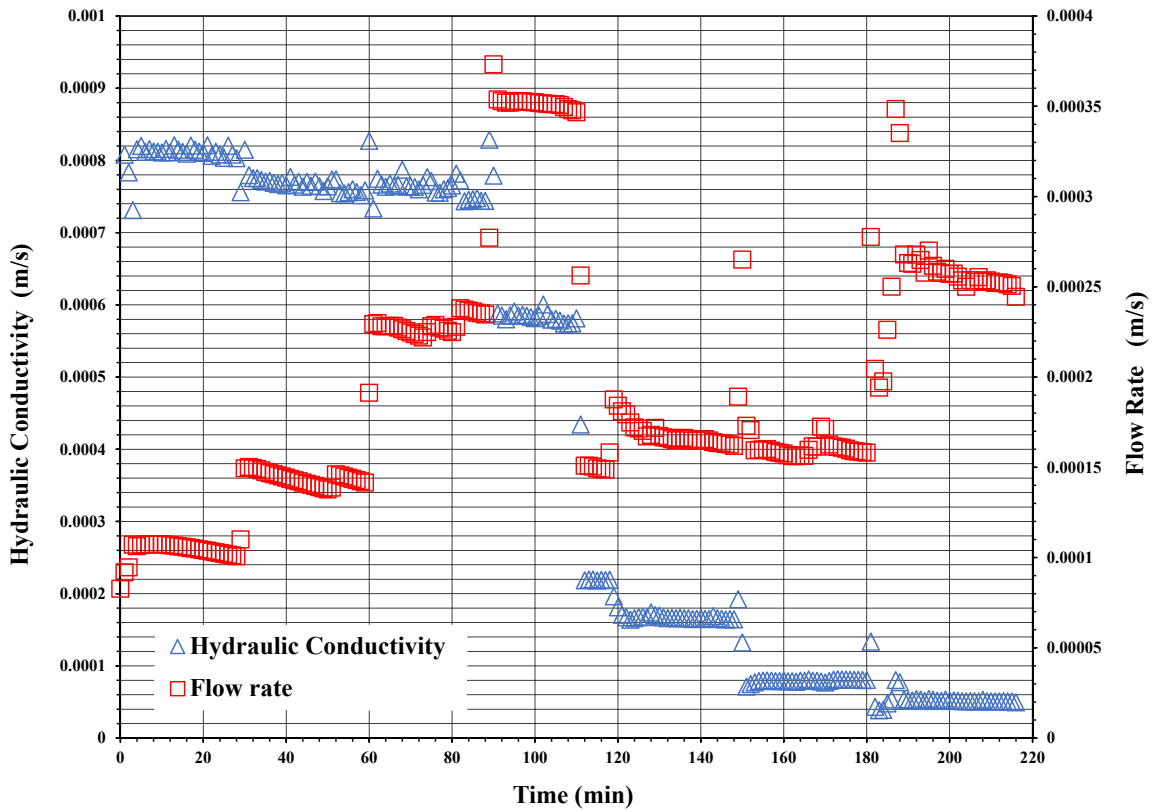


Figure IV.11 – The variation of the global hydraulic conductivity and flow rate with the increasing time for W-b-I

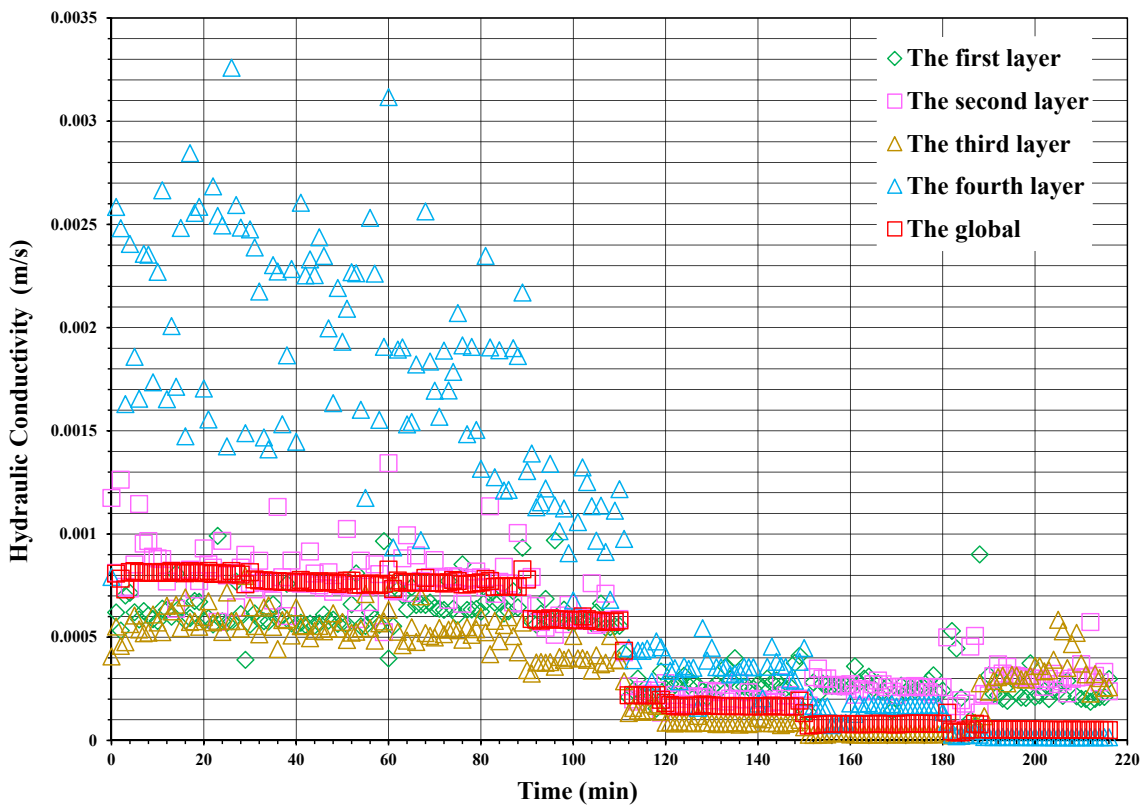


Figure IV.12 – The relationship between the hydraulic conductivity of each layer and time for W-b-I

Through the analysis of the variation trend of permeability parameters, we found that the per-

meability of each layer decreased during the entire experimental period and tended to be stable at the end. Therefore, the soil met the silting conditions, and the silting in each layer could be preliminarily determined.

Gradation analysis

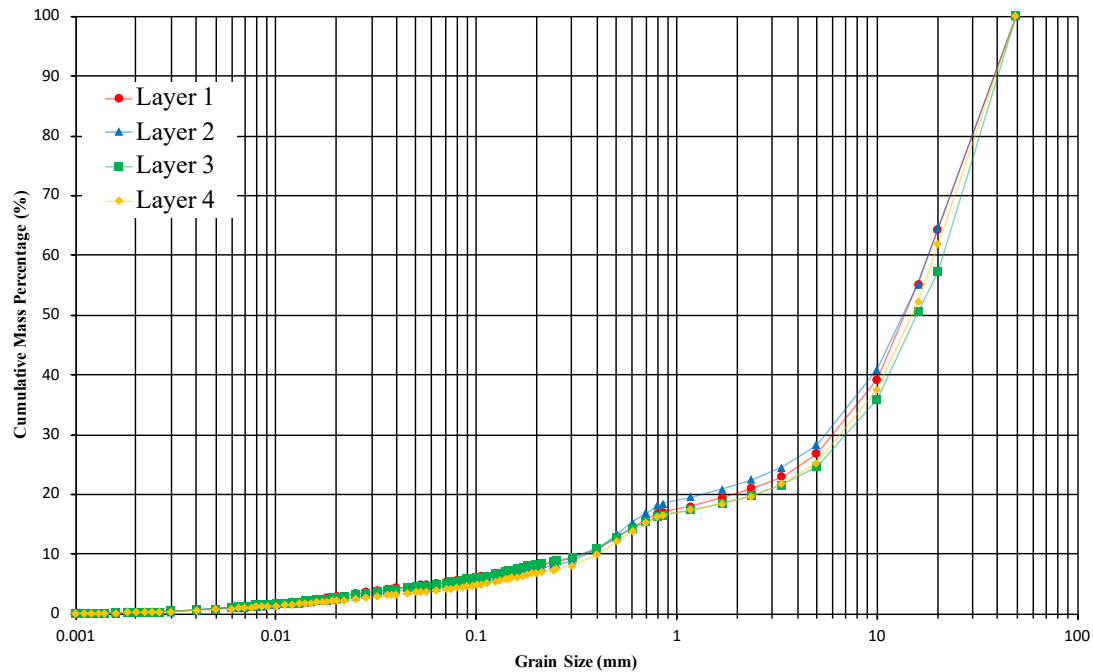


Figure IV.13 – Grain size distribution after test for W-b-I

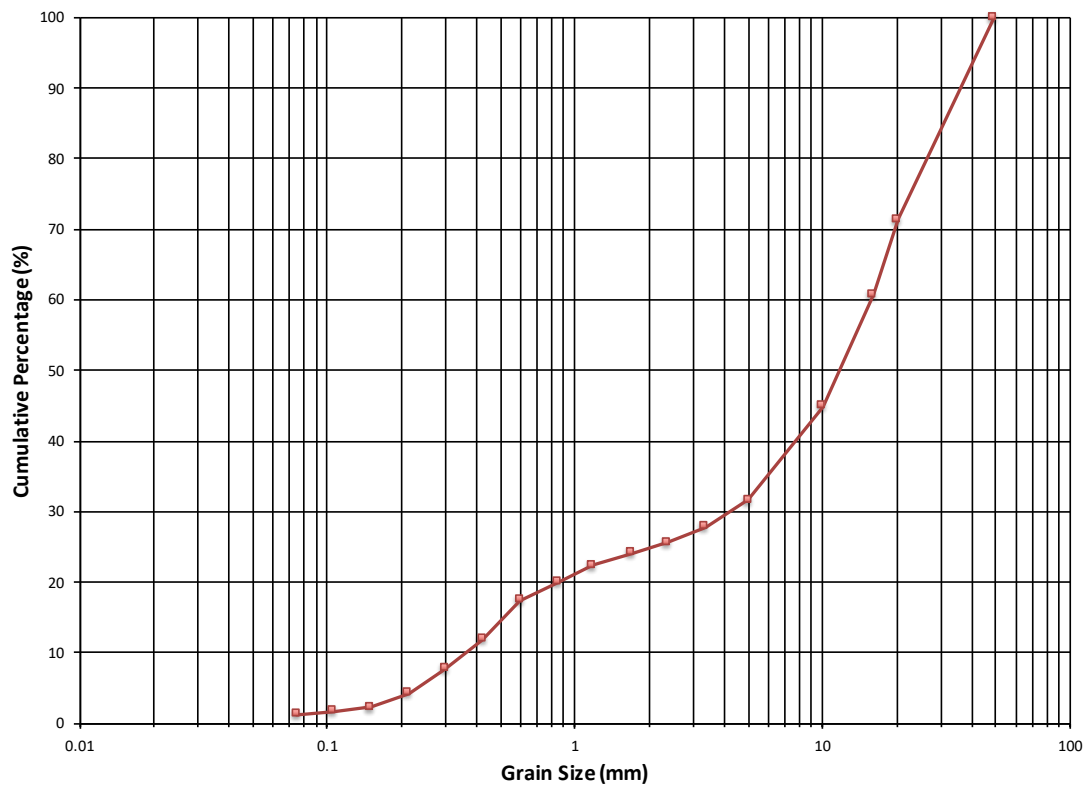


Figure IV.14 – Grain size distribution before test for W-b-I

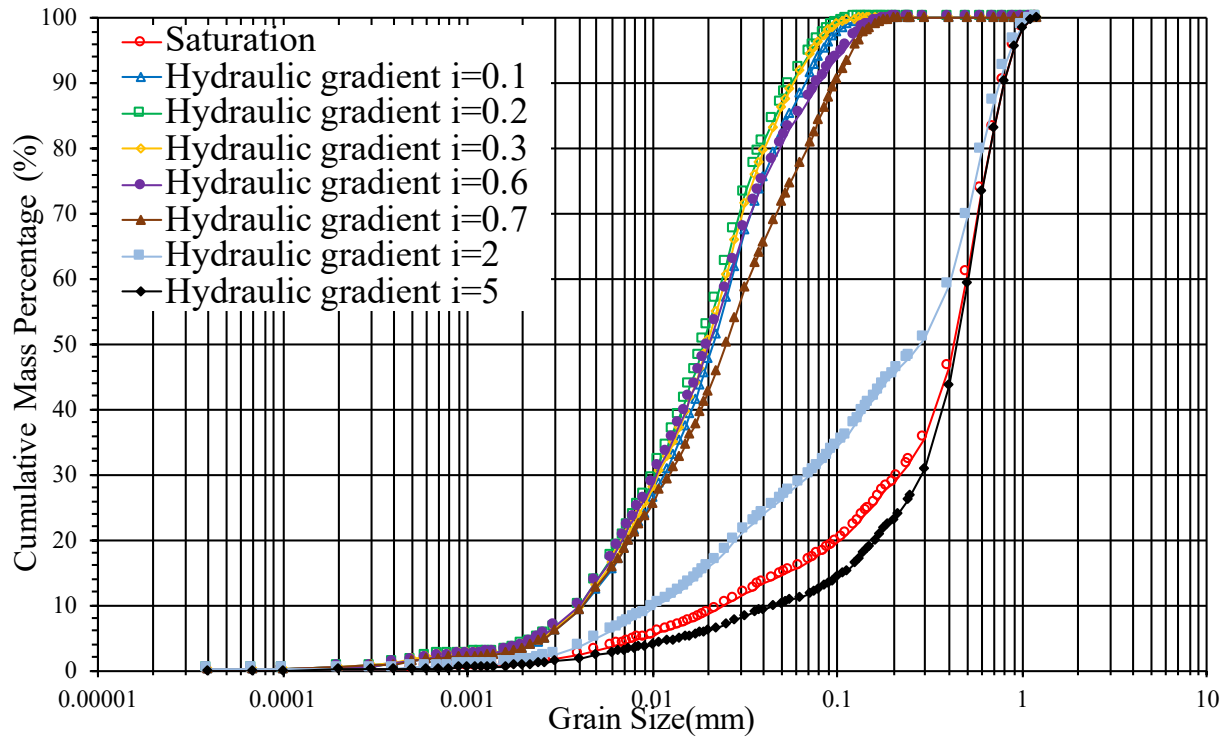


Figure IV.15 – Grain size distribution of eroded particles for *W-b-I*

At the end of the experiment, the grain size distribution of each layer of the soil specimen was analyzed as follows (see Figure IV.13). Considering the similar grain size distribution of each layer, a large hydraulic conductivity variation can be caused by a small variation of gradation. Compared with the original gradation, the fine material content of each layer changed in different degrees.

By comparing and analyzing the fine particle content of each layer after testing with that before (Figure IV.13 and Figure IV.14), the reader may observe that the fine particle content of each layer decreased slightly and unevenly, which was concentrated on the particle sizes of 0-0.075 mm, 0.075-0.25 mm, and 0.25-0.5 mm, followed by 0.5-2 mm, almost unchanged. And the fourth layer decreased most, indicating that it was seriously eroded. The influence of the seepage on fine particles was mainly concentrated in the ranges of 0-0.075 mm and 0.075-0.25 mm, followed by the range of 0.25-0.5 mm, which was the main object of scouring or silting up, and the influence of particles in the range of 0.5-2 mm was very small. The screening of eroded particles after the test is shown in Figure IV.15. Movable particles were concentrated in 0-0.5 mm.

In summary, the data analysis shows different degrees of the particle loss in each layer. Based on the variation of the loss and particle size, the second and third layers appear to have been mainly subjected to slight erosion. The particle size of erodible particles was mainly between 0 and 0.5 mm. The particle size of eroded particles in the fourth layer was mainly between 0

and 1 mm. The increased content of the corresponding particle size interval in the second layer indicates that the eroded fine particles are moved by the seepage from the first layer into the second layer and cause siltation in the second layer.

At the same time, the indication is that the key particle size in the particle composition, which determines the hydraulic conductivity is the fine grain. The particle size of the grain plays a decisive role in the pore size of soil. The addition of appropriate coarse particles in fine materials only increases the density of the soil and reduces the porosity. Fine particles still play a major role in the permeability coefficient and a small variation of gradation has a great influence on the variation of the hydraulic conductivity. From the grain size distribution of the eroded particles, it is clear that the suffusion process concerns progressively coarser and coarser particles.

Hydraulic gradient and seepage stability

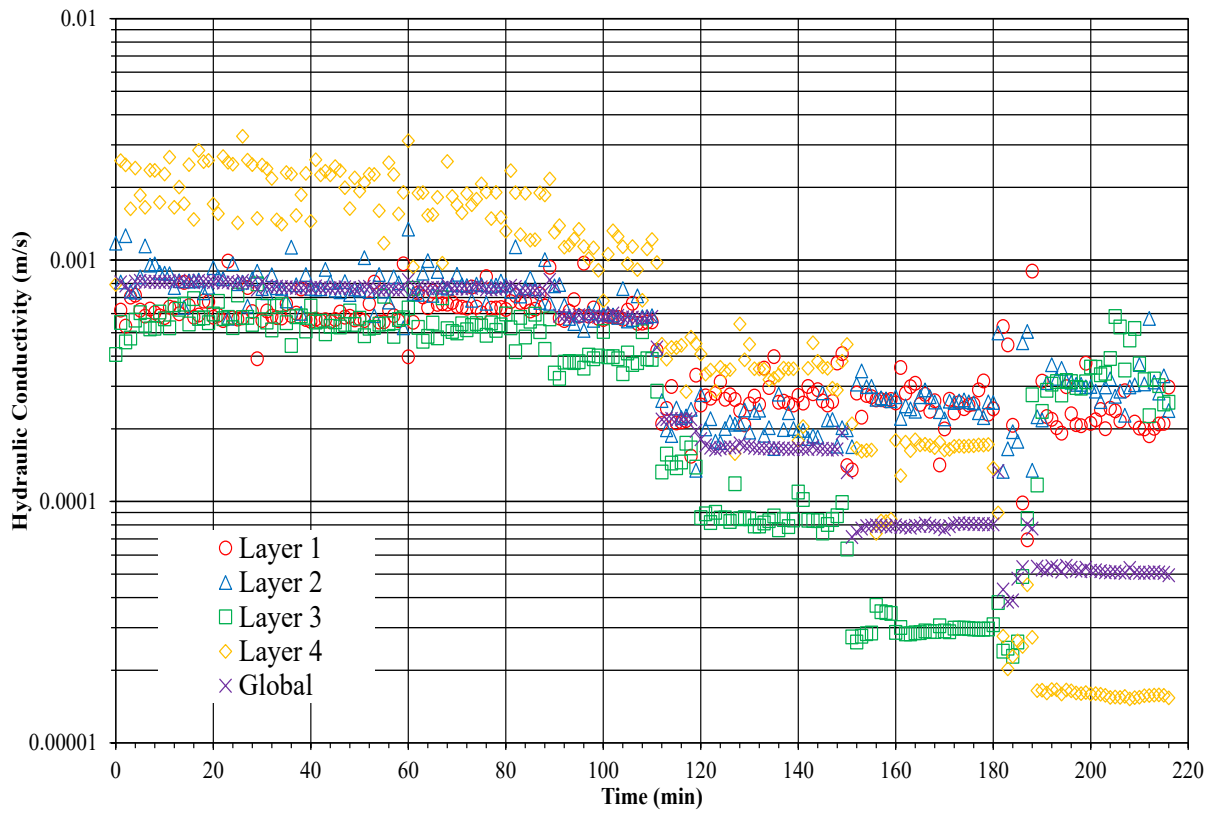
Figure IV.9 shows that the local hydraulic gradient of each layer and the global hydraulic gradient were between i_{allow} and i_{damage} , which indicates that the hydraulic gradient of each layer did not reach the critical value of failure, but different degrees of the erosion may have been in evidence, and the fine particles involved in the seepage flow had sufficient power to enter the soil pore.

With the increase of the hydraulic load, the hydraulic gradient of the fourth layer increased sharply, and that of the third layer increased to a certain extent. The permeation damage should have occurred in the third and fourth layers.

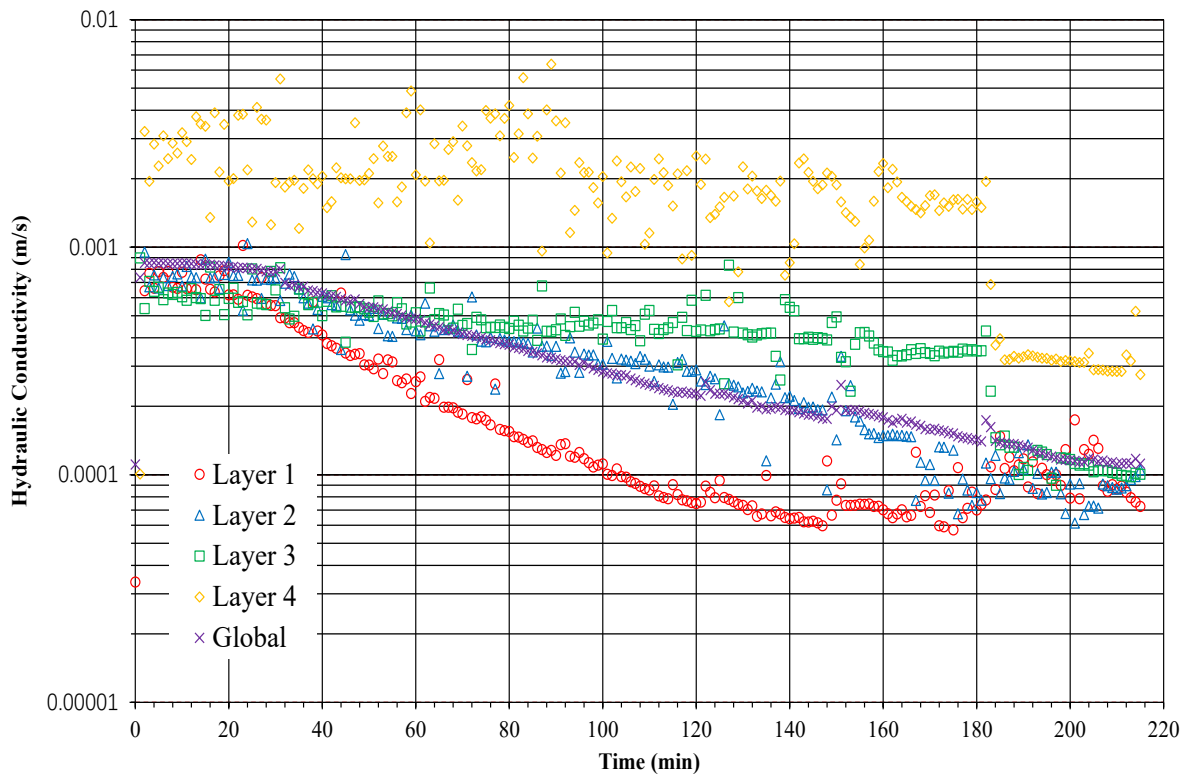
Judgment of siltation

Through the comprehensive analysis of Figures IV.9 - IV.12, we can see that the decrease of the hydraulic conductivity indicates that the permeability decreased due to a small variation of gradation, compared with the initial hydraulic conductivity and soil gradation. The hydraulic gradient tended to increase slightly in the first and second layers, and the hydraulic conductivity decreased during the test. The fine particle content of the second layer was greatest of all layers, and the reverse trend was seen in the third layer. Moreover, $GR3$ was larger than the critical value 3 ($GR2$ had no obvious change), which indicates that the soil had a certain effect of the stability and silting, which was concentrated in the third and fourth layers. In the second layer, both the erosion and silting occurred, while the first layer was eroded; in other words, the third layer controlled the permeability of the system.

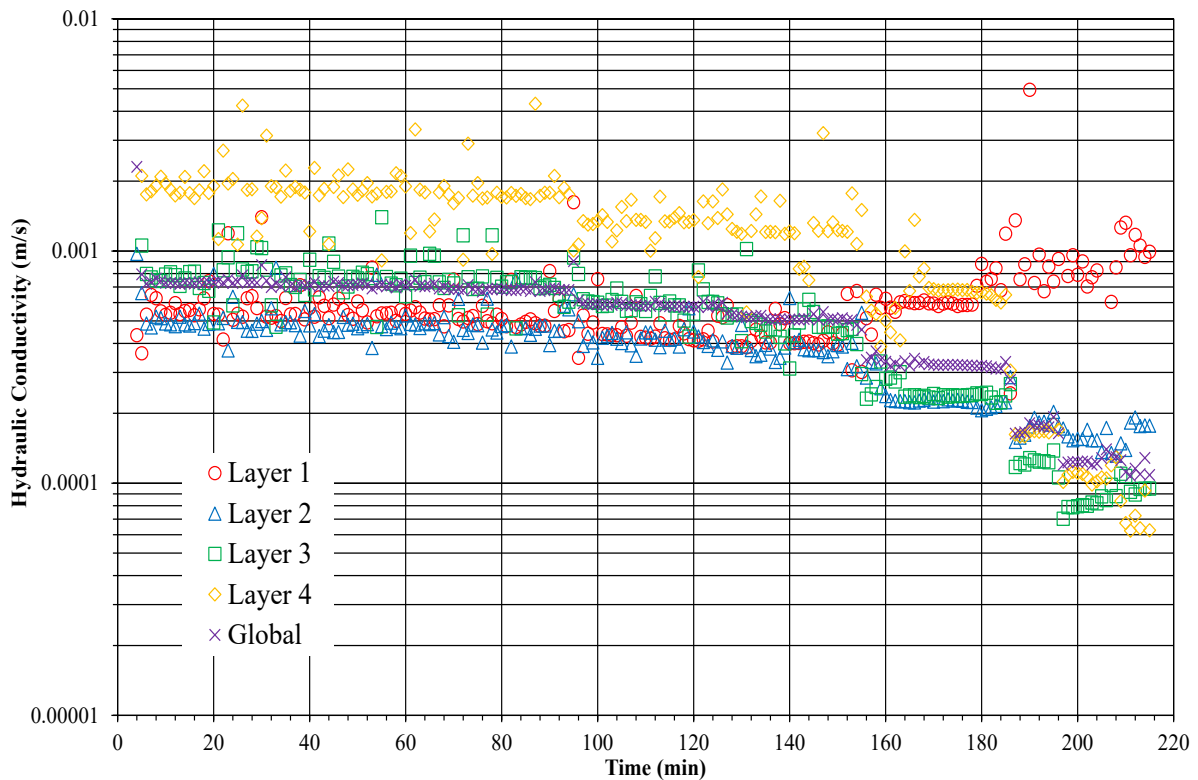
4.4.4 Hydraulic conductivity



(a)



(b)



(c)

Figure IV.16 – Time evolutions of hydraulic conductivity: (a) *W-b-I*, (b) *W-d*, (c) *W-e-I*

Thanks to the measurements of the local hydraulic gradient, and based on the assumption that the flow rate was the same in the entire specimen cross section, the local hydraulic conductivity was computed. Figure IV.16(a–c) displays the variation of the global and local hydraulic conductivity with the test’s development. Considering the hydraulic conductivity for layers 1 to 3, we may observe that the initial hydraulic conductivity was basically the same for *W-b-I*, *W-d*, and *W-e-I*. For layer 4, the hydraulic conductivity was slightly higher as long as the applied hydraulic gradient was lower than 2.

However, for test *W-b-I*, when the applied hydraulic gradient was increased from 2 to 5, the local hydraulic conductivity within layer 3 rose sharply and, within layer 4, dropped more rapidly than before. For specimen *W-e-I*, under the same hydraulic loading (from 185 to 195 min), the local hydraulic conductivity within layer 4 also dropped more quickly than before, but no increase was seen within the other layers. Although the global hydraulic conductivity continued to decline for both *W-b-I* and *W-e-I*, the appearance of the local hydraulic conductivity increase meant further progress and a further degree of suffusion. Hence a little more fine particles help maintain the internal stability of well-graded soil.

However, the evaluation of *W-d* was very different from that of *W-b-I* and *W-e-I*. For the specimen *W-d*, when the applied hydraulic gradient was greater than 0.16, local hydraulic conduct-

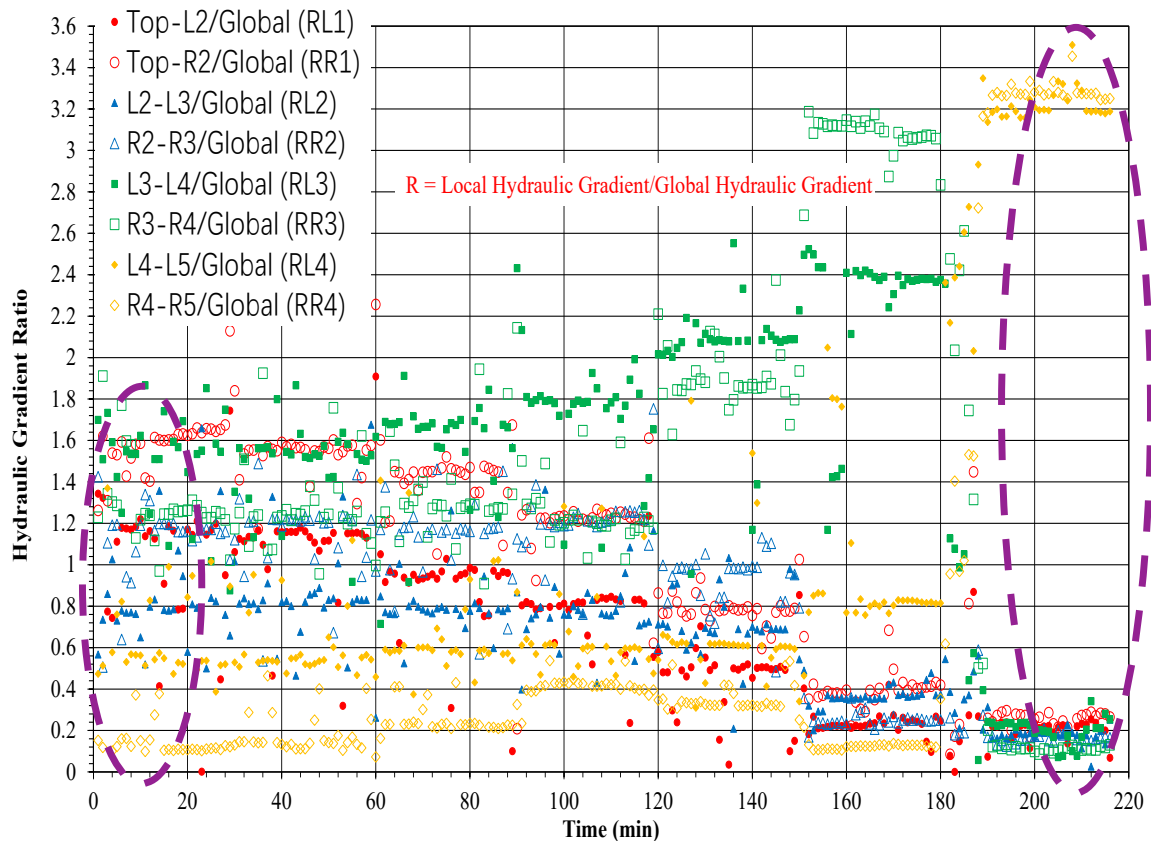
ivity within layers 1 and 2 began to decrease. Meanwhile, the hydraulic conductivity of W-b-I and W-e-I remained constant until the applied hydraulic gradient at $i = 1$ and 0.59, respectively. The process of filtration prevents the soil particles from internal erosion, which means that a smaller critical hydraulic gradient to trigger the filtration process may lead to a higher internal stability.

In one word, the hydraulic conductivity of each layer varies differently. At the end, the hydraulic conductivity in upstream begins to increase when the hydraulic conductivity of layer 4 (in downstream) keeps decreasing, which leads to the decrease of the global hydraulic conductivity.

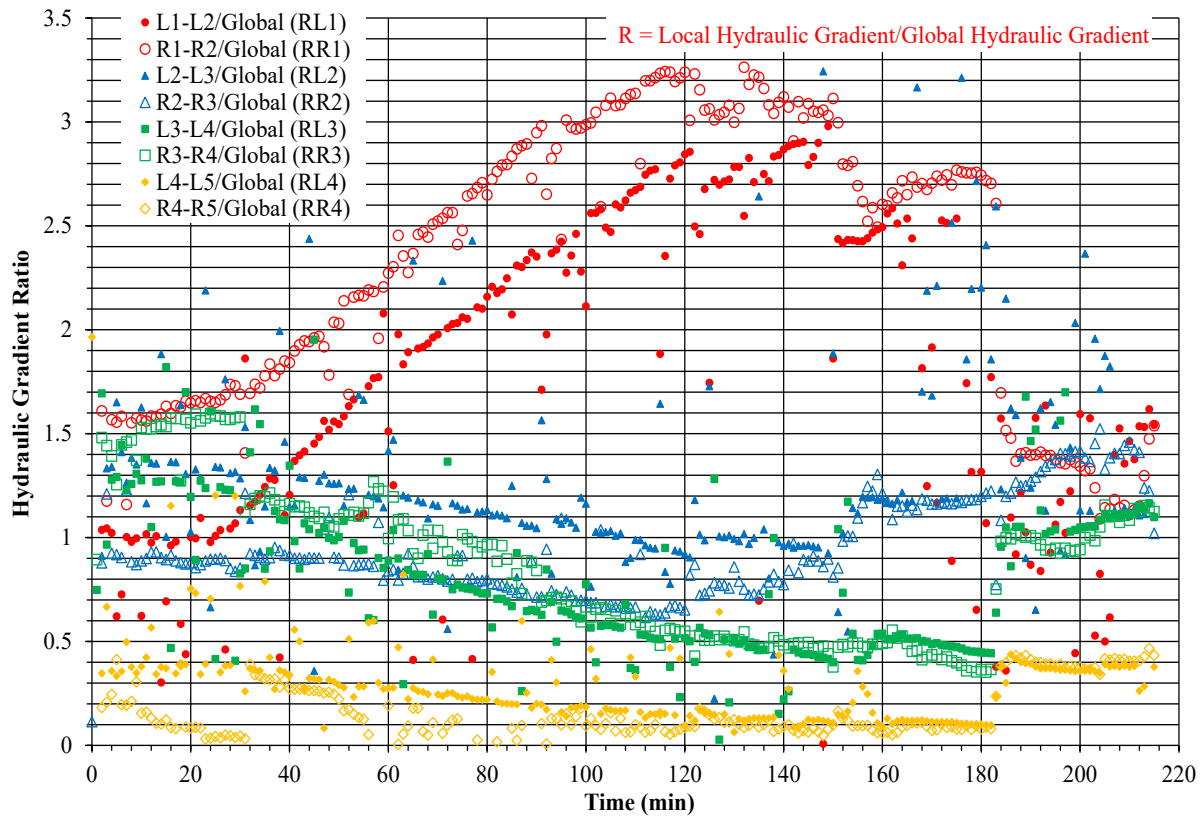
4.5 Discussion

4.5.1 Hydraulic gradient ratio

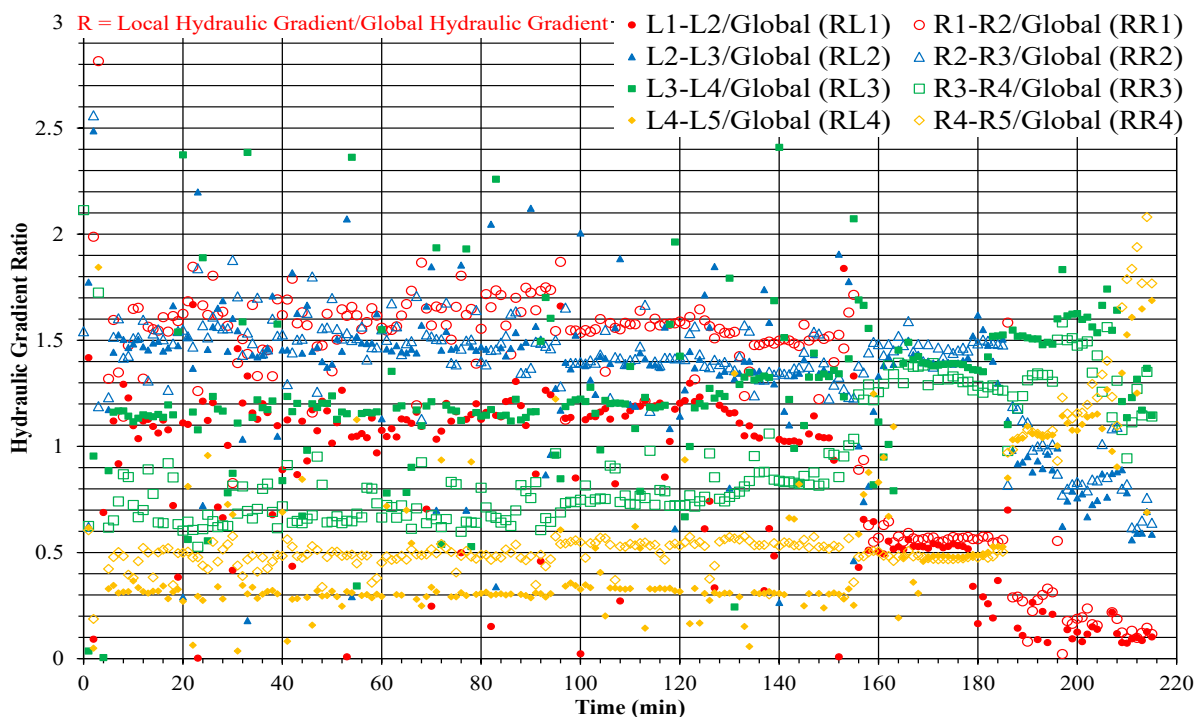
With the aim of studying the influence of the local hydraulic gradient, here hydraulic gradient ratio R was used ($R = \text{local hydraulic gradient} / \text{global hydraulic gradient}$). Figure IV.17(a–c) displays the time evolutions of the hydraulic gradient ratio for specimens W-b-I, W-d, and W-e-I. From Figure IV.17(a–c), we can observe that the suffusion was not a homogeneous process even for a homogeneous specimen.



(a)



(b)



(c)

Figure IV.17 – Time evolutions of hydraulic gradient ratio: (a) *W-b-I*, (b) *W-d*, (c) *W-e-I*

At the beginning, local hydraulic gradients on both sides were not the same; however, with the development of suffusion, the local gradients on both sides gradually become equal, as high-

lighted in Figure IV.17(a).

Soil seems to show a greater internal stability if the local hydraulic gradients are more closed to the global hydraulic gradient. In other words, the development of suffusion induces local heterogeneities, which in turn produce variations of local hydraulic gradient.

At the beginning of the test, the position of the maximal local hydraulic gradient is the upstream part of the specimen, however, at the end of the test, the position of the maximal local hydraulic gradient changes to the downstream part of the specimen.

4.5.2 Position of the maximum local hydraulic gradient

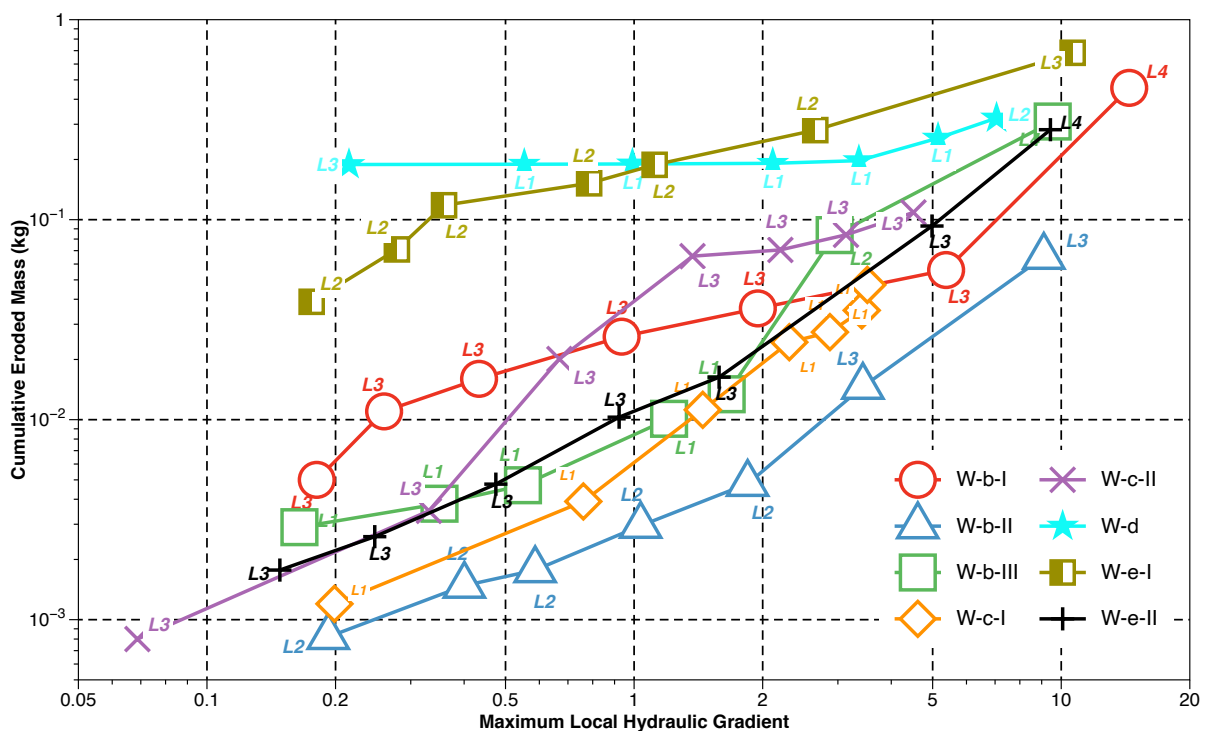


Figure IV.18 – Cumulative eroded mass versus the position of maximum local hydraulic gradient for each step

Figure IV.18 presents the relationship between the cumulative eroded mass and the position of the maximum local hydraulic gradient for the well-graded specimens. Taking the specimen W-b-III as an example, the maximum local hydraulic gradient appeared small and concerned the upstream part at the beginning of the test. Progressively, the maximum local hydraulic gradient increased and gradually concerned the downstream part of the specimen, from layer 1 to layer 2, finally to layer 4. And the overpressure in the downstream part induced a lot of eroded particles. From this figure, the suffusion appeared to be a gradual process from the upstream to the downstream part. This result agrees with those of Sail et al. (Sail et al., 2011), who measured an increase of interstitial pressure that preceded the onset of localized blowout. When the filtration

is the principal process in a given layer, in this layer the local hydraulic gradient is maximum. However, if this maximum hydraulic gradient appears at the bottom of the specimen, it leads to a large amount of eroded particles.

4.6 Qualitative analysis of seepage test

4.6.1 The three stages of the seepage process

Here, the variation laws of flow rate, hydraulic gradient, and hydraulic conductivity are summarized, and the microscopic characteristics of samples before and after testing are analyzed. The seepage process can be summarized as the following three stages:

1. Particle adjustment stage: at the beginning of the test, the particle structure of the soil was shown in Figure IV.19(a) and was then affected by the permeability force. Subsequently, under the action of osmotic force, fine particles in the skeleton particles moved into the seepage; that is, fine particles in the upper soil layer were carried by the seepage flow, and harmless piping occurred. Under the influence of the seepage boundary, fine particles gradually accumulated in the lower soil layer. At this time, the structure of the soil was slightly adjusted, and the whole soil body exhibited the phenomenon of “osmotic compaction” from top to bottom, as shown in Figure IV.19(b).

At this time, the hydraulic gradient of the entire soil body changed from the fluctuation to the basic stability, while the hydraulic conductivity decreased with time until it was relatively stable, as shown in Figures IV.20 - IV.31.

2. Stable seepage stage: after the “particle adjustment” stage, under the continuous action of seepage flow and after a period of time, the flow and soil entered a relative balance of mechanical properties, and the variations of the flow velocity and hydraulic conductivity reached a relatively stable state, as shown in Figures IV.20 - IV.31.
3. In the “seepage change” stage, the third stage, two phenomena occurred:

The phenomenon of “base erosion” This phenomenon basically ran through the whole seepage process, but it was more obvious at this stage. The main part of the phenomenon was located in the third and fourth layers of the tested soil. At the end of the test, the hydraulic gradient of the lower layer of the soil had changed little or even decreased in parts. The internal soil particles are gradually lost and hollowed out during the test, and the soil was damaged by seepage. As shown in Figures IV.21, IV.23, IV.25, IV.27, IV.29,

and IV.31, from the beginning to the end of the test, the hydraulic gradient of the third layer of samples W-b-I and W-b-III changed little, a downward trend in the curve of the hydraulic gradient of the third layer was evident, and the phenomenon of “base erosion” manifested.

Seepage and silting phenomenon This phenomenon mainly occurred in the middle and the upper part of the tested soil. The macroscopic characteristics are that the hydraulic gradient increases and that the velocity of the entire soil decreases, while the meso-characteristic is that the particle size of a certain section increases. At this time, the silted particles accumulated on the surface of the skeleton particles or plugged in the internal pores of said particles, and the flow velocity and hydraulic conductivity decreased, as shown in Figures IV.20, IV.22, IV.24, IV.26, IV.28, and IV.30. The particle structure characteristics are shown in Figure IV.19(c).

Through the analysis of the three stages of the seepage and filtration process, the seepage deformation shows four distinct characteristics: the first is the compression of the soil under the action of seepage force; the second is the seepage compaction; the third is the loss of fine particles, mainly by harmless piping and latent erosion; and the last is the filtration, which is mainly composed of silting and clogging. During the whole experiment, we found that the occurrences of these three stages did not develop in a single order. Under certain conditions, a phenomenon of interpenetration occurred among them.

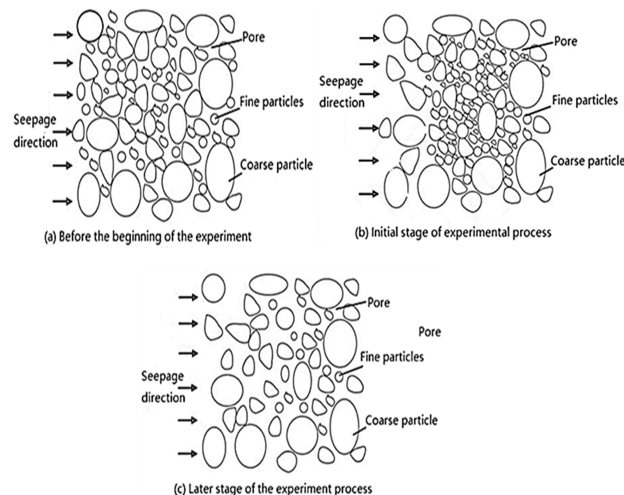


Figure IV.19 – Schematic diagram for seepage extrusion

Note:

I–“particle adjustment” stage;

II–“stable seepage” stage;

III–“seepage change” stage.

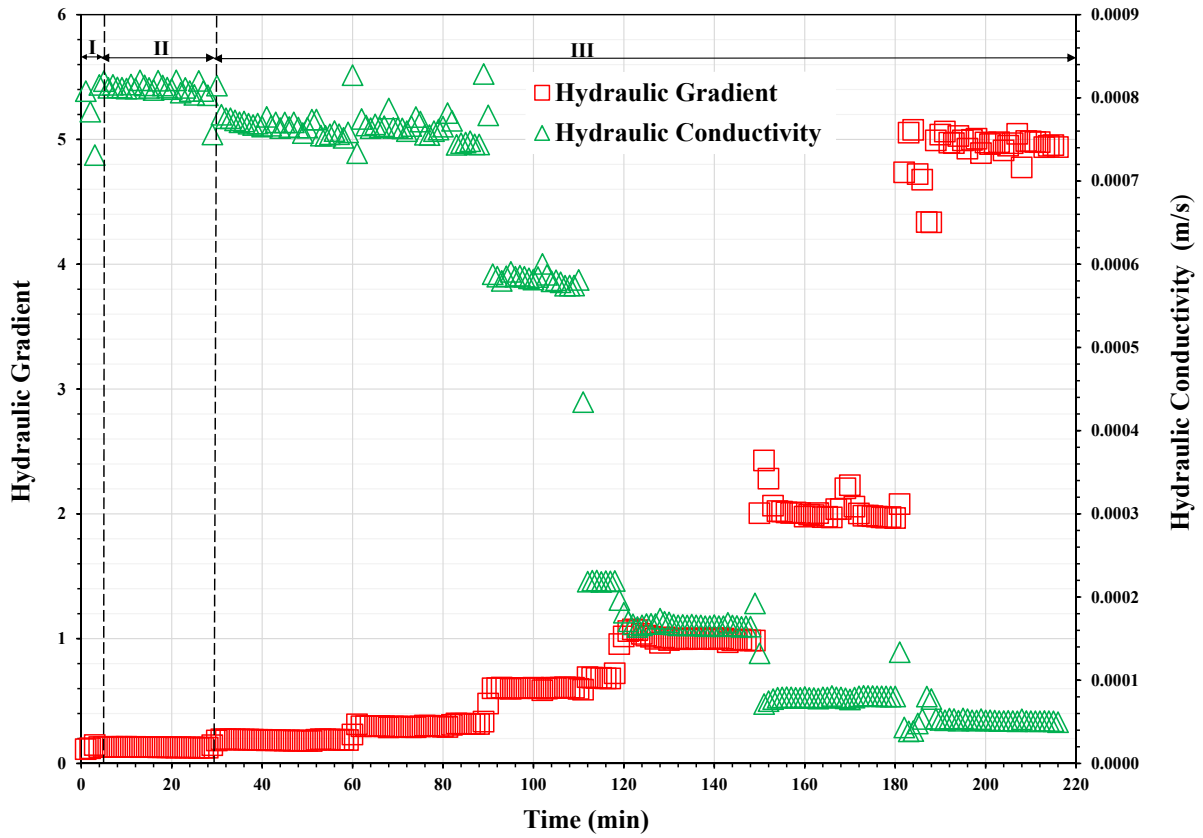


Figure IV.20 – Hydraulic conductivity and hydraulic gradient versus time curve of the whole soil layer (W-b-I)

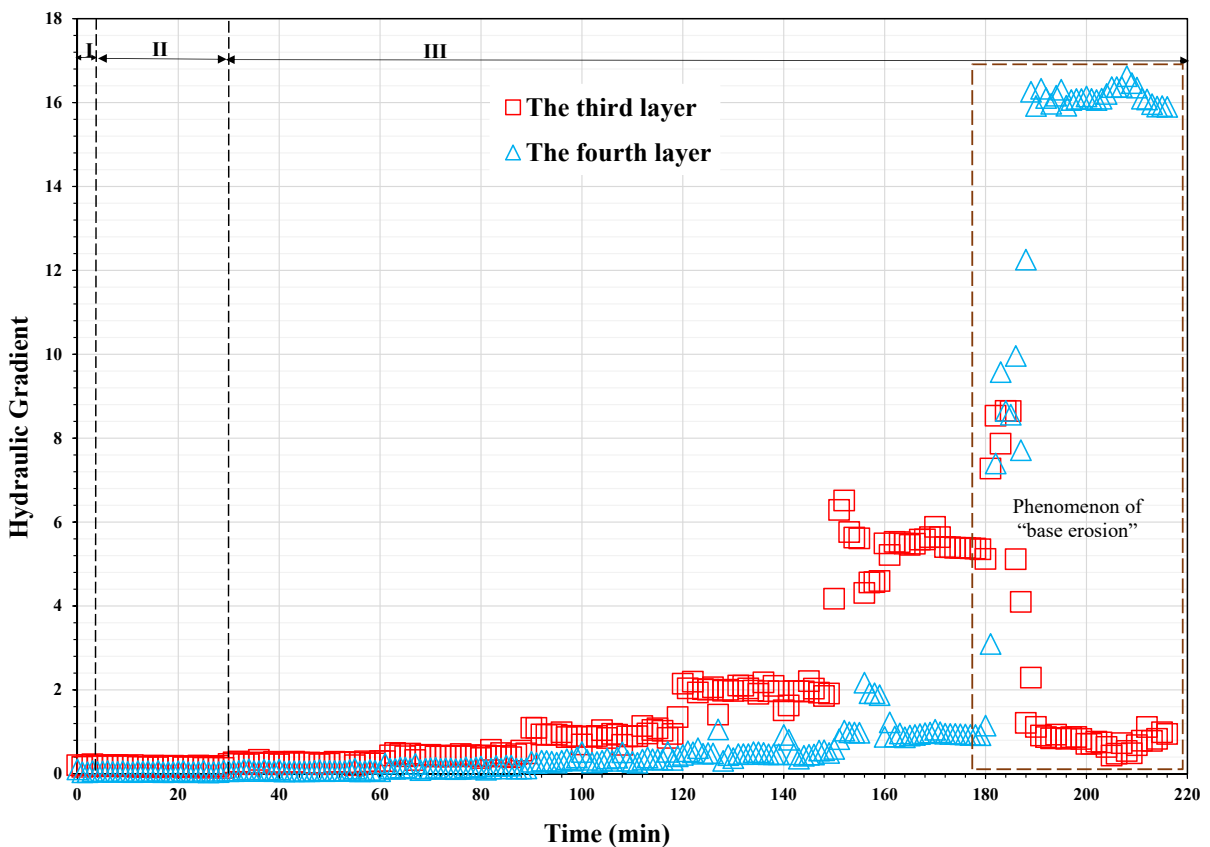


Figure IV.21 – Hydraulic gradient of third and fourth layers versus time curve (W-b-I)

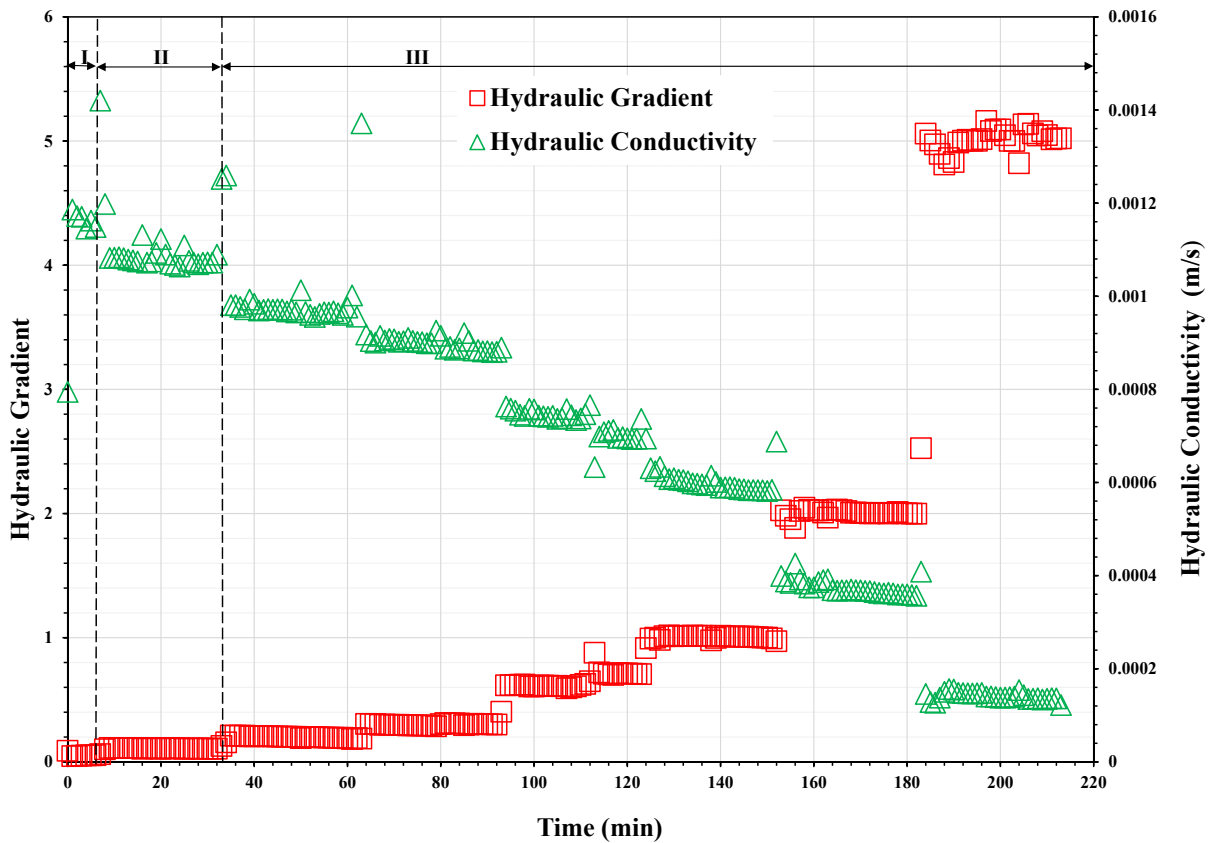


Figure IV.22 – Hydraulic conductivity and hydraulic gradient versus time curve of the whole soil layer (W-b-III)

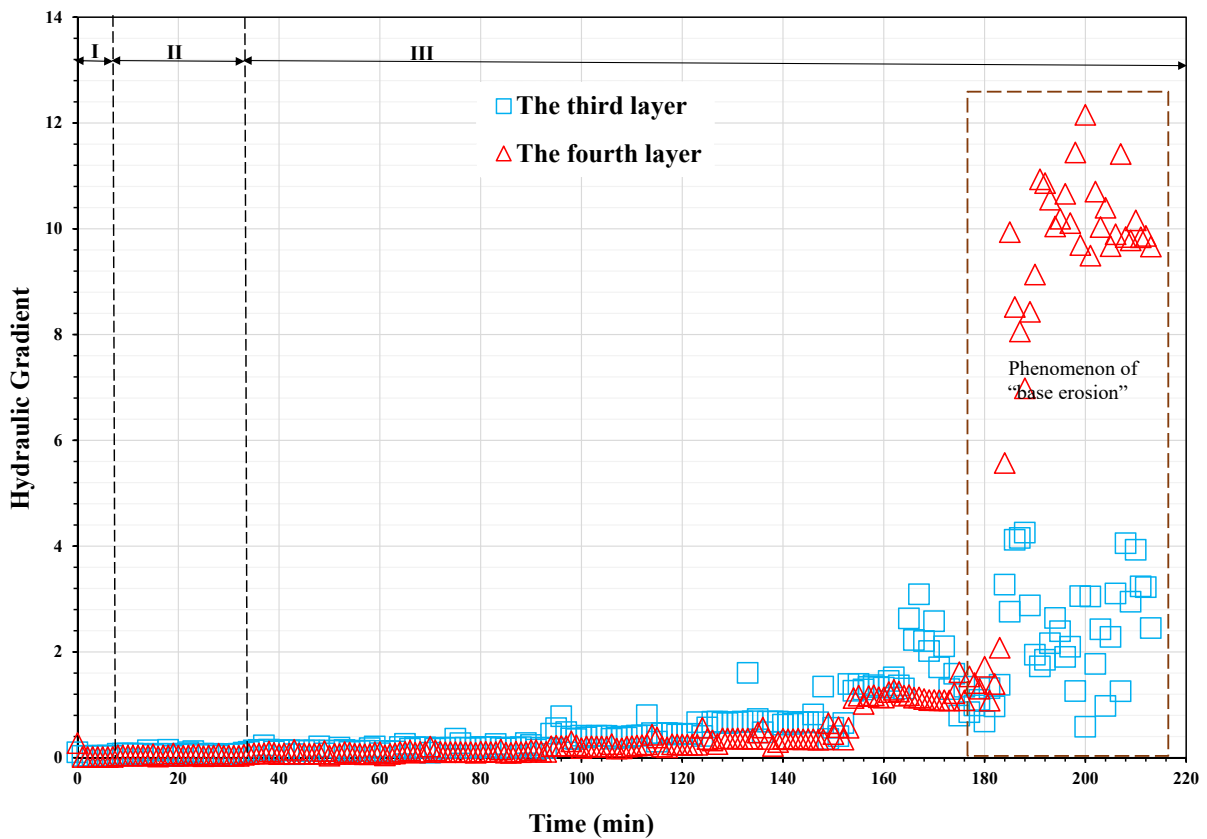


Figure IV.23 – Hydraulic gradient of third and fourth layers versus time curve (W-b-III)

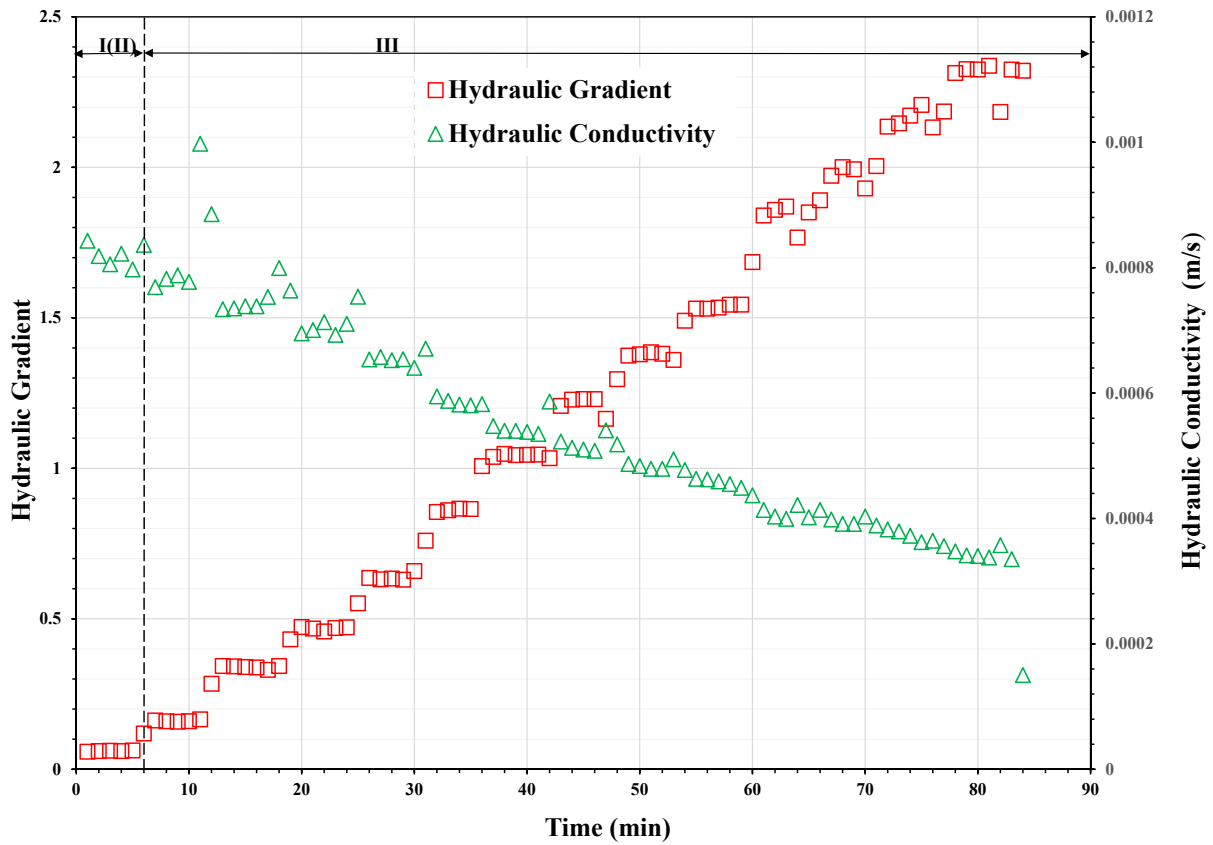


Figure IV.24 – Hydraulic conductivity and hydraulic gradient versus time curve of the whole soil layer (W-c-I)

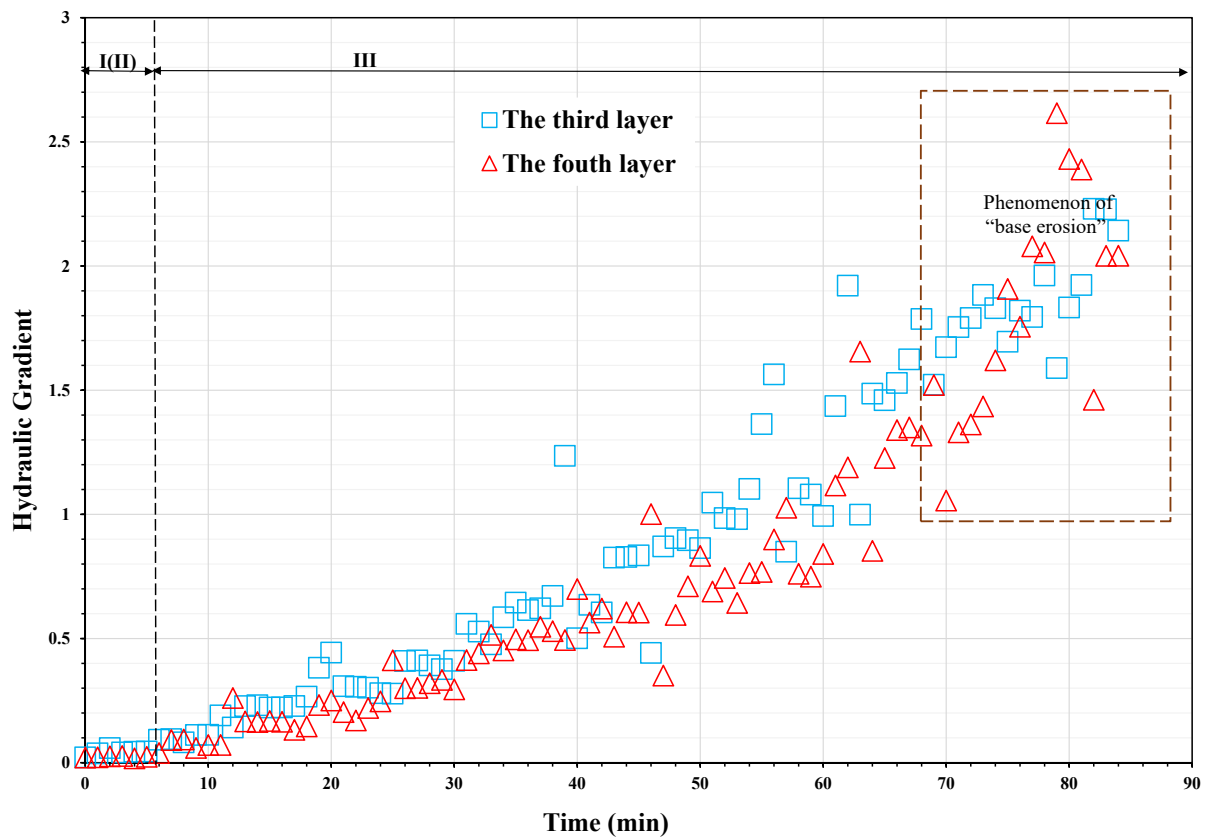


Figure IV.25 – Hydraulic gradient of third and fourth layers versus time curve (W-c-I)

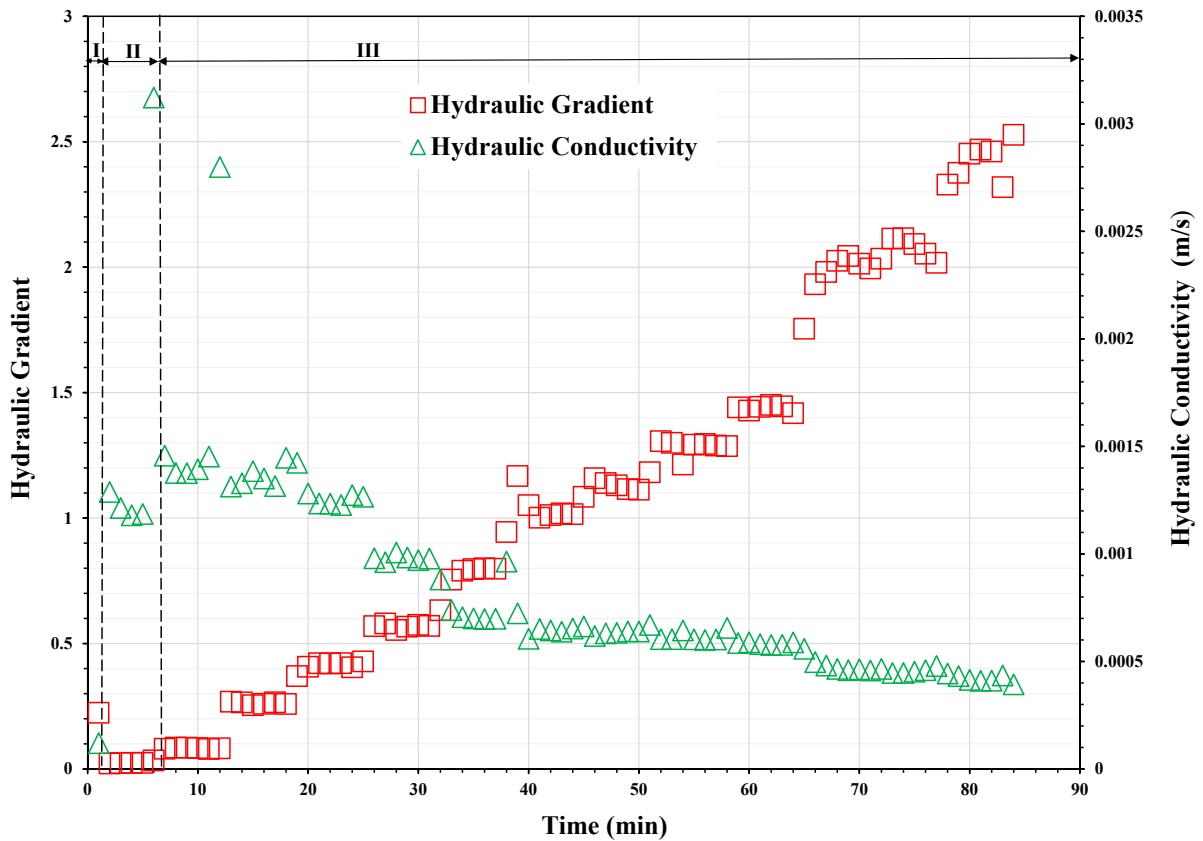


Figure IV.26 – Hydraulic conductivity and hydraulic gradient versus time curve of the whole soil layer (W-c-II)

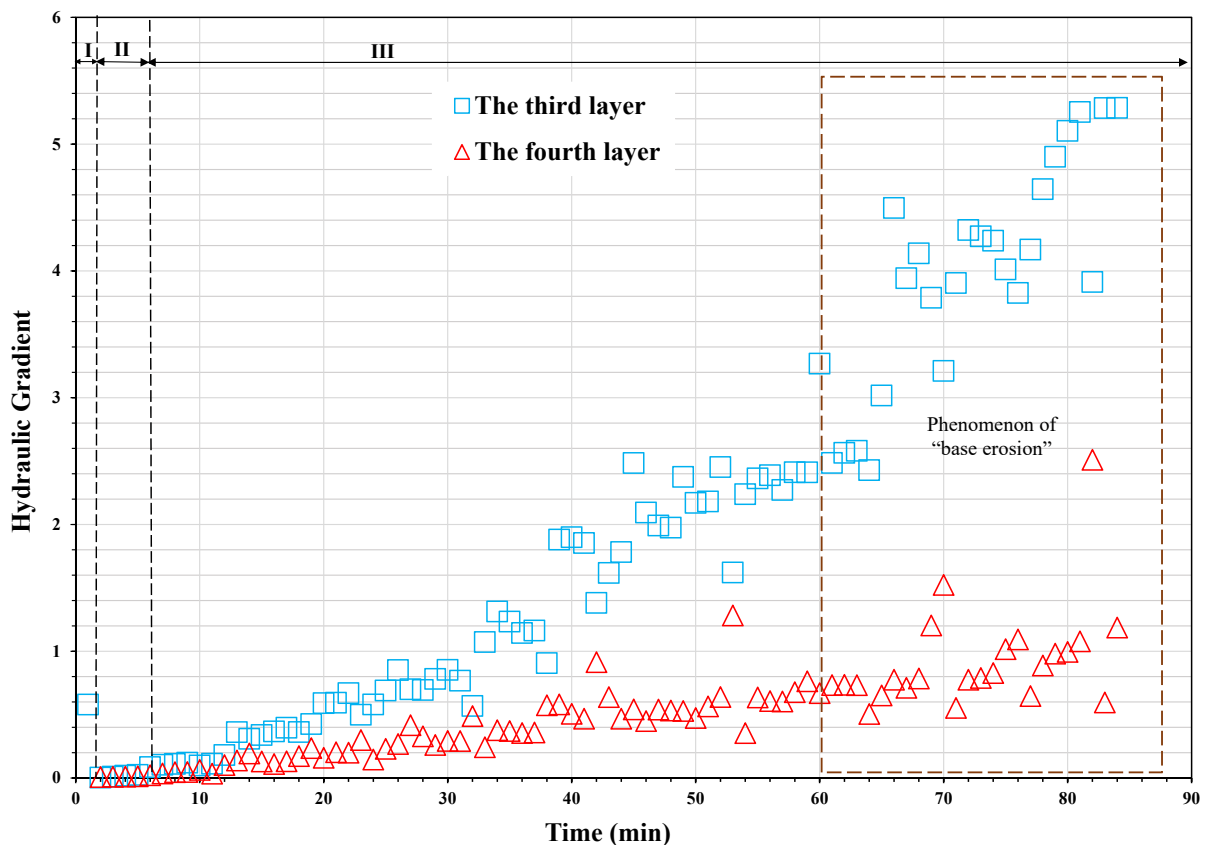


Figure IV.27 – Hydraulic gradient of third and fourth layers versus time curve (W-c-II)

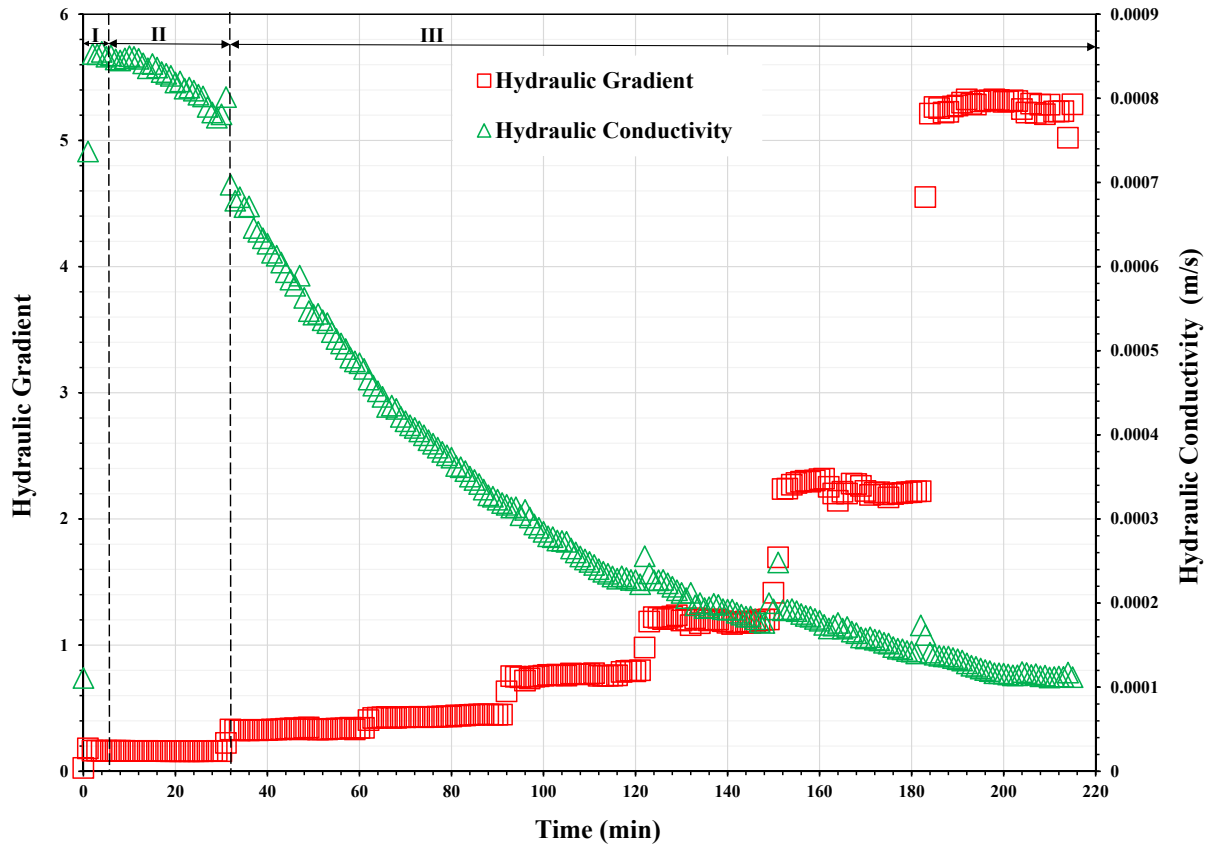


Figure IV.28 – Hydraulic conductivity and hydraulic gradient versus time curve of the whole soil layer (W-d)

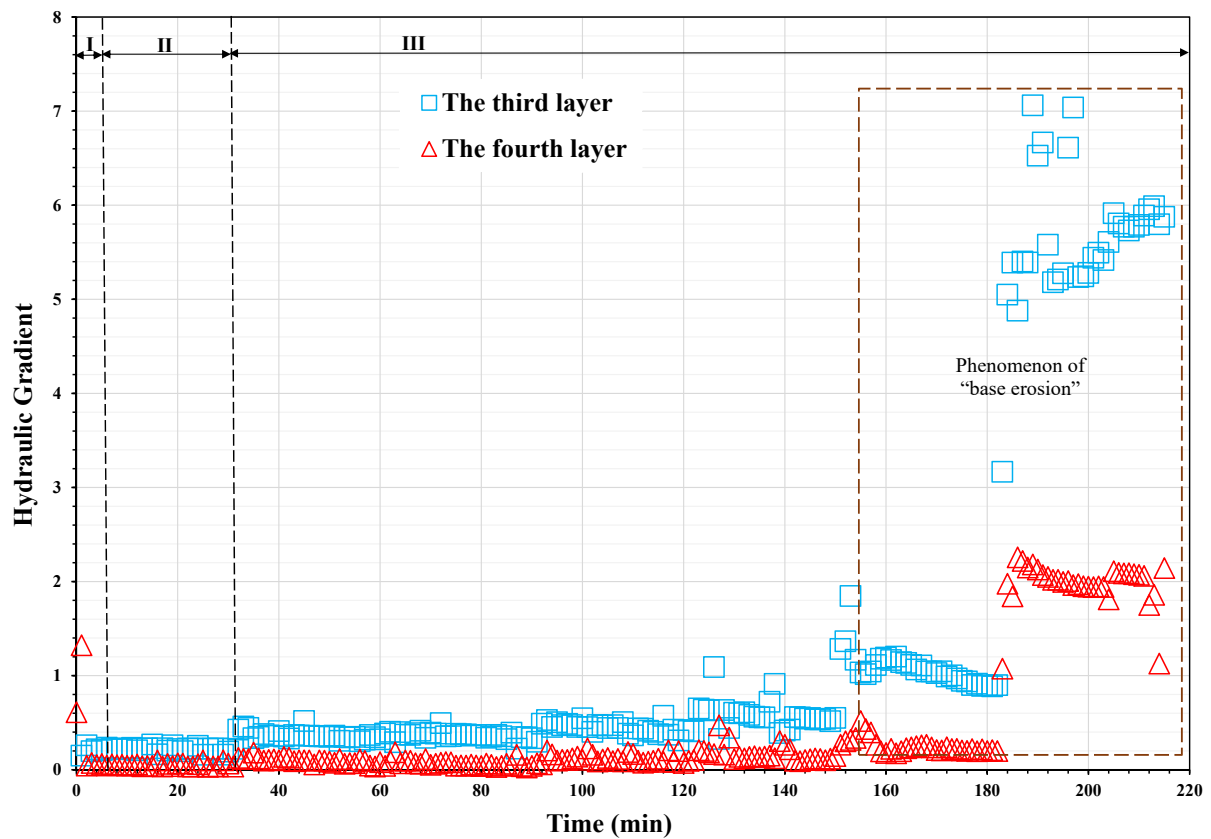


Figure IV.29 – Hydraulic gradient of third and fourth layers versus time curve (W-d)

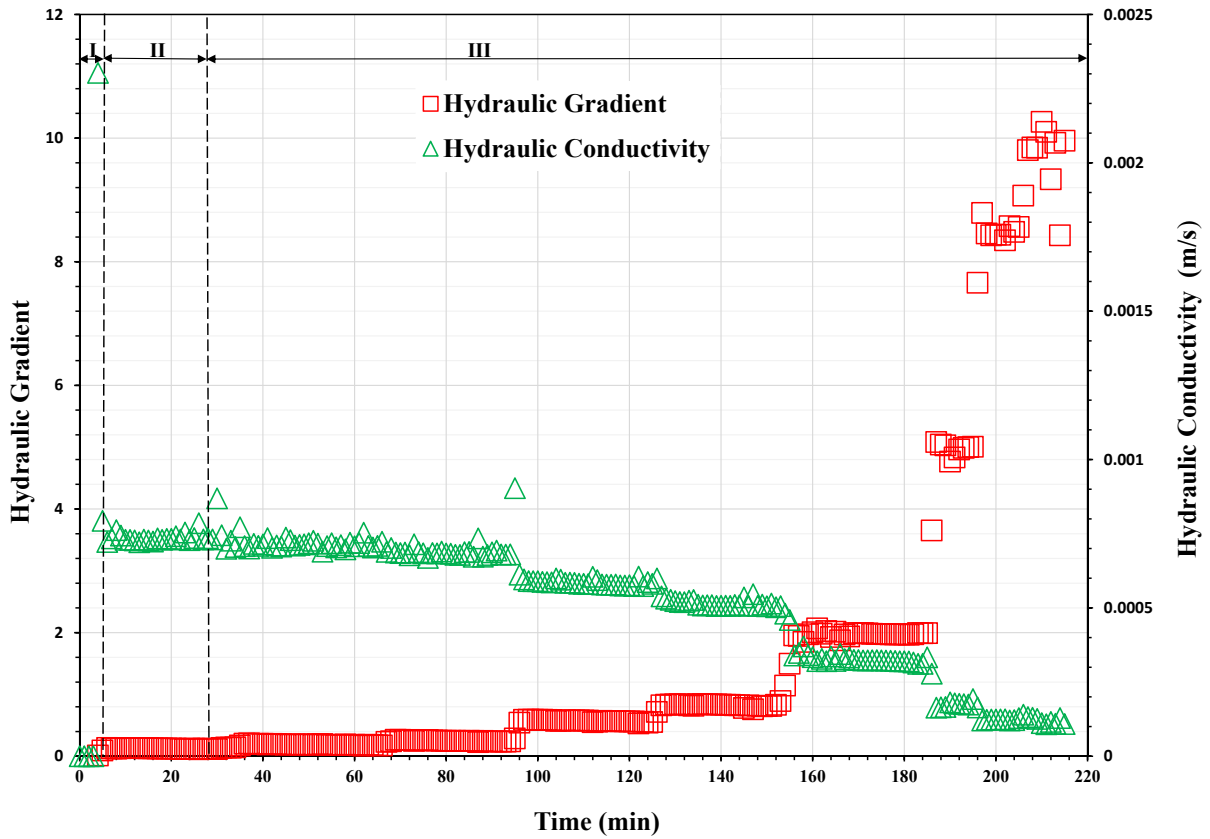


Figure IV.30 – Hydraulic conductivity and hydraulic gradient versus time curve of the whole soil layer (W-e-I)

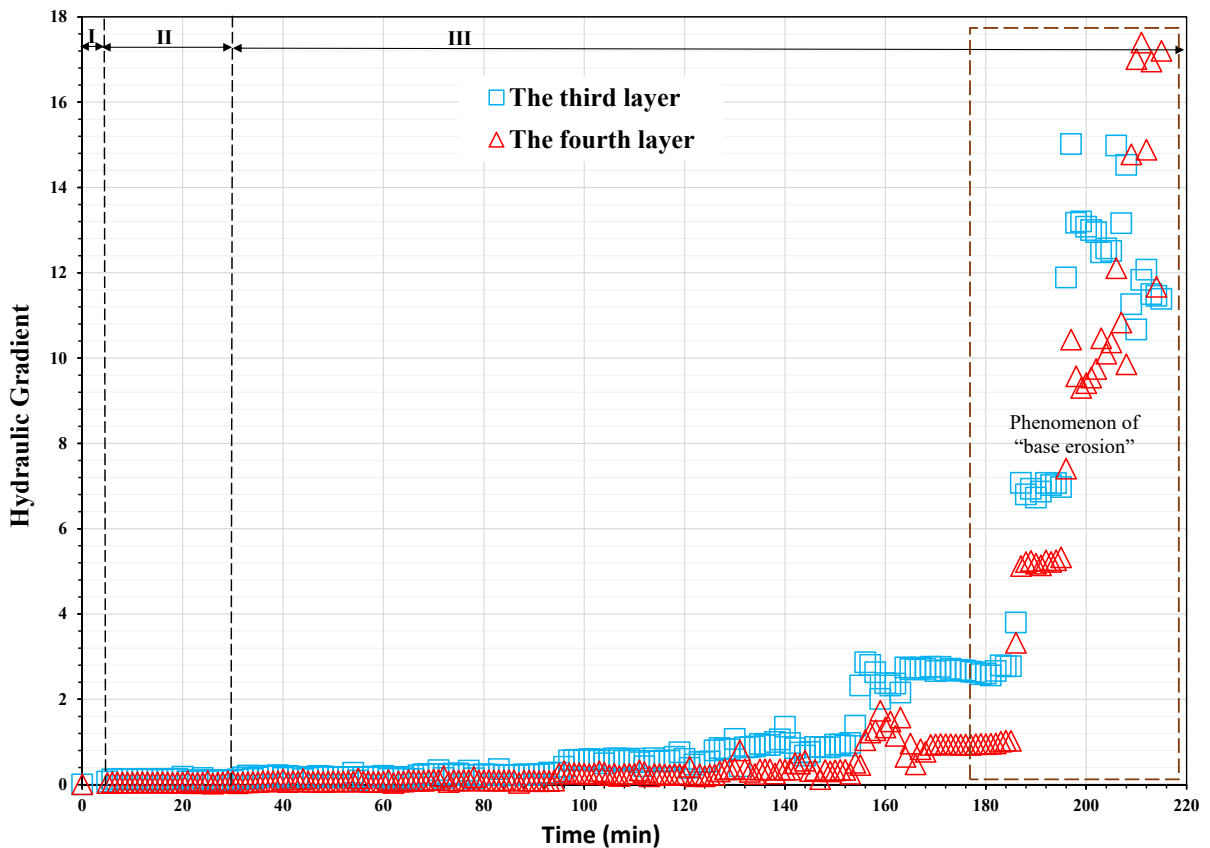


Figure IV.31 – Hydraulic gradient of third and fourth layers versus time curve (W-e-I)

4.6.2 Study of the permeation deformation mechanism

Analysis of osmotic compaction mechanism

Based on the seepage theory, the basic equation of seepage movement in soil is simplified to one dimensional vertical flow.

$$\frac{\partial^2 H}{\partial z^2} = 0 \quad \text{IV.2}$$

The boundary conditions are:

$$z = 0, H = H_1, z = L, H = H_2 \quad \text{IV.3}$$

Where H is the head function; H_1 and H_2 are the upstream and downstream head, respectively; and L is the length of seepage diameter.

The distribution of water head in the soil layer along the direction of seepage is obtained by introducing boundary conditions into Equation IV.2.

$$H = \frac{H_2 - H_1}{L}z + H_1 \quad \text{IV.4}$$

$$i = -\frac{dH}{dz} = \frac{H_1 - H_2}{L} \quad \text{IV.5}$$

Equation IV.4 can be written as follows:

$$H_1 - H = iz \quad \text{IV.6}$$

$$\gamma_w (H_1 - H) = \gamma_w iz \quad \text{IV.7}$$

From these two formulae, we can attain:

$$\sigma_{wz} = \gamma_w iz \quad \text{IV.8}$$

Where γ_w is the gravity of water; i is the hydraulic gradient; z is the distance of a point in the soil from the infiltration point along the streamline direction; and σ_{wz} is the seepage force of the point soil.

In the test, the soil was layered along the streamline.

$$\sigma_{wz} = \sum_{j=1}^n \gamma_w i_j z_j = \gamma_w \sum_{j=1}^n i_j z_j \quad \text{IV.9}$$

According to soil mechanics, the self-weight stress of the soil along the vertical direction is as follows:

$$\sigma_{cz} = \sum_{i=j}^n \gamma'_j z_j \quad \text{IV.10}$$

Where γ'_j is the floating weight of layer j soil.

Under the action of osmotic force, the vertical force at a certain depth is composed of osmotic force and self-weight stress, and the distribution of the osmotic force on the soil is the same as that of the self-weight stress on the soil. The stress state of each soil layer at the stage of osmotic compaction is as follows:

$$\sigma_z = \sigma_{wz} + \sigma_{cz} = \gamma_w \sum_{i=j}^n i_j z_j + \sum_{i=j}^n \gamma'_j z_j \quad \text{IV.11}$$

Under the action of seepage force, the internal stress of soil loses its original equilibrium state. To overcome frictional resistance, particles move and fill with each other, forming a new arrangement, which shows the phenomenon of compaction. The larger the infiltration force applied to the soil, the more obvious the particle movement and filling, and the more compact the soil. When the soil is compacted to a certain degree, it shows the characteristics of seepage consolidation. Its characteristics can be expressed by the change of permeability coefficient. The hydraulic conductivity is relatively stable in the stage of seepage stability shown in Figures IV.20 - IV.31. From osmotic compaction to osmotic consolidation, the density of the soil sample also changes, which shows that the upper soil layer decreases relatively and the lower soil layer increases relatively.

Force Analysis of Movable Particles

In the process of infiltration, the movement of soil particles is characterized by the migration or retention of individual particles in the pore formed by skeleton particles.

A single soil particle was taken as the research object, and a stress analysis was carried out. We assumed that the movable particles moved in the throat tube formed by the skeleton particles. As shown in Figure IV.32, the force acting on the movable particles was as follows:

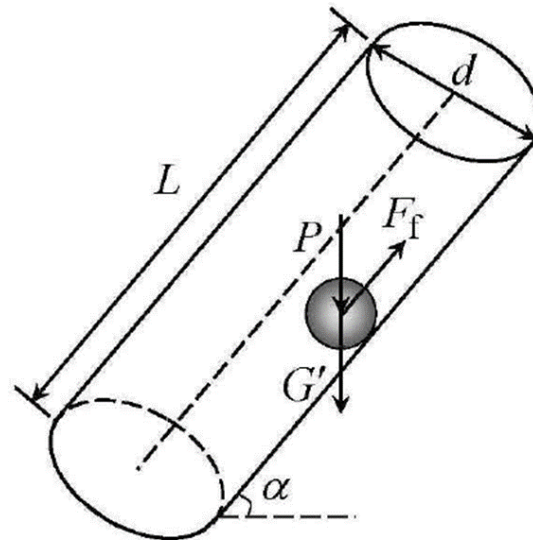


Figure IV.32 – Force diagram of particles in laryngeal tube

Particles were subjected to gravity and buoyancy.

$$G' = \frac{3}{4}\pi r^3 \cdot \gamma' \quad \text{IV.12}$$

Dragging force of hydrodynamic pressure on particles:

$$P = \pi r^2 i L \gamma_w \quad \text{IV.13}$$

Friction between particles and throat:

$$F_f = (G' + P) \cos \alpha \cdot f \quad \text{IV.14}$$

Therefore, the forces acting on movable particles are:

$$F = (G' + P) \sin \alpha \cdot f - F_f \quad \text{IV.15}$$

Where r is the radius of movable particles; γ' is the floating weight of soil particles; γ_w is the gravity of water; i is the hydraulic gradient; L is the length of the pipe passage; f is the friction coefficient between the movable particles and the wall of the pipe; and α is the angle between the pipe passage and the horizontal plane.

When $F > 0$, the particles have a downward force component along the throat, showing the phenomenon of particle migration or harmless piping and latent erosion along the pore.

When $F < 0$, the movable particles are suspended.

When $F = 0$, the movable particles are balanced in force and stay in the pore, which is characterized by seepage and deposition.

Fluid movement in the pore formed by skeleton particles produces a series of complex mechanical properties such as dragging, adsorption, and repulsion for the added particles, which causes the microstructure of the entire soil to change. Ultimately, the phenomenon of seepage destruction or seepage blockage is manifested.

4.7 Conclusion

In this study, a series of suffusion tests was carried out with an oedo-permeameter to assess the suffusion susceptibility by studying the local process. Twelve specimens, including widely graded and gap-graded soils and homogeneous and heterogeneous specimens, were tested in terms of seepage flow in a downward direction under a multistage hydraulic gradient condition. Not only post-suffusion gradations and size distribution of eroded particles, but also the time evolution of the local hydraulic gradient and conductivity, highlight the complexity of suffusion that appears as the combination of detachment–filtration transport processes. Moreover, heterogeneous specimens appear to be less stable for gap-graded soil. Finally, a large number of eroded particles are measured when the maximum hydraulic gradient concerns the specimen's downstream part.

The conditions and degree of silting in the process of seepage were analyzed, and a set of experimental results were discussed thoroughly. The process of seepage was shown to be a complex process. In the overall process of seepage, silting and erosion are intertwined. Thus, judging the occurrence of silting and erosion necessarily involves comprehensive analysis of the changes in multiple parameters.

The process of infiltration erosion can be divided into three stages: grain adjustment stage, “seepage stability” stage, and “seepage change” stage. According to the mechanical characteristics of seepage deformation of soil or soil particles, the mechanism of seepage deformation was analyzed. Combined with the movement of particles in the pore, the force analysis of a single soil particle showed that when the particles have a downward force component along the throat, this is the phenomenon of particle migration, harmless piping, or latent erosion. When the particles have an upward force component along the throat, the movable particles are suspended, and when the forces of said particles are balanced, they constitute seepage and deposition.

SPATIAL SCALE EFFECTS ON SUFFUSION SUSCEPTIBILITY

5.1 Introduction

Erosion is an intricate phenomenon which is one of the most common origins of failure for dikes and embankment dams. From the literature it can be found that, in the past few decades, many research methods have been proposed and lots of instruments have been designed to investigate the internal erosion. This variety of testing devices is accompanied with various tested specimen sizes: diameter from 50 mm to 300 mm and height from 50 mm to 600 mm. However, the potential influence of the specimen volume on suffusion susceptibility is not well established. Thus, this chapter aims to investigate this potential spatial scale influence by comparing results of suffusion tests performed with two different sized devices. In partnership with Le Van Thao, PhD thesis student of our research team, a campaign of suffusion tests was performed on gap-graded and widely graded soils. For each tested soil, the results are discussed in terms of suffusion susceptibility (Marot et al., 2016). Specimens of different sizes are compared provided that their initial hydraulic conductivity are similar.

5.2 Laboratory experiments

5.2.1 Main characteristics of testing devices

Two different apparatuses were designed to perform suffusion tests with a flow in a downward direction. The larger device, named as oedo-permeameter, has been introduced in Chapter III. The oedo-permeameter is composed of a 280 mm inner diameter rigid wall cylinder cell, and the specimen height can reach 600 mm (see Figure V.1(a)). The second device which was used

by Le Van Thao consists essentially of a modified triaxial cell and specimen sizes are 50 mm in diameter and up to a 100 mm in height (see Figure V.1(b)). A detailed description of each device was reported by Sail et al. (Sail et al., 2011) and by Bendahmane et al. (Bendahmane et al., 2008), respectively; however, a brief summary is provided here.

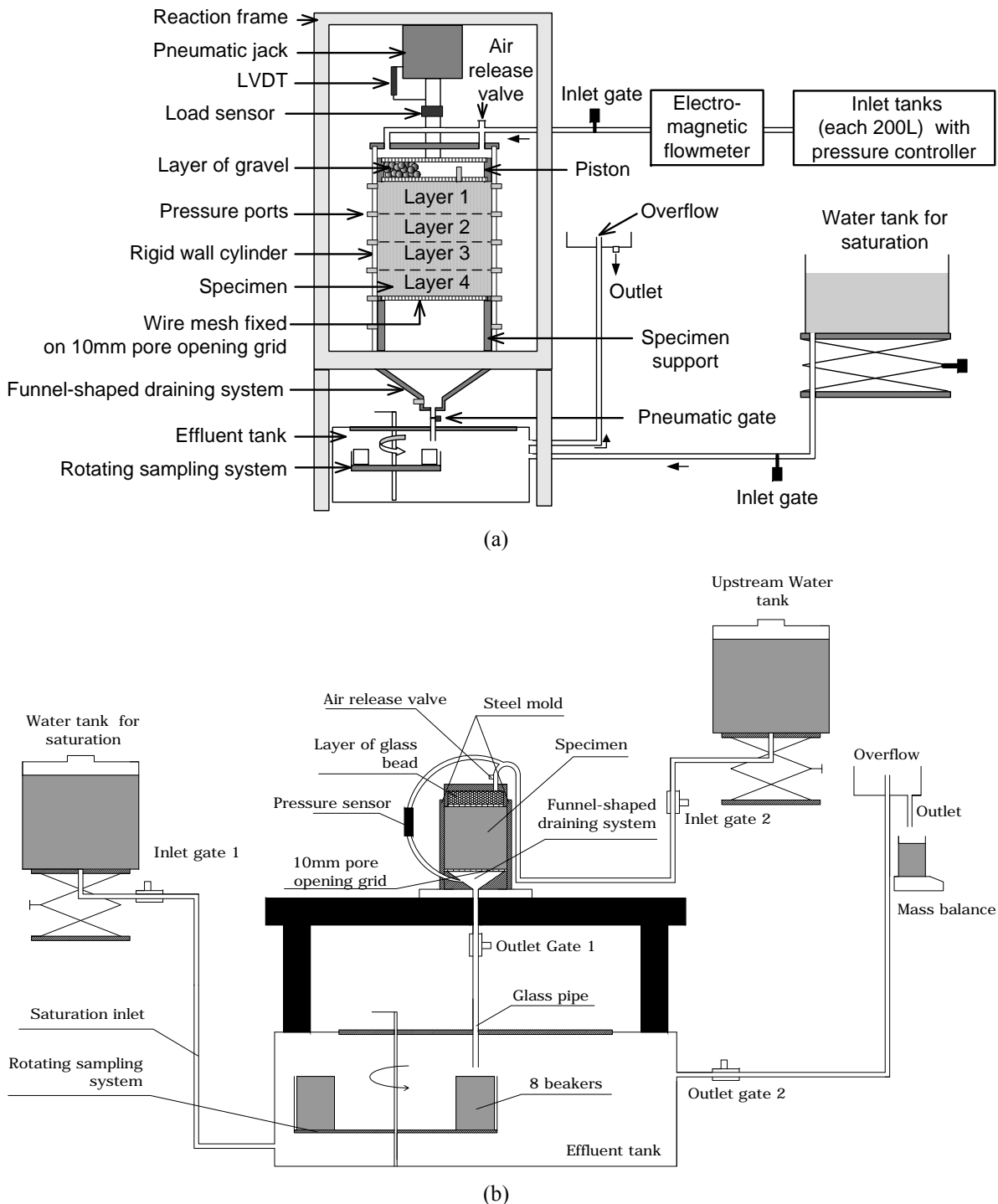


Figure V.1 – Permeameter apparatus (a) oedo-permeameter, and (b) triaxial erodimeter

For both devices, the fluid circulates into the top cap which contains a layer of gravel or glass beads to diffuse the fluid uniformly on the specimen top surface. Both cell bases have a vertical funnel-shaped draining system, specially designed to avoid clogging. Each draining system is

connected to a collecting system which is composed of an effluent tank containing a rotating support with eight beakers to catch the loss particles during testing. With the objective to test specimens in oedometric condition with both devices, the membrane of the triaxial erodimeter is surrounded by a steel mold. However, due to the different weights of specimens and top caps in both devices, the vertical effective stress at the specimen bottom is 5.9 kPa greater in the oedo-permeameter. In both devices, the specimen is placed on a sieve with 1.2 mm pore opening size which is fixed on a 10 mm mesh screen. According to the used apparatus, the range of flow rate is completely different; thus two configurations are used: a flowmeter is used in the case of oedo-permeameter, whereas at the overflow outlet of triaxial erodimeter, water falls in a beaker which is continuously weighed. The hydraulic controlled system is composed of a pressure controller connected to two 200 L tanks alternatively used in the oedo-permeameter apparatus, and one upstream water tank for the triaxial erodimeter. The differential pore water pressure across the specimen is measured using a differential pressure transducer connected to the top cap and the base pedestal of the triaxial erodimeter. The rigid wall of the oedo-permeameter cell is equipped with 12 pressures ports; in addition, a pressure port is placed on the piston base plate (i.e. at the specimen-piston interface) and a fourteenth pressure port is located below the specimen on top of the funnel-shaped draining system. All these pressure ports are connected to a multiplex unit which is connected with a manometer to avoid discrepancy. For each device, a dedicated computer operates the data acquisition thanks to LabVIEW software developed by the author's team.

5.2.2 Testing materials

A laser diffraction particle size analyzer was used to measure the grain size distribution of tested soils (see Figure V.2). Tests were performed with demineralized water and without using a deflocculating agent. Two types of gradations were selected, gap-graded and widely graded. The four gap-graded soils were composed of either sand and gravel (numbered 1, 4 and 6) or silt, sand, and gravel (number 5). The gradations of these four gap-graded soils differed slightly, mainly with respect to the fines content ranging from 16.5 % to 25 %. Considering the two widely graded soils, the cohesionless one is composed of silt, sand, and gravel (number 3) and the clayey soil (number 2) is composed of 25 % of Kaolinite Proclay and 75 % of Fontainebleau sand. All these soils were selected to obtain internally unstable soils. According to criteria based on grain size proposed by Kenney and Lau (Kenney and Lau, 1985) and Indraratna et al. (Indraratna et al., 2015), all these soils are indeed internally unstable (see Table V.1). However, as the percentage of fines P is higher than 20 % for soil 2 and as the gap ratio G_r is smaller than

3 for soil 4, Chang and Zhang's method (Chang and Zhang, 2013b) classifies these two soils as internally stable. Wan and Fell's (Wan and Fell, 2008) method seems not to be applicable for gap-graded soils nor for soils with a mass of fine fraction lower than 15 %. Then this method is only relevant for soil 3 which is classified as internally stable.

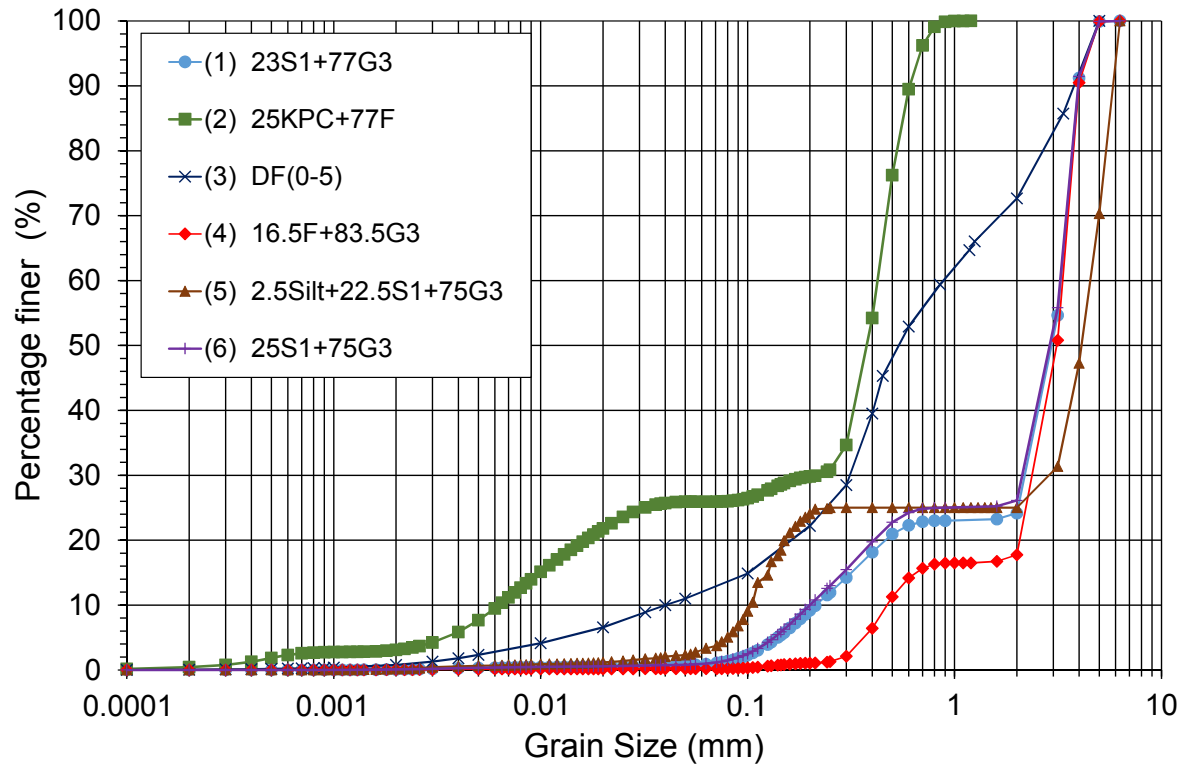


Figure V.2 – Grain size distribution of tested soils

Table V.1 – Properties of tested gradations

Properties	Tested gradations					
	1	2	3	4	5	6
P (%)	0.91	25.94	12.02	0.21	3.34	0.99
G_r	3.33	3.61	WG	2.29	9.43	3.33
C_u	15.70	67.68	22.16	7.06	43.70	16.24
d_{15}/d_{85}	0.083	0.018	0.031	0.169	0.022	0.076
$(H/F)_{min}$	0.161	0.110	0.446	0.600	0	0.155
$D(H/F)_{min}$ (mm)	0.494	0.030	0.606	0.490	0.414	0.494
$D_{c35}^c/d_{85,SA}^f$	2.773	14.251	17.411	1.273	6.503	2.773
Kenney and Lau's criterion	U	/	U	U	U	U
Wan and Fell's criterion	/	/	S	/	/	/
Chang and Zhang's criterion	U	S	U	S	U	U

Indraratna's criterion	U	U	U	U	U	U
------------------------	---	---	---	---	---	---

Note: P = percentage of particle smaller than 0.063 mm; $G_r = d_{max}/d_{min}$ (d_{max} and d_{min} : maximal and minimal particle sizes characterizing the gap in the grading curve); C_u = uniformity coefficient; d_{15} and d_{85} are the sieve sizes for which 15 and 85 % respectively of the weighed soil is finer; F and H are the mass percentages of the grains with a size, lower than a given particle diameter d and between d and $4d$ respectively; $D(H/F)_{min}$ is the corresponding diameter with the minimum value of ratio H/F ; D_{c35}^c is the controlling constriction for coarser fraction from constriction size distribution by surface area technique; $d_{85,SA}^f$ is the representative size for finer fraction by surface area technique; WG = widely graded soil; U = unstable; S = stable; / = method not relevant for considered soil.

5.2.3 Specimen preparation and testing program

With the objective to improve the readability, the first number of each test name is related to the gradation (Figure V.2). The letter indicates the used apparatus: O for the oedo-permeameter test and T for the triaxial erodimeter test, and the last number details the specimen number.

For each soil, the whole quantity for oedo-permeameter and triaxial erodimeter tests was prepared at the same time to avoid segregation and discrepancy. The first step of specimen preparation consists of moistening the soil with a water content of about 8 % and mixing thoroughly. Then specimens were placed in the oedo-permeameter cell in three layers and each layer was compacted to reach the initial fixed dry density. For triaxial erodimeter tests, the specimens were prepared using a single layer semistatic compaction technique, in order to reach the target value of initial dry density. For both devices, CO_2 was upwardly injected to improve dissolution of gases into water and finally, upward saturation was completed using demineralized water. This operation was performed through a low hydraulic gradient by increasing the position of the dedicated water tank (see Figure V.1(a) and Figure V.1(b)), until the water reached the air release valve. Two different procedures of the saturation phase were tested for both devices in order to saturate specimens during the same duration or under the same moistening velocity.

A beaker was systematically used to catch the loss of particles during the saturation phase. The dry mass of collected particles was measured after drying at 105 °C for 24 hours. The order of magnitude of dry mass loss depends on the specimen volume and the accuracy of dry mass measurement is evaluated to ± 2 mg for the triaxial erodimeter test and ± 0.02 g for the oedo-permeameter test.

Table V.2 summarizes the initial lengths and the initial dry densities of each of the 16 tested specimens.

For soil 6, two specimens were prepared for each device at the same initial dry density (see Table V.2). The percentage of particles lost during the saturation step is expressed as the ratio of lost particle mass over the initial mass of fines in the specimen. Figure V.3 shows the great influence of this percentage on the initial hydraulic conductivity. Moreover, it was observed that the loss of particles increased with the wetting front velocity. In consequence, the saturation of specimens was systematically applied for both devices under the same wetting front velocity to limit the discrepancy in the initial hydraulic conductivity, which is also indicated in Table V.2. Rochim et al. (Rochim et al., 2017) showed that the history of hydraulic loading has a significant influence on the development of suffusion, and with the objective of following the development of all possible combinations, tests must be realized by increasing the applied hydraulic gradient. Thus, in this study, specimens were systematically tested under a multistage hydraulic gradient (see Table V.2) and each stage lasted 30 minutes. The total duration of each test is detailed in Table V.2. A beaker was used to catch the eroded particles during each hydraulic gradient stage and the corresponding dry masses were measured.

Moreover, after each oedo-permeameter test, the quantity of detached particles was large enough to perform one accurate grain size distribution; in addition, each eroded specimen was divided into four layers (see Figure V.1(a)) to determine the gradations after the suffusion test. Finally, the repeatability of our specimen preparation and testing procedure was verified by performing two tests under identical conditions: 6-O-1 and 6-O-2.

Table V.2 – Properties of tested specimens and summary of testing program

Specimen reference in thesis	Specimen length (mm)	Initial dry density γ_d (kN/m ³)	Applied hydraulic gradient i	Initial hydraulic conductivity (10 ⁻³ m/s)	Test duration (min)
1-O	425	16.50	From 0.04 to 0.23	2.02	134
1-T	100	16.43	From 0.07 to 0.20	0.25	135
2-O-1	430	16.61	From 0.21 to 11.24	0.06	268
2-O-2	240	17.47	From 0.92 to 22.17	0.02	245
2-T	50	16.00	From 0.15 to 5.77	0.02	243
3-O	240	17.79	From 0.56 to 15.81	0.05	150
3-T	100	17.00	From 0.11 to 4.65	0.06	215
4-O	437	15.88	From 0.04 to 0.16	37.83	167
4-T	50	16.08	From 0.10 to 1.50	0.64	153

5-O	440	16.84	From 0.04 to 0.26	12.70	147
5-T-1	50	17.00	From 0.40 to 4.00	0.41	167
5-T-2	100	17.00	From 0.01 to 0.81	0.87	247
6-O-1	430	17.04	From 0.04 to 0.50	3.54	181
6-O-2	435	16.56	From 0.04 to 0.42	5.64	310
6-T-1	50	17.00	From 0.09 to 7.50	0.03	252
6-T-2	100	17.00	From 0.07 to 1.13	1.08	157

Note: First number refers to the tested gradation and the last number is the specimen number;
O = oedo-permeameter; T = triaxial erodimeter.

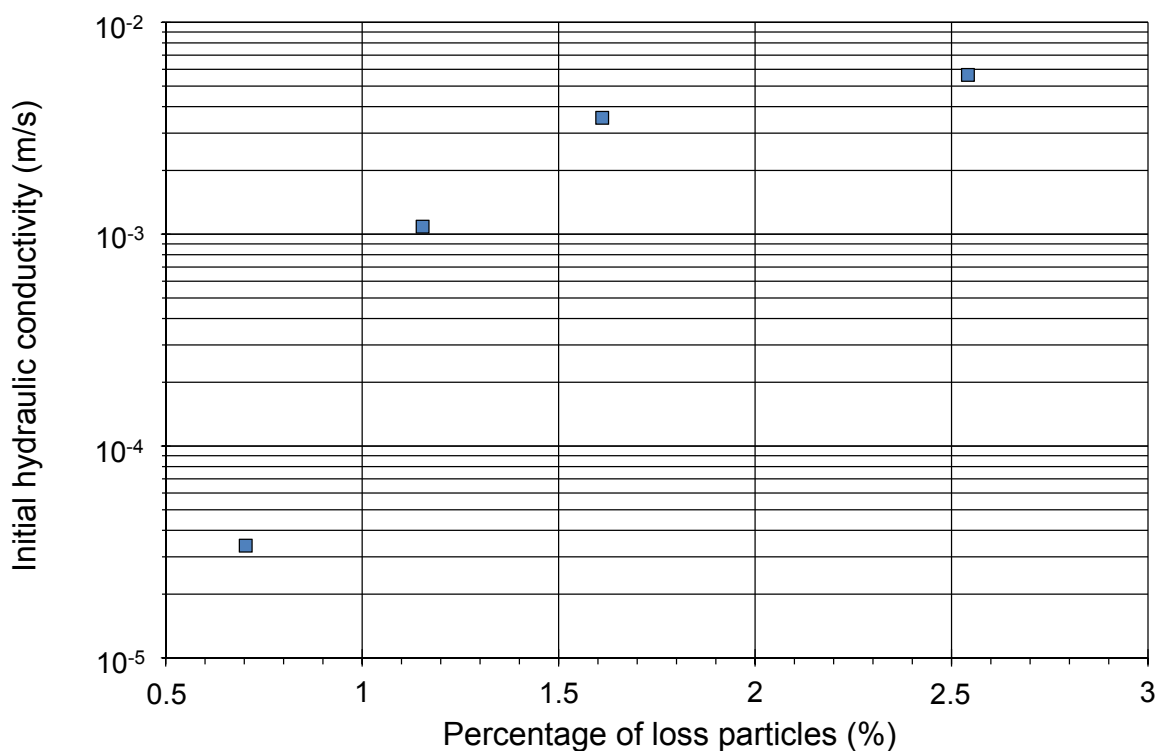


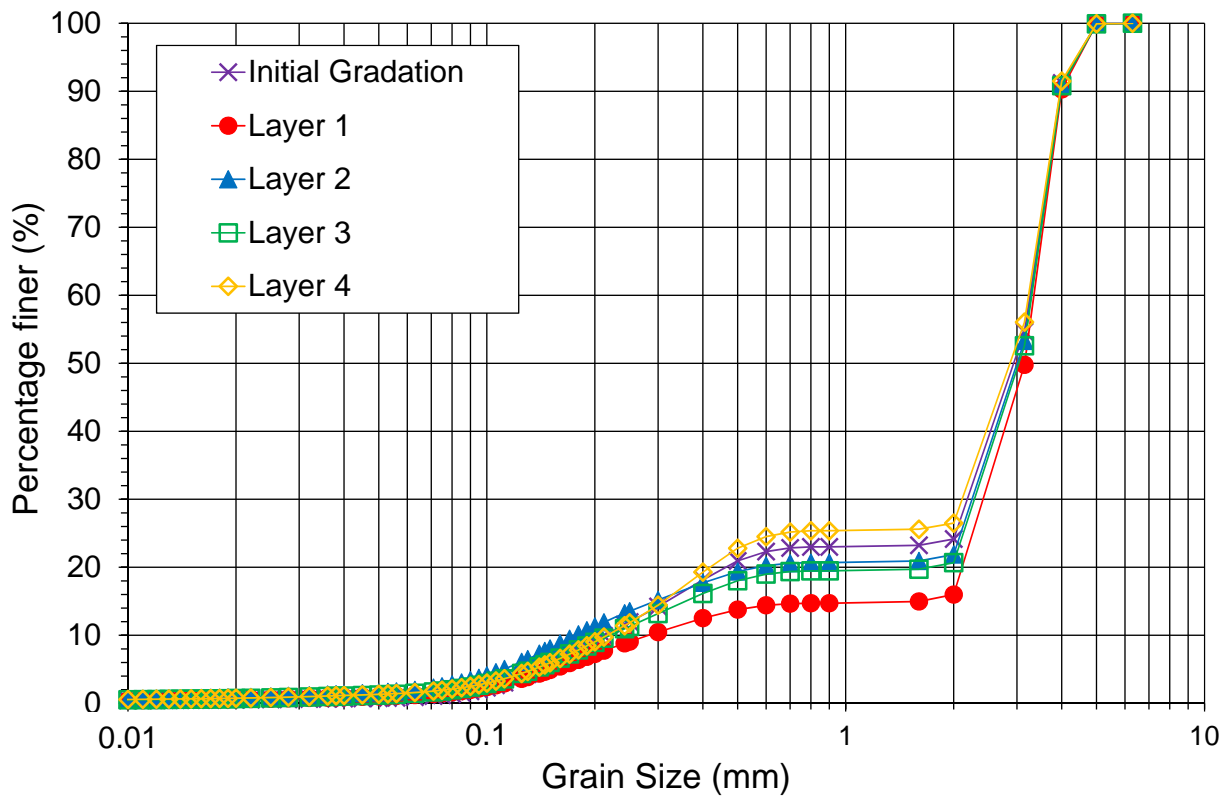
Figure V.3 – Influence of loss particles during saturation on initial hydraulic conductivity on soil 6

5.3 Results

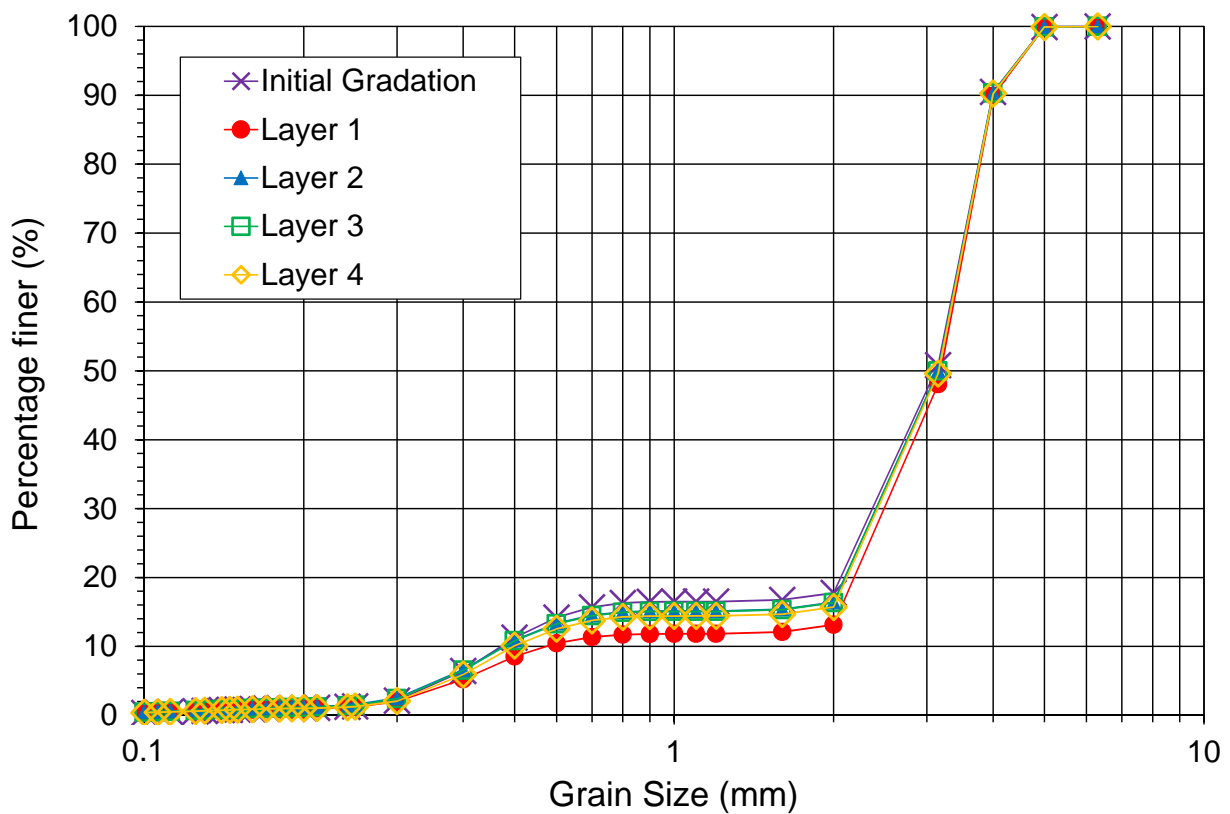
5.3.1 Post-test particle size distributions of specimens

Figure V.4(a) and Figure V.4(b) show the initial gradation and the gradation of post-suffusion specimen divided into four layers for specimens 1-O and 4-O respectively. For both specimens, it can be noted that the loss of fine particles is slightly higher in the upstream part of the specimen in comparison with the middle part. This result agrees with results of Ke and Takahashi (Ke and

Takahashi, 2012).



(a)



(b)

Figure V.4 – Initial soil gradation and post-suffusion gradations of (a) specimen 1-O; and (b) specimen 4-O

The transport of detached particles from upstream to downstream parts can partly offset the loss

of particles in the downstream part. For layer 4 (i.e., at the specimen's downstream part), the final percentage of fines exceeds the initial percentage for specimen 1-O, whereas it is lower than the initial percentage for specimen 4-O. It is worth stressing that the final percentage of fine particles in layer 1 (i.e., at the specimen's upstream part) represents only 64 % of the initial fine percentage of fines in specimen 1-O but about 87 % in specimen 4-O. In consequence, the filtration, which appears obvious in specimen 1-O, seems to be raised by the amount of detached particles.

5.3.2 Grain size distribution of eroded particles

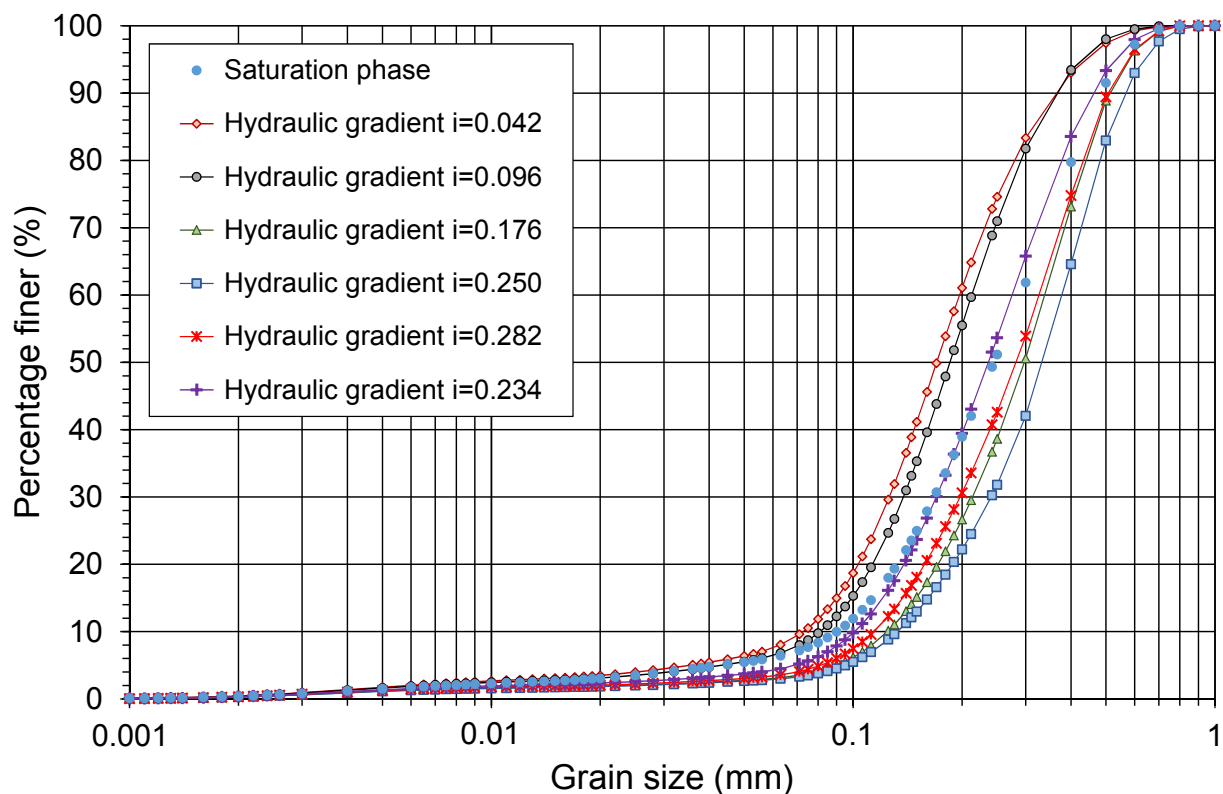


Figure V.5 – Grain size distribution of eroded particles for test 1-O

Only a few data exist in the literature concerning the grain size distribution of eroded particles during the suffusion process. Thanks to the collecting system of the oedo-permeameter, the eroded soils at different stages are caught separately. Figure V.5 displays the grain size distribution of eroded particles for test 1-O at each loading stage. The sieve under the specimen has a 1.2 mm pore opening size and therefore allows the migration of all particles of the finer fraction. As the maximum diameter of the finer fraction of this soil is 0.8 mm (see Figure V.2), Figure V.5 shows that even coarser particles of finer fraction can be eroded. From the first stage of the hydraulic gradient ($i = 0.042$) to the fourth one ($i = 0.250$), the maximum grain size increases. This evolution seems to show that the suffusion process firstly concerns only the finest

particles of the finer fraction and progressively, all sizes of the finer fraction. However, during the last two stages, the maximum grain size of detached particles decreases. In consequence, the time evolution of the grain size distribution of detached particles combined with the spatial variation of the specimen's grain size distribution highlights the complexity of the suffusion process, which appears as a combination of three processes: detachment, transport, and possible filtration of the finer fraction.

5.3.3 Rate of erosion and hydraulic conductivity

As described in Chapter II, Reddi et al. (Reddi et al., 2000) expressed the erosion rate of soils per unit pore area \dot{m} by:

$$\dot{m}(t) = \frac{m(t)}{N_p S_p \Delta t} \quad \text{V.1}$$

Where m is the eroded dry mass during the elapsed time Δt , N_p is the number of average pores, and S_p means the average pore area. Reddi et al. (Reddi et al., 2000) assumed that the equivalent radius r_p is representing the effects of all pores and is defined by:

$$r_p = \sqrt{\frac{8k\mu}{\phi\gamma_w}} \quad \text{V.2}$$

Where k is the hydraulic conductivity, μ is the dynamic viscosity, γ_w means the unit weight of water and ϕ is the porosity.

N_p and S_p can be computed respectively by:

$$S_p = 2\pi r_p L \quad \text{V.3}$$

Where L is the length of the specimen.

$$N_p = \frac{Sn}{\pi r_p^2} \quad \text{V.4}$$

Where S is the cross-sectional area of the specimen.

Hence, the erosion rate per unit pore area depends both on the hydraulic conductivity and the porosity, which evolve in time. During the suffusion process, the measurements show that the maximum value of axial strain did not exceed 0.56% (maximum axial strain of 0.558% was obtained for test 3-O). In consequence, for the computation of porosity during the testing time, the specimen height is assumed constant and sole the eroded dry mass measurement is taken

into account.

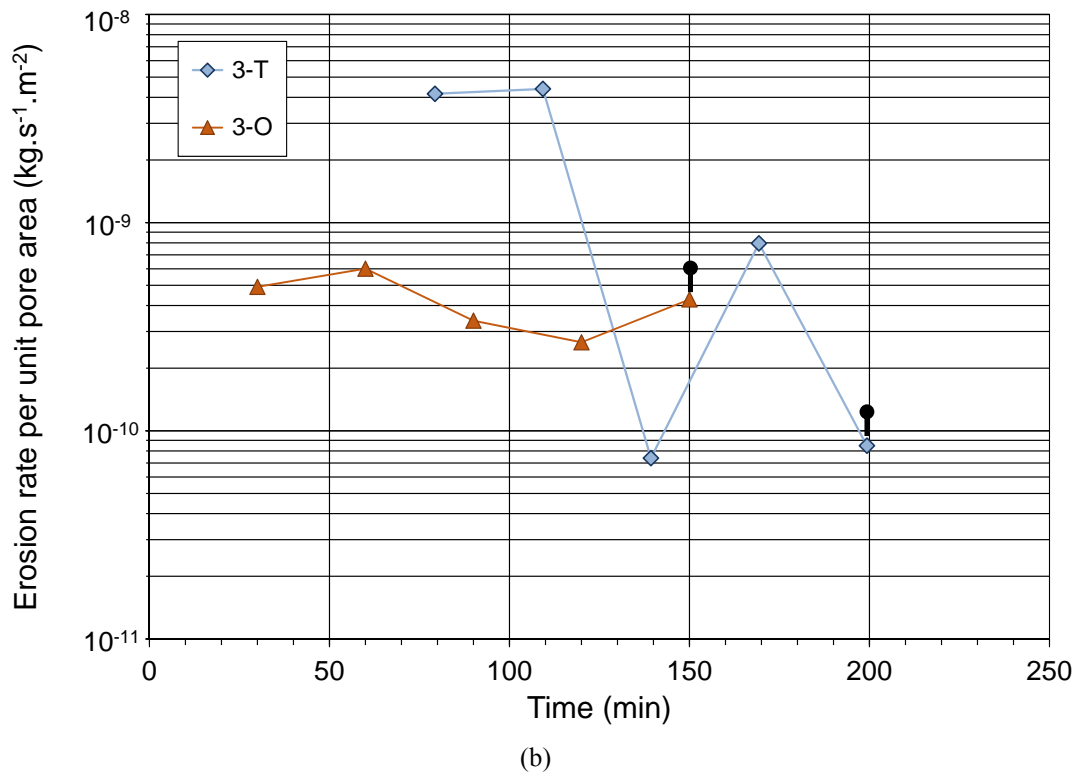
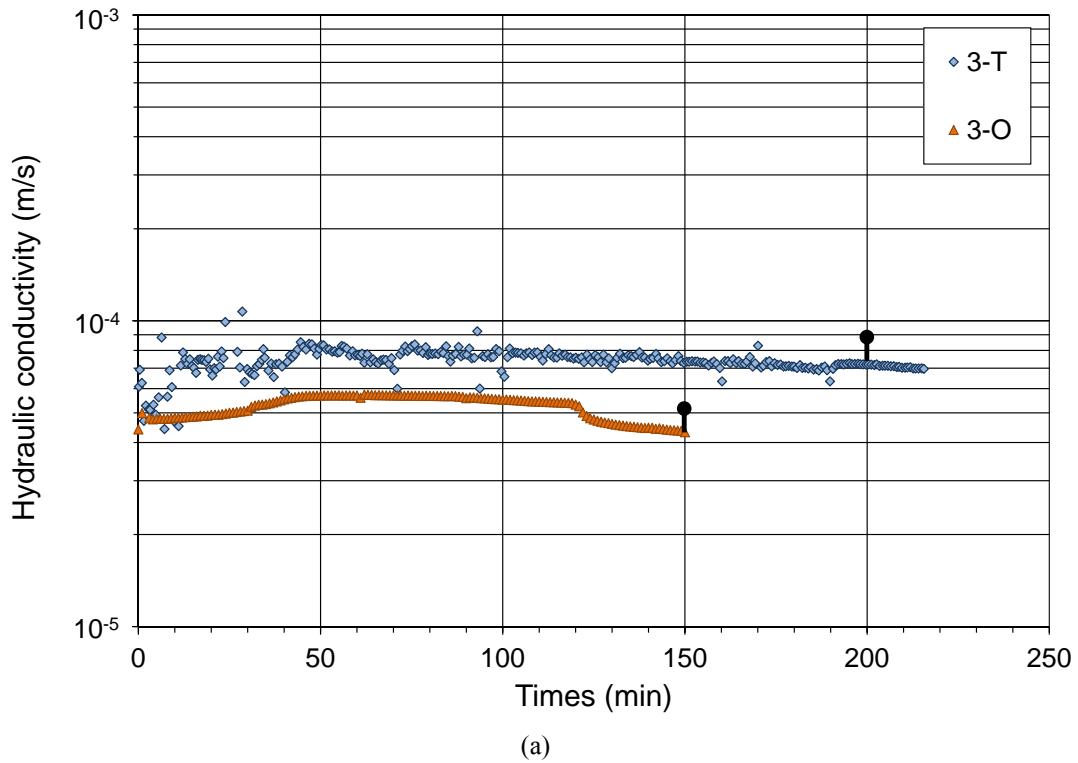
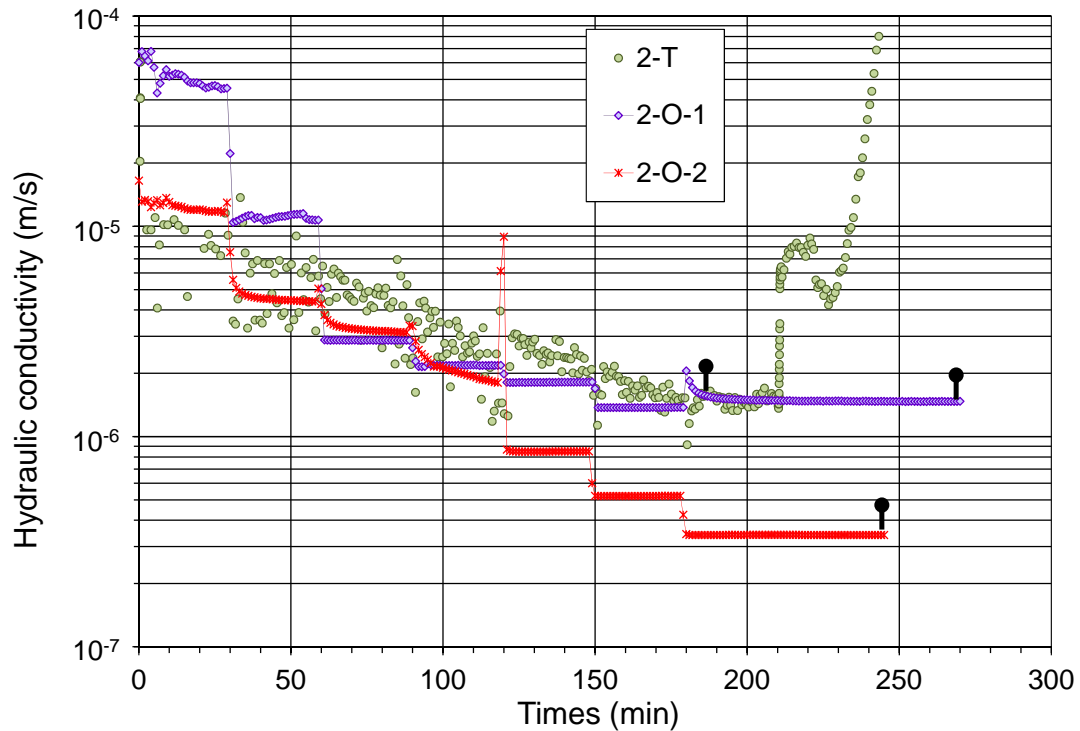


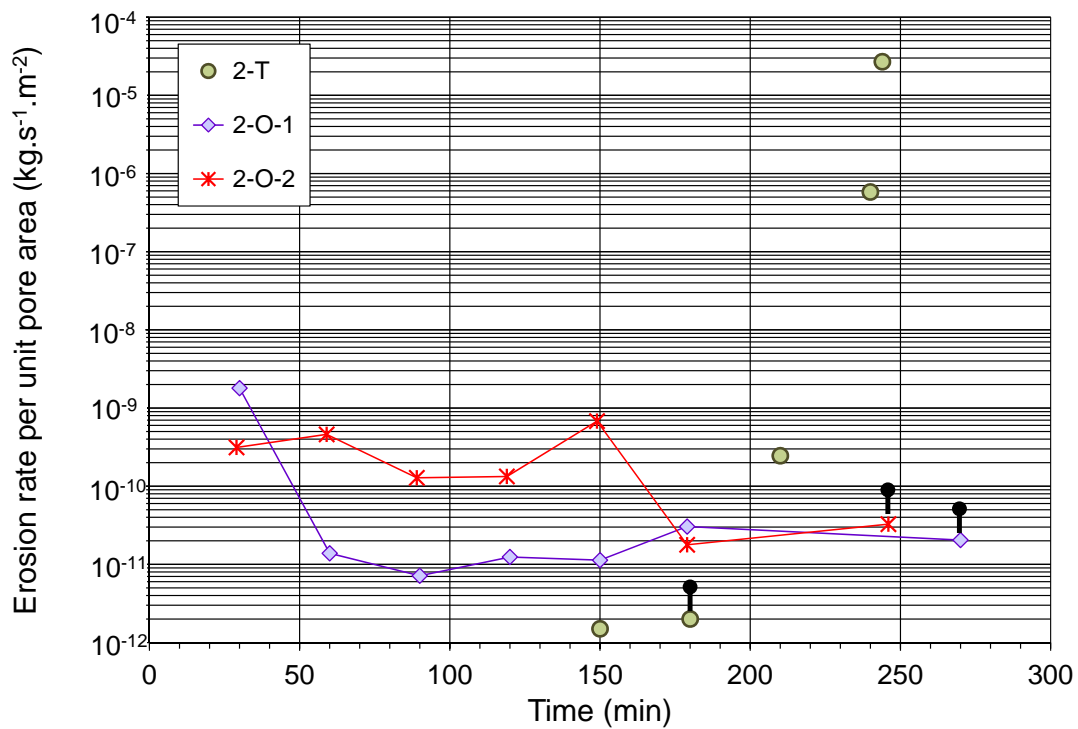
Figure V.6 – Time evolution of (a) the hydraulic conductivity; and (b) the erosion rate per unit pore area for soil 3

For tests on soil 3, Figure V.6(a) and Figure V.6(b) show the time evolution of the hydraulic conductivity and the time evolution of the erosion rate per unit pore area, respectively. The results in these figures are rather scattered. It is worth noting that the imprecision regarding the hydraulic conductivity computation can be valued at $\pm 3.5 \times 10^{-6} \text{ m}\cdot\text{s}^{-1}$ and $\pm 0.8 \times 10^{-6} \text{ m}\cdot\text{s}^{-1}$ for tri-

axial erodimeter and oedo-permeameter, respectively. Similarly, the accuracy of the erosion rate measurement is estimated at $\pm 3 \times 10^{-11} \text{ kg} \cdot \text{s}^{-1} \cdot \text{m}^{-2}$. Thus, these discrepancies cannot be attributed to the imprecisions but rather to the complexity of the suffusion process. In the case of soil 3, as for soils 1, 4, 5 and 6, the hydraulic conductivity and the rate of erosion stay relatively constant during suffusion tests with both devices.



(a)



(b)

Figure V.7 – Time evolution of (a) the hydraulic conductivity; and (b) the erosion rate per unit pore area for soil 2

For soil 2, the hydraulic conductivity firstly decreases (see Figure V.7(a)). However, for test 2-T when the applied hydraulic gradient was increased from 3.8 to 5.8, the hydraulic conductivity sharply increased. This sudden hydraulic conductivity increase is accompanied by an increase of erosion rate (see Figure V.7(b)), and sand grains are detected in the effluent. In consequence, this erosion process can be named global backward erosion. During tests 2-O-1 and 2-O-2, a sudden increase in hydraulic conductivity could be also measured when the applied hydraulic gradient reached 11 and 13, respectively, yet this increase was immediately followed by a decrease. At the same time, the erosion rate stayed relatively constant and a settlement was detected (the final axial strain reached 1.48 % for test 2-O-1 and 8.52 % for test 2-O-2). It is worth stressing that the effective stress applied in oedo-permeameter tests was larger than that in triaxial erodimeter tests. Considering the weight of the piston and the specimen's weight, in tests performed with oedo-permeameter, the effective stress at the bottom of the specimen can reach 8.4 kPa, whereas, in test 2-T, the effective stress is about 2.5 kPa. Thus, a slight rise of the effective stress seems to avoid the onset of global backward erosion, and only clay suffusion is detected. This emphasis on the influence of the effective stress on suffusion development is in good agreement with the results obtained by Moffat and Fannin (Moffat and Fannin, 2006) who showed that a rise in the effective stress causes an increase in the soils' resistance to suffusion.

For each test, the simultaneous stabilization of the hydraulic conductivity and the rate of erosion is highlighted by a black spot (see Figure V.6(a), Figure V.6(b), Figure V.7(a) and Figure V.7(b)). The corresponding time is interpreted as at the end of the suffusion.

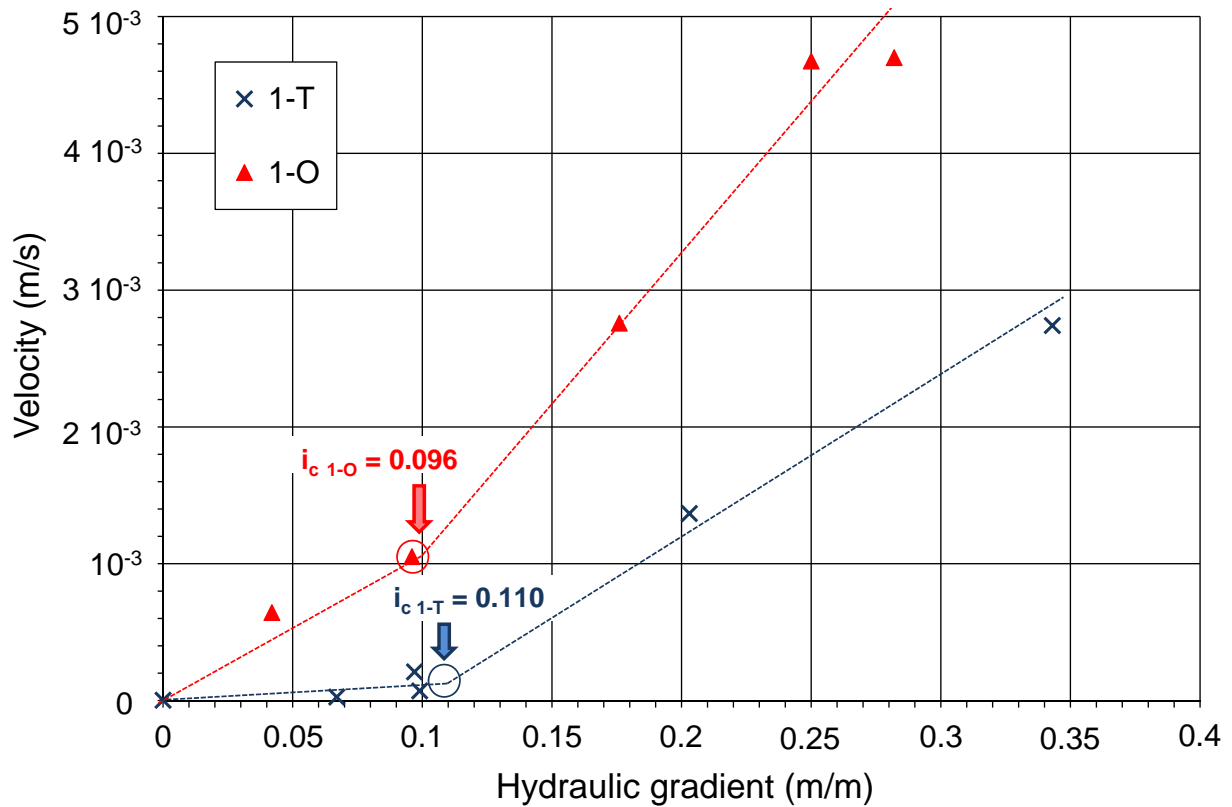
5.4 Discussion

5.4.1 Onset of suffusion

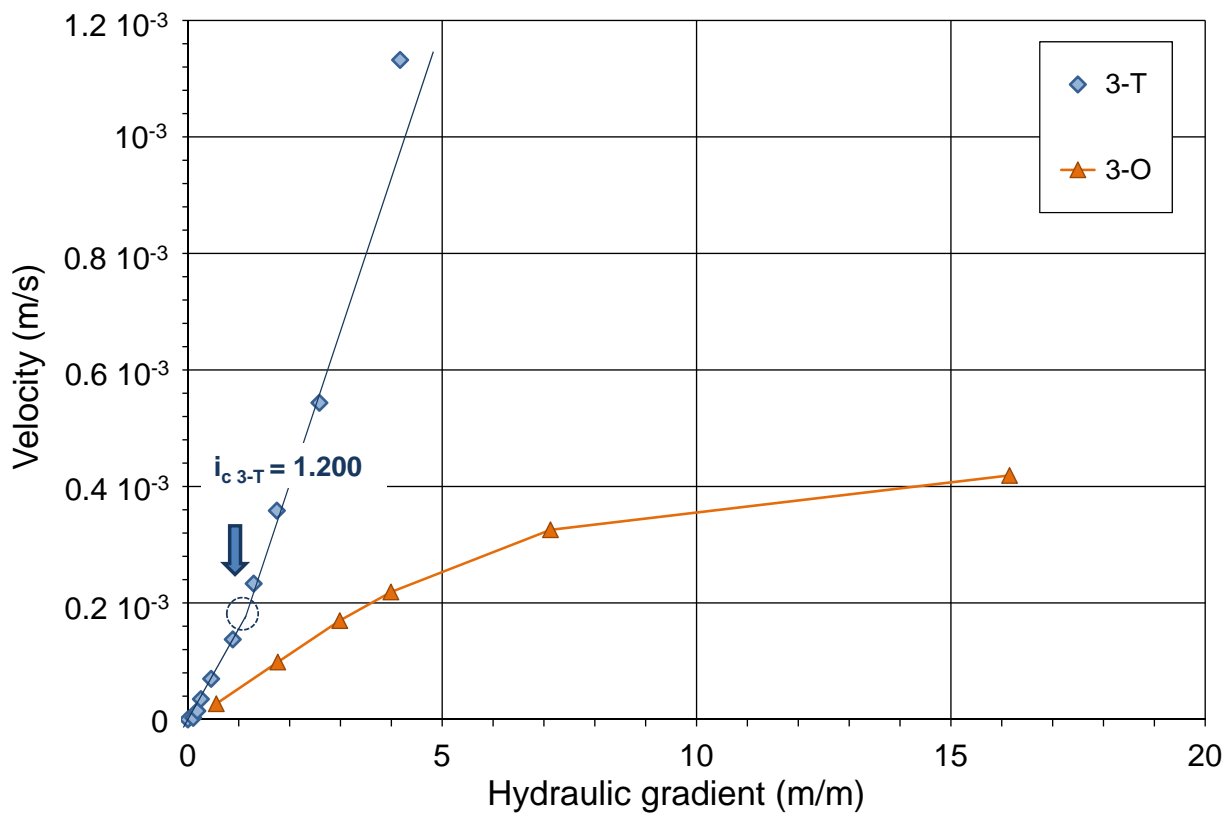
In literature, several studies restricted the suffusion characterization to the initiation of the process. Three methodologies are used in order to detect the suffusion onset: (i) the increase of hydraulic conductivity (Skempton and Brogan, 1994), (ii) the variations of local hydraulic gradient (Moffat and Fannin, 2006), or (iii) the increase of erosion rate (Chang and Zhang, 2013a). To date, those methodologies suffer from various limitations.

1. The first method of detecting the onset of suffusion is based on the variation of the hydraulic conductivity. The advantage of this method is related to spatial scale of the characterization as it is realized at specimen scale. The flow velocity versus the hydraulic gradient is plotted in Figure V.8(a) for tests on soil 1 and in Figure V.8(b) for tests on soil 3.
3. With the objective to determine with accuracy the onset of suffusion, the relative evolu-

tion of the hydraulic conductivity is computed, and the onset of suffusion is systematically defined by the first relative increase of 10 %.



(a)



(b)

Figure V.8 – Flow velocity versus hydraulic gradient, critical hydraulic gradients for (a) soil 1; and (b) soil 3

The corresponding value of the hydraulic gradient is determined by linear interpolation and selected as the critical hydraulic gradient (see Figure V.8(a)). As shown by test 3-O in Figure V.8(b), the determination of the critical hydraulic gradient with this systematic approach is not possible for all realized tests. When this approach can be used, the values of the critical hydraulic gradient are indicated in Table V.3. According to the writers, the pitfall of this method lies in the description of the hydraulic loading based on the hydraulic gradient. In fact, Figure V.9 shows that critical hydraulic gradient decreases with the specimen length, with a ratio between 1.15 (soil 1) and 1.73 (soil 4). It is worth noting that the specimen length corresponds to the seepage path in the case of a vertical seepage flow. This decrease of the critical hydraulic gradient with seepage length is in agreement with expressions of critical hydraulic gradient proposed by Li (Li, 2008) for the suffusion process and by Sellmeijer (Sellmeijer, 1988) for the backward erosion piping process. Moreover, thanks to a centrifuge bench, Marot et al. (Marot et al., 2012) showed that even under a controlled effective stress, the critical hydraulic gradient decreases with the length of the seepage path.

Table V.3 – Critical hydraulic gradient and erosion coefficient

Specimen reference in thesis	Critical hydraulic gradient i_c	Erosion coefficient ($10^{-5} \text{ s} \cdot \text{m}^{-1}$)
1-O	0.096	1.22
1-T	0.110	0.03
2-O-1	/	/
2-O-2	/	/
2-T	4.000	/
3-O	/	/
3-T	1.200	/
4-O	0.075	/
4-T	0.130	/
5-O	0.075	0.58
5-T-1	1.600	/
5-T-2	0.120	0.05
6-O-1	0.085	1.19
6-O-2	/	0.25
6-T-1	/	/

6-T-2

0.100

0.18

Notes: / = determination not possible for considered specimen.

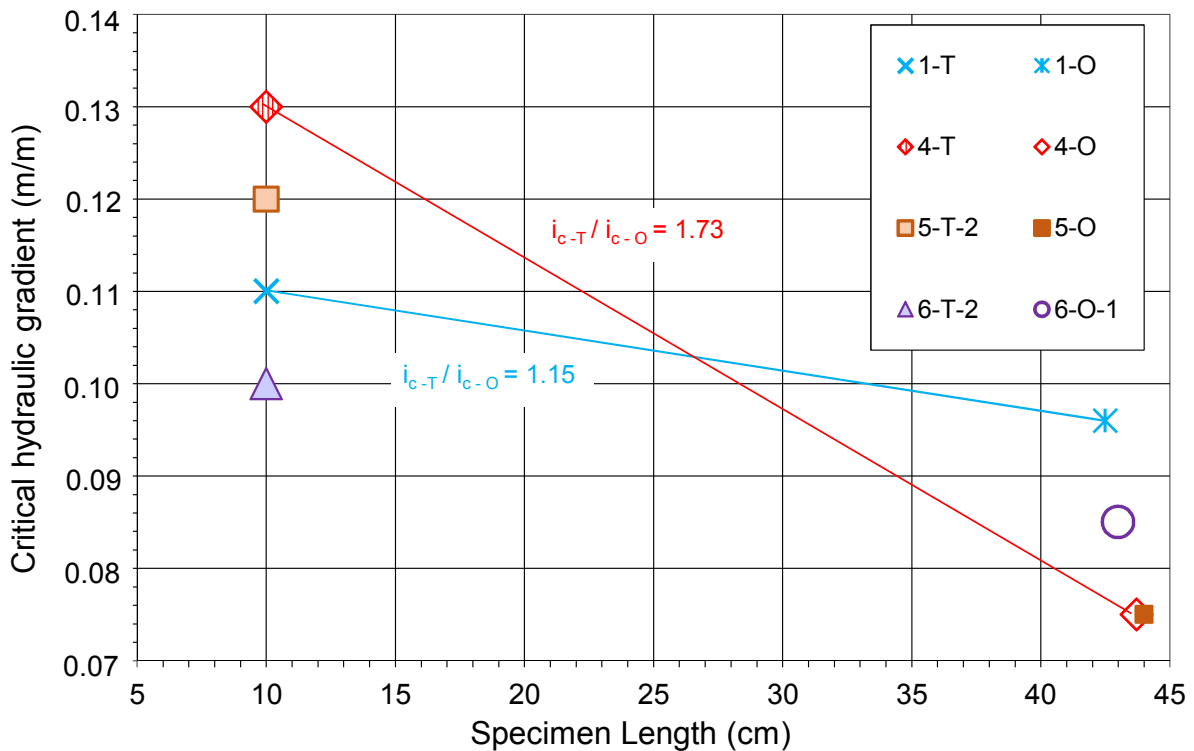


Figure V.9 – Critical hydraulic gradient versus specimen length

- Moffat and Fannin (Moffat and Fannin, 2006) assumed that the onset of large erosion of fine particles is governed by a significant drop of a hydraulic gradient that they named local hydraulic gradient. It is worth noting that the vertical spacing between ports for the measurement of this hydraulic gradient was 100 mm, which represents 500 times the diameter of the coarser grains of tested finer fraction. Sail et al. (Sail et al., 2011) showed that a significant drop of local hydraulic gradient can be preceded by a variation of local hydraulic head in another part of the specimen. These results indicate that the onset of suffusion does not concern the whole specimen but is a localized process and that its detection strongly depends on the position of the pressure sensors.
- Rochim et al. (Rochim et al., 2017) highlighted that according to the type of hydraulic loading (i.e. tests performed under hydraulic gradient controlled conditions or under flow rate controlled conditions), the predominant process can be either filtration or erosion. Moreover, under a multistage hydraulic gradient, these results show that the rate of erosion is influenced by the increment of the applied hydraulic gradient and the duration of each stage. Based on these results, it seems to be difficult to define the onset of suffusion by a threshold of erosion rate independently of the hydraulic loading history.

The interpretative method based on the critical hydraulic gradient assumes that the hydraulic gradient is independent of the considered spatial scale, and the soil is expected to remain homogenous all along the considered flow path. On the contrary, post-suffusion gradations (see Figure V.4(a) and Figure V.4(b)) show that the soil rapidly becomes heterogeneous, i.e., some grains are detached, others are blocked and a few are transported. In addition, it is worth noting that the spatial distribution of these mobilized grains is not homogenous all along the seepage path so that the head losses also are heterogeneous. Now if we consider the interstitial overpressure at the scale of several grains, which induces the suffusion onset, it represents the main component of the head losses along the considered flow path. The spacing between ports for hydraulic gradient measurement represents several hundred times the diameter of finer grains. So, these hydraulic gradients decreases with the considered length of the flow path. In other words, for a given local overpressure, the hydraulic gradient decreases with the length of flow path. Consequently, the value of critical hydraulic gradient determined by laboratory tests can be larger by several orders of magnitude than any value predicted for the real scale. It is worth stressing that this interpretative method based on the critical hydraulic gradient, which decreases with seepage path length, is completely opposite with the risk assessment.

5.4.2 Erosion coefficient

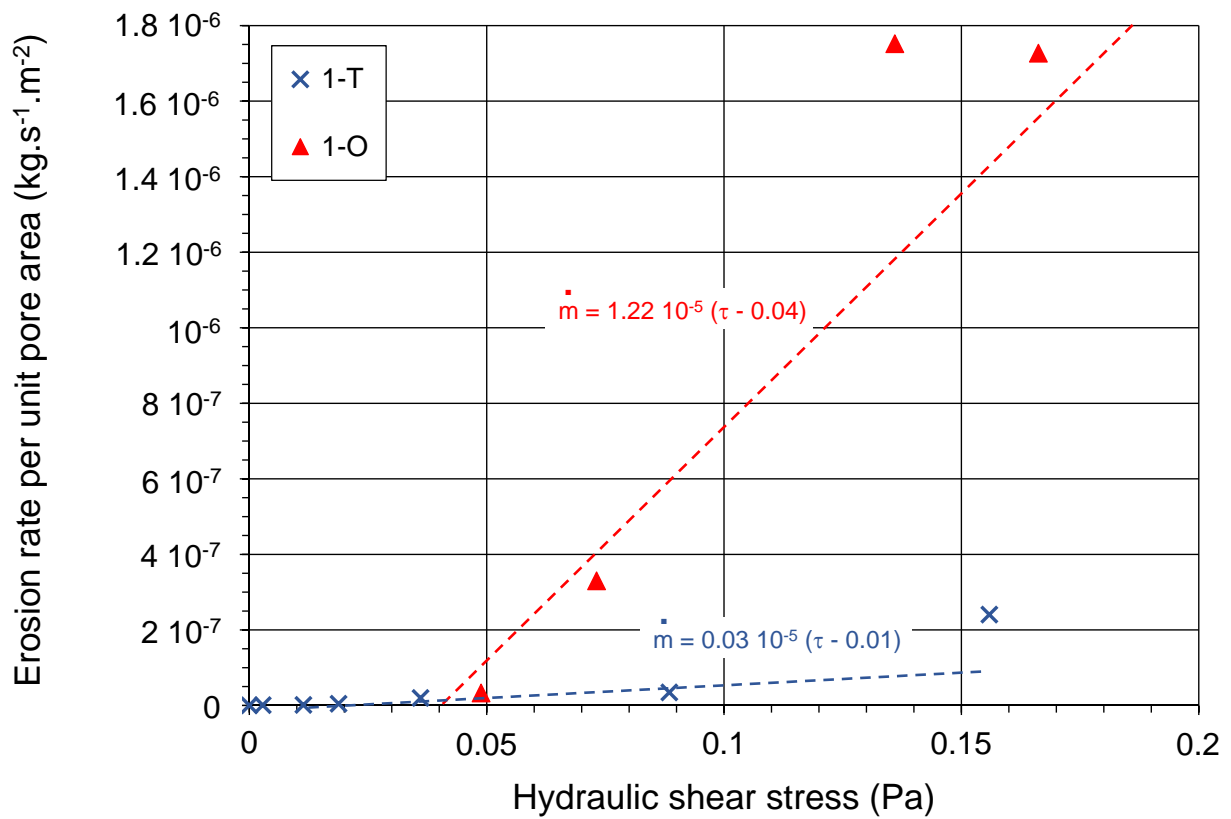
As described in Chapter II, according to the concept of system of parallel capillary tubes to represent the porous medium (Reddi et al., 2000), the hydraulic shear stress is expressed by (Marot et al., 2016):

$$\tau = \frac{\Delta h}{\Delta z} \sqrt{\frac{2k\mu\gamma_w}{\phi}} \quad \text{V.5}$$

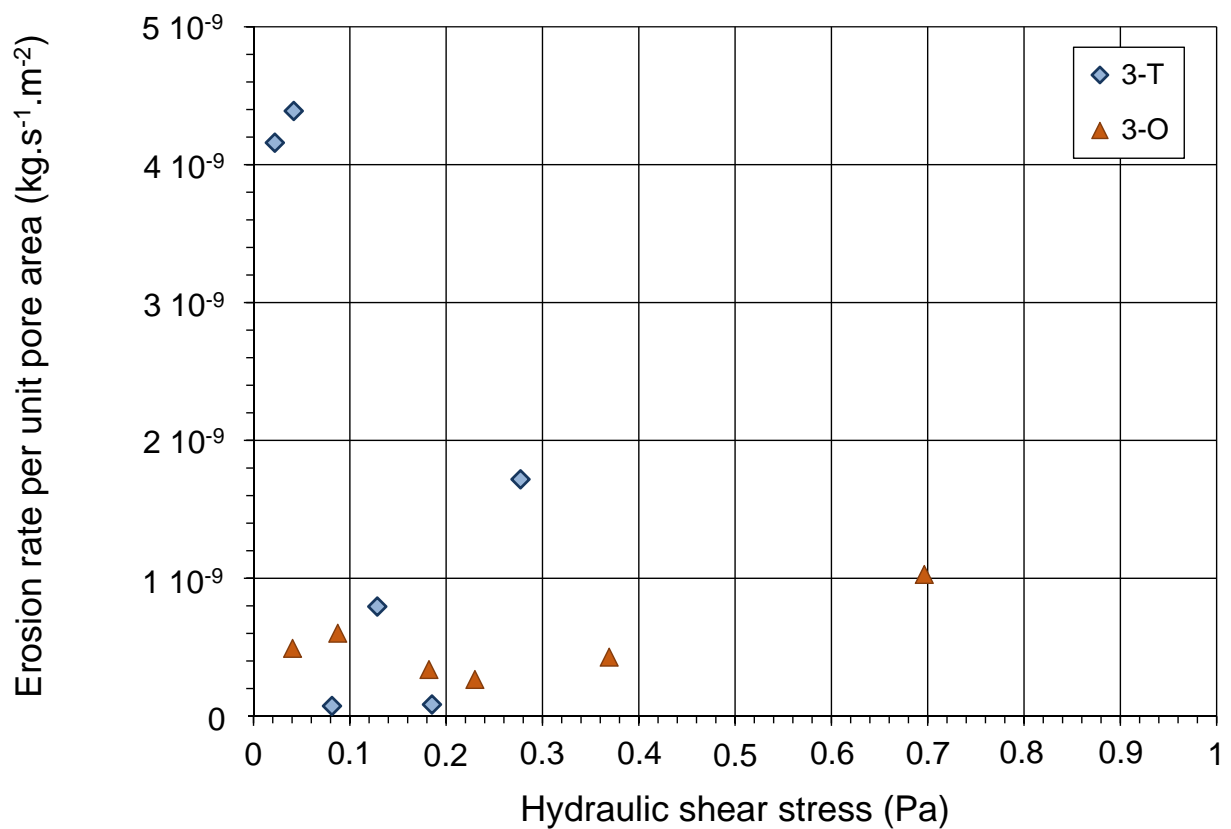
Where Δh is the drop of hydraulic head between an upstream section A and a downstream section B, $\Delta z = z_A - z_B$, z_A and z_B are altitudes of sections A and B, respectively, μ is the dynamic viscosity and ϕ is the porosity.

Figure V.10(a) and Figure V.10(b) show the erosion rate per unit pore area (Equation V.1) versus the hydraulic shear stress (Equation V.5) for soils 1 and 3, respectively. The suffusion development phase starts from the suffusion onset, which is defined thanks to the aforementioned identification based on hydraulic conductivity increase. The commonly used interpretative method for hole erosion tests (Wan and Fell, 2004) consists of describing the erosion rate from the linear excess shear stress equation, and the slope of this equation corresponds to the erosion coefficient. As shown by the test 3-T in Figure V.10(b), it is not possible to determine the erosion

coefficient for all suffusion tests. Table V.3 details the obtained values of erosion coefficient.



(a)



(b)

Figure V.10 – Erosion rate per unit pore area versus hydraulic shear stress for (a) soil 1; and (b) soil 3

It is worth noting that the values determined thanks to the oedo-permeameter tests are systematically larger than results obtained with the triaxial erodimeter. Thus the characterization of suffusion susceptibility based on this interpretative method depends on specimen size.

5.5 Method based on energy

As already mentioned in Chapter II, the power expended by the seepage flow P_{flow} and the erosion resistance index I_α are expressed as (Marot et al., 2016):

$$P_{flow} = Q\gamma_w\Delta h \quad \text{V.6}$$

Where Q is the fluid flow rate and Δh is the drop of hydraulic head.

And:

$$I_\alpha = -\log_{10} \frac{\text{total dry eroded mass}}{\text{total expended flow energy}} \quad \text{V.7}$$

Considering that the suffusion induces several heterogeneities by the combination of detachment, transport, and possible filtration of the finer fraction, P_{flow} is used to characterize the hydraulic load which produces these combined effects at the specimen spatial scale. Moreover, with the objective to take into account the history of hydraulic loading, the energy expended by the seepage flow E_{flow} is determined by the time integration of total flow power for the test duration. Rochim et al. (Rochim et al., 2017) showed that at the stabilization of both the hydraulic conductivity and the erosion rate (see Figure V.6(a), Figure V.6(b), Figure V.7(a) and Figure V.7(b)), the value of the erosion resistance index I_α can be determined with accuracy for different hydraulic loadings. In consequence, for characterizing the erosion susceptibility, the erosion resistance index is computed at this stabilization time.

Figure V.11 shows the cumulative expended loss dry mass versus the cumulative expended energy for all realized tests with both devices. Firstly, this figure shows that repeatability is fairly good, as the two representation points of tests 6-O-1 and 6-O-2 are very close. Moreover, it is worth noting that the value of the erosion resistance index can be determined with accuracy for the different specimen sizes (see Table V.4). The expended energy depends on the specimen size but also the eroded dry mass. Therefore, the erosion resistance index (i.e. which corresponds to the ratio of these two parameters) does not depend on the specimen size and the suffusion susceptibility classification is the same for both devices. I_α is between 2.89 and 2.94 for tests on soil 1 (i.e. this soil is erodible according to the suffusion susceptibility classification (Marot

et al., 2016)), between 4.22 and 4.48 for soil 2 (moderately resistant), between 4.64 and 4.73 for soil 3 (moderately resistant), between 3.06 and 3.26 for soil 4 (moderately erodible), between 3.36 and 3.92 for soil 5 (moderately erodible) and between 2.95 and 3.70 for soil 6 (erodible, moderately erodible).

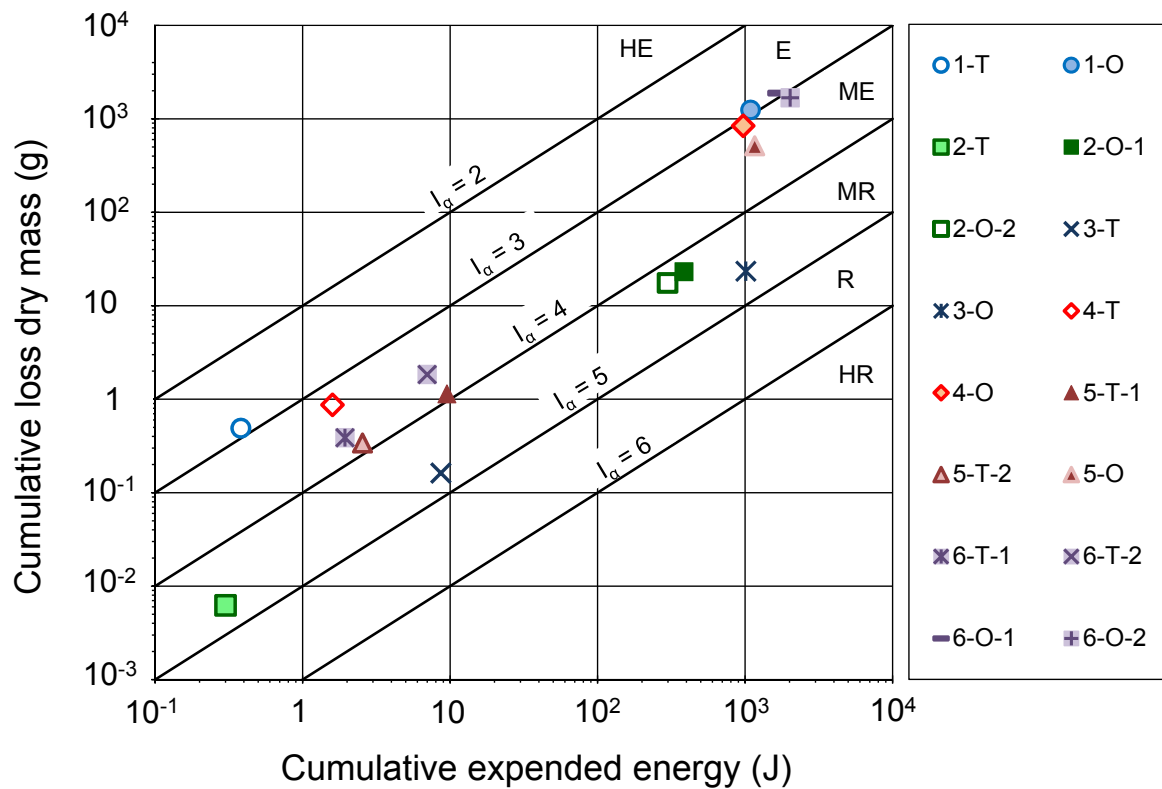


Figure V.11 – Cumulative loss mass versus cumulative expended energy

Table V.4 – Cumulative loss dry mass, cumulative expended energy, erosion resistance index and suffusion susceptibility classification

Specimen reference in thesis	Cumulative eroded mass (kg)	Cumulative expended energy (J)	Erosion resistance index	Suffusion susceptibility classification
1-O	1.2473	1087.9	2.94	E
1-T	0.00049	0.38	2.89	E
2-O-1	0.0231	385.2	4.22	MR
2-O-2	0.0176	298.14	4.23	MR
2-T	0.00001	0.3	4.48	MR
3-O	0.0234	1011.93	4.64	MR
3-T	0.00016	8.66	4.73	MR
4-O	0.8434	971.35	3.06	ME
4-T	0.00087	1.59	3.26	ME

5-O	0.5138	1167.67	3.36	ME
5-T-1	0.00114	9.52	3.92	ME
5-T-2	0.00034	2.55	3.88	ME
6-O-1	1.8778	1666.8	2.95	E
6-O-2	1.6787	2020.55	3.08	ME
6-T-1	0.00039	1.94	3.7	ME
6-T-2	0.00184	7	3.59	ME

Note: MR = Moderately Resistant; ME = Moderately Erodible; E = Erodible.

Finally, it can be observed that for soils 1, 5, and 6, all the grain size distribution criteria used give an indication of internal instability and the suffusion susceptibility classification is erodible or moderately erodible. Whereas for soils 2, 3, and 4, the conclusions of the criteria based on the geometric assessment are opposite, and the suffusion susceptibility classification permits distinction of the tested soils, from moderately erodible (soil 4) to moderately resistant (soils 2 and 3).

5.6 Conclusion

In this study, a series of suffusion tests was carried out on two different sized devices to assess the suffusion susceptibility of six gradations. The tests with triaxial erodimeter were performed by Le Van Thao. Sixteen specimens including widely graded, gap-graded, clayey, and cohesionless soils were tested involving seepage flow in a downward direction under multistage hydraulic gradient condition.

Firstly, a loss of particles was observed during the saturation phase even under upward flow. Thus, for limiting the discrepancy of the initial hydraulic conductivity, a systematic saturation approach, adopting the same velocity of the wetting front was applied to both devices.

Post-suffusion gradations and size distribution of eroded particles highlight the complexity of suffusion, which appears as the combination of detachment-filtration-transport processes. Due to this coupling between erosion and filtration, the time evolutions of hydraulic conductivity and rate of erosion can be complex.

The method to identify critical hydraulic gradient based on the increase of hydraulic conductivity cannot be used for all specimens. Moreover, the values of the critical hydraulic gradient decrease with the length of the seepage path. The interpretative method can also consist of describing the erosion rate by using the excess shear stress equation. However, in the case of suffusion, the

erosion coefficient increases with specimen size.

The method based on energy is applied to study the suffusion susceptibility of tested specimens. The energy expended by the water seepage and the cumulative loss dry mass are both computed until the simultaneous invariability of the hydraulic conductivity and the erosion rate. At this time, the erosion sensibility classification can be evaluated by the value of the erosion resistance index, which is in the same range for both used devices.

Finally, for the clayey soil tested, under low effective stress, suffusion development can induce backward erosion. Further studies are required to confirm this result for other soils.

Due to the spatial scale effects, the result from a small device is also different with the real scale in the triaxial condition for the mechanical tests. In order to study the mechanical effects of the suffusion, we need a big triaxial device to close the real engineering condition. Therefore, the contribution to the development of a new triaxial device is introduced in the Appendix A.

NUMERICAL MODELING OF THE INTERNAL EROSION

6.1 Introduction

Internal erosion is a significant issue in civil and environmental engineering impacting the safety of dams and dikes. Statistical analyses of accidents in embankment dams indicate that the two main causes (Fell and Fry, 2007; Foster et al., 2000; Fry et al., 2012) of failure are internal erosion and overtopping. Meanwhile, recent studies indicate that internal erosion is also an important issue in underground structures, such as land subsidence due to water piping induced erosion (Shen and Xu, 2011), lateral displacement induced by erosion during jet grouting (Shen et al., 2017), surface settlement induced by erosion because of tunnel leakage (Wu et al., 2017), and landslides or slope instability induced by fines migration under heavy rainfall condition (Hu et al., 2018; Lei et al., 2017). Four forms of internal erosion have been distinguished (Bonelli and Marot, 2008; Fell and Fry, 2007; Fell et al., 2003; Wan and Fell, 2004): concentrated leak erosion, backward erosion, contact erosion and suffusion. Among them, suffusion is a complex phenomenon appearing as a combination of detachment and transport of the finer particles driven by water flow. As a result, the particle size distribution, the porosity, and the hydraulic conductivity of the soil are changed. The mechanical properties of the soil are, therefore, progressively degraded with time, which causes the hydraulic earth structures to face a considerable risk of failure (Chang and Yin, 2011; Yin et al., 2014, 2016). Thus, to ensure the safety assessment of earth structures, suffusion has been widely studied by laboratory testing over the last few decades, focusing on the effect of soil grading, critical hydraulic gradient, critical pore water velocity, with the purpose of characterizing the susceptibility of soils to suffusion (Bendahmane et al., 2006, 2008; Chang and Zhang, 2011; Ke and Takahashi,

2014; Kenney and Lau, 1985; Marot et al., 2016; Moffat et al., 2011; Reddi et al., 2000; Rochim et al., 2017; Sherard et al., 1984; Skempton and Brogan, 1994; Sterpi, 2003). Several criteria have been proposed to evaluate the internal stability of gap-graded or broadly graded granular materials (Chang and Zhang, 2013b; Indraratna et al., 2015; Kenney and Lau, 1985; Wan and Fell, 2008). Extensive theoretical works have also been performed to study the fines migration in the applications of petroleum engineering (Papamichos et al., 2001; Vardoulakis et al., 1996; Wennberg et al., 1995).

Based on these experimental findings, many constitutive models have been proposed under the framework of the porous continuous medium theory to enhance the design of hydraulic earth structures (Bear and Bachmat, 2012; Cividini and Gioda, 2004; Fujisawa et al., 2010; Schaufler et al., 2013; Vardoulakis et al., 1996; Wong et al., 2013). Most of these models can describe the detachment and transport of finer soil particles within the solid matrix induced by erosion (Bendahmane et al., 2006, 2008; Chang and Zhang, 2011; Fujisawa et al., 2010; Marot et al., 2016; Moffat et al., 2011; Reddi et al., 2000; Sterpi, 2003).

More recently, the discrete approach has been applied in the studies of fines migration (Lominé et al., 2013; Reboul, 2008; Sari et al., 2011; Scholtès et al., 2010; Sibille et al., 2015; Zhao and Shan, 2013). For instance, Zou (Zou et al., 2013) applied the coupled discrete element method and computational fluid dynamics technique to simulate the transient transport of eroded base soil particles. Wang (Wang et al., 2017) applied the Boltzmann method of the coupled bonded particle and lattice to investigate the erosion process of soil particles. The microscopic migration of soil particles can be clearly visualized. The discrete methods can represent fairly well the microstructure and describe better the physical mechanisms within granular materials. However, they are still restricted to the problem with a limited number of particles which is far from real engineering structures. The continuous approach is thus strongly recommended for solving boundary value problems.

Therefore, the research attempts to formulate a new numerical approach considering the process of suffusion under the framework of the porous continuous medium theory. Firstly, four-constituent based on the mass exchange formulations are proposed to describe the detachment of finer particles and the transport in soil pores. The coupled formulations are solved numerically by a finite difference method. Then, the model is validated by simulating 1D internal erosion tests by demonstrating that it can reproduce the main features of soil particles during the suffusion process.

For the simulation of seepage velocity and erosion mass, the Darcy's law and erosion laws used in this chapter come from the literature. The purpose of this chapter is to verify the possibility

of simulating the suffusion process and the simulation of erosion quality in experiments.

6.2 Model formulations

6.2.1 Mass exchange and mass balance equations

According to Schaufler et al. (Schaufler et al., 2013), it is possible to consider the saturated porous medium as a material system composed of four constituents: the stable fabric of the solid skeleton (ss), the erodible fines (se), the fluidized particles (fp) and the pure fluid phase (ff), as shown in Figure VI.1. The fines can behave either as a fluid (described as fluidized particles) or as a solid material (described as erodible fines). Thus, a liquid-solid phase transition process has been accounted by the introduction of a mass and volume production term into the corresponding mass and volume balances in the present model for erodible fines (se) and fluidized particles (fp).

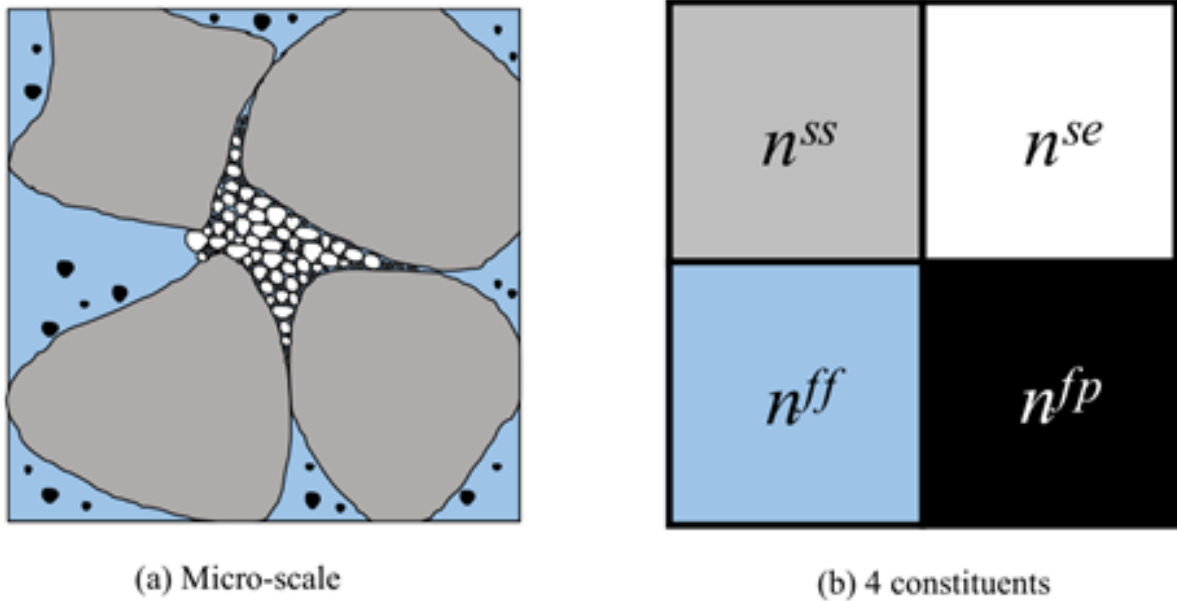


Figure VI.1 – REV of a fully saturated soil mixture and the four-constituent continuum model

In a given representative elementary volume (REV), dV is constituted by the four constituents and the volume fraction of a single constituent i is expressed as follows:

$$n^i(x, t) = \frac{dV^i(x, t)}{dV} \quad \text{VI.1}$$

Where $i = \{ss, se, ff, fp\}$ denotes the four constituents and V^i is the volume of the corresponding constituent.

At a material point level, the mass balance for the i phase is given, neglecting the hydro-

mechanical dispersion tensor, by Schaufler (Schaufler et al., 2013):

$$\frac{\partial(\rho^i)}{\partial t} + \text{div}(\rho^i \mathbf{v}^i) = \rho^{ex,i} \quad \text{VI.2}$$

Where $\rho^{ex,i}$ and \mathbf{v}^i denote, respectively, the mass exchange term and the velocity of the corresponding constituent. The partial density ρ^i is defined as the ratio between the mass dm^i of the constituent i with respect to the total volume dV of the REV, leading to a relation between partial density ρ^i and effective density ρ^{iR} , which corresponds to the bulk density of the corresponding constituents:

$$\rho^i = \frac{dm^i}{dV} = \frac{dm^i}{dV^i} \frac{dV^i}{dV} = \rho^{iR} n^i \quad \text{VI.3}$$

The mass balance for the four constituents are then reduced to the corresponding volume fraction balance:

$$\frac{\partial(n^i)}{\partial t} + \text{div}(n^i \mathbf{v}^i) = n^{ex,i} \quad \text{VI.4}$$

Where $n^{ex,i}$ is the term of the volume of mass exchange to be discussed in the following section.

Moreover, it is assumed that fluid and fluidized particles have the same velocity at any time and at all given points. The solid skeleton is assumed to be deformable but non-erodible. The porosity field $\phi(x, t)$, the amount of erodible fines $f_c(x, t)$ and the concentration of the fluidized particles $c(x, t)$ are defined as follows:

$$\phi = \frac{dV_v}{dV} = \frac{dV^{ff} + dV^{fp}}{dV} = n^{ff} + n^{fp} \quad \text{VI.5}$$

$$f_c = \frac{n^{se}}{n^{ss} + n^{se}} = \frac{n^{se}}{1 - \phi} \quad \text{VI.6}$$

$$c = \frac{n^{fp}}{n^{ff} + n^{fp}} = \frac{n^{fp}}{\phi} \quad \text{VI.7}$$

The phase transition of the fine particles from solid to fluidized particles leads to:

$$-n^{ex,fp} = n^{ex,se} = \hat{n}, \quad n^{ex,ss} = 0, \quad n^{ex,ff} = 0 \quad \text{VI.8}$$

The mass balance equations are then given by the following expressions:

$$-\frac{\partial \phi}{\partial t} + \text{div}(\mathbf{v}_s) - \text{div}(\phi \mathbf{v}_s) = \hat{n} \quad \text{VI.9}$$

$$\frac{\partial(f_c)}{\partial t} - \frac{\partial(f_c \phi)}{\partial t} + \text{div}(f_c \mathbf{v}_s) - \text{div}(f_c \phi \mathbf{v}_s) = \hat{n} \quad \text{VI.10}$$

$$\frac{\partial(c\phi)}{\partial t} + \text{div}(c\mathbf{q}_w) + \frac{\partial(c\phi \mathbf{v}_s)}{\partial t} = -\hat{n} \quad \text{VI.11}$$

$$\text{div}(\mathbf{q}_w) = \text{div}(\mathbf{v}_s) \quad \text{VI.12}$$

Where \mathbf{q}_w denotes the volume discharge rate (the volume of flow through the unit cross-sectional area in unit time):

$$\mathbf{q}_w = \phi(\mathbf{v}_f - \mathbf{v}_s) \quad \text{VI.13}$$

$$\mathbf{v}_s = \frac{\partial \mathbf{u}(x, t)}{\partial t} \quad \text{VI.14}$$

Where $\mathbf{u}(x, t)$ indicates the displacement field of the soil skeleton. The strain ϵ_{ij} and volumetric strain ϵ_v are then given by the following expressions under small strain assumption:

$$\epsilon_{ij} = \frac{1}{2}(u_{i,j} + u_{j,i}) \quad \text{VI.15}$$

$$\frac{\partial(\epsilon_v)}{\partial t} = -\text{div}(\mathbf{v}_s) \quad \text{VI.16}$$

This study focuses on the internal erosion process, in which only elastic model is used to calculate the displacement field according to the change of effective stress due to the pore pressure evolution. The selected experimental tests used to compare with the simulation are also only under hydraulic loadings for this purpose.

Note that the irreversible coupling between mechanics and hydraulics has already been considered implicitly by introducing the volume deformation in the mass balance Equations VI.9 - VI.12, the mechanical coupling can be easily implemented if the elastic model is replaced by

elastoplastic models. For the cases with external mechanical loadings, the strength degradation induced by the evolution of the porosity and the fines may then be captured which will be discussed in future studies.

Equation VI.9 describes the behavior of the solid phase (solid skeleton and erodible fines). Equation VI.10 represents the balance of volume of the erodible fines, whereas Equation VI.11 is the balance of volume of the fluidized particles. The balance of the mass of the mixture, i.e., the continuity equation, is given by Equation VI.12.

Note that the amount of erodible fines f_c can be obtained explicitly from the current porosity ϕ and the volumetric strain ϵ_v , which indicates that Equation VI.10 can be replaced by:

$$f_c = 1 - \frac{(1 + \epsilon_v)(1 - (\phi_0)(1 - f_{c0}))}{1 - \phi} \quad \text{VI.17}$$

Where $\phi_0(x)$ and $f_{c0}(x)$ denote the initial value of $\phi(x, t)$ and $f_c(x, t)$, respectively.

6.2.2 Constitutive equation for seepage erosion

Three types of the constitutive equations for the eroded particles are adopted in this chapter.

Erosion law 1 (model 1)

The \hat{n} is a mass generation term, it represents the rate at which the soil skeleton phase can be transformed into movable fine grained phase at any time. Its value is the difference between the erosion of soil skeleton and the quality of sediment per unit time. The constitutive equation of the rate of the eroded mass, suggesting that erosion is mainly driven by the discharge of the fluidized particles, is given by the following relation (Vardoulakis et al., 1996):

$$\hat{n} = \lambda_e(1 - \phi)c|\mathbf{q}_w| \quad \text{VI.18}$$

Where the coefficient λ_e is in inverse proportion to the seepage length. c is the concentration of fluidized fine particles. $|\mathbf{q}_w|$ is the norm of fluid velocity. ϕ is the porosity.

Erosion law 2 (model 2)

The eroded mass exchange is related to fine content rate.

$$\hat{n} = (1 - \phi) \frac{D^s f_c}{Dt} \quad \text{VI.19}$$

Fine content rate dependent on Darcy's flow velocity and the ultimate fine content (Cividini et al., 2009; Sterpi, 2003).

$$\frac{D^s f_c}{Dt} = -\lambda_e (f_c - f_{c\infty}) |\mathbf{q}_w| \quad \text{VI.20}$$

A model for the rate of the eroded mass is given by the relation (Uzuoka et al., 2012).

$$\hat{n} = -\lambda_e (1 - \phi) (f_c - f_{c\infty}) |\mathbf{q}_w| \quad \text{VI.21}$$

Where $f_{c\infty}$ is the ultimate fine content fraction after a long seepage period, ϕ is the porosity, λ_e is a material parameter, $|\mathbf{q}_w|$ is the norm of fluid velocity. The ultimate fine content fraction $f_{c\infty}$ is assumed to be decreasing with the increase of the hydraulic gradient, shown as below (Cividini et al., 2009):

$$f_{c\infty} = f_{c0} [(1 - \beta_1) \exp(-|\mathbf{q}_w| \times 10^{\beta_2}) + \beta_1] \quad \text{VI.22}$$

Where f_{c0} is the initial fine content fraction, β_1 and β_2 are material parameters. The term $(f_c - f_{c\infty})$ in Equation VI.21 corresponds to the residual erodible fine content fraction. The erosion rate depends not only on the flow velocity of liquid \mathbf{q}_w but also on the residual erodible fine content fraction as shown by Equation VI.21.

Erosion law 3 (model 3)

Another form of the erosion law as described in Chapter II, the driving force of the erosion caused by the seepage in the soil is the shear stress τ , which is generated by the action of the pore fluid flowing in the solid skeleton of the soil. As described in Chapter II, according to the concept of the parallel capillary tubes system to represent the porous medium, the hydraulic shear stress is expressed by Reddi et al. (Reddi et al., 2000):

$$\hat{n} = k_d (\tau - \tau_c) \quad \text{VI.23}$$

Where k_d is the erosion rate coefficient and τ_c is the material constant.

The eroded mass exchange rate is related to the hydraulic shear stress. And τ_c means the minimum hydraulic shear stress to trigger off the suffusion process, which reflects the stability of

the soil to suffusion. The hydraulic shear stress τ is expressed as follow:

$$\tau = \frac{\Delta h}{\Delta z} \sqrt{\frac{2k\mu\gamma_w}{\phi}} \quad \text{VI.24}$$

Where Δh is the drop of hydraulic head between an upstream section A and a downstream section B , $\Delta z = z_A - z_B$, z_A and z_B are altitudes of sections A and B , respectively, μ is the dynamic viscosity of the fluid (unit: Pa·s), ϕ is the porosity and k means the hydraulic conductivity.

6.2.3 One dimensional suffusion process

This chapter focuses on one dimensional suffusion problems along the axial direction, which are chosen to be perpendicular to the free surface and pointing downward to the interior of a specific finite domain (see Figure VI.2. The flow in the porous medium is governed by 1D Darcy's law which states that the flow rate is driven by the gradient of the pore fluid pressure:

$$q_w = -\frac{K(\phi)}{\mu\bar{\rho}(c)} \frac{\partial(p_w)}{\partial x} \quad \text{VI.25}$$

Where K denotes the intrinsic permeability of the medium (unit: m^2), μ is the dynamic viscosity of the fluid, p_w is the pore fluid pressure, and $\bar{\rho}(c)$ is the density of the mixture defined as:

$$\bar{\rho}(c) = c\rho_s + (1 - c)\rho_f \quad \text{VI.26}$$

Where ρ_s is the density of the solid and ρ_f is the density of the fluid. For a mixture, the intrinsic permeability of the porous medium K depends on the current porosity ϕ via the Kozeny-Carman relationship:

$$K = K_0 \frac{\phi^{k_1}}{(1 - \phi)^{k_2}} \left(\frac{\phi_0^{k_1}}{(1 - \phi_0)^{k_2}} \right)^{-1} \quad \text{VI.27}$$

Where k_1 and k_2 are permeability parameters. ϕ_0 is the initial porosity, K_0 is the value of K at the initial state $\phi = \phi_0$.

Therefore, by combining Equations VI.9 - VI.27, the governing equations for the pore pressure $p_w(x, t)$, the porosity $\phi(x, t)$ and the concentration of fluidized particles $c(x, t)$ can be expressed as followed under one dimensional condition:

$$\frac{\partial(p_w)}{\partial t} - \frac{EK}{\mu\bar{\rho}(c)} \frac{\partial^2(p_w)}{\partial x^2} = 0 \quad \text{VI.28}$$

$$\frac{\partial \phi}{\partial t} + \frac{\partial u}{\partial t} \frac{\partial \phi}{\partial x} - \frac{\partial \epsilon_v}{\partial t} \phi + \frac{\partial \epsilon_v}{\partial t} - \lambda_e (1 - \phi) (f_c - f_{c\infty}) |q_w| = 0 \quad \text{VI.29}$$

$$\frac{\partial c}{\partial t} + \left(\frac{q_w}{\phi} + \frac{\partial u}{\partial t} \right) \frac{\partial c}{\partial x} + \frac{1}{\phi} \left[\frac{\partial \phi}{\partial t} + \text{div}(q_w) + \frac{\partial \phi}{\partial x} \frac{\partial u}{\partial t} - \phi \frac{\partial \epsilon_v}{\partial t} \right] c - \frac{1}{\phi} \lambda_e (1 - \phi) (f_c - f_{c\infty}) |q_w| = 0 \quad \text{VI.30}$$

The coupled non-linear problem is supplemented by the following boundary and initial conditions:

$$p_w(x_0, t) = p_0, \quad p_w(x_L, t) = p_L, \quad c(x_0, t) = c_0, \quad \frac{\partial c(x_L, t)}{\partial t} = 0 \quad \text{VI.31}$$

$$p_w(x, 0) = 0, \quad c(x, 0) = 0, \quad \phi(x, 0) = \phi_0(x), \quad f_c(x, 0) = f_{c0}(x) \quad \text{VI.32}$$

The initial porosity and fine content depend on the homogeneity of the soil, which can vary along the space.

6.3 Finite difference based numerical solution

Equations VI.28 - VI.30 make up an unsteady, coupled non-linear system of partial differential equations. The current state of the system depends on its previous state. The primary unknowns are the pore pressure $p_w(x, t)$, the porosity $\phi(x, t)$, and the particles concentration in the seepage $c(x, t)$. Other unknowns such as the displacement $u(x, t)$, the attached fine content $f_c(x, t)$ and the flow rate $q_w(x, t)$ can be determined explicitly from Equation VI.15, Equation VI.17 and Equation VI.25.

This system of partially differential equations has been solved through an explicit finite difference procedure. Based on Figure VI.2, Equations VI.28 - VI.30 become:

$$\frac{p_w^j{}^{k+1} - p_w^j{}^k}{\Delta t} - \frac{[A_{p_w}]_{j+\frac{1}{2}}^k (p_w^{j+1}{}^{k+1} - p_w^j{}^{k+1}) + [A_{p_w}]_{j-\frac{1}{2}}^k (p_w^j{}^{k+1} - p_w^{j-1}{}^{k+1})}{(\Delta x)^2} = 0 \quad \text{VI.33}$$

$$\frac{\phi_j^{k+1} - \phi_j^k}{\Delta t} + [A_\phi]_j^k \frac{\phi_j^{k+1} - \phi_{j-1}^{k+1}}{\Delta x} + [B_\phi]_j^k \phi_j^k + [C_\phi]_j^k = 0 \quad \text{VI.34}$$

$$\frac{c_j^{k+1} - c_j^k}{\Delta t} + [A_c]_j^k \frac{c_j^{k+1} - c_{j-1}^{k+1}}{\Delta x} + [B_c]_j^k c_j^k + [C_c]_j^k = 0 \quad \text{VI.35}$$

Where the subscripts $j(0, 1 \dots, N)$ represent the variation in the length, described by the x coordinate, and the subscripts $k(0, 1 \dots, M)$ represent the variation of the time t coordinate. $K(f_c, \phi)$, $\bar{\rho}(c)$ and $q_w(x, t)$ vary with depth and time. As a simple approximation, their values at (j, k) are used. A , B and C are equation coefficients given in the appendix B.

Equations VI.33 - VI.35 can then be solved with initial and boundary conditions for $p_w(x, t)$, $\phi(x, t)$, and $c(x, t)$ given in Equations VI.31 - VI.32. The model has been coded with MATLAB software (Guide, 1998). For accuracy and running efficiency, the sensitivity of the results to space and time increments was examined. The computations of the following sections were carried out with 100 nodes and 3000 increments in time.

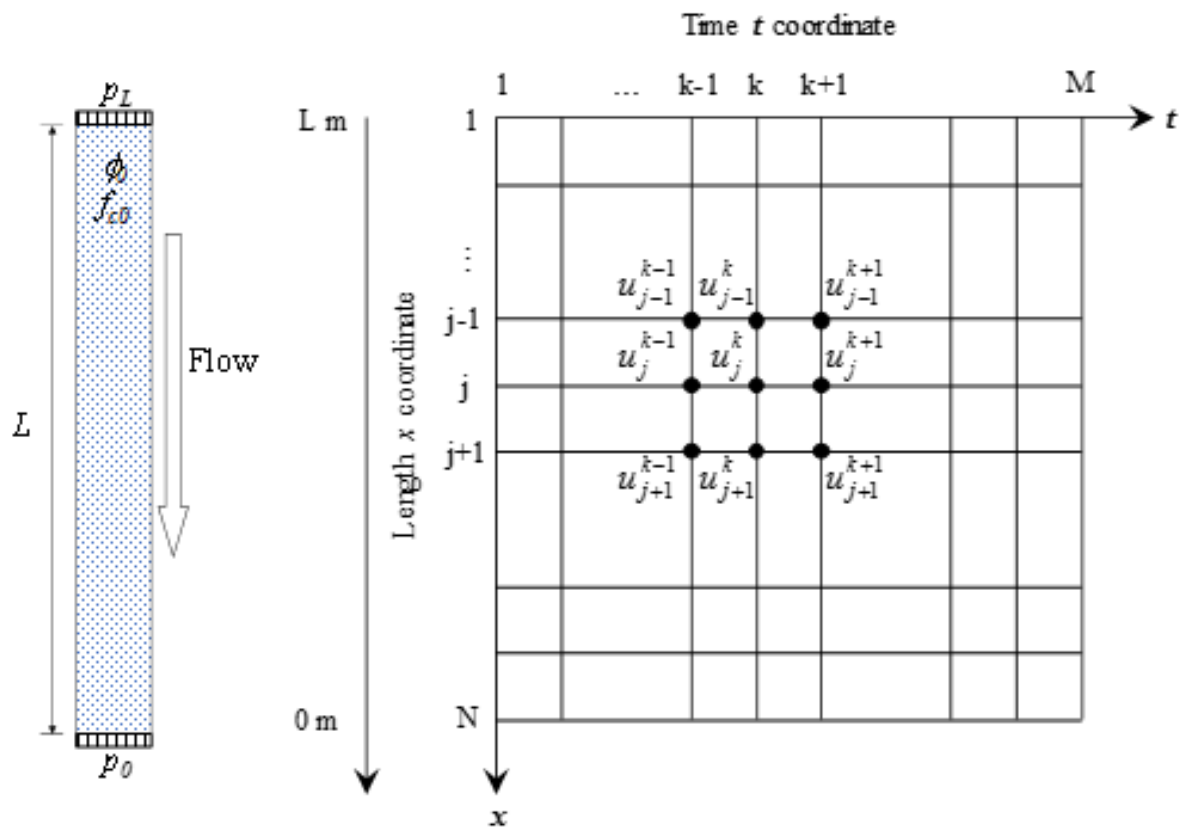


Figure VI.2 – Geometry and finite difference grid in space-time of analyzed 1D internal erosion

6.4 Numeric simulations of laboratory tests

6.4.1 Analysis of parameters affecting simulation results

The main purpose of this part is to investigate the effect of model node, specimen length, initial permeability, and fine content on the numeric results. Model 1 and specimen 1-O described in Chapter V were selected for investigating the effect of each parameter.

The model node

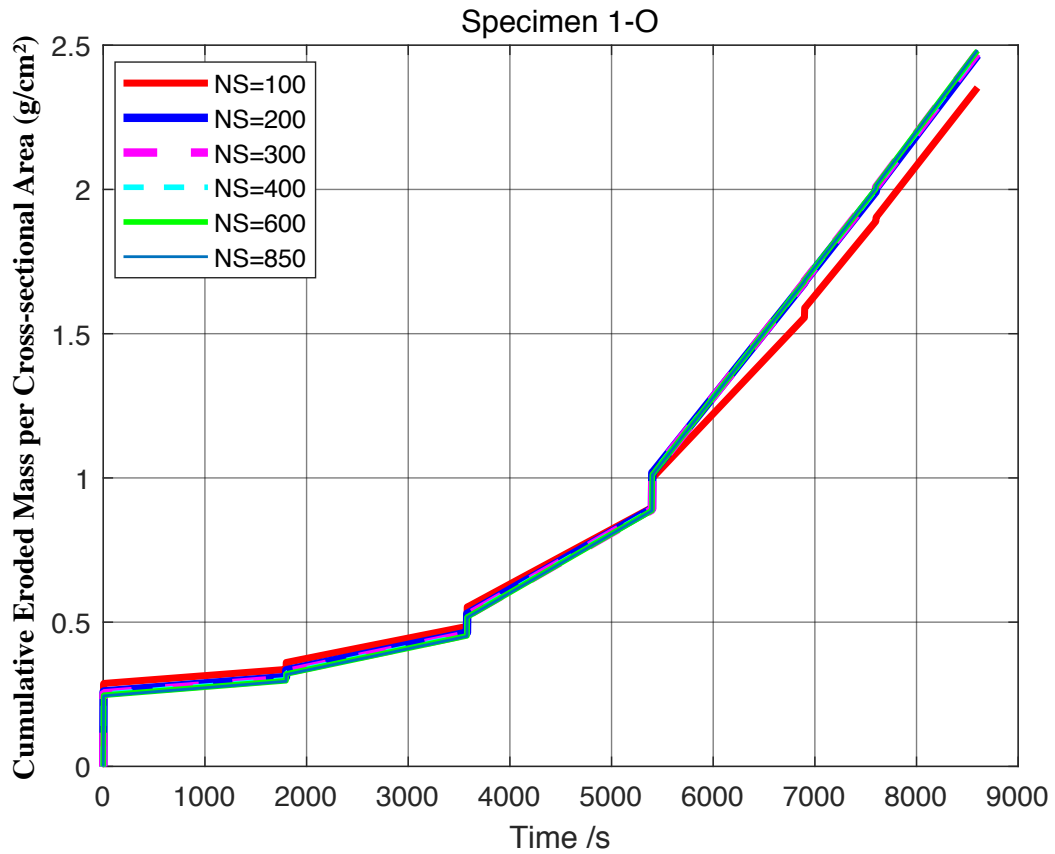


Figure VI.3 – Variations in the cumulative eroded mass per cross-sectional area with time for different nodes

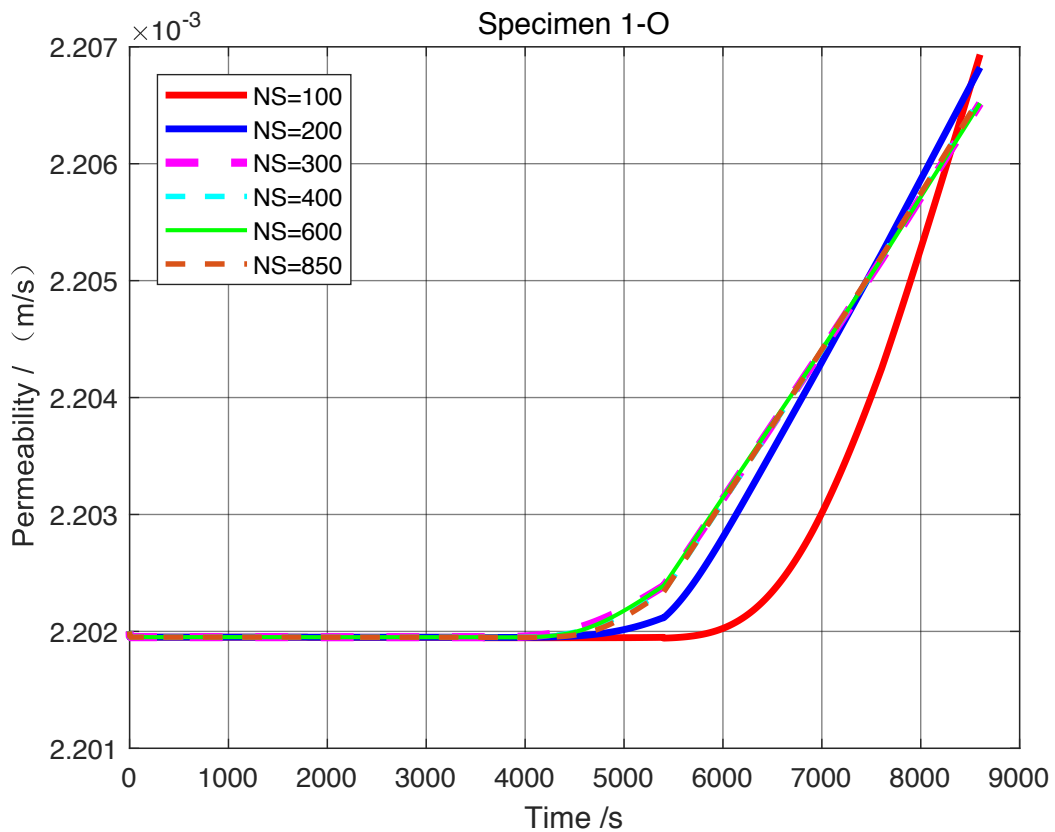


Figure VI.4 – Variations in the hydraulic conductivity with time for different nodes

To investigate the influence of the model node on numeric results, six cases of spatial mesh with 100, 200, 300, 400, 600, and 850 cells were examined.

The results showed that the increased spatial grid density had some influences on calculation results, but the spatial grid $NS = 300$ basically had no effect on settlement results, as shown in Figure VI.3 and Figure VI.4.

Specimen height

To allow studying the influence of specimen height on simulation results, the heights of specimen 1-O are divided into three types: $H = 0.225$ m, $H = 0.325$ m, and $H = 0.42$ m. Other model parameters remain unchanged.

For the three different specimen heights, variations in the cumulative eroded mass per cross-sectional area are shown in Figure VI.5, variations of the hydraulic conductivity with time are shown in Figure VI.6, and variations in the concentration with depth at different times are shown in Figure VI.7, variations in the concentration with time in Figure VI.8, variations in the porosity with time are shown in Figure VI.9, and variations in the flow rate with time in Figure VI.10.

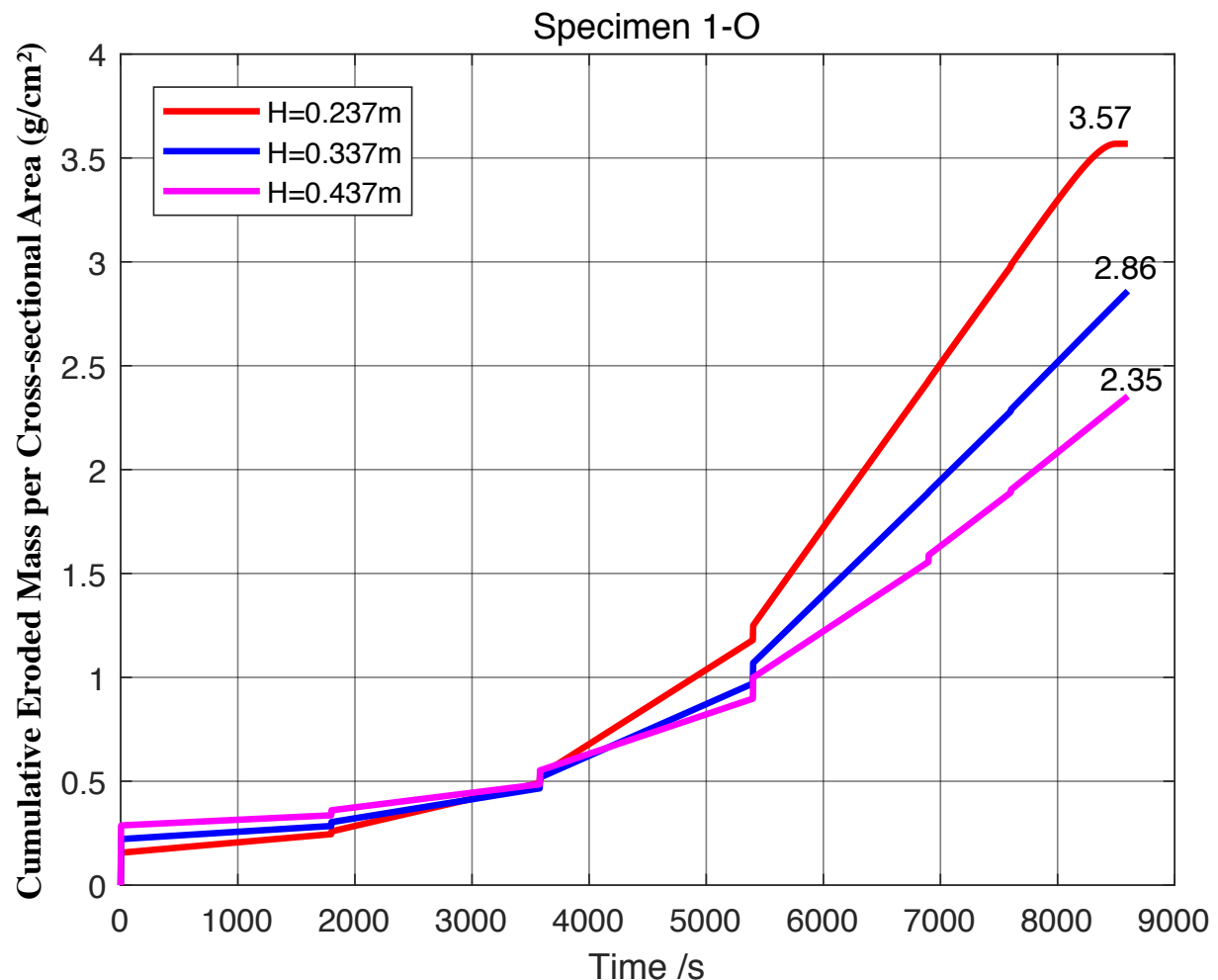


Figure VI.5 – Variations in the cumulative eroded mass per cross-sectional area with time for different specimen heights

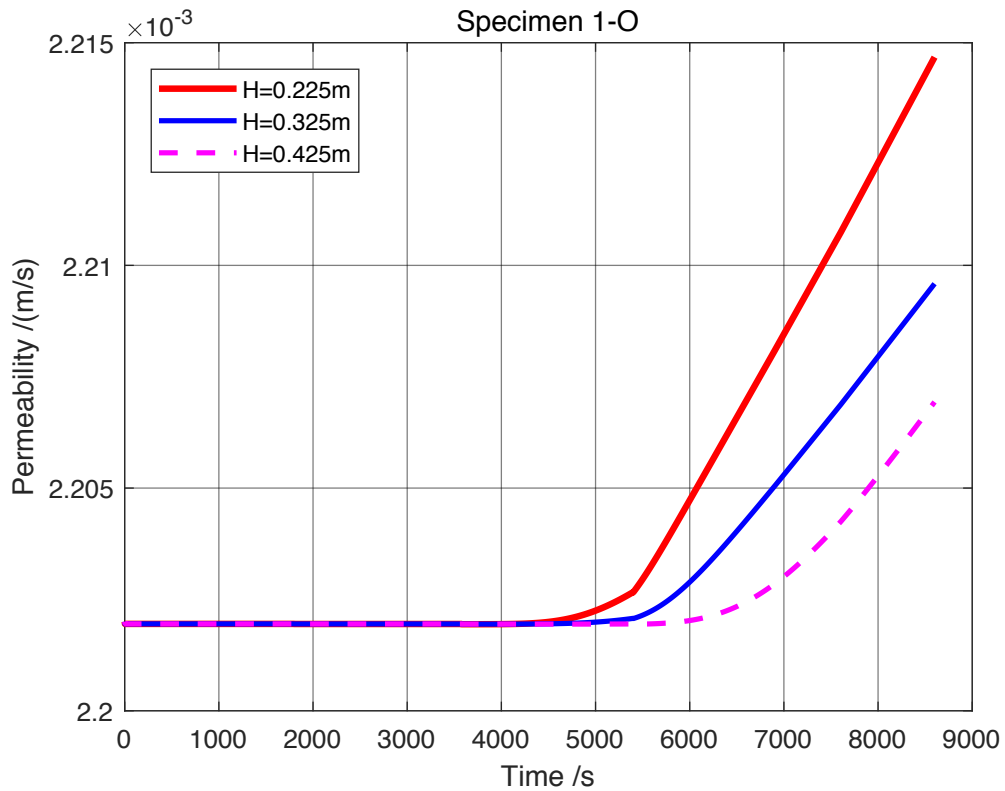


Figure VI.6 – Variations in the hydraulic conductivity with time for different specimen heights

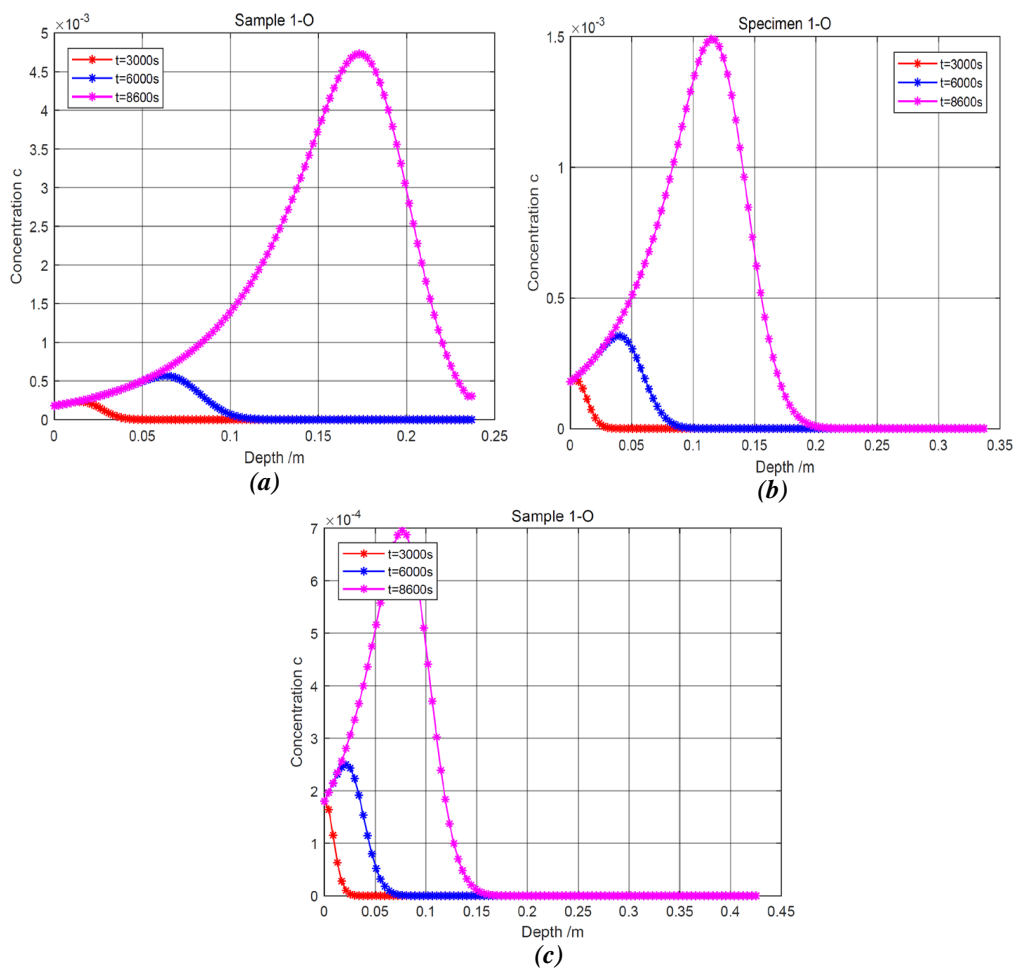


Figure VI.7 – Variations in the concentration with depth at different times (a) $H = 0.225$ m, (b) $H = 0.325$ m, and (c) $H = 0.42$ m

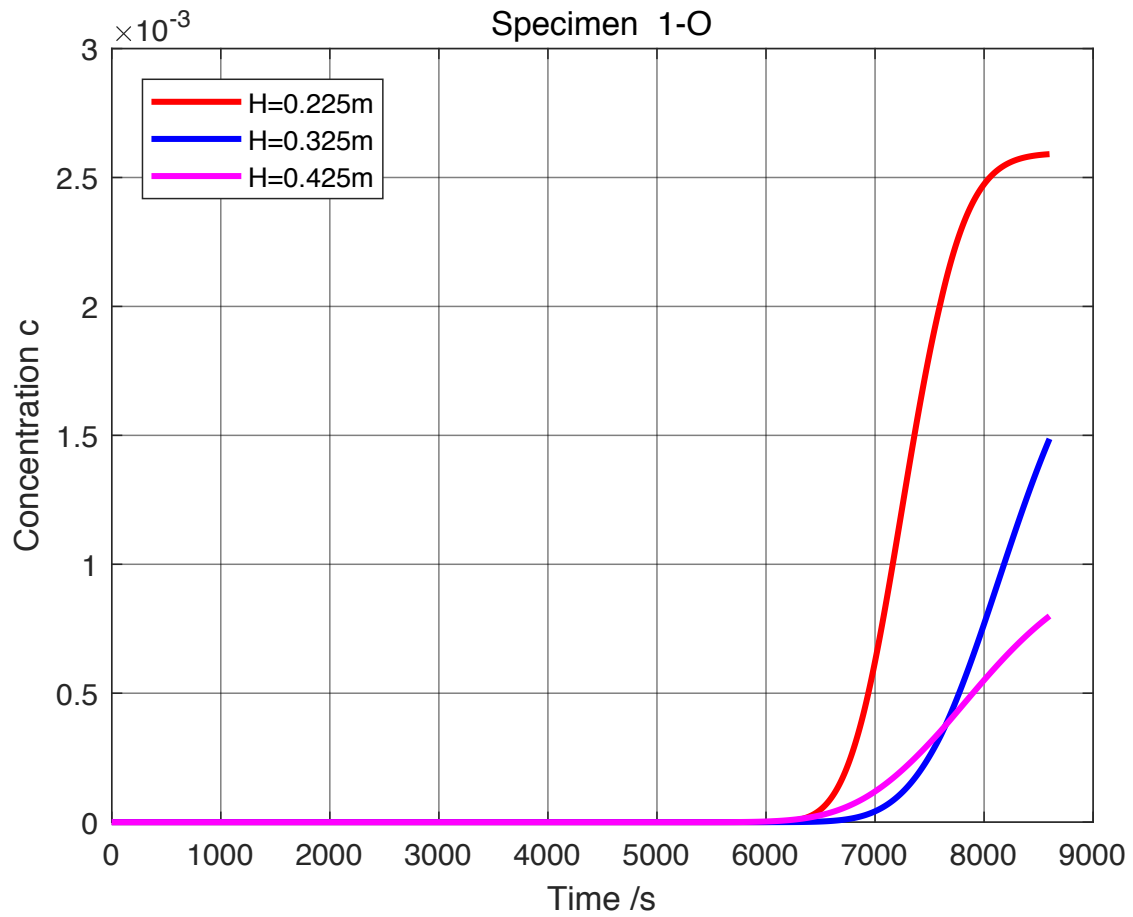


Figure VI.8 – Variations in the concentration with time for different specimen heights

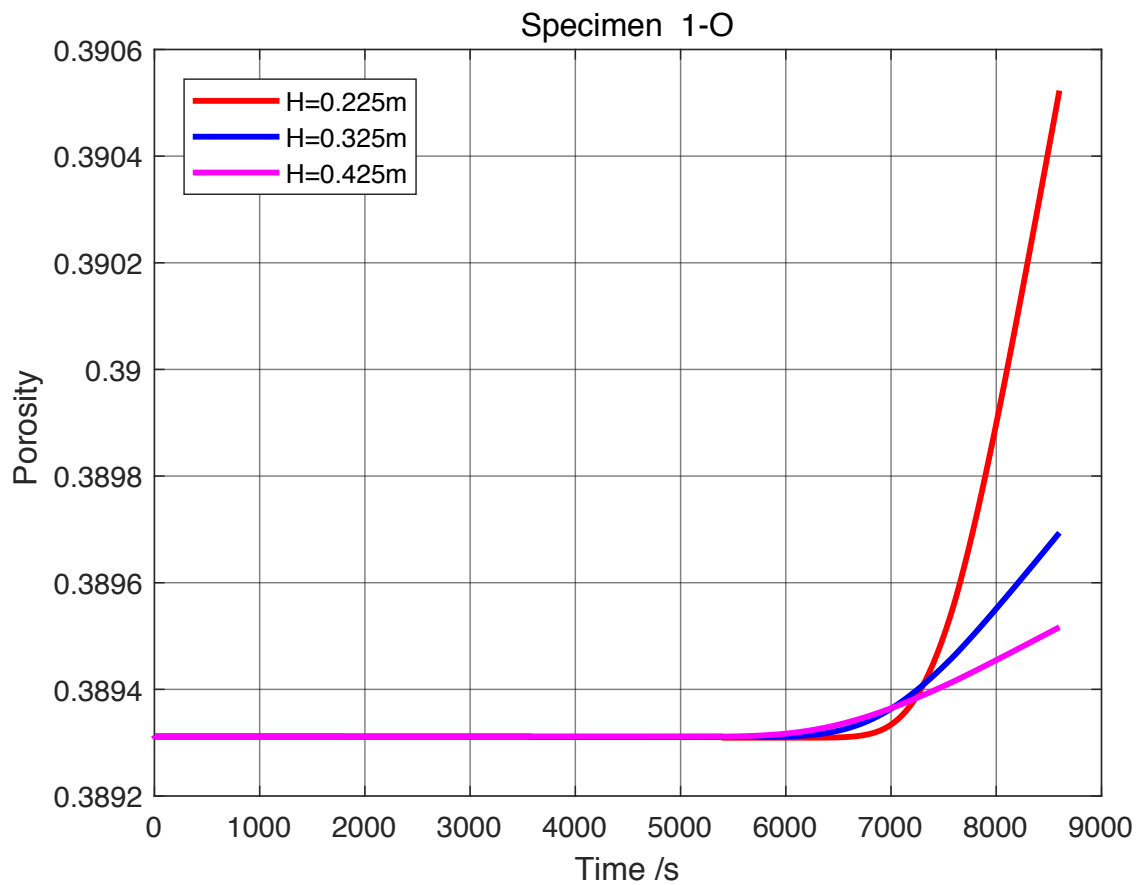


Figure VI.9 – Variations in the porosity with time for different specimen heights

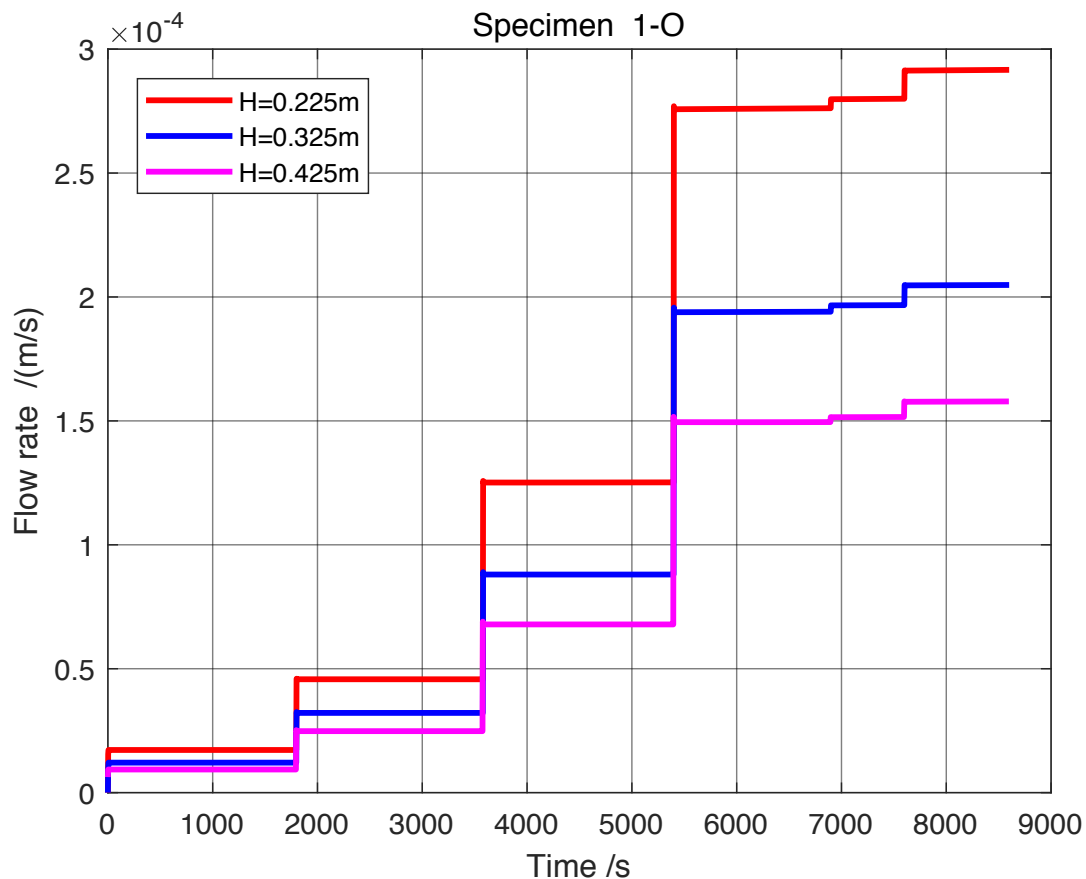


Figure VI.10 – Variations in the flow rate with time for different specimen heights

Figures VI.5 - VI.10 show that changes of specimen height influence the simulation results. For the hydraulic conductivity, the concentration of movable fine particles and porosity show similar tendencies for different specimen heights. After the onset of suffusion, the concentration of movable fine particles changed slowly for the first 6000 s, then accelerated after 6000 s. At this point the effect of specimen height begins to appear but it is relatively small. The calculation results show that hydraulic conductivity, concentration, and porosity decrease with increased specimen height, as shown in Figure VI.6, Figure VI.8, and Figure VI.9. Concentration of fine particles gradually approached the critical point and tended to be stable. Because of the corresponding relationship between the hydraulic gradient and the eroded mass, under the action of certain hydraulic gradients, particles that can be eroded in the soil skeleton phase are gradually eroded into movable fine particles phase and migrate out of the soil along with the water phase. In the initial stage of erosion, the flow rate of the mixture is small, and the sediment carrying capacity of the water phase is weak. Because the fine particles produced by suffusion and the fine particles brought from upstream are more than those taken away by the water phase, the concentration of fine particles at the outlet gradually increases with the flow rate. Then, as the erosion process develops, porosity and permeability increase, and the concentration of fine particles at the outlet decreases gradually with increased flow rate. Thus sediment carrying

capacity is enhanced in the water phase and the fraction of erodible particles is decreased in the skeleton particle phase.

The calculation results show that specimen height also affects the cumulative eroded mass per cross-sectional area and flow rate, especially for the large specimen, as shown in Figure VI.5. As well as the cumulative eroded mass per cross-sectional area, the influence of the height on the flow rate is more obvious, as shown in Figure VI.10. The curves show similar tendencies. With increased Darcy's flow velocity, the cumulative eroded mass per cross-sectional area increased at a gradually decreasing rate. At 8000 s, the cumulative eroded mass per cross-sectional area was $3.57 \text{ g}\cdot\text{cm}^{-2}$, $2.86 \text{ g}\cdot\text{cm}^{-2}$, and $2.35 \text{ g}\cdot\text{cm}^{-2}$ ($H = 0.225 \text{ m}$, $H = 0.325 \text{ m}$, $H = 0.42 \text{ m}$), respectively. The calculation results show decreased cumulative eroded mass per cross-sectional area and flow rate with increased specimen height, mainly as a result of a decreasing concentration of fluidized particles in the outlet flow. Erosion model 1 was able to capture the main features of the suffusion tests. The height of the calculation model does the influence on simulation results, so an appropriately sized calculation model should be selected in the simulation calculation.

Initial permeability

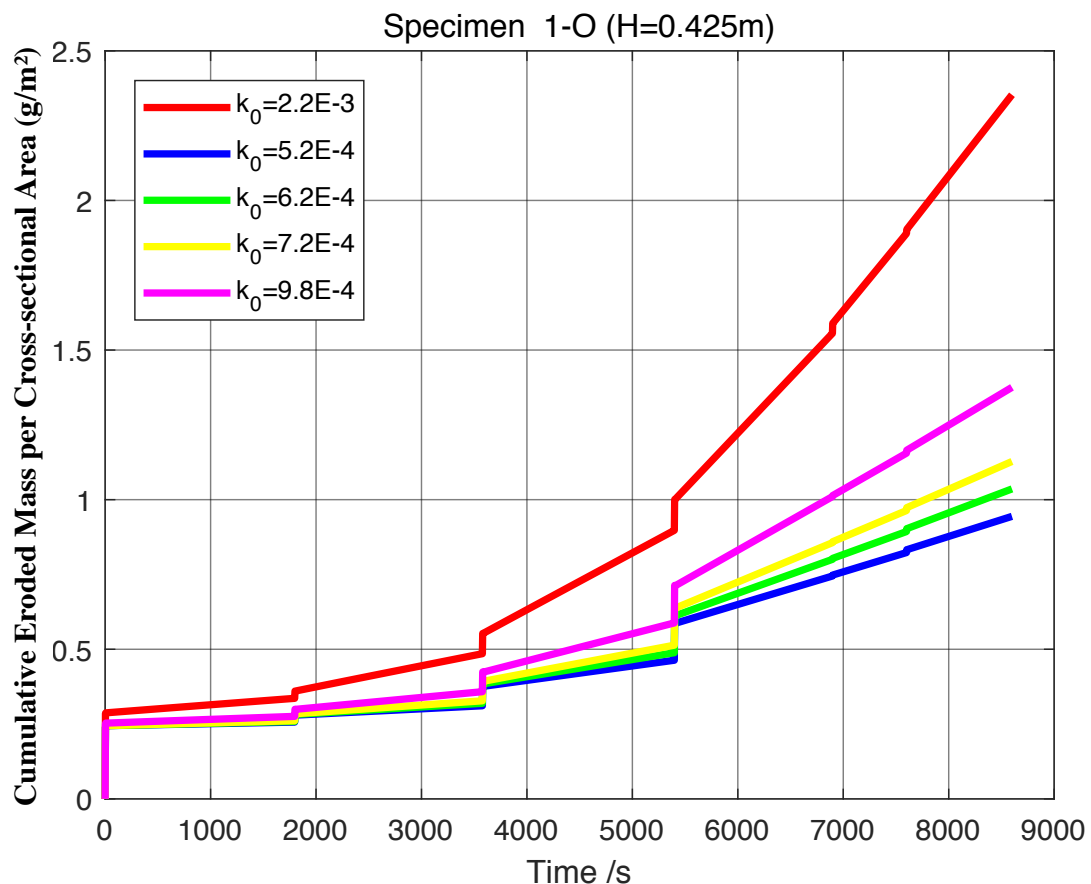


Figure VI.11 – Variations in the cumulative eroded mass per cross-sectional area with time for different initial permeabilities

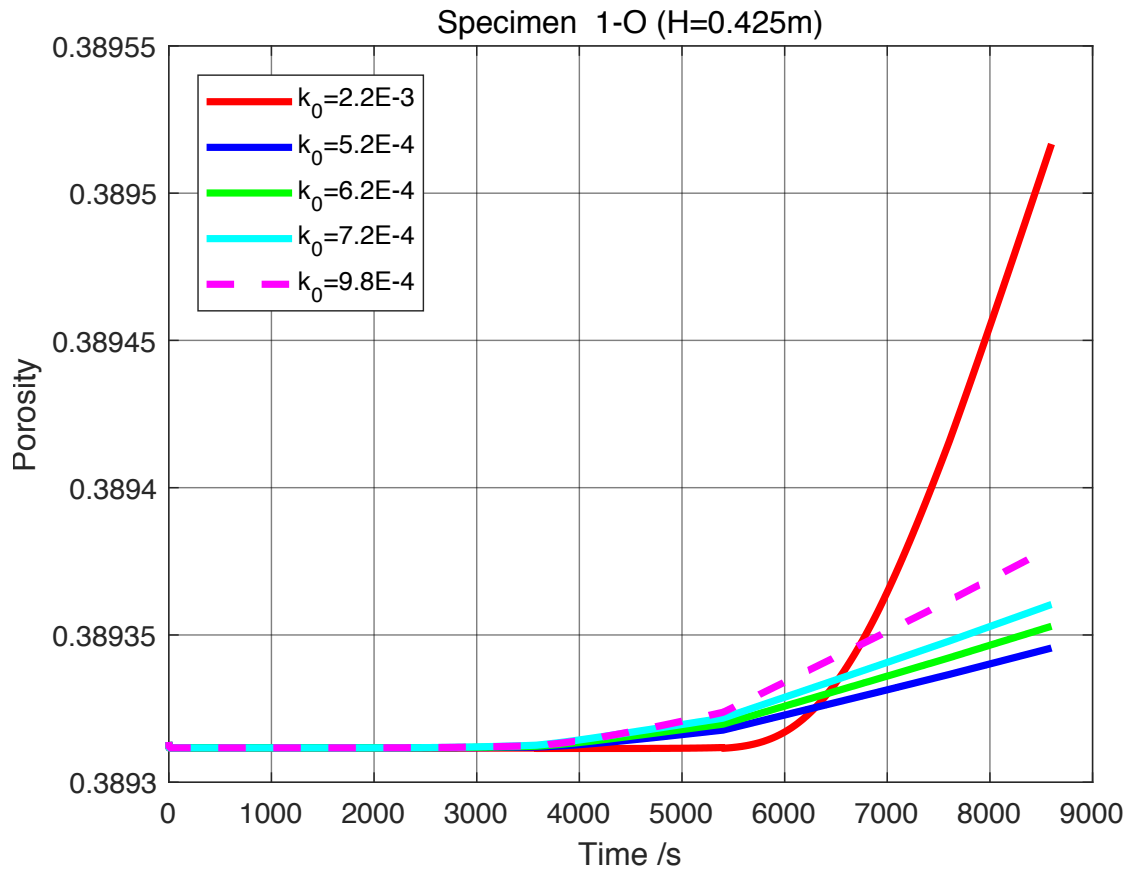


Figure VI.12 – Variations in the porosity with time for different initial permeabilities

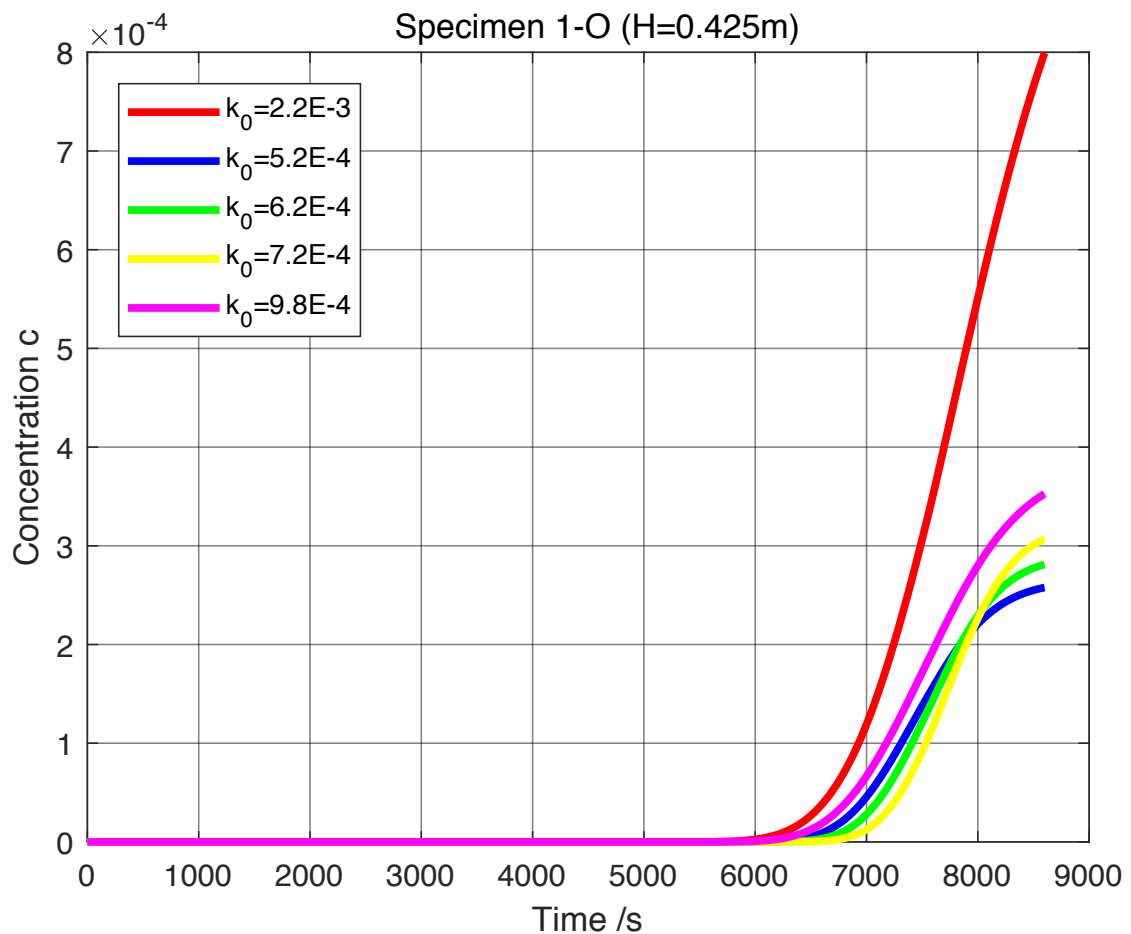


Figure VI.13 – Variations in the concentration with time for different initial permeabilities

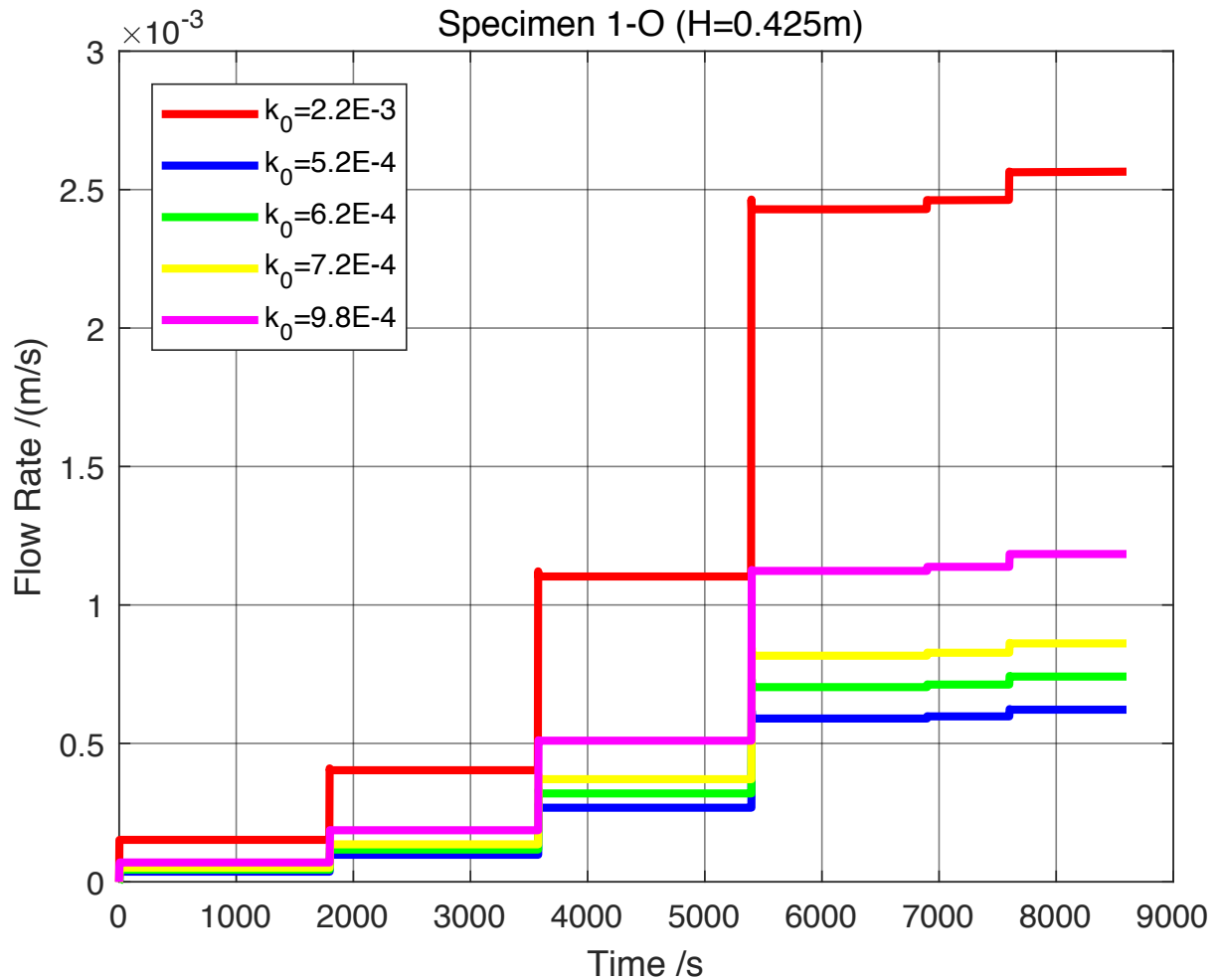


Figure VI.14 – Variations in the flow rate with time for different initial permeabilities

To investigate the influence of initial hydraulic conductivity on numeric results, five initial hydraulic conductivities are assumed: $k_0 = 2.2 \times 10^{-3}$ m/s, $k_0 = 5.2 \times 10^{-4}$ m/s, $k_0 = 6.2 \times 10^{-4}$ m/s, $k_0 = 7.2 \times 10^{-4}$ m/s, and $k_0 = 9.8 \times 10^{-4}$ m/s. Other model parameters remain unchanged. The simulation results show that changes of the initial hydraulic conductivity significantly affect cumulative eroded mass per cross-sectional area, concentration, flow rate, and porosity. The calculation results are shown in Figure VI.11, Figure VI.12, Figure VI.13 and Figure VI.14. The curves show similar tendencies for different initial hydraulic conductivities. Cumulative eroded mass per cross-sectional area is very sensitive to the change of the initial hydraulic conductivity, and cumulative eroded mass per cross-sectional area increases with the initial hydraulic conductivity. However, the initial hydraulic conductivity should be within a certain range and a too large or too small value will lead to a strong oscillation or even to non-convergence and failure of the simulation.

Porosity, flow rate, and initial permeability coefficient are interrelated, so that flow rate and porosity increase with permeability. In the simulation calculation, initial hydraulic conductivity is an important parameter affecting simulation results.

Initial fine content

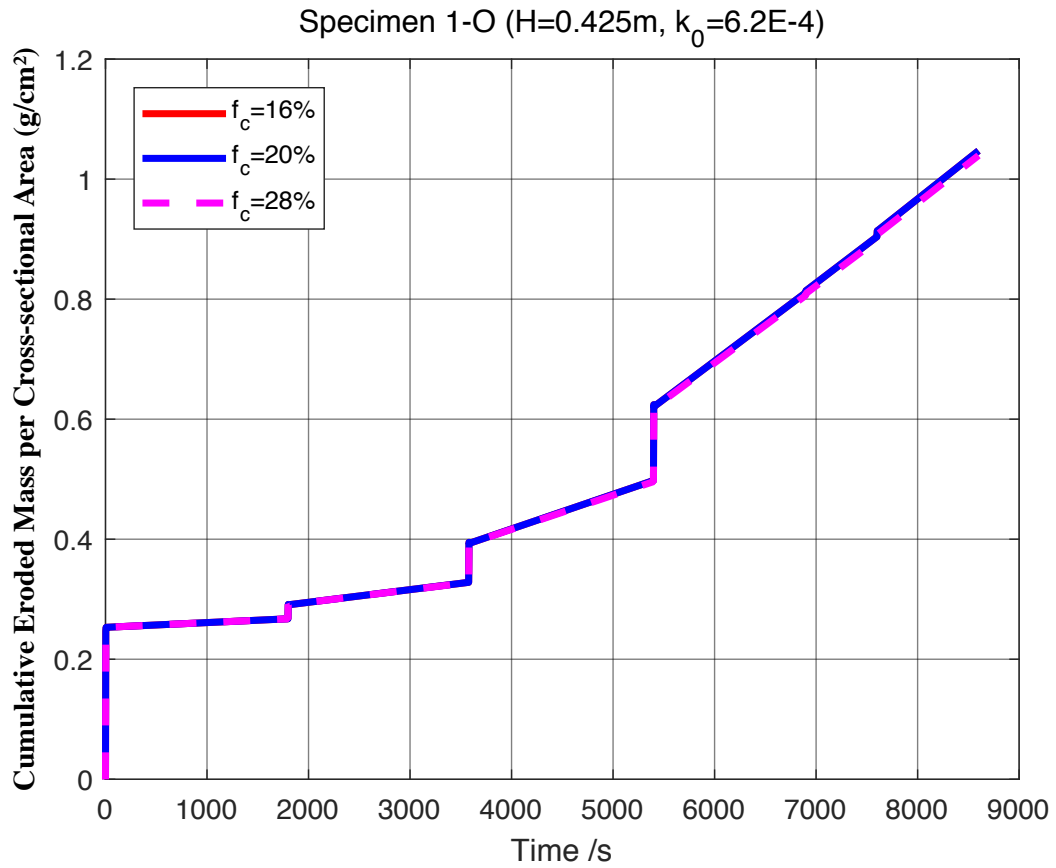


Figure VI.15 – Variations in the cumulative eroded mass per cross-sectional area with time for different fine content

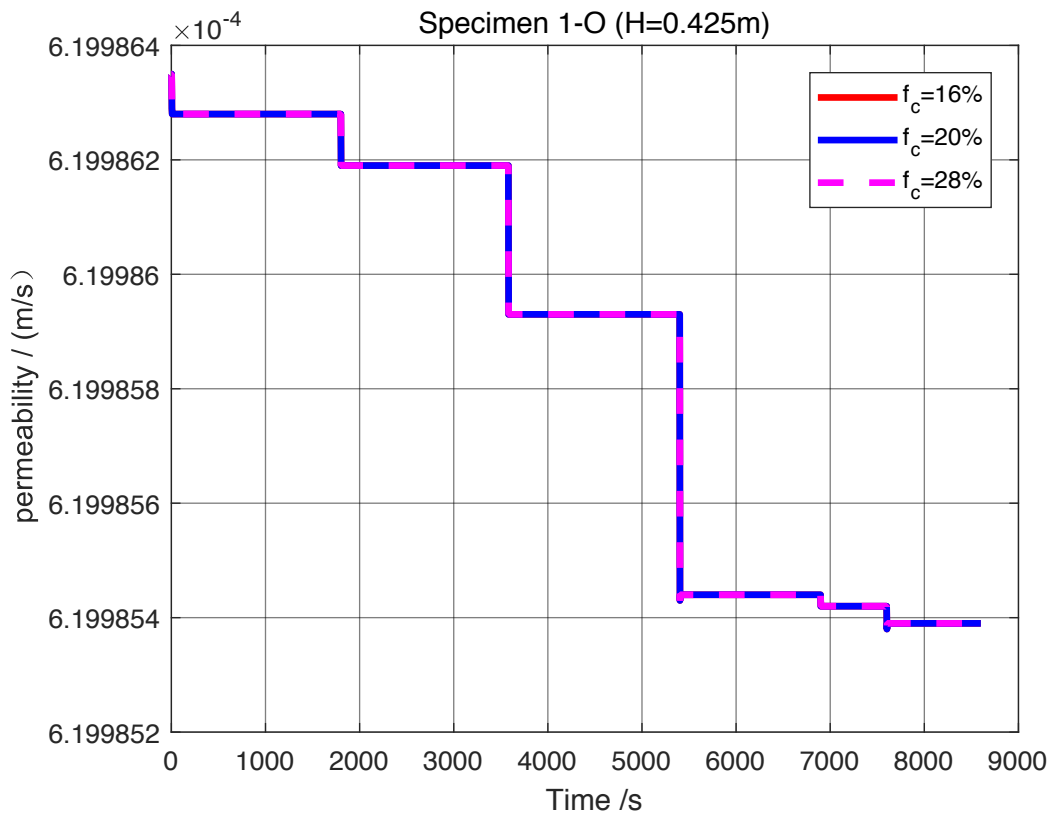


Figure VI.16 – Variations in the hydraulic conductivity with time for different fine content

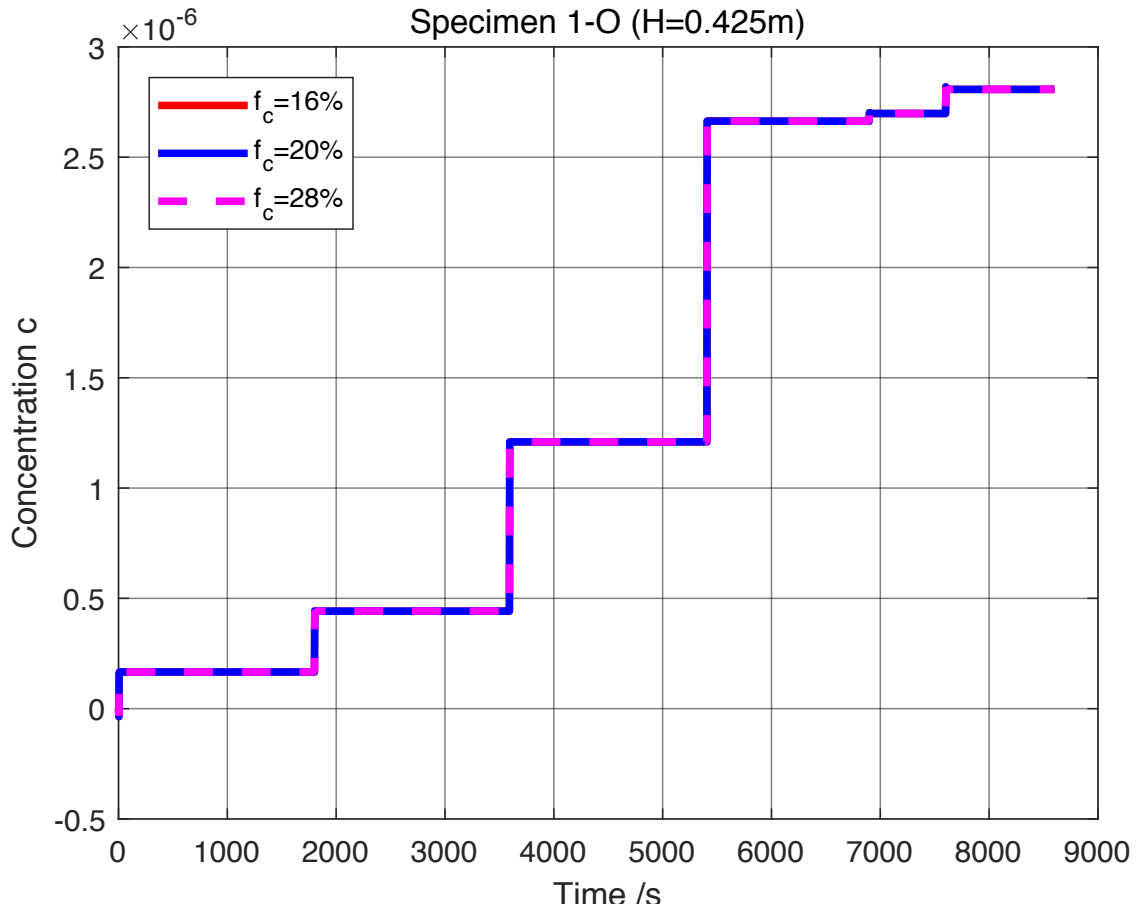


Figure VI.17 – Variations in the concentration with time for different fine content

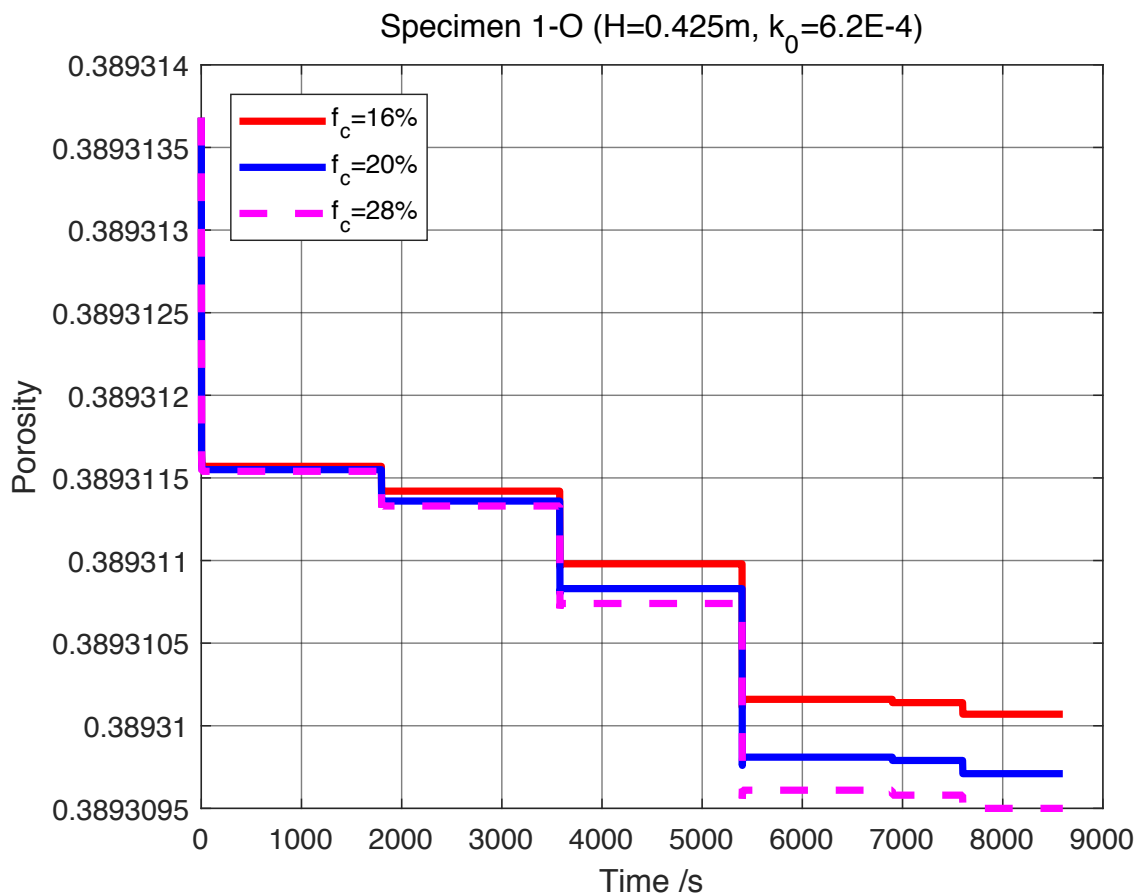


Figure VI.18 – Variations in the porosity with time for different fine content

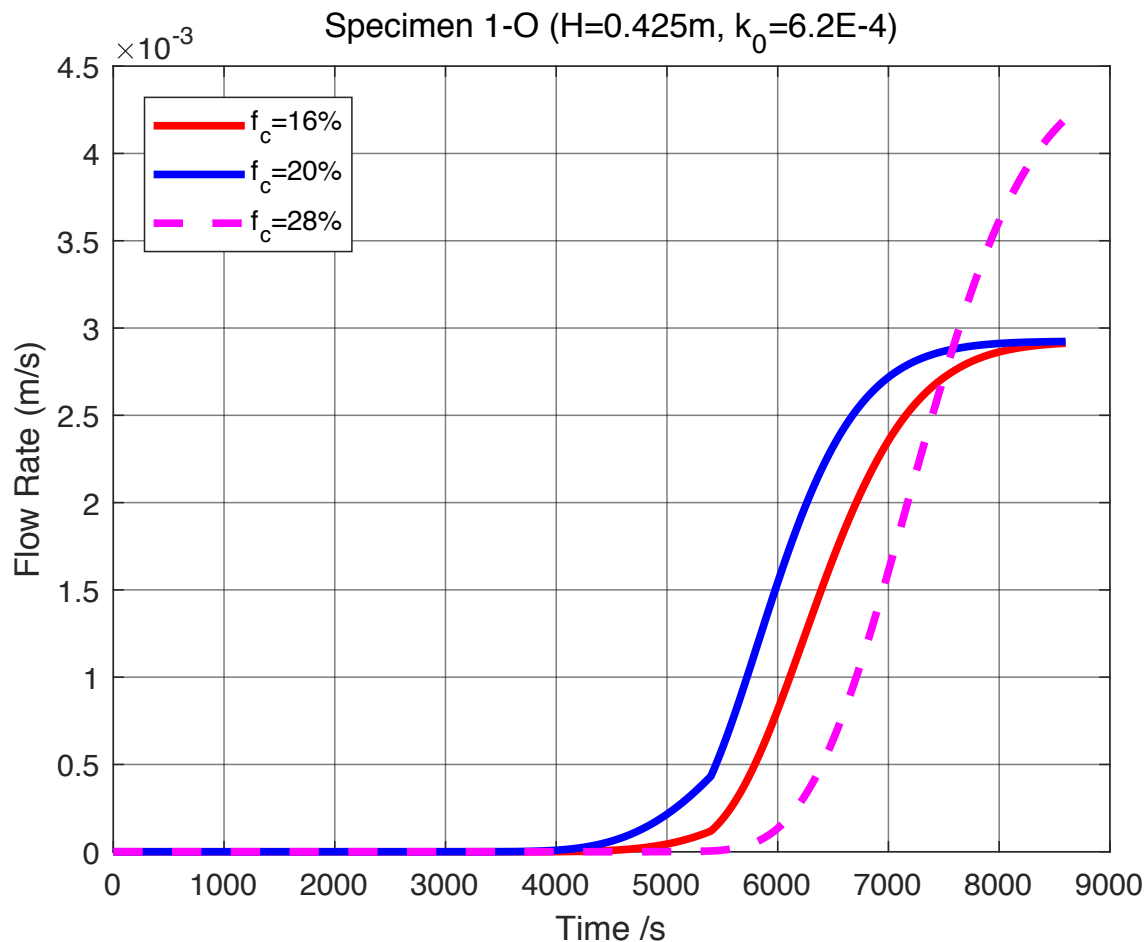


Figure VI.19 – Variations in the flow rate with time for different fine content

To investigate the influence of fine content on numeric results, three values for fine content are assumed: $f_c = 16\%$, $f_c = 20\%$, $f_c = 28\%$. Other model parameters remain unchanged. The simulation results show that changes of fine content have no effect on cumulative eroded mass per cross-sectional area, permeability, and concentration and that they have little effect on porosity and flow rate. The calculation results are shown in Figures VI.15 - VI.19. The curves show similar tendencies for different values of initial fine content. In the simulation calculation, a single change of initial fine content has little effect on the simulation results and thus should not be taken into account.

6.4.2 Comparison of three erosion laws

Suffusion experiments were completed in Chapter V of this report for eight specimens on six soil gradations. The suffusion tests were carried out using oedo-permeameter made up of a cylindrical rigid cell (maximum 0.6 m height with an internal diameter of 0.28 m), a pressurized water supply system, and a fine collector. Three erosion laws were used to simulate experiments. For the convenience of later analysis, erosion law 1, erosion law 2, and erosion law 3 correspond to model 1, model 2, and model 3, respectively.

The properties of eight specimens and the detailed experimental results are shown in Table V.2 and Table V.4 of Chapter V, the brief experimental results are shown in Table VI.1, and the model parameters are shown in Table VI.2.

The experimental results of eight specimens are compared with the simulation results to verify the practicability of three constitutive models. The results show that three erosion models are able to capture the main characteristics of the hydraulic gradient controlled suffusion test. The simulation results obtained for three constitutive models are very close, with small difference in experimental results.

Figure VI.20, Figure VI.21 and Figure VI.22 indicate that for eight specimens of six soil gradations, values of the cumulative eroded mass per cross-sectional area calculated by three erosion models were very close. And the curves of models 1 and 3 are very similar and exhibit the same variation trend. Compared with the experimental results, the simulation results of model 1 are the least different from the experimental results for the cumulative eroded mass per cross-sectional area. The maximum error occurs in the comparison of the specimen 4-O: 9.66 % at 7200 s.

Figure VI.23 and Figure VI.24 show the calculated results of the hydraulic conductivity using three erosion models and the experimental results of specimens 2-O-1, 2-O-2, 4-O, and 6-O, respectively. Figure VI.23 shows that the hydraulic conductivity of the specimen 4-O decreases rapidly within 4000 s, slows down after 4000 s, and tends to be stable. After 8000 s, the hydraulic conductivity increases rapidly and then decreases, exhibiting the instability. The simulation results of the specimen 6-O-2 show that the hydraulic conductivity tends to be stable within 6000 s, decreases rapidly after 6000 s, and then becomes stable, which is consistent with results of the corresponding experiment. The simulation results of specimens 4-O and 6-O-2 are very similar and exhibit the same trend of variation, but their initial fine content is different. The initial fine content of specimen 4-O is 16.2 %, and that for specimen 6-O-2 is 25 %. Therefore, the initial fine content influences the simulation result of the hydraulic conductivity. Figure VI.24 indicates that the hydraulic conductivity of soil 2 decreases rapidly within 6000 s. After 6000 s, the rate of decline decreases and tends gradually toward zero, which is consistent with the suffusion tests, due to the amount of clay in soil 2. Figure VI.24 shows that the calculated results of model 1 are in agreement with the experimental results. Values of the hydraulic conductivity calculated by the three models are very similar and vary with the same trend, which can be used to analyze the development process of suffusion. Figure VI.23 and Figure VI.24 display that the results of the hydraulic conductivity for specimens 2-O-1, 2-O-2, 4-O, and 6-O-2 calculated by model 1 are the most consistent with the experimental results, reflecting the responses of soil to the

hydraulic load during the suffusion process. For the simulation calculation, model 1 is the most suitable of the three models.

Model 1 is in good agreement with the experimental results, and the trends of model 1 and model 3 are very consistent, indicating that models 1 and 3 are suitable for the simulation of suffusion with a vertical downward seepage. It is worth noting that there are several changes in the initial hydraulic conductivity in order to make simulation results closer to the experimental results.

Table VI.1 – Experimental results of computational specimen

Specimen number	Time (s)	Cumulative eroded mass per cross-sectional area (g/cm ²)	Hydraulic conductivity (m/s)
1-O	0	0.292	9.77E-03
	1800	0.305	8.68E-03
	3596	0.417	1.10E-02
	5412	0.971	1.47E-02
	6905	1.535	1.64E-02
	7653	1.911	1.79E-02
	8051	2.026	2.03E-02
2-O-1	0	0.024	5.86E-04
	1821	0.034	5.16E-04
	3620	0.034	1.12E-04
	5410	0.034	2.91E-05
	7207	0.034	2.20E-05
	9022	0.035	1.82E-05
	10790	0.036	1.35E-05
	16218	0.038	1.50E-05
2-O-2	0	0.005	1.25E-04
	1803	0.007	1.17E-04
	3605	0.012	4.39E-05
	5410	0.013	3.15E-05
	7206	0.015	1.87E-05
	8996	0.026	8.50E-06
	10803	0.026	5.22E-06
	14814	0.029	3.40E-06
	0	0.033	4.80E-04
	1770	0.035	4.78E-04

	3593	0.037	5.57E-04
	5368	0.038	5.68E-04
	7177	0.039	5.49E-04
	8975	0.041	4.58E-04
4-O	0	0.285	4.58E-02
	1813	0.431	4.03E-02
	3608	0.596	3.78E-02
	5404	0.877	3.63E-02
	7204	1.231	3.53E-02
	8746	1.389	4.30E-02
	10077	1.622	3.06E-02
5-O	0	0.023	1.27E-02
	1803	0.046	1.26E-02
	3580	0.123	1.35E-02
	5386	0.295	1.58E-02
	7187	0.509	1.77E-02
	8390	0.717	1.91E-02
	8879	0.834	2.88E-02
6-O-1	0	0.327	3.57E-03
	1631	0.492	3.57E-03
	3421	0.526	2.83E-03
	5227	0.607	2.35E-03
	7016	0.892	2.59E-03
	9429	2.137	4.36E-03
	10900	3.227	1.25E-02
6-O-2	0	0.476	5.59E-03
	1806	0.5	5.59E-03
	3563	0.508	5.97E-03
	5444	0.53	5.89E-03
	7191	0.579	5.35E-03
	9291	0.794	4.28E-02
	11136	1.099	2.78E-03
	18616	2.726	1.78E-03

Table VI.2 – Model parameters

Reference	λ_e	k_0	k_1	k_2	c_0	ρ_f (kg/m ³)	ρ_s (kg/m ³)	μ (Pa·s)	$f_{c\infty}$
1-O	10	2.02E-3	1.40	1.17	1E-4	1000	2650	5.0E-6	0.2078
4-O	10	3.78E-2	1.80	3.76	1E-4	1000	2650	5.0E-6	0.1455
2-O-1	10	6.00E-5	1.60	3.67	1E-4	1000	2650	5.0E-6	0.2496
2-O-2	20	2.00E-5	1.60	3.67	1E-4	1000	2650	5.0E-6	0.2494
6-O-1	10	3.54E-3	9.20	1.60	1E-4	1000	2650	5.0E-6	0.2168
6-O-2	10	5.64E-3	9.20	1.60	1E-4	1000	2650	5.0E-6	0.2216
3-O	20	5.0E-5	2.85	0.81	1E-4	1000	2650	5.0E-6	0.5303
5-O	10	1.27E-2	0.10	1.50	1E-4	1000	2650	5.0E-6	0.2415

Note: $f_{c\infty}$ is the fraction of fine particles in the specimen at the end of the test. λ_e is a physical parameter of material properties, which characterizes the ability of the soil to resist internal erosion. It is constant for the same material, however, it varied in simulations of soil 2 in order to make simulation results closer to the experimental results for the cumulative eroded mass per cross-sectional area.

6.5 Conclusions

A new numerical approach to simulate the development process of suffusion was given in this report. For modeling the erosion of the soil skeleton, the governing differential equations were formulated based on the mass balance of four assumed constituents: the stable fabric of the solid skeleton, the erodible fines, the fluidized particles, and the pure fluid. The terms of mass exchange were introduced into the mass balance equations. The coupled formulations are solved numerically by a finite difference method. The model is very sensitive to initial conditions and some initial conditions may lead to strong oscillation or even non-convergence of the fluidized fine particle concentration, followed by the oscillation of the porosity, however, the water pore pressure generally does not fluctuate.

For specimen 1-O, the influences of number of calculation mesh nodes, length of specimen, initial hydraulic conductivity and initial fine content on the simulation results of suffusion are comparatively analyzed through the erosion model 1. The results show that the increased number of spatial grid nodes had an influence on calculation results, but the spatial grid $NS = 300$ basically had no effect on simulation results. The specimen height also affects the cumulative

eroded mass per cross-sectional area and flow rate, especially for large specimens. As well as the cumulative eroded mass per cross-sectional area, the effect of height on the flow rate is more obvious. The cumulative eroded mass per cross-sectional area and flow rate decrease if the specimen height increases, mainly as a result of a decreasing concentration of fluidized particles. The initial hydraulic conductivity is an important parameter influencing simulation results. The cumulative eroded mass per cross-sectional area increases with the increasing initial hydraulic conductivity. A single change to initial fines content has little effect on the simulation results and thus should not be taken into account.

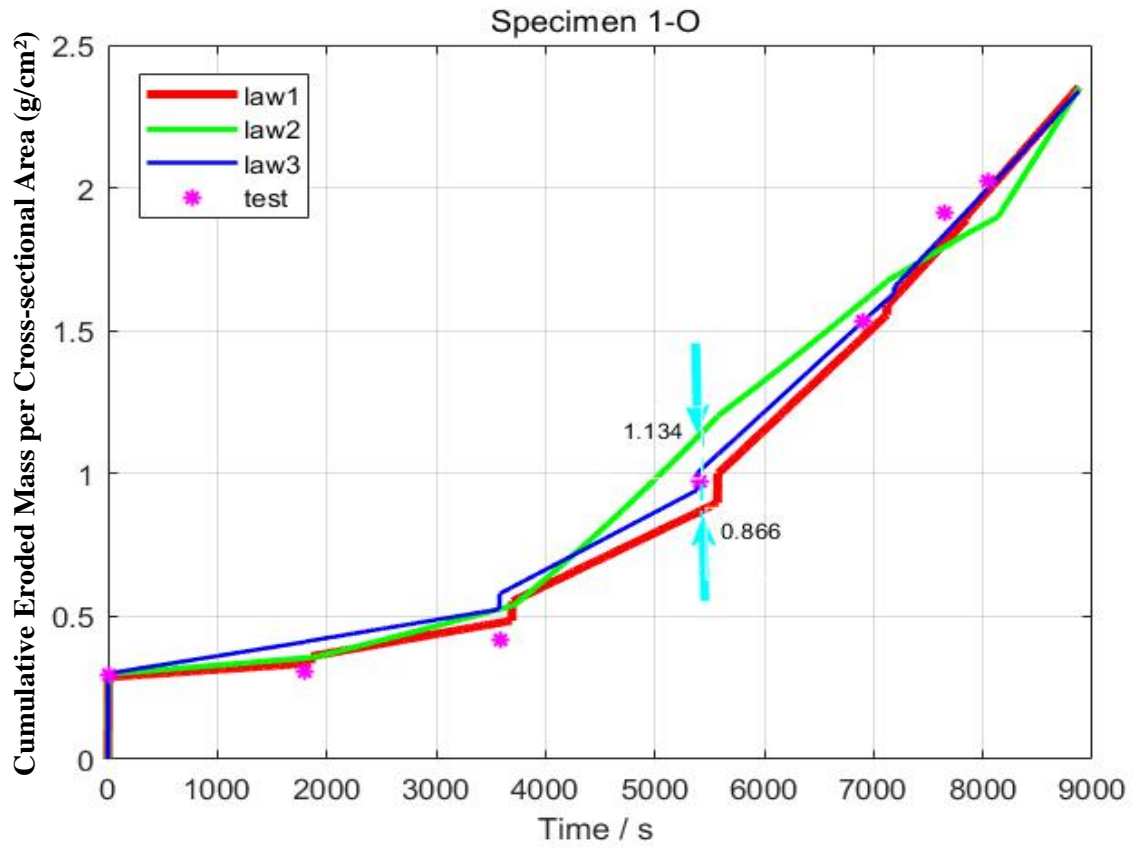
Three erosion models are given by considering three erosion laws (including model 1). Then, three models are validated by simulating 1D suffusion tests. Simulation results present that these three models can reproduce the main features of the suffusion process. To further improve the performance of the three simulation models, eight experimental specimens were selected in order to test the practicability of three models. The calculation results of the three models are compared with the experimental results at the same time. The results of the three erosion models used for simulation were very close, with the curves showing the similar tendencies. There are two phases of the suffusion process distinguished from the time evolution of the hydraulic conductivity and both were well reproduced by the three erosion models. Hydraulic conductivity firstly slowly increased, or depending on the hydraulic loading history, even decreased. The second phase of the hydraulic conductivity evolution was characterized by a rapid increase. Finally, hydraulic conductivity reached a constant value. The results showed that the numeric model is able to describe the suffusion process, and the calculated results agree well with the experimental results. The finite difference program is correct and can reflect the entire process of occurrence and development in the suffusion. Based on the comparison and analysis of the simulation results of three models, model 1 is the most suitable of the three models.

This chapter is the first step to simulate the suffusion process. There are spatial scale effects in simulations using these three models. Therefore, it is necessary to give a new erosion law to avoid the spatial scale effects.

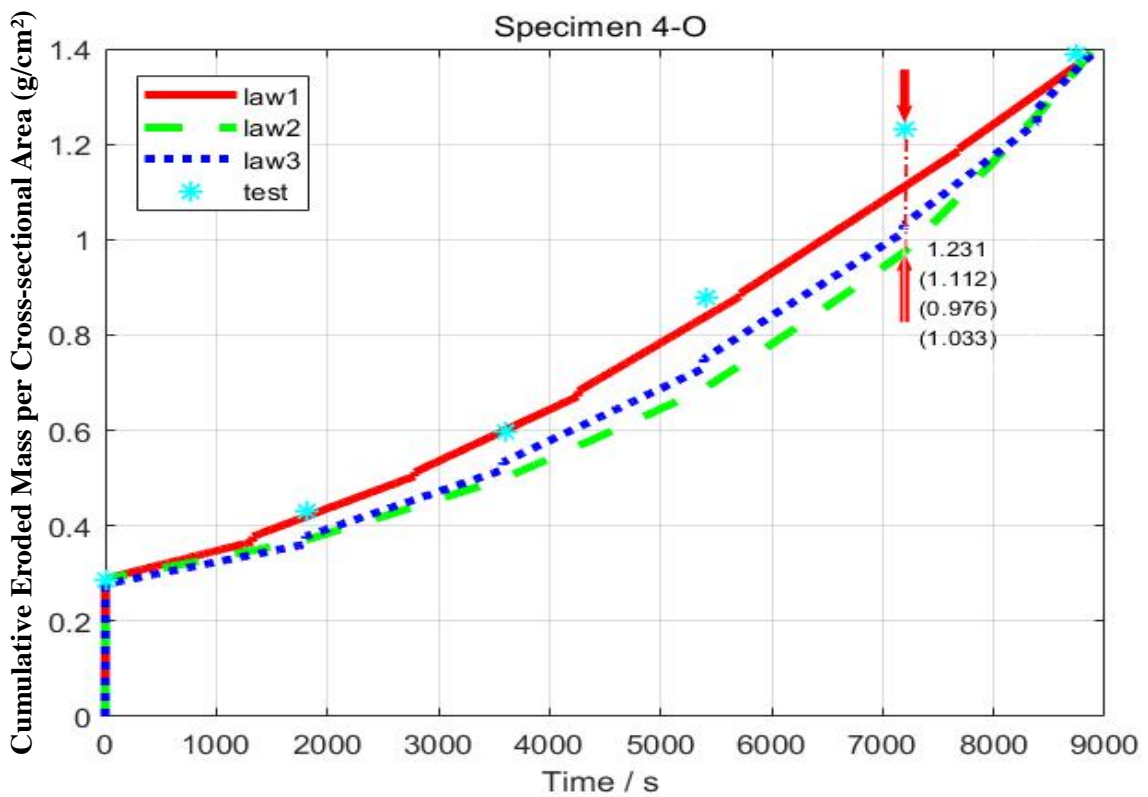
6.5.1 FEM in the future

A numeric method for solving boundary problems along the whole engineering structure scale of granular soils with gap gradation or wide gradation is presented. For simplicity, parameters related to granularity or granularity distribution are not considered. In future work, particle size parameters will be calibrated according to well documented experimental measurements and introduced into erosion or filtration laws. Coupled models will also be extended to three

dimensional conditions so as to obtain more complex geometric boundary conditions.

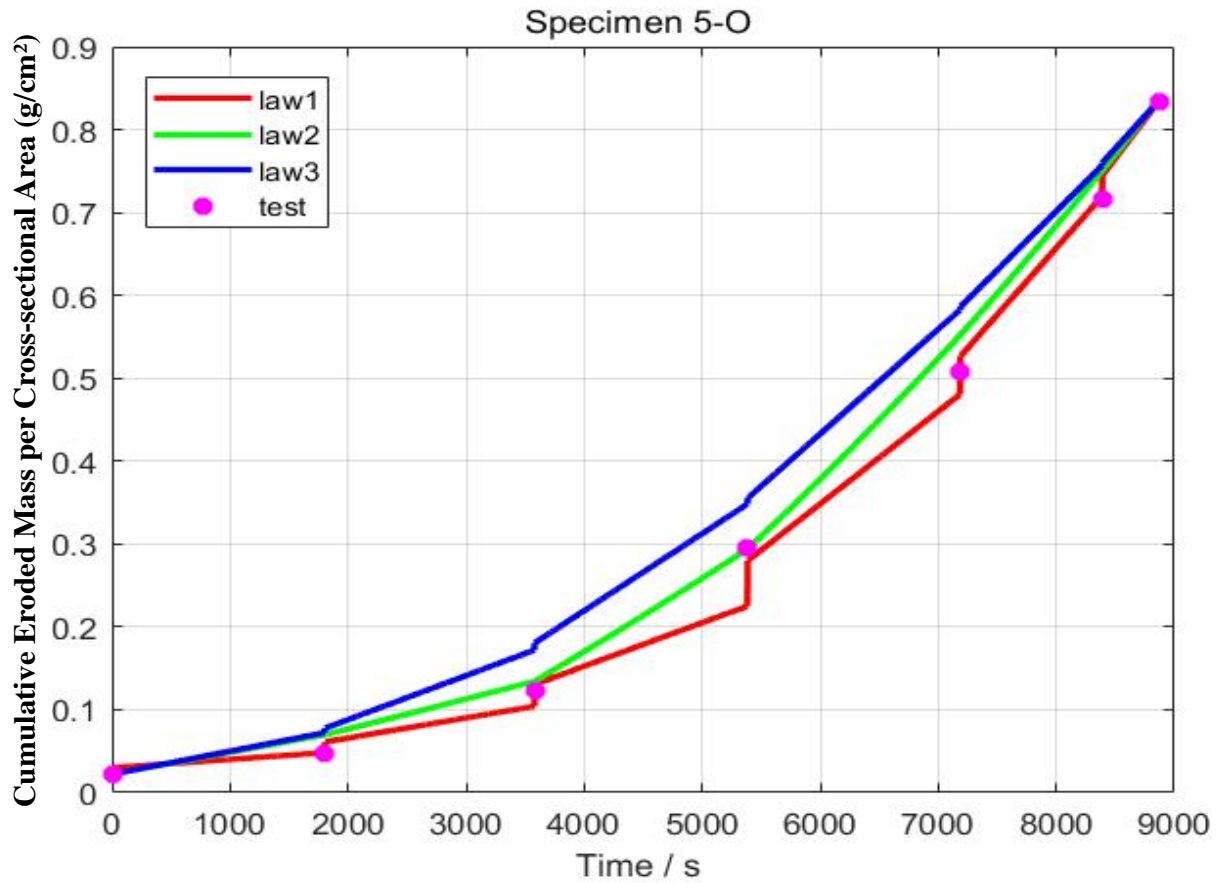


(a)

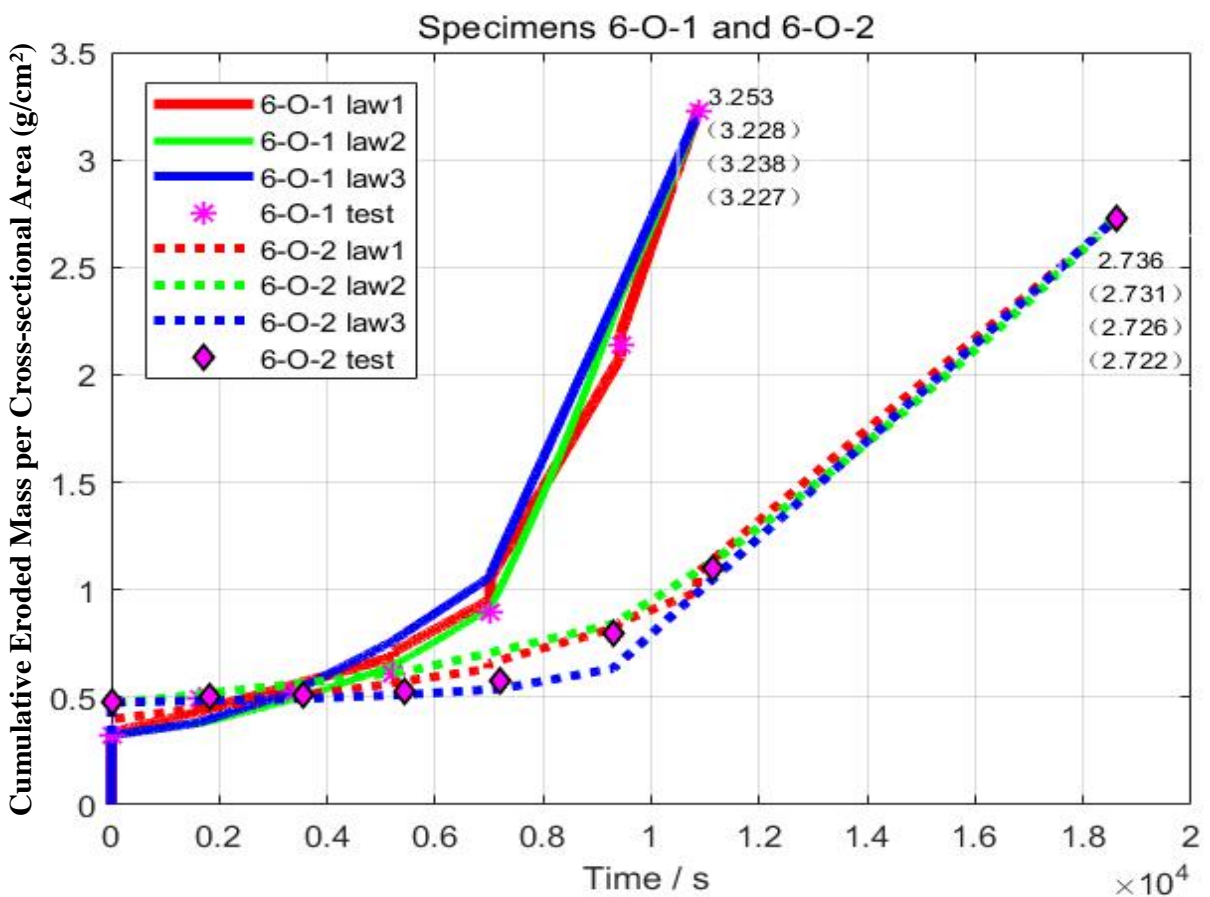


(b)

Figure VI.20 – Comparison of the calculated results of the cumulative eroded mass per cross-sectional area among three models (including experimental results) (a) specimen 1-O (b) specimen 4-O

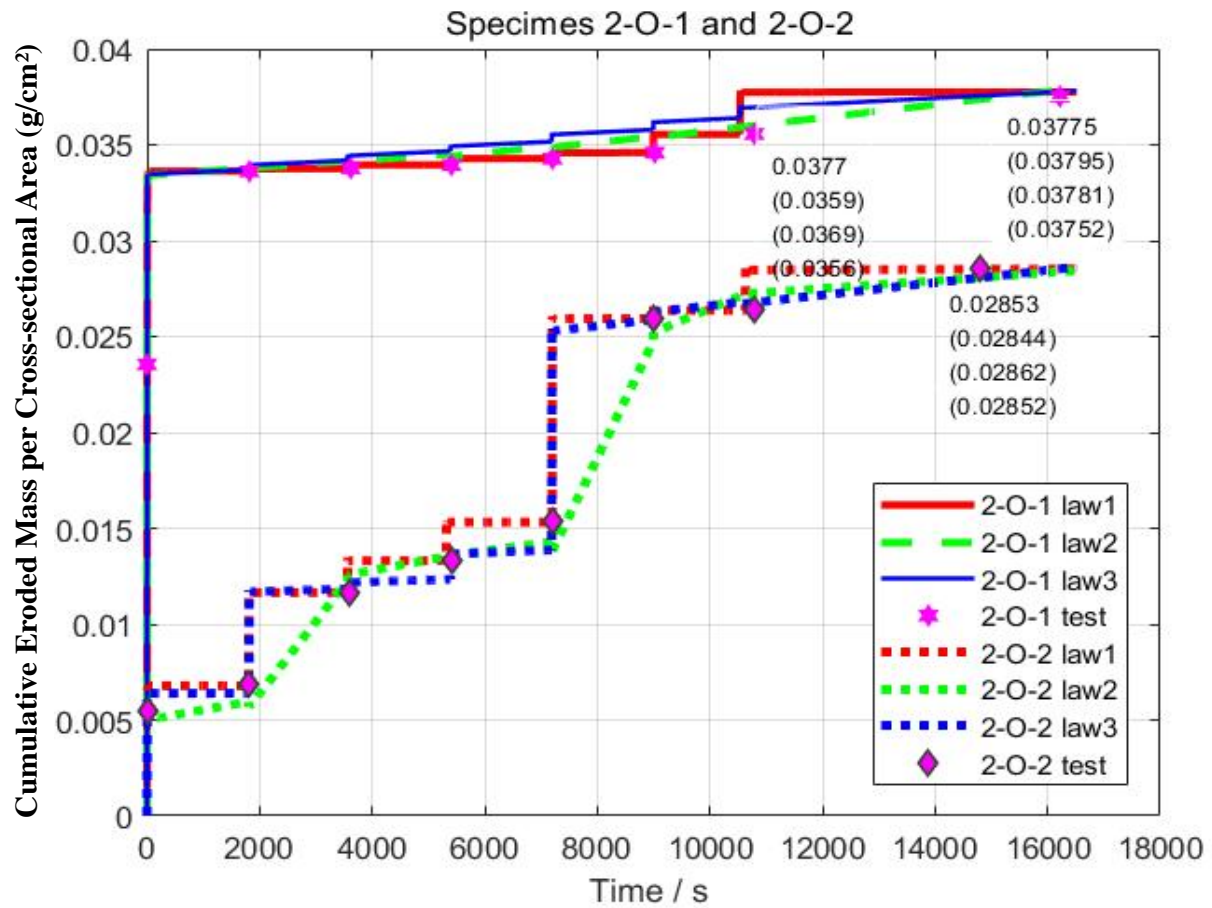


(a)

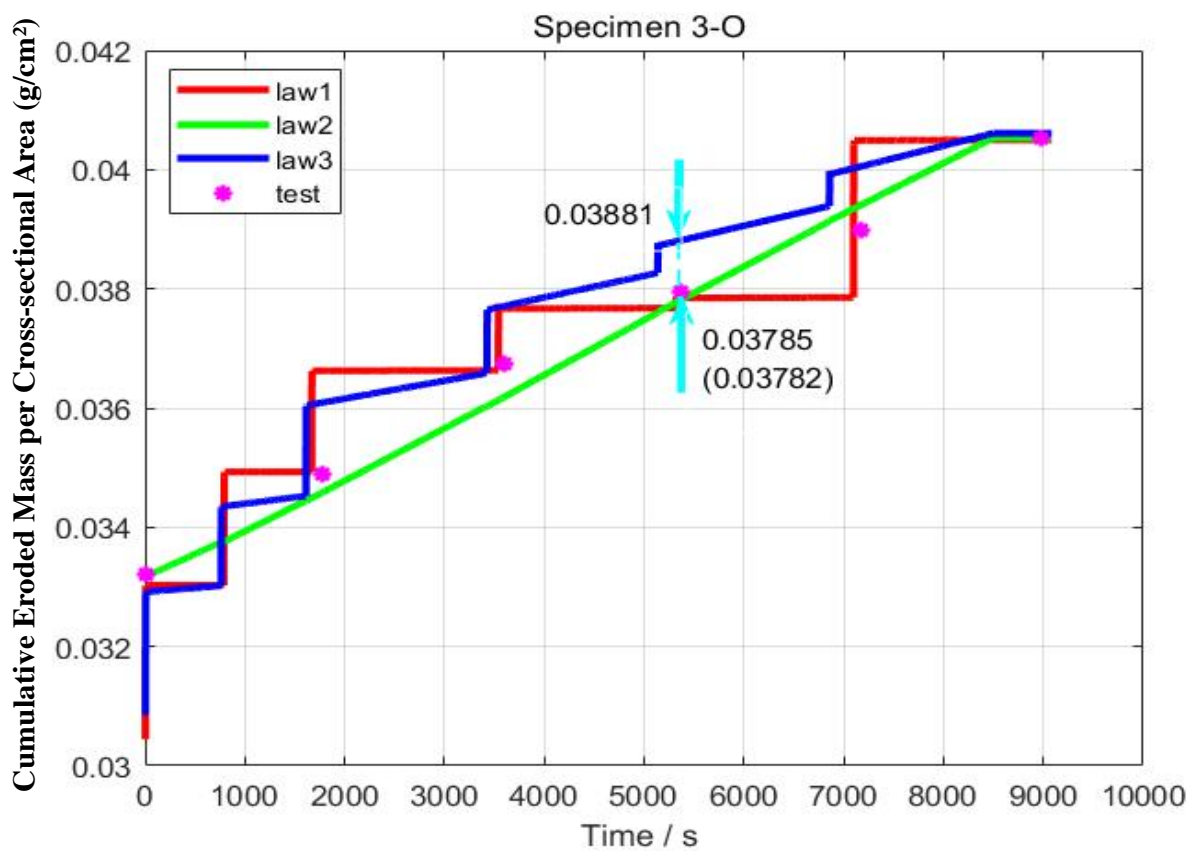


(b)

Figure VI.21 – Comparison of the calculated results of the cumulative eroded mass per cross-sectional area among three models (including experimental results) (a) specimen 5-O (b) specimens 6-O-1 and 6-O-2

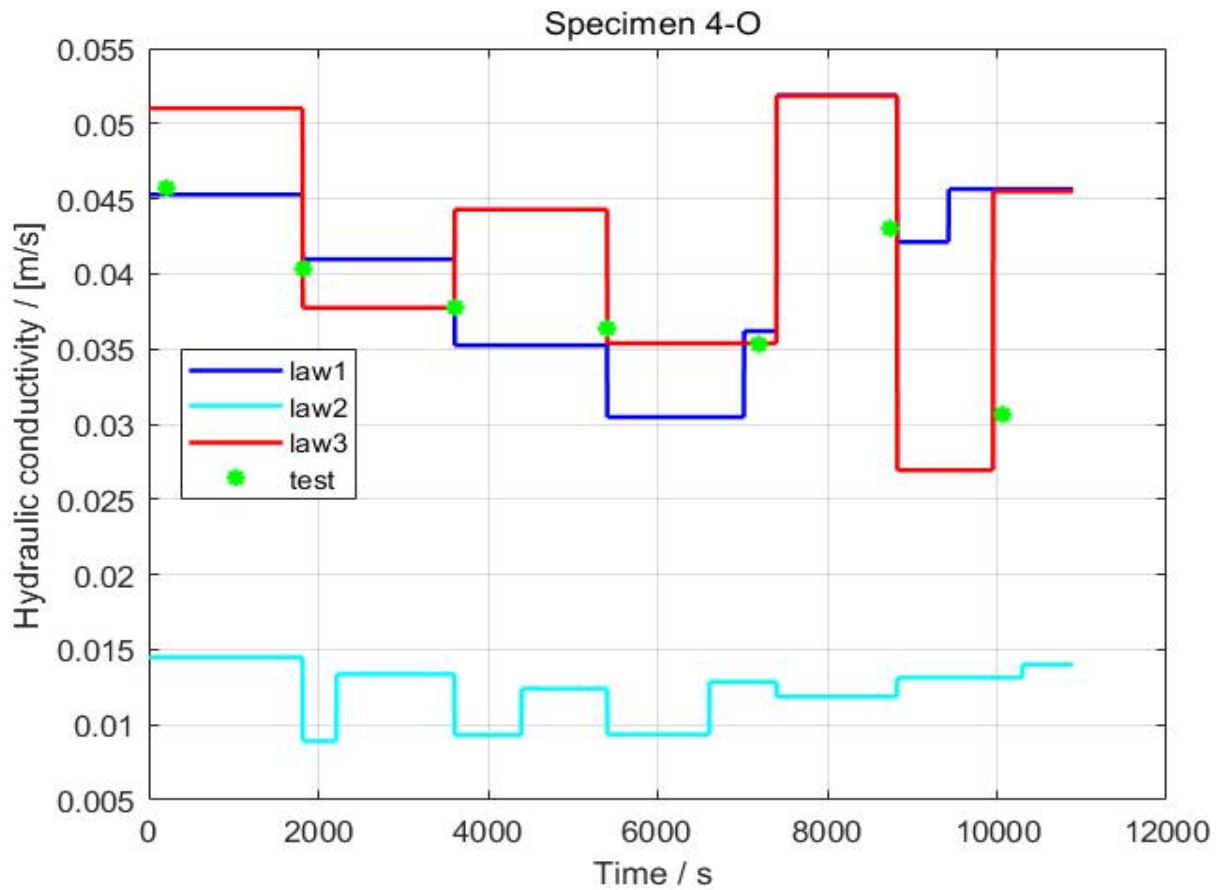


(a)

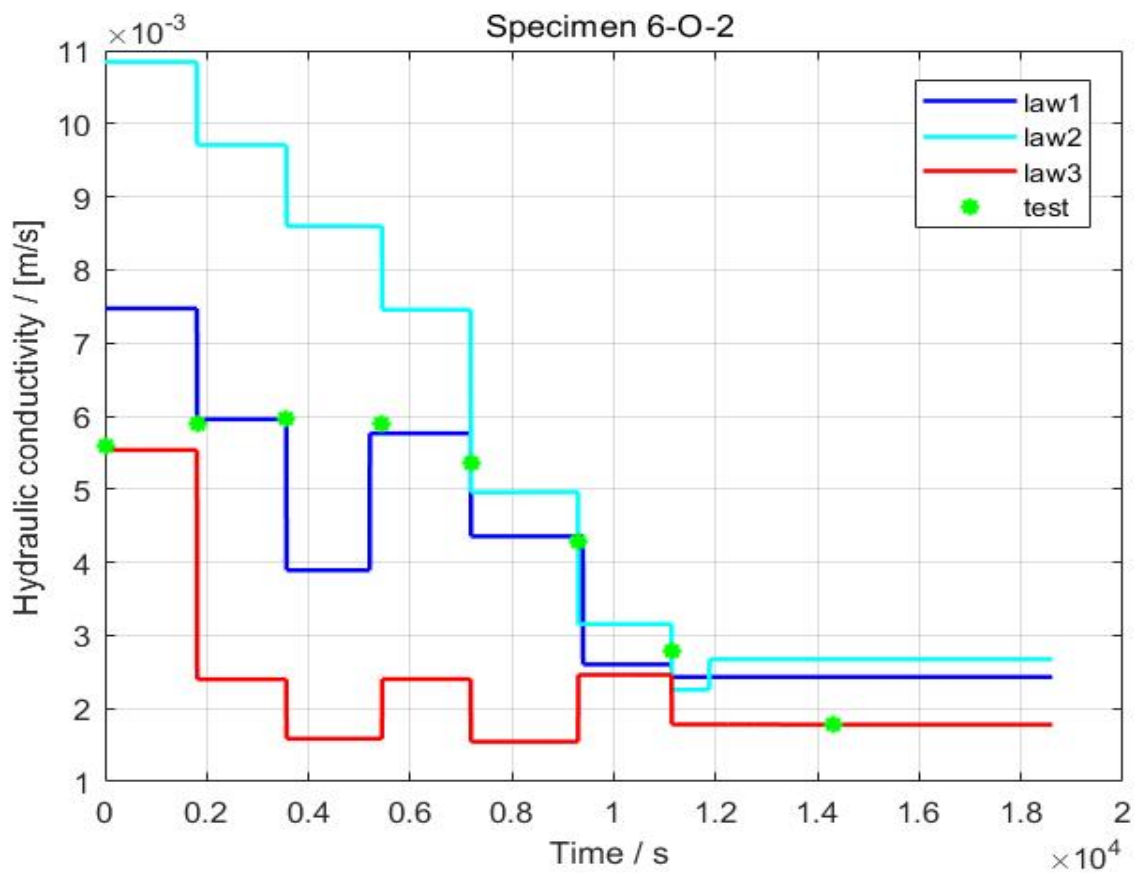


(b)

Figure VI.22 – Comparison of the calculated results of the cumulative eroded mass per cross-sectional area among three models (including experimental results) (a) specimens 2-O-1 and 2-O-2 (b) specimen 3-O



(a)



(b)

Figure VI.23 – Comparison of the calculated results of the hydraulic conductivity among three models (including experimental results) (a) specimen 4-O (b) specimen 6-O-2

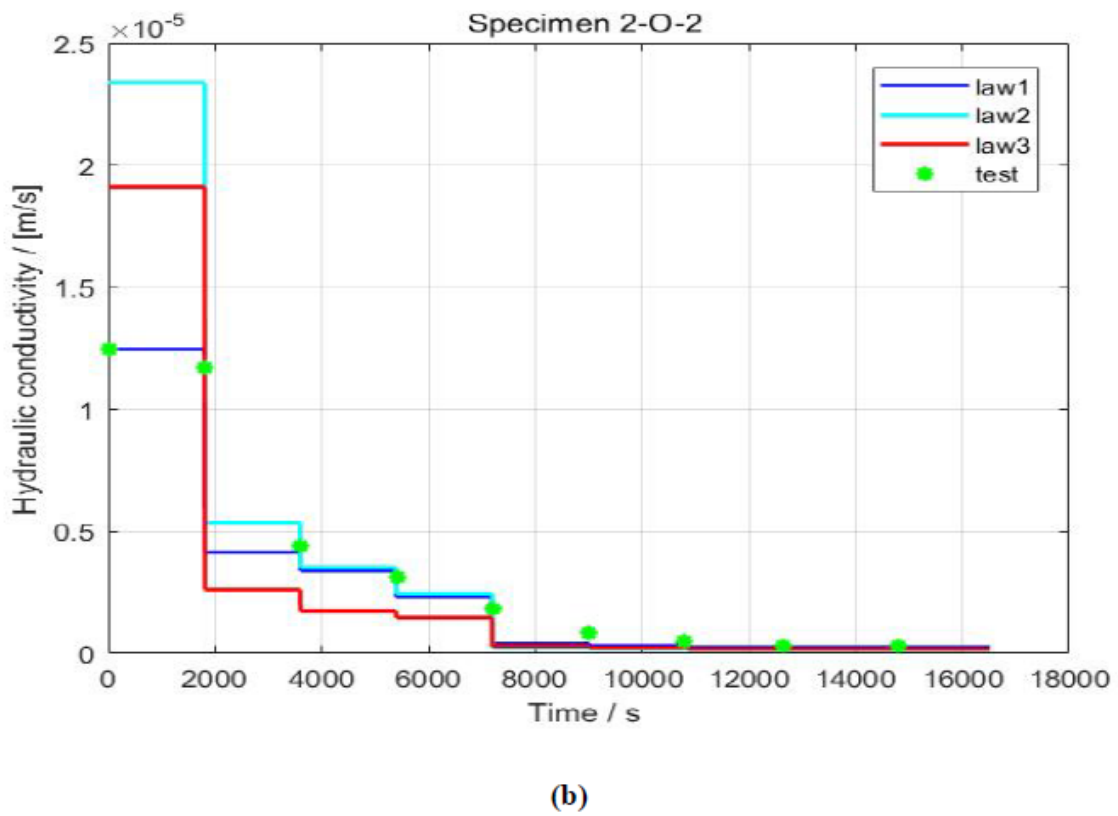
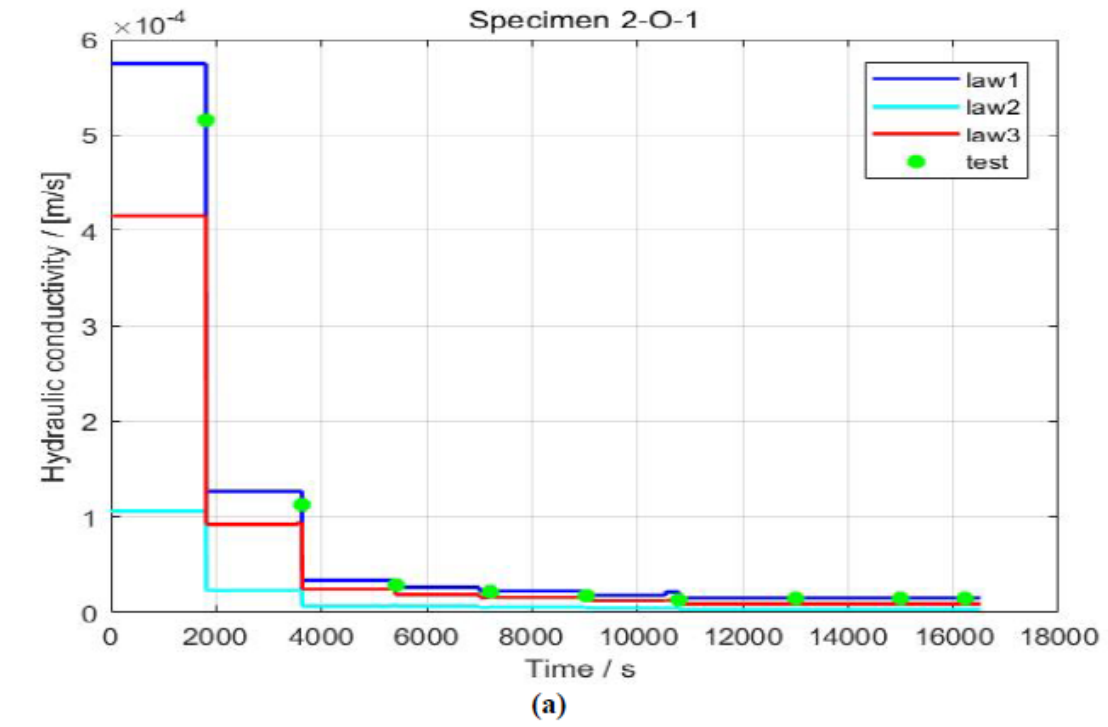


Figure VI.24 – Comparison of the calculated results of the hydraulic conductivity among three models (including experimental results) (a) specimen 2-O-1 (b) specimen 2-O-2

CONCLUSION AND PERSPECTIVES

7.1 Conclusion

Internal erosion is a complex phenomenon and one of the most common causes of damage to dikes and dams. Internal erosion is closely related to the urban environment. Dams and dikes are usually built upstream of the city. If there is the internal erosion in the dam, it will pose a huge threat to urban security. Therefore, researches on the internal erosion of earth structures will help protect life and property. Internal erosion is a multiphase and multi-field coupled problem, so it is also related to the multidisciplinary research of soil mechanics, fluid mechanics, environmental science, etc. The internal erosion problem is very complicated. Laboratory experiments are the main means used to study internal erosion problems, however, undoubtedly, the actual size of the earth structure is much larger than that of the laboratory specimen. Therefore whether the soil stability standard established, according to the experimental results of the laboratory, is applicable or not remains doubtful.

As one of the four types of internal erosion, suffusion refers to the selective erosion of fine particles from the soil by the flow. It is a type of internal erosion that has been widely discussed recently. The eroded fine particles are moved downstream by the flow, and during this movement, the fine particles may be filtered by the coarse particles as the filter layer to form a deposit. It can be seen that suffusion is a coupled process of the separation, movement and sedimentation of fine particles, and the microstructure of the soil is also changed. Since the fine particles are unevenly deposited, suffusion can lead to the heterogeneity of the specimen. Thus, the further development of suffusion depends on the influence of heterogeneity on suffusion.

Based on the factors mentioned above, a series of specially designed experiments was used to study the coupled process of erosion and filtration and the spatial scale effect of the specimen on suffusion. The flow direction for all experiments was downward.

The specimen used to study the coupled process of erosion and filtration was divided into two parts. The lower part consists entirely of coarse gravel as a filter layer and in the upper part, the binary mixture of sand and gravel mixed by 1:1 was placed in two ways, in the middle or in the gap. After analyzing the post-test particle size distribution, it can be found that the filtration exists not only in the vertical direction as the seepage direction but also in the horizontal direction. The fine particles are mainly filtered in the contact layer of the binary mixture and the filter layer, and the most filtered particles appear in the area closed to the mixture. The filtered fine particles decrease rapidly along the seepage length. Comparing the variation of permeability with the post-test gradation, it is obvious that a few fine particles can have a large impact on hydraulic conductivity. The filtration law is suitable in the filtration process of suffusion, which indicates the final state of the filtration process. In the suffusion process, the filtration process ends when the fine content is closed to the value computed by the basic filtration equation. The interface area between the binary mixture and filter layer has a certain influence on the permeability of the specimen. Because the contact area of two parts is not equal, the seepage direction in the binary mixture at the contact interface will change.

Both gap-graded and well-graded soils are selected to investigate the suffusion susceptibility by studying the local process. Due to the filtration of fine particles, the post-test fine content of some layers in the specimen exceeds the initial value. After comparing the homogeneous and heterogeneous specimens, it seems that heterogeneous specimens appear to be less stable for gap-graded soil. Thanks to the hydraulic pressure measuring ports, the local process of the suffusion can be analyzed. The position of the maximum value of the local hydraulic gradient is transferred from upstream to downstream. Finally, a large number of eroded particles are measured when the maximum local hydraulic gradient concerns the specimen's downstream part. The grain size of eroded particles becomes coarser with the development of the suffusion. But when this trend reaches a certain level, the grain size of eroded particles suddenly decreases and then increases. The trend is spiral. With the increase of the global hydraulic gradient, the blockage continuously forms and then disappears.

The process of the suffusion can be divided into three stages: "particle adjustment" stage, "stable seepage" stage, and "seepage change" stage. According to the mechanical characteristics of seepage deformation of soil, the mechanism of seepage deformation was analyzed. Combined with the movement of particles in the pore, the force analysis of a single soil particle showed that when the particles have a downward force component along the seepage path, this is the phenomenon of particle migration, harmless piping, or latent internal erosion. When the particles have an upward force component along the seepage path, the movable particles are suspended,

and when the forces of said particles are balanced, they constitute the deposition.

In the study of the spatial scale effect, a series of suffusion tests was carried out with two different sized devices to assess the suffusion susceptibility of six gradations. Tests with triaxial erodimeter were performed by Le Van Thao.

There is a loss of fine particles during the saturation phase even under upward flow and the quantity is not negligible. Thus, the saturation of specimens was systematically realized for both devices under the same moistening velocity to limit the discrepancy of the initial hydraulic conductivity.

For the tested clayey soil, the development of suffusion can induce backward erosion under low effective stress.

Among three methods used to study the suffusion susceptibility of tested specimens, the method of hydraulic gradient based on the increase of hydraulic conductivity cannot be used for all specimens and moreover the values of critical hydraulic gradient decrease with the length of the seepage path. In addition, for the method considering the shear stress of seepage, the erosion coefficient cannot be defined for all specimens and it increases with specimen size in the case of suffusion. The method based on energy is compatible to study the suffusion susceptibility. The reason is that the energy expended by the seepage and the cumulative loss dry mass are both computed at the steady state. The cumulative loss mass of tests on large device should be more than that of small device, however, the expanded energy of seepage on large device is also greater. At this time, the suffusion sensibility classification can be evaluated by the erosion resistance index which is in the same range for the same soil on both used devices.

The undisturbed soil is used in some specimens of Chavanay. These specimens formed with Chavanay contain some relatively large grains. The diameter of oedo-permeameter is 280 mm and the maximum height can be 600 mm, which is compatible with specimens containing relatively large grains. It increase the difficulty and the uncertainty of the experiment, but the experimental results are closer to the actual situation.

A new numerical approach considering the suffusion was given in this report. For modeling the erosion of the soil skeleton, the governing differential equations were formulated based on the mass balance of four assumed constituents: the stable fabric of the solid skeleton, the erodible fines, the fluidized particles, and the pure fluid. The terms of mass exchange were introduced into the mass balance equations. The coupled formulations are solved numerically by a finite difference method.

For specimen 1-O, the influences of number of calculation mesh nodes, length of specimen, initial hydraulic conductivity and initial fine content on the simulation results of suffusion are

comparatively analyzed through the erosion model 1. The results show that the increased number of spatial grid nodes had an influence on calculation results, but the spatial grid $NS = 300$ basically had no effect on simulation results. The specimen height also affects the cumulative eroded mass per cross-sectional area and flow rate, especially for large specimens. As well as the cumulative eroded mass per cross-sectional area, the effect of height on the flow rate is more obvious. The cumulative eroded mass per cross-sectional area and flow rate decrease if the specimen height increases, mainly as a result of a decreasing concentration of fluidized particles. The initial hydraulic conductivity is an important parameter influencing simulation results. The cumulative eroded mass per cross-sectional area increases with the increasing initial hydraulic conductivity. A single change to initial fines content has little effect on the simulation results and thus should not be taken into account.

Three erosion models are given by considering three erosion laws (including model 1). Then, three models are validated by simulating 1D suffusion tests. Simulation results present that these three models can reproduce the main features of the suffusion process. To further improve the performance of the three simulation models, eight experimental specimens were selected in order to test the practicability of three models. The results of the three erosion models used for simulation were very close, with the curves showing the same tendencies. There are two phases of the suffusion process distinguished from the time evolution of the hydraulic conductivity and both were well reproduced by the three erosion models. Hydraulic conductivity slowly increased at first, or depending on the hydraulic loading history, possibly decreased. The second phase of the hydraulic conductivity evolution was characterized by a rapid increase. Finally, hydraulic conductivity reached a constant value. The results showed that the numeric model is able to describe the suffusion process, and the calculated results agree well with the experimental results. The finite difference program is correct and can reflect the entire process of occurrence and development in the suffusion. Based on the comparison and analysis of the simulation results of three models, model 1 is the most suitable of the three models.

7.2 Perspectives

Further study on the impact of the saturation phase on the experimental results is necessary. And the interaction between the development and consequence of suffusion and soil mechanical behavior is also important.

For the numerical part, particle size parameters could be calibrated according to well documented experimental measurements and introduced into erosion or filtration laws. Coupled

models could also be extended to three dimensional conditions so as to obtain more complex geometric boundary conditions. As well as the experimental part, soil mechanical behavior could also be modeled.

REFERENCE

- Abrahamsen, P. and Hansen, S. Daisy: an open soil-crop-atmosphere system model. *Environmental Modelling and Software*, 15(3):313–330, 2000.
- ASTM Committee D18 on Soil and Rock. Standard Test Method for Unconsolidated-Undrained Triaxial Compression Test on Cohesive Soils. ASTM International, 2003.
- Bartsch, M. and Nilsson, Å. Leakage in embankment dams - Functional analysis and strengthening by adding a downstream berm. In Rutschmann, P., editor, *Proceedings of the 7th ICOLD European Club Dam Symposium*, pages 15–20, Freising, 2007. German Dams Committee.
- Bear, J. and Bachmat, Y. *Introduction to modeling of transport phenomena in porous media*, volume 4. Springer Science & Business Media, 2012.
- Benahmed, N. and Bonelli, S. Internal erosion of cohesive soils: laboratory parametric study. In Fry, J.-J. and Chevalier, C., editors, *Proceedings of 6th International Conference on Scour and Erosion*, pages 1041–1048, Paris, 2012.
- Bendahmane, F., Marot, D., Rosquoët, F., and Alexis, A. Characterization of internal erosion in sand kaolin soils: Experimental study. *Revue européenne de génie civil*, 10(4):505–520, 2006.
- Bendahmane, F., Marot, D., and Alexis, A. Experimental Parametric Study of Suffusion and Backward Erosion. *Journal of Geotechnical and Geoenvironmental Engineering*, 134(1): 57–67, 2008.
- Blind, H. Safety of dams. *International Water Power and Dam Construction*, 35(5):17–21, 1983.
- Bonelli, S. and Marot, D. On the modelling of internal soil erosion. In Jadhav, M. N., ed-

- itor, *Proceedings of 12th International Conference of International Association for Computer Methods and Advances in Geomechanics*, Goa, 2008.
- Chang, C. S. and Yin, Z.-Y. Micromechanical modeling for behavior of silty sand with influence of fine content. *International Journal of Solids and Structures*, 48(19):2655–2667, 2011.
- Chang, D. and Zhang, L. A Stress-controlled Erosion Apparatus for Studying Internal Erosion in Soils. *Geotechnical Testing Journal*, 34(6):579–589, 2011.
- Chang, D. and Zhang, L. Critical Hydraulic Gradients of Internal Erosion under Complex Stress States. *Journal of Geotechnical and Geoenvironmental Engineering*, 139(9):1454–1467, 2013a.
- Chang, D. and Zhang, L. Extended internal stability criteria for soils under seepage. *Soils and Foundations*, 53(4):569–583, 2013b.
- Chung, K. Y. and Kikuchi, N. Adaptive methods to solve free boundary problems of flow through porous media. *International Journal for Numerical and Analytical Methods in Geomechanics*, 11(1):17–31, 1987.
- Cividini, A. and Gioda, G. Finite-Element Approach to the Erosion and Transport of Fine Particles in Granular Soils. *International Journal of Geomechanics*, 4(3):191–198, 2004.
- Cividini, A., Bonomi, S., Vignati, G. C., and Gioda, G. Seepage-induced erosion in granular soil and consequent settlements. *International Journal of Geomechanics*, 9(4):187–194, 2009.
- Cryer, C. W. A Comparison of the Three-Dimensional Consolidation Theories of Biot and Terzaghi. *The Quarterly Journal of Mechanics and Applied Mathematics*, 16(4):401–412, 1963.
- Cyganiewicz, J., Sills, G., Fell, R., Davidson, R., Foster, M., and Vroman, N. Seepage and piping toolbox-overview. In *Proceedings of the 28th USSD Annual Meeting and Conference*, Portland, 2008.
- de Frias Lopez, R., Silfwerbrand, J., Jelagin, D., and Birgisson, B. Force transmission and soil fabric of binary granular mixtures. *Géotechnique*, 66(7):578–583, 2016.
- DeKay, M. L. and McClelland, G. H. Predicting Loss of Life in Cases of Dam Failure and Flash Flood. *Risk Analysis*, 13(2):193–205, 1993.

- Desai, C. S. Finite element residual schemes for unconfined flow. *International Journal for Numerical Methods in Engineering*, 10(6):1415–1418, 1976.
- Fell, R. and Fry, J.-J. The state of the art of assessing the likelihood of internal erosion of embankment dams, water retaining structures and their foundations. In Fell, R. and Fry, J.-J., editors, *Internal Erosion of Dams and Their Foundations*, pages 1–23. Taylor & Francis, London, 2007.
- Fell, R. and Fry, J.-J. State of The Art on the Likelihood of Internal Erosion of Dams and Levees by Means of Testing. In Bonelli, S., editor, *Erosion in Geomechanics Applied to Dams and Levees*, pages 1–99. London, 2013.
- Fell, R., Wan, C. F., Cyganiewicz, J., and Foster, M. Time for Development of Internal Erosion and Piping in Embankment Dams. *Journal of Geotechnical and Geoenvironmental Engineering*, 129(4):307–314, 2003.
- Fell, R., MacGregor, P., Stapledon, D., and Bell, G. *Geotechnical Engineering of Dams*. Taylor & Francis, London, 1st edition, 2005.
- Foster, M., Fell, R., and Spannagle, M. The statistics of embankment dam failures and accidents. *Canadian Geotechnical Journal*, 37(5):1000–1024, 2000.
- Fredlund, D. G. and Hasan, J. U. One-dimensional consolidation theory: unsaturated soils. *Canadian Geotechnical Journal*, 16(3):521–531, 1979.
- Fredlund, D. G. and Xing, A. Equations for the soil-water characteristic curve. *Canadian Geotechnical Journal*, 31(3):521–532, 1994.
- Freeze, R. A. Three-Dimensional, Transient, Saturated-Unsaturated Flow in a Groundwater Basin. *Water Resources Research*, 7(2):347–366, 1971.
- Fry, J.-J., Vogel, A., Royet, P., and Courivaud, J.-R. Dam failures by erosion: lessons from ERINOH data bases. In *Proceedings of 6th International Conference on Scour and Erosion*, pages 273–280, Paris, 2012.
- Fujisawa, K., Murakami, A., and Nishimura, S.-i. Numerical analysis of the erosion and the transport of fine particles within soils leading to the piping phenomenon. *Soils and Foundations*, 50(4):471–482, 2010.
- Garner, S. J. and Fannin, R. J. Understanding internal erosion: A decade of research following a sinkhole event. *International Journal on Hydropower and Dams*, 17(3):93–100, 2010.

- Guide, M. U. The mathworks. *Inc., Natick, MA*, 5:333, 1998.
- Hansbo, S. *Consolidation of clay, with special reference to influence of vertical sand drains. A Study Made in Connection with Full-Scale Investigations at Skå-Edeby*. Swedish Geotechnical Institute, Stockholm, 1st edition, 1960.
- Hoffmans, G. J. C. M. *The Influence of Turbulence on Soil Erosion*. Eburon Academic Publishers, Delft, 1st edition, 2012.
- Hu, W., Hicher, P.-Y., Scaringi, G., Xu, Q., Van Asch, T., and Wang, G. Seismic precursor to instability induced by internal erosion in loose granular slopes. *Géotechnique*, pages 1–13, 2018.
- Hunter, R. P. Development of Transparent Soil Testing using Planar Laser Induced Fluorescence in the Study of Internal Erosion of Filters in Embankment Dams. Master's thesis, University of Canterbury, Canterbury, 2012.
- ICOLD. *Lessons from dam incidents*. Complete edition. International Commission on Large Dams (ICOLD), Paris, 1974.
- ICOLD. *Dam failures statistical analysis*. Bulletin 99. International Commission on Large Dams (ICOLD), Paris, 1995.
- Indraratna, B., Nguyen, V. T., and Rujikiatkamjorn, C. Assessing the Potential of Internal Erosion and Suffusion of Granular Soils. *Journal of Geotechnical and Geoenvironmental Engineering*, 137(5):550–554, 2011.
- Indraratna, B., Israr, J., and Rujikiatkamjorn, C. Geometrical Method for Evaluating the Internal Instability of Granular Filters Based on Constriction Size Distribution. *Journal of Geotechnical and Geoenvironmental Engineering*, 141(10):04015045, 2015.
- Iwasaki, T., Slade, J. J., and Stanley, W. E. Some Notes on Sand Filtration [with Discussion]. *Journal American Water Works Association*, 29(10):1591–1602, 1937.
- Javandel, I. and Witherspoon, P. A. Application of the Finite Element Method to Transient Flow in Porous Media. *Society of Petroleum Engineers Journal*, 8(3):241–252, 1968.
- Jonkman, S. N., Vrijling, J. K., and Vrouwenvelder, A. C. W. M. Methods for the estimation of loss of life due to floods: a literature review and a proposal for a new method. *Natural Hazards*, 46(3):353–389, 2008.

- Juncu, G., Nicola, A., and Popa, C. Nonlinear multigrid methods for solving Richards' equations in two space dimensions. *Transport in Porous Media*, 83(3):637–652, 2009.
- Ke, L. and Takahashi, A. Strength reduction of cohesionless soil due to internal erosion induced by one-dimensional upward seepage flow. *Soils and Foundations*, 52(4):698–711, 2012.
- Ke, L. and Takahashi, A. Experimental investigations on suffusion characteristics and its mechanical consequences on saturated cohesionless soil. *Soils and Foundations*, 54(4):713–730, 2014.
- Ke, L. and Takahashi, A. Drained Monotonic Responses of Suffusional Cohesionless Soils. *Journal of Geotechnical and Geoenvironmental Engineering*, 141(8):04015033, 2015.
- Kenney, T. C. and Lau, D. Internal stability of granular filters. *Canadian Geotechnical Journal*, 22(2):215–225, 1985.
- Kézdi, Á. *Soil physics: selected topics*, volume 25. Elsevier, 1st edition, 1979.
- Kovács, G. *Seepage Hydraulics*, volume 10 of *Developments in Water Science*. Elsevier, Amsterdam, 1st edition, 1981.
- Lafleur, J., Mlynarek, J., and Rollin, A. L. Filtration of Broadly Graded Cohesionless Soils. *Journal of Geotechnical Engineering*, 115(12):1747–1768, 1989.
- Lam, L. and Fredlund, D. G. Saturated-unsaturated transient finite element seepage model for geotechnical engineering. *Advances in Water Resources*, 7(3):132–136, 1984.
- Lee, D. H. and Abriola, L. M. Use of the Richards equation in land surface parameterizations. *Journal of Geophysical Research: Atmospheres*, 104(D22):27519–27526, 1999.
- Lei, X., Yang, Z., He, S., Liu, E., Wong, H., and Li, X. Numerical investigation of rainfall-induced fines migration and its influences on slope stability. *Acta Geotechnica*, 12(6):1431–1446, 2017.
- Li, M. *Seepage induced instability in widely graded soils*. PhD thesis, University of British Columbia, Vancouver, 2008.
- Li, M. and Fannin, R. J. Comparison of two criteria for internal stability of granular soil. *Canadian Geotechnical Journal*, 45(9):1303–1309, 2008.
- Li, M. and Fannin, R. J. A theoretical envelope for internal instability of cohesionless soil. *Géotechnique*, 62(1):77–80, 2012.

- Lominé, F., Scholtès, L., Sibille, L., and Poullain, P. Modeling of fluid–solid interaction in granular media with coupled lattice Boltzmann/discrete element methods: application to piping erosion. *International Journal for Numerical and Analytical Methods in Geomechanics*, 37(6):577–596, 2013.
- Marot, D., Regazzoni, P.-L., and Wahl, T. Energy-Based Method for Providing Soil Surface Erodibility Rankings. *Journal of Geotechnical and Geoenvironmental Engineering*, 137(12): 1290–1293, 2011.
- Marot, D., Le, V. D., Garnier, J., Thorel, L., and Audrain, P. Study of scale effect in an internal erosion mechanism: centrifuge model and energy analysis. *European Journal of Environmental and Civil Engineering*, 16(1):1–19, 2012.
- Marot, D., Rochim, A., Nguyen, H.-H., Bendahmane, F., and Sibille, L. Assessing the susceptibility of gap-graded soils to internal erosion: proposition of a new experimental methodology. *Natural Hazards*, 83(1):365–388, 2016.
- Marot, D., Bendahmane, F., Andrianatrehina, R., and Gelet, R. Large triaxial device for suffusion erodibility and mechanical behavior characterization of coarse soils. In van Beek, V. M. and Koelewijn, A. R., editors, *25th Meeting of the European Working Group on Internal Erosion*, pages 123–132, Delft, 2017.
- McNamee, J. and Gibson, R. E. Plane Strain and Axially Symmetric Problems of the Consolidation of a Semi Infinite Clay Stratum. *The Quarterly Journal of Mechanics and Applied Mathematics*, 13(2):210–227, 1960.
- Miller, C. T., Abhishek, C., and Farthing, M. W. A spatially and temporally adaptive solution of Richards’ equation. *Advances in Water Resources*, 29(4):525–545, 2006.
- Moffat, R., Fannin, R. J., and Garner, S. J. Spatial and temporal progression of internal erosion in cohesionless soil. *Canadian Geotechnical Journal*, 48(3):399–412, 2011.
- Moffat, R. A. and Fannin, R. J. A Large Permeameter for Study of Internal Stability in Cohesionless Soils. *Geotechnical Testing Journal*, 29(4):273–279, 2006.
- Murad, M. A. and Loula, A. F. D. Improved accuracy in finite element analysis of Biot’s consolidation problem. *Computer Methods in Applied Mechanics and Engineering*, 95(3):359–382, 1992.

- Neuman, S. P. Saturated-Unsaturated Seepage by Finite Elements. *Journal of the Hydraulics Division*, 99(12):2233–2250, 1973.
- NPDP. NPDP Database, 2017. URL http://npdp.stanford.edu/consequences_fatalities.
- Papamichos, E., Vardoulakis, I., Tronvoll, J., and Skjaerstein, A. Volumetric sand production model and experiment. *International Journal for Numerical and Analytical Methods in Geomechanics*, 25(8):789–808, 2001.
- Perzmaier, S. Hydraulic criteria for internal erosion in cohesionless soil. In Fell, R. and Fry, J.-J., editors, *Internal Erosion of Dams and Their Foundations*, pages 179–190. Taylor & Francis, London, 2007.
- Rank, E. and Werner, H. An adaptive finite element approach for the free surface seepage problem. *International Journal for Numerical Methods in Engineering*, 23(7):1217–1228, 1986.
- Reboul, N. *Transport de particules dans les milieux granulaires: Application à l'érosion interne*. PhD thesis, Ecole Centrale de Lyon, Ecully, 2008.
- Reddi, L. N., Lee, I.-M., and Bonala, M. V. Comparison of Internal and Surface Erosion Using Flow Pump Tests on a Sand-Kaolinite Mixture. *Geotechnical Testing Journal*, 23(1):116–122, 2000.
- Richards, K. S. and Reddy, K. R. Critical appraisal of piping phenomena in earth dams. *Bulletin of Engineering Geology and the Environment*, 66(4):381–402, 2007.
- Rochim, A., Marot, D., Sibille, L., and Le, V. T. Effects of Hydraulic Loading History on Suffusion Susceptibility of Cohesionless Soils. *Journal of Geotechnical and Geoenvironmental Engineering*, 143(7):04017025, 2017.
- Sail, Y., Marot, D., Sibille, L., and Alexis, A. Suffusion tests on cohesionless granular matter. *European Journal of Environmental and Civil Engineering*, 15(5):799–817, 2011.
- Sandhu, R. S. and Wilson, E. L. Finite-Element Analysis of Seepage in Elastic Media. *Journal of the Engineering Mechanics Division*, 95(3):641–652, 1969.
- Sari, H., Chareyre, B., Catalano, E., Philippe, P., and Vincens, E. Investigation of internal erosion processes using a coupled dem-fluid method. In E., O. and DRJ, O., editors, *Particles 2011 II International Conference on Particle-Based Methods*, pages 1–11, Barcelona, 2011.

- Schaufler, A., Becker, C., and Steeb, H. Infiltration processes in cohesionless soils. *ZAMM- Journal of Applied Mathematics and Mechanics/Zeitschrift für Angewandte Mathematik und Mechanik*, 93(2-3):138–146, 2013.
- Scholtès, L., Hicher, P.-Y., and Sibille, L. Multiscale approaches to describe mechanical responses induced by particle removal in granular materials. *Comptes Rendus Mécanique*, 338 (10-11):627–638, 2010.
- Schuler, U. How to deal with the problem of suffusion. In *Proceedings of European Symposium on Research and Development in the Field of Dams*, pages 145–159, Crans-Montana, 1995. Swiss National Committee on Large Dams.
- Sellmeijer, H., López de la Cruz, J., van Beek, V. M., and Knoeff, H. Fine-tuning of the backward erosion piping model through small-scale, medium-scale and IJkdijk experiments. *European Journal of Environmental and Civil Engineering*, 15(8):1139–1154, 2011.
- Sellmeijer, J. B. *On the mechanism of piping under impervious structures*. PhD thesis, Technische Universiteit Delft, Delft, 1988.
- Shen, S.-L. and Xu, Y.-S. Numerical evaluation of land subsidence induced by groundwater pumping in Shanghai. *Canadian Geotechnical Journal*, 48(9):1378–1392, 2011.
- Shen, S. L., Wang, Z. F., and Cheng, W. C. Estimation of lateral displacement induced by jet grouting in clayey soils. *Géotechnique*, 67(7):621–630, 2017.
- Sherard, J. L. Sinkholes in Dams of Coarse, Broadly Graded Soils. In *Proceedings of 13th ICOLD Congress*, pages 25–35, New Delhi, 1979.
- Sherard, J. L., Woodward, R. J., and Gizienski, S. F. *Earth and Earth Rock Dams : Engineering Problems of Design and Construction*. John Wiley & Sons, New York, 1st edition, 1963.
- Sherard, J. L., Dunnigan, L. P., and Talbot, J. R. Filters for silts and clays. *Journal of Geotechnical Engineering*, 110(6):701–718, 1984.
- Sibille, L., Lominé, F., Poullain, P., Sail, Y., and Marot, D. Internal erosion in granular media: direct numerical simulations and energy interpretation. *Hydrological Processes*, 29(9):2149–2163, 2014.
- Sibille, L., Lominé, F., Poullain, P., Sail, Y., and Marot, D. Internal erosion in granular media: direct numerical simulations and energy interpretation. *Hydrological Processes*, 29(9):2149–2163, 2015.

- Skempton, A. W. and Brogan, J. M. Experiments on piping in sandy gravels. *Géotechnique*, 44 (3):449–460, 1994.
- Stein, P. C. *A study of the theory of rapid filtration of water through sand*. PhD thesis, Massachusetts Institute of Technology, Cambridge, 1940.
- Sterpi, D. Effects of the Erosion and Transport of Fine Particles due to Seepage Flow. *International Journal of Geomechanics*, 3(1):111–122, 2003.
- Teh, I. C. and Xiaoyan, N. Coupled consolidation theory with non-Darcian flow. *Computers and Geotechnics*, 29(3):169–209, 2002.
- Terzaghi, K. v. Der Grundbruch an Stauwerken und seine Verhütung. *Wasserkraft*, 17(24): 445–449, 1922.
- Terzaghi, K. v. 45th James Forrest Lecture, 1939. Soil Mechanics – A new chapter in Engineering Science. *Journal of the Institution of Civil Engineers*, 12(7):106–142, 1939.
- USCOLD. *Lessons from dam incidents*. USA. American Society of Civil Engineers, 1975.
- USCOLD. *Lessons from dam incidents*. USA-2. American Society of Civil Engineers, 1988.
- Uzuoka, R., Ichiyama, T., Mori, T., and Kazama, M. Hydro-mechanical analysis of internal erosion with mass exchange between solid and water. In *6th International Conference on Scour and Erosion*, pages 655–662, 2012.
- Vardoulakis, I., Stavropoulou, M., and Papanastasiou, P. Hydro-mechanical aspects of the sand production problem. *Transport in porous media*, 22(2):225–244, 1996.
- Vermeer, P. A. and Verruijt, A. An Accuracy Condition for Consolidation by Finite Elements. *International Journal for Numerical and Analytical Methods in Geomechanics*, 5(1):1–14, 1981.
- Vogel, A. *Bibliography of the history of dam failures*. Data-Station for Dam Failures, Vienna, 1981.
- Wan, C. F. and Fell, R. Investigation of Rate of Erosion of Soils in Embankment Dams. *Journal of Geotechnical and Geoenvironmental Engineering*, 130(4):373–380, 2004.
- Wan, C. F. and Fell, R. Assessing the Potential of Internal Instability and Suffusion in Embankment Dams and Their Foundations. *Journal of Geotechnical and Geoenvironmental Engineering*, 134(3):401–407, 2008.

- Wang, M., Feng, Y. T., Pande, G. N., Chan, A., and Zuo, W. X. Numerical modelling of fluid-induced soil erosion in granular filters using a coupled bonded particle lattice Boltzmann method. *Computers and Geotechnics*, 82:134–143, 2017.
- Wennberg, K., Batrouni, G., and Hansen, A. Modelling Fines Mobilization, Migration and Clogging. In *SPE European Formation Damage Conference*. Society of Petroleum Engineers, 1995.
- Wong, H., Zhang, X. S., Leo, C. J., and Bui, T. A. Internal Erosion of Earth Structures as a Coupled Hydromechanical Process. *Applied Mechanics and Materials*, 330:1084–1089, 2013.
- Wu, H.-N., Shen, S.-L., and Yang, J. Identification of tunnel settlement caused by land subsidence in soft deposit of Shanghai. *Journal of Performance of Constructed Facilities*, 31(6): 04017092, 2017.
- Yang, D., Feng, Y., Liu, J., and Liu, Q. Study on Equation of the Granular Bedding Clarification Filtration and its Theoretical Solution. *Journal of Shenyang University of Chemical Technology*, 14(1):48–50, 2000.
- Yao, K.-M., Habibian, M. T., and O’Melia, C. R. Water and Waste Water Filtration: Concepts and Applications. *Environmental Science & Technology*, 5(11):1105–1112, 1971.
- Yin, Z.-Y., Zhao, J., and Hicher, P.-Y. A micromechanics-based model for sand-silt mixtures. *International Journal of Solids and Structures*, 51(6):1350–1363, 2014.
- Yin, Z.-Y., Huang, H.-W., and Hicher, P.-Y. Elastoplastic modeling of sand–silt mixtures. *Soils and Foundations*, 56(3):520–532, 2016.
- Zhang, L., Xu, Y., and Jia, J. S. Analysis of earth dam failures: A database approach. *Georisk: Assessment and Management of Risk for Engineered Systems and Geohazards*, 3(3):184–189, 2009.
- Zhang, L., Peng, M., Chang, D., and Xu, Y. *Dam Failure Mechanisms and Risk Assessment*. John Wiley & Sons, Singapore, 1st edition, 2016.
- Zhao, J. and Shan, T. Coupled CFD–DEM simulation of fluid–particle interaction in geomechanics. *Powder technology*, 239:248–258, 2013.
- Zou, Y.-H., Chen, Q., Chen, X.-Q., and Cui, P. Discrete numerical modeling of particle transport in granular filters. *Computers and Geotechnics*, 47:48–56, 2013.

PUBLICATION

1. Zhong C., Le V.T., Bendahmane F., Marot D., Yin Z.Y. (2018). Investigation of spatial scale effects on suffusion susceptibility. *Journal of Geotechnical and Geoenvironmental Engineering (ASCE)*, 144(9): 04018067. DOI: 10.1061/(ASCE)GT.1943-5606.0001935
2. Chen, J., Chen, J., Zhong, C., Chen, S., Chen, B., Fang, S., & Xiang, W. (2017). Mesoscopic probes in asphaltene nanoaggregate structure: from perpendicular to parallel orientation at the water-in-oil emulsions interface. *RSC Advances*, 7(61), 38193-38203. <http://doi.org/10.1039/C7RA06717H>
3. Zhong C., Le V.T., Bendahmane F., Marot D., Yin Z. (2018). Investigation of Local Processes and Spatial Scale Effects on Suffusion Susceptibility. In: Farid A., Chen H. (eds) *Proceedings of GeoShanghai 2018 International Conference: Geoenvironment and Geohazard*. GSIC 2018. Springer, Singapore. (298-305). ISBN 978-981-13-0128-5. DOI https://doi.org/10.1007/978-981-13-0128-5_34.
4. Tejada I.G., Sibille L., Chareyre B., Zhong C., Marot D. (2017). Multiscale modeling of transport of grains through granular assemblies. *Powders and grains*. 3-7 July 2017, Montpellier, France.
5. Marot D., Zhong C., Le V. T., Bendahmane F. (2016). Spatial and time scale-effects on suffusion characterizations - what alternatives? *The International Symposium on the Mechanics of Internal Erosion for Dams and Levees*. U.S. Society on Dams. 9-11 August, 2016, Salt Lake City, Utah, USA
6. Zhong C., Le V.T., Marot D., Bendahmane F. (2016). Comparison of erodimeters and interpretative methods for suffusion susceptibility characterization. *EMI International Conference*. 25-27 October 2016, Metz, France.
7. Marot D., Bendahmane F., Gelet R., Le V. T., Zhang L., Zhong C. (2019). Sensibilité à la suffusion, de l'échantillon à l'ouvrage. *Digue 2019*, 20-21 mars 2019, Aix-en-Provence.

8. Le V. T., Zhong C., Bendahmane F., Marot D. (2017). Effets d'échelles spatiale et temporelle sur les caractérisations de la sensibilité des sols à la suffusion. 35èmes Rencontres de l'AUGC, 22-24 mai 2017, Nantes.

CONTRIBUTION TO THE DEVELOPMENT OF A NEW TRIAXIAL DEVICE

A.1 Introduction

As a result of researchers' focus on characterizing suffusion susceptibility, a number of methods for describing suffusion potential based on soil gradation and the onset of internal erosion according to hydraulic loading have been proposed during the past few decades (see Chapters II, IV and V). However, suffusion's mechanical influences of suffusion on soil remains an open question, with the findings of several already published investigations having contradicted one another. Chang and Zhang (Chang and Zhang, 2013a) performed drained monotonic compression tests at different stress states on a gap-graded cohesionless soil and concluded that after the loss of a significant amount of fine particles in the soil, the original dilative stress-strain behavior becomes a contractive one and the peak stress decreases. In the same way, Ke and Takahashi (Ke and Takahashi, 2015) tested three gap-graded mixtures, composed of two sands, and showed that the soil strength decreases after suffusion.

To the contrary, Sterpi (Sterpi, 2003) tested samples of well-graded silty sand and concluded that the partial or total removal of the fine particles produces an increase of stiffness and shear strength. However, it is worth stressing that for this study, the drained triaxial compression tests were performed on non-eroded specimens. The homogeneous specimens were reconstituted with a fine percentage which should represent the post-suffusion gradation.

Such opposition among conclusions may arise from the different types of gradation involved because mechanical responses to the suffusion of gap-graded and well-graded soils perhaps are

different. Yet another reason, however, might be the heterogeneity triggered by the suffusion process, which cannot be appropriately represented by a reconstituted specimen, even one having the same gradation as of a post-suffusion specimen.

To arrive at a methodology for characterizing the mechanical influences of suffusion on undisturbed soils, a dedicated apparatus and methodology are required. Because the largest particle diameter must be less than a sixth the specimen diameter (ASTM Committee D18 on Soil and Rock, 2003), the triaxial apparatus must permit testing of a specimen of sufficient size to approximate, as much as possible, the real scale. The development of a new experimental device, called a large triaxial erodimeter, was initiated with funding obtained under the Contrat de Plan Etat - Région (CPER) and finalized thanks to a financial support from Électricité de France (EDF). While performing filtration and suffusion tests during my period of research for this PhD, I had the opportunity to use this device (with the help of Fateh Bendahmane, as safety considerations prevent use of the device alone) to initiate a study of the consequences of suffusion development on soil mechanical behavior.

A.2 Validation tests

A.2.1 Main characteristics of testing device

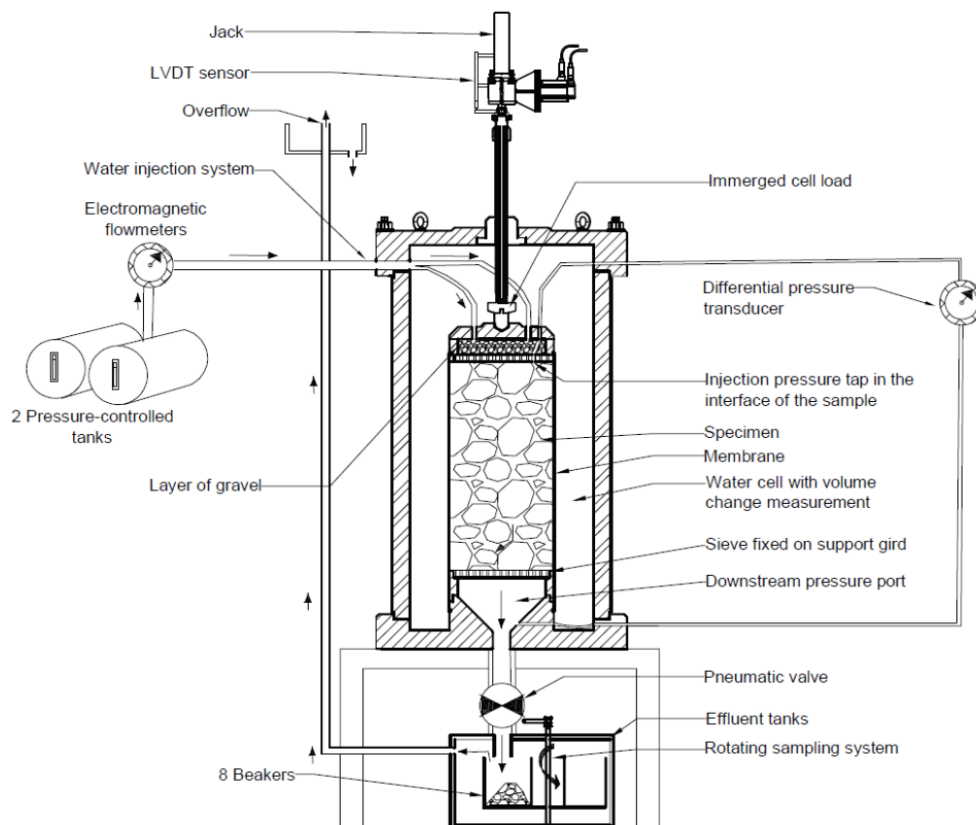


Figure A.1 – Schematic diagram of the large triaxial erodimeter



Figure A.2 – General view of the large triaxial erodimeter

This device is composed of a large triaxial cell that can support a sample up to 300 mm in diameter and 600 mm in height and thus is compatible with the specimens containing a relatively large maximum grain size which is typical for several dikes in France. During the verification phase, the device is configured to test the specimens having a 200 mm diameter. The main bench characteristics of the invention are described in Figure A.1 (Marot et al., 2017). Figure A.2 displays a general view of the device. This device allows performance of triaxial mechanical tests and internal erosion tests with independent controlling of multistage hydraulic gradient and stress state. For the hydraulic loading, the fluid is provided by two pressure tanks of 200 L each, controlled by a control panel (see Figure A.1), allowing continuous variation of tank pressure to inject water into the sample. Seepage flow circulates into the top cap, which contains a layer of gravel with which to diffuse the hydraulic loading uniformly on the top surface of the specimen. The cell base is equipped with a funnel-shaped draining system, specially designed to avoid clogging. Eroded particles are collected by using a collection tank that contains a rotating support with eight beakers, which maintains a constant hydraulic head downstream. The specimen is placed on a sieve with 1.2 mm pore opening size, fixed on a 10 mm mesh screen. Based on the seepage flow range, two electromagnetic flowmeters can be selected. The differential pore water pressure between upstream and downstream is measured by using a differential pressure transducer connected to the top cap and base pedestal of the triaxial cell. The mechanical stress is ensured by a mechanical jack that can be driven either under constant strain rate, or constant stress rate up to an axial force of 64 kN. An immersed load cell is equipped to measure the axial force on the loading rod. A linear variable differential transducer (LVDT) sensor is used to measure the piston displacement and thus the specimen axial strain. During the tests, an acquisition system is set up to measure the deviatoric stress, the injection flow, the differential pore water pressure under the hydraulic stress, and the axial and volume deformation of the sample. The evolution of all these quantities can be visualized during the tests.

A.2.2 Specimen preparation and testing program

The processes of saturation and consolidation follow the methodology described in Bendahmane et al. (Bendahmane et al., 2008). For this validation experiment, two identical specimens are used. The first specimen is subjected to a monotonic compression triaxial test under the drained condition to evaluate the mechanical strength of the intact soil. To evaluate the mechanical strength of the soil after suffusion test, the second specimen is subjected to a suffusion-triaxial test. This second test comprises three successive steps: 1) apply the same mechanical loading

path as the first specimen until the deviatoric stress reaches the value of geostatic stress applied in situ on the considered sample, 2) a full suffusion test on the second specimen is performed with a downward seepage flow under a multistage hydraulic gradient and 3) increase the deviatoric stress until the specimen fails to study the influence of suffusion on the mechanical consequences.

A.2.3 Testing materials

To verify the validity of the new instrument, the suffusion susceptibility and the mechanical consequences of suffusion were evaluated for the well-graded soil (named as soil 11.2-11.7) coming from a French dike. The soil name relates to its depth location within the dike (see Figure A.3).

The grain size distribution of the gradation, measured by a laser diffraction particle size analyzer, is shown in Figure A.4. According to criteria based on grain size, proposed by Kenney and Lau (Kenney and Lau, 1985) and Indraratna et al. (Indraratna et al., 2015), the soil is internally unstable (see Table A.1). As the percentage of fine P is smaller than 5%, and as $(H/F)_{min}$ is smaller than 1, the assessment using Chang and Zhang's method (Chang and Zhang, 2013b) classifies the soil as internally unstable. According to Wan and Fell (Wan and Fell, 2008), however, the widely graded soil is classified as internally stable. Consequently, it seems difficult to draw conclusions about the potential susceptibility and the suffusion test is required.



Figure A.3 – Picture of the soil in site

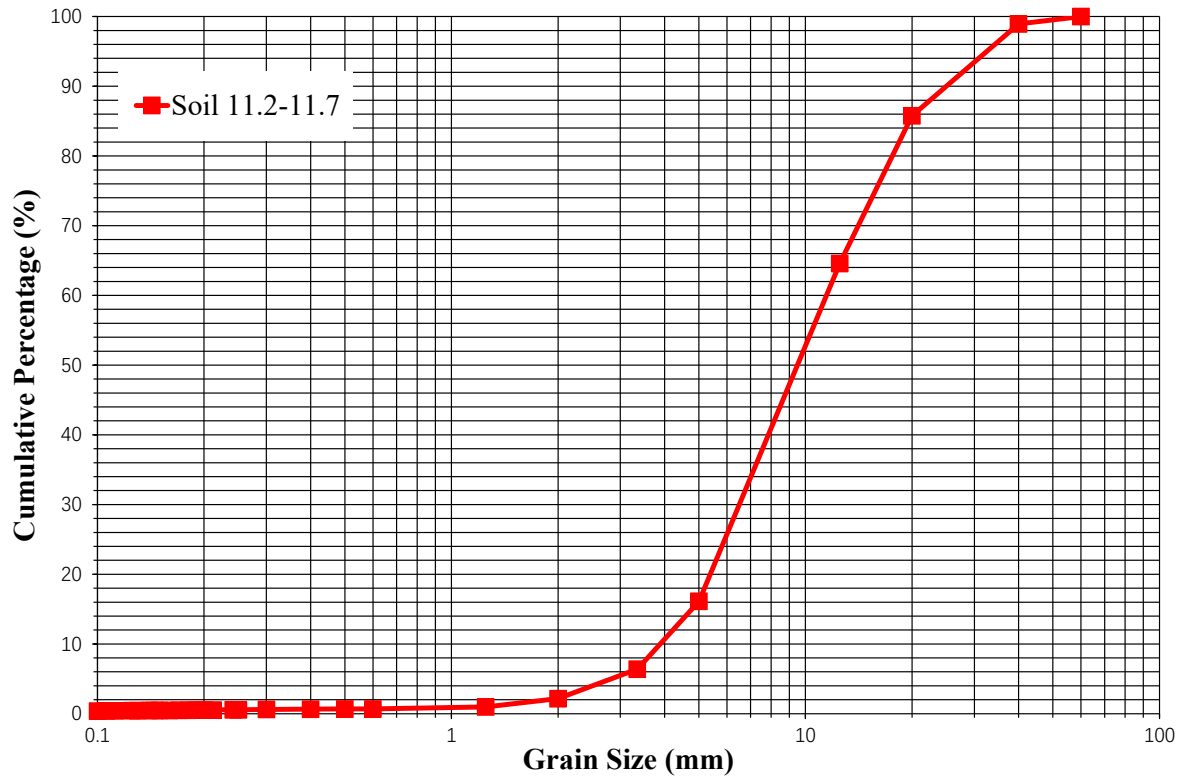


Figure A.4 – Grain size distribution before test

Table A.1 – Properties of tested soil

P (%)	0.31
G_r	WG
C_u	2.98
d_{15}/d_{85}	0.24
$(H/F)_{min}$	0.40
$D(H/F)_{min}$ (mm)	15.00
$D_{c35}^c/d_{85,SA}^f$	145.74
Kenney and Lau's criterion	U
Wan and Fell's criterion	S
Chang and Zhang's criterion	U
Indraratna's criterion	U

Note: P = percentage of particle smaller than 0.063 mm; $G_r = d_{max}/d_{min}$ (d_{max} and d_{min} : maximum and minimum particle sizes characterizing the gap in the grading curve); C_u = uniformity coefficient; d_{15} and d_{85} are the sieve sizes for which 15% and 85% of the weighed soil is finer, respectively; F and H are the mass percentages of the grains with a size, lower than a given particle diameter d and between d and $4d$, respectively; $D(H/F)_{min}$ is the corresponding

diameter with the minimum value of ratio H/F ; D_{c35}^c is the controlling constriction for coarser fraction from constriction size distribution by surface area technique; $d_{85,SA}^f$ is the representative size for a finer fraction using a surface area technique; WG = widely graded soil; U = unstable; S = stable.

A.3 Test results and discussion

A.3.1 Post-test particle size distributions of specimens

After test, the second specimen was divided into four layers to measure the post-suffusion grain size distribution for each layer. The layer 1 is in the upstream portion of the specimen and layer 4 is in the downstream part. Figure A.5 shows the initial gradation and the post-suffusion gradation for each layer. As described in Chapter IV, the loss of fine particles is slightly greater in the upstream part of the specimen than in the middle, consistent with the result of Ke and Takahashi (Ke and Takahashi, 2012). The detached particles carried downstream by flow from the upstream part can partially offset the loss of particles in the downstream part. The results further indicate that suffusion is a complex combination of three processes: detachment, transport, and possible filtration of the fine fraction. Consequently, a homogeneous reconstituted specimen cannot represent an eroded specimen even if both have the same average particle size distribution.

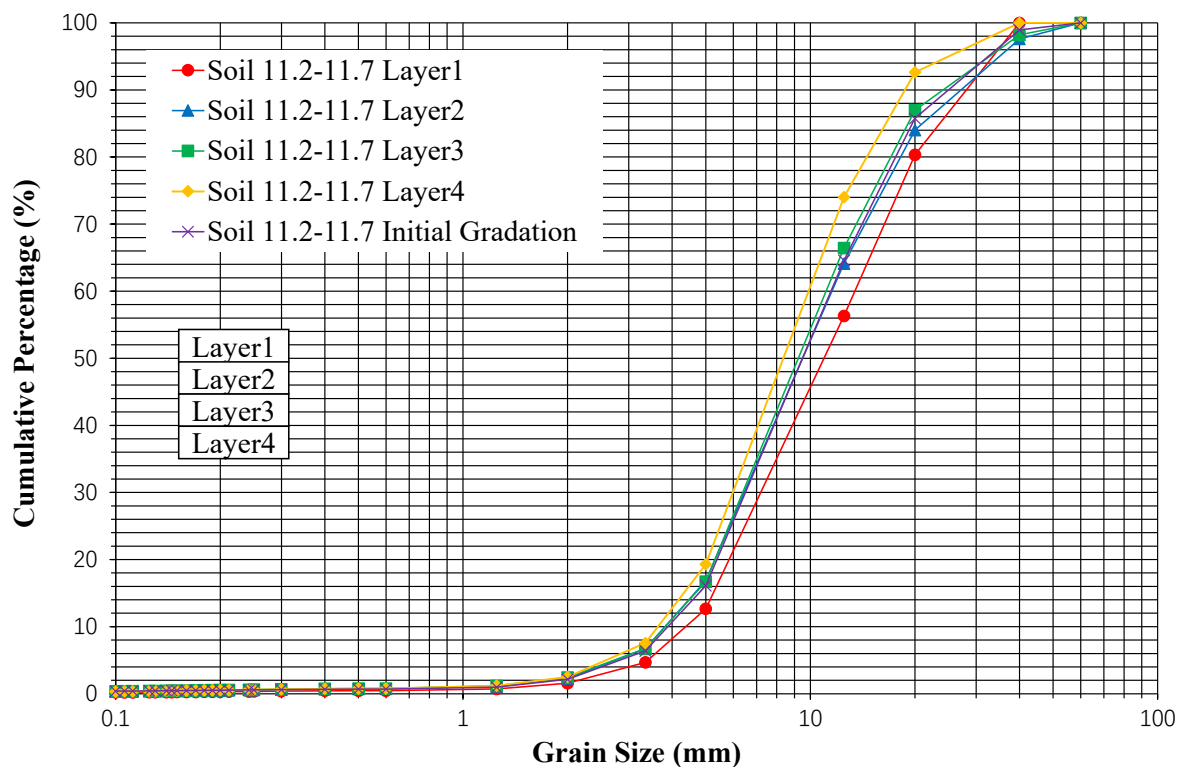
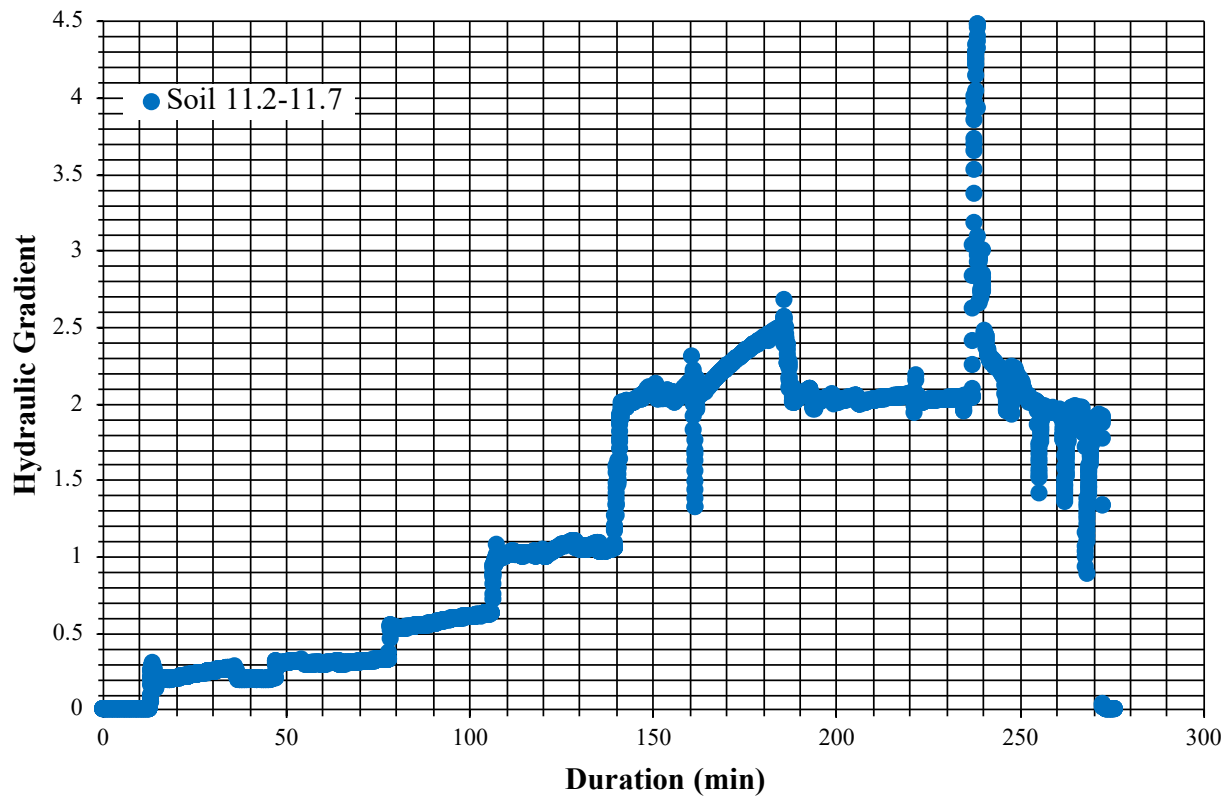


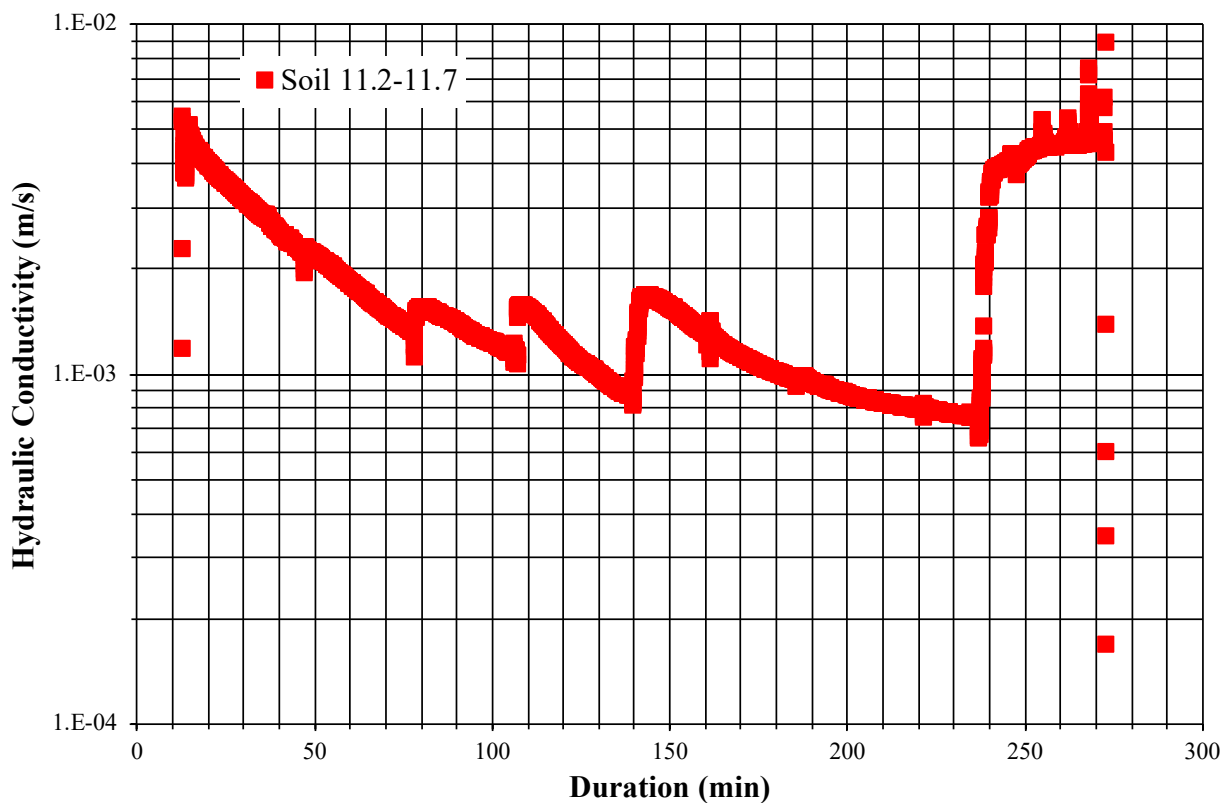
Figure A.5 – Grain size distribution after suffusion test

A.3.2 Hydraulic conductivity and rate of erosion

Figure A.6 displays the time evolution of hydraulic parameters.



(a)



(b)

Figure A.6 – Time series of the applied hydraulic gradient (a) and the computed hydraulic conductivity (b) during the suffusion test

Figure A.6(a) displays the time evolution of the hydraulic gradient that was applied during the suffusion test on the second specimen, and Figure A.6(b) shows the corresponding evolution of the hydraulic conductivity. From Figure A.6(b), it is noteworthy that there is a sharp rise of hydraulic conductivity immediately following the increase of the applied hydraulic gradient at the beginning of each stage. After the moment when hydraulic gradient begins to increase, the hydraulic conductivity starts slowly decreasing.

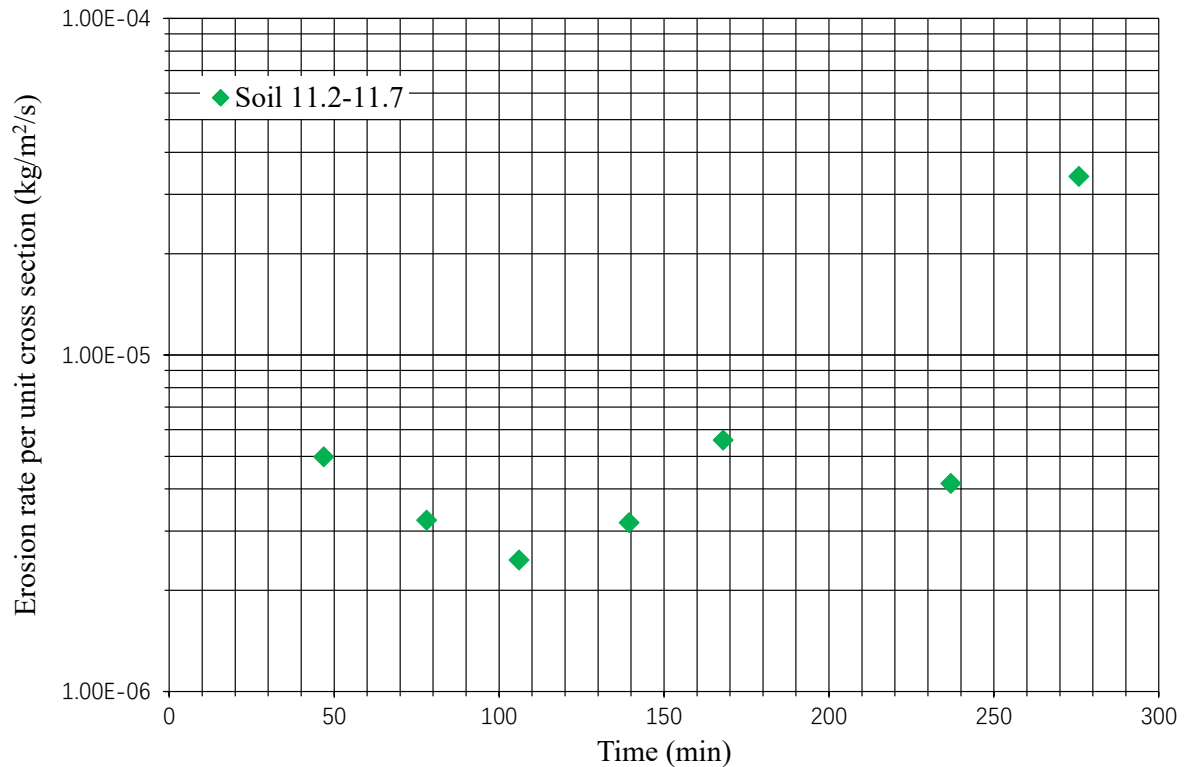


Figure A.7 – Time series of the erosion rate per unit cross section

The erosion rate per unit cross section is expressed by the eroded dry mass $m(\Delta t)$ during the elapsed time Δt and the specimen cross section S as $\dot{m} = \frac{m(\Delta t)}{S\Delta t}$. Figure A.7 displays the time evolution of corresponding values.

At the beginning of the suffusion test, hydraulic conductivity decreases with a very low value of the erosion rate, suggesting that the filtration is the main mechanism during the first phase. An increase in the hydraulic gradient then leads to a clear increase in the hydraulic conductivity and erosion rate. The second phase is the development of the suffusion, which is mainly characterized primarily by the detachment and transport of fine particles.

After comparing the time evolutions of the hydraulic conductivity with the erosion rate per unit cross section, a large increase in erosion rate appears when the applied hydraulic gradient reaches 4.5 in conjunction with a substantial increase in hydraulic conductivity at the same time. These simultaneous increases indicate that the clogging within soil pore spaces can be removed by a

sudden increase in hydraulic loading, after which hydraulic conductivity tends to stabilize.

A.3.3 Influence of suffusion on the mechanical strength

Figure A.8 shows the deviatoric stress versus the axial strain for the non-eroded specimen and for the same soil after a full suffusion test. The maximum value of the deviatoric stress of the specimen with suffusion is 14 kPa lower than that measured on the sample without suffusion, which is corresponding to a relative difference of 5 % of the maximum deviatoric stress. This first result indicates that the decrease in mechanical strength can be induced by a full suffusion process.

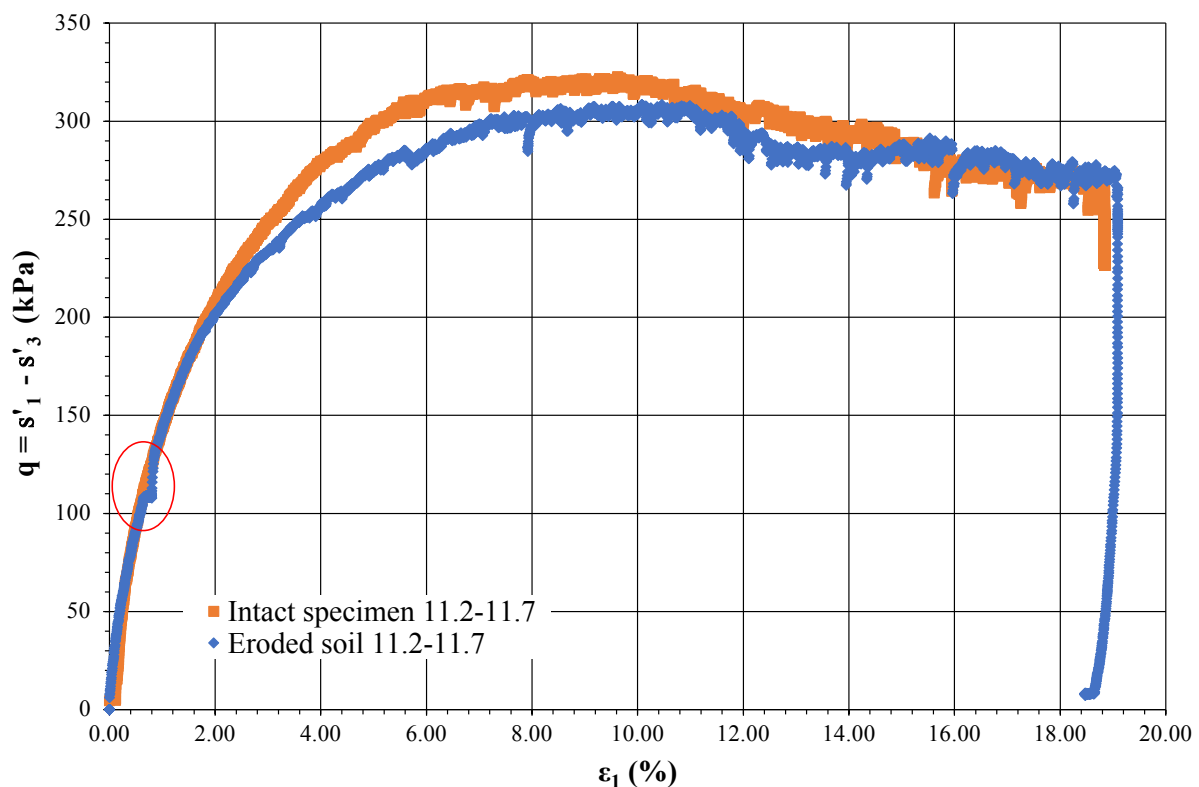


Figure A.8 – Deviatoric stress vs axial strain, with and without a full suffusion process

A.3.4 Suffusion susceptibility characterization

Suffusion susceptibility is analyzed by using the method based on energy proposed by Marot et al. (Marot et al., 2016), which characterizes both the hydraulic loading and the induced erosion. As described in Chapter II, sensitivity to suffusion can be determined when the hydraulic conductivity is constant, and the rate of erosion decreases. The hydraulic loading is represented by the total energy expended by the seepage flow (P_{flow}), and the total eroded dry mass is measured to characterize the corresponding soil response.

Figure A.9 shows the evolution of the cumulative dry mass of eroded particles (including the

lost mass during the saturation phase) versus the cumulative expanded energy. In the case of this test, the value of the erosion resistance index I_α was computed at the end of this test. The obtained erosion resistance index of 6.2 from this test indicates that the soil is very resistant to suffusion.

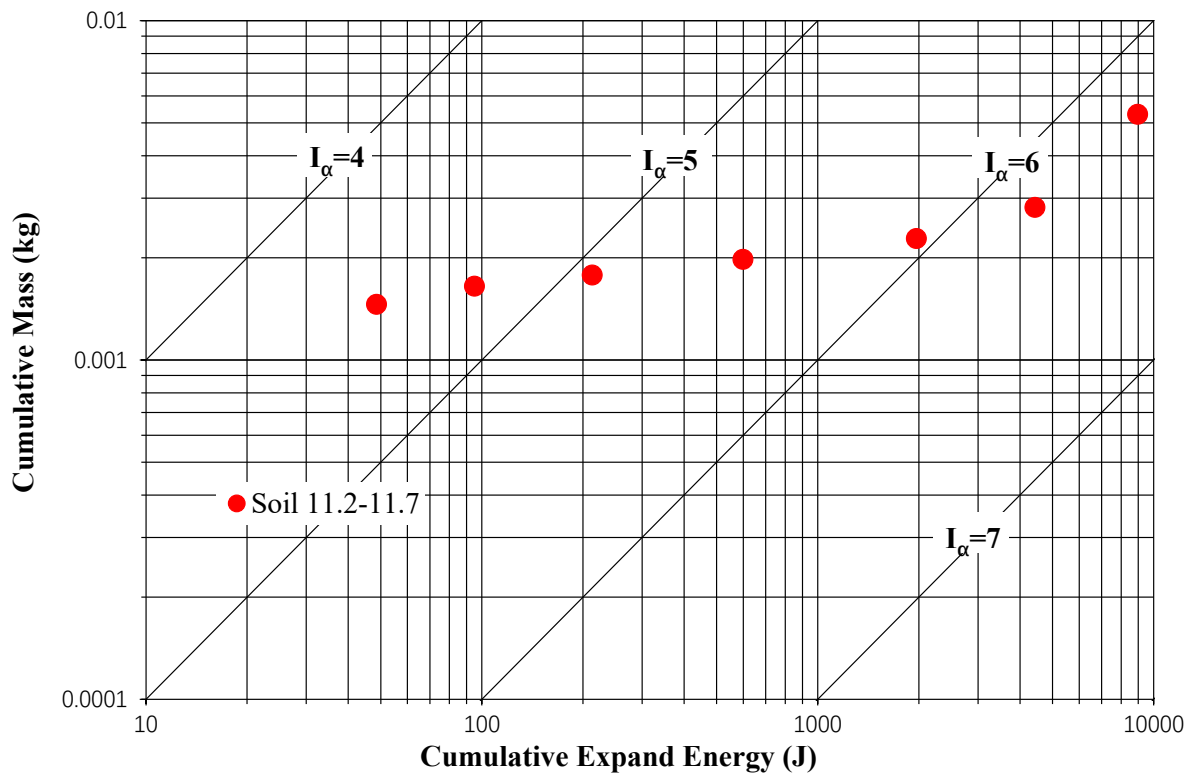


Figure A.9 – Cumulative eroded mass vs cumulative expanded energy for the full suffusion test

A.4 Conclusion

In this study, a newly developed large triaxial device was used to investigate the influence of the suffusion on the mechanical consequences. The soil selected to verify the validity of the apparatus was a well-graded coarse soil coming from a French dike, assessed as internally unstable by some criteria in the literature. To study the effect of suffusion on the mechanical responses, two monotonic compression triaxial tests were carried out on both non-eroded and post-suffusion specimens. A suffusion test was performed under multistage hydraulic gradient condition. A method linking the cumulative loss of dry mass to the energy dissipated by the seepage flow is used to describe the potential for suffusion. According to the results, hydraulic conductivity and erosion rate will increase when clogging within soil pore spaces is blown away by a sudden increase in hydraulic loading. Post-test grain size distribution analysis reveals that suffusion is a complex combination of three processes: detachment, transport, and possible filtration of the fine fraction. Mechanical tests show that a suffusion process induces a relative decrease of 5 %

of the maximum deviatoric stress. Further studies are required, however, before generalizing these conclusions to other types of gradation and/or other shapes of grains.

FINITE DIFFERENCE SOLUTION FOR 1D SUFFUSION PROCESS

The governing equations for the pore pressure $p_w(x, t)$, the porosity $\phi(x, t)$ and the concentration of fluidized particles $c(x, t)$ can be expressed as follows under one dimensional condition:

$$\frac{\partial(p_w)}{\partial t} - \frac{EK}{\mu\bar{\rho}(c)} \frac{\partial^2(p_w)}{\partial x^2} = 0 \quad \text{B.1}$$

$$\frac{\partial\phi}{\partial t} + \frac{\partial u}{\partial t} \frac{\partial\phi}{\partial x} - \frac{\partial\epsilon_v}{\partial t} \phi + \frac{\partial\epsilon_v}{\partial t} - \lambda_e(1 - \phi)(f_c - f_{c\infty})|q_w| = 0 \quad \text{B.2}$$

$$\frac{\partial c}{\partial t} + \left(\frac{q_w}{\phi} + \frac{\partial u}{\partial t} \right) \frac{\partial c}{\partial x} + \frac{1}{\phi} \left[\frac{\partial\phi}{\partial t} + \text{div}(q_w) + \frac{\partial\phi}{\partial x} \frac{\partial u}{\partial t} - \phi \frac{\partial\epsilon_v}{\partial t} \right] c - \frac{1}{\phi} \lambda_e(1 - \phi)(f_c - f_{c\infty})|q_w| = 0 \quad \text{B.3}$$

This system of partially differential equations has been solved through an explicit finite difference procedure. Chosen normal to the free surface and pointing downward into the interior of the specific finite domain (see Figure B.1). Equation B.1-Equation B.3 become:

$$\frac{p_w^{k+1} - p_w^k}{\Delta t} - \frac{[A_{p_w}]_{j+1/2}^k (p_w^{k+1} - p_w^k) + [A_{p_w}]_{j-1/2}^k (p_w^{k+1} - p_w^k)}{(\Delta x)^2} = 0 \quad \text{B.4}$$

$$\frac{\phi_j^{k+1} - \phi_j^k}{\Delta t} + [A_\phi]_j^k \frac{\phi_j^{k+1} - \phi_{j-1}^{k+1}}{\Delta x} + [B_\phi]_j^k \phi_j^k + [C_\phi]_j^k = 0 \quad \text{B.5}$$

$$\frac{c_j^{k+1} - c_j^k}{\Delta t} + [A_c]_j^k \frac{c_j^{k+1} - c_{j-1}^{k+1}}{\Delta x} + [B_c]_j^k c_j^k + [C_c]_j^k = 0 \quad \text{B.6}$$

Where the subscripts $j(0, 1, \dots, N)$ represent the variation in length, described by the x coordinate, and the subscripts $k(0, 1, \dots, M)$ represent the variation in the time t coordinate. $K(f_c, \phi)$, $\bar{\rho}(c)$ and $q_w(x, t)$ vary with depth and time. As a simple approximation, their values at (j, k) are used.

Defining $r_1 = \frac{\Delta t}{(\Delta x)^2}$ and $r_2 = \frac{\Delta t}{\Delta x}$ allows the Equation B.4-Equation B.6 to be rewritten:

$$-r_1[A_{pw}]_{j-1/2}^k p_{w_{j-1}}^{k+1} + \{1 + r_1 ([A_{pw}]_{j-1/2}^k + [A_{pw}]_{j+1/2}^k)\} p_{w_j}^{k+1} - r_1[A_{pw}]_{j+1/2}^k p_{w_{j+1}}^{k+1} = p_{w_j}^k \quad \text{B.7}$$

$$\begin{aligned} \text{With } [A_{pw}]_{j-\frac{1}{2}}^k &= \left(\frac{0.5}{[A_{pw}]_{j-1}^k} + \frac{0.5}{[A_{pw}]_j^k} \right)^{-1}, \\ [A_{pw}]_{j+\frac{1}{2}}^k &= \left(\frac{0.5}{[A_{pw}]_j^k} + \frac{0.5}{[A_{pw}]_{j+1}^k} \right)^{-1}, \\ [A_{pw}]_j^k &= \left[\frac{EK(f_c, \phi)}{\mu \bar{\rho}(c)} \right]_j^k. \end{aligned}$$

$$-r_2 A_\phi \phi_{j-1}^{k+1} + (1 + r_2 A_\phi) \phi_j^{k+1} = (1 - \Delta t B_\phi) \phi_j^k - \Delta t C_\phi \quad \text{B.8}$$

$$\begin{aligned} \text{with } A_\phi &= \frac{u_j^{k+1} - u_j^k}{\Delta t}, \\ B_\phi &= -\frac{\epsilon_{v_j}^{k+1} - \epsilon_{v_j}^k}{\Delta t}, \\ C_\phi &= \frac{\epsilon_{v_j}^{k+1} - \epsilon_{v_j}^k}{\Delta t} + [-\lambda_e(1 - \phi)(f_c - f_{c\infty})|q_w|]_j^k. \end{aligned}$$

$$-r_2 A_c c_{j-1}^{k+1} + (1 + r_2 A_c) c_j^{k+1} = (1 - \Delta t B_c) c_j^k - \Delta t C_c \quad \text{B.9}$$

$$\begin{aligned} \text{with } A_c &= \left(\left[\frac{q_w}{\phi} \right]_j^k + \frac{u_j^{k+1} - u_j^k}{\Delta t} \right), \\ B_c &= \frac{1}{\phi_j^k} \left(\frac{\phi_j^{k+1} - \phi_j^k}{\Delta t} + [\text{div}(q_w)]_j^k + \frac{\phi_{j+1}^k - \phi_{j-1}^k}{2\Delta x} \frac{u_j^{k+1} - u_j^k}{\Delta t} - \phi_j^k \frac{\epsilon_{v_j}^{k+1} - \epsilon_{v_j}^k}{\Delta t} \right), \\ C_c &= \left[\frac{-\lambda_e(1 - \phi)(f_c - f_{c\infty})|q_w|}{\phi} \right]_j^k. \end{aligned}$$

Where $j = 1, 2, 3, \dots, N - 1$; $k = 1, 2, 3, \dots, M - 1$.

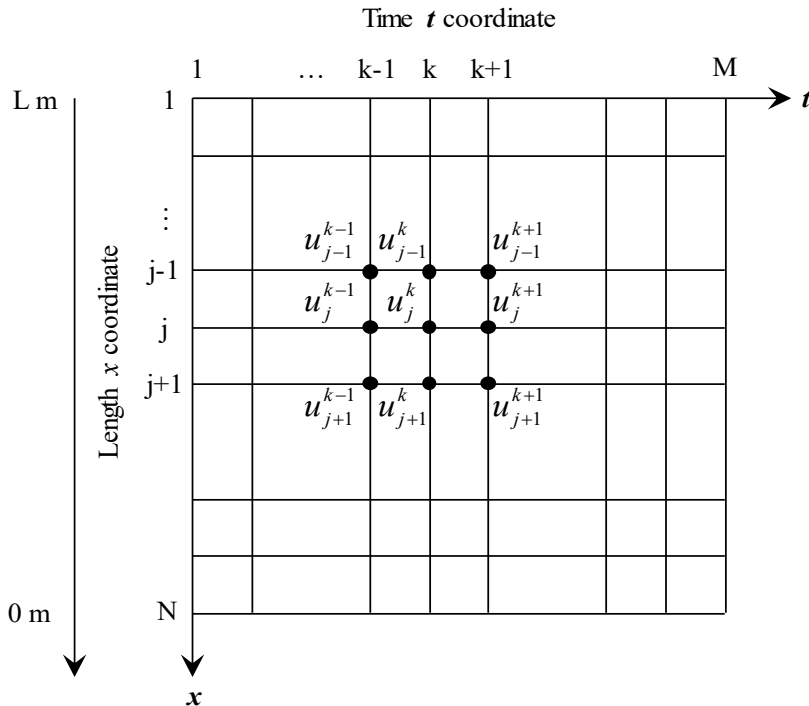


Figure B.1 – Geometry and finite difference grid in space-time of analyzed 1D internal erosion

ACKNOWLEDGEMENTS

Upon finishing this thesis, I would like to express my great gratitude towards all those who have offered me sincere assistance.

Firstly and foremostly, my hearty thanks go to my supervisor Professor Didier Marot and co-supervisor Professor Zhenyu Yin. They have given me insightful suggestions and constant encouragement both in my study and in my life. Furthermore, Professor Marot and Yin's painstaking guiding and valuable advice have profoundly contributed to the completion of the present thesis.

Also, I own my thanks to all the teachers who have taught and enlightening me during my studies in the campus, for guiding me in the field of research work, which is both challenging and fantastic. The experience and profit I obtained will be of grand importance to my further studies.

Then, I must own my thanks to the China Scholarship Council for the financial support to complete my study.

Finally, I am also grateful to my family and friends, who encourage and support me and share with me my worries, frustrations, and happiness.

Titre : Etude du comportement du sol soumis à un processus d'érosion interne

Mots clés : Suffusion; Filtration; Processus local; Effet d'échelle; Simulation

Résumé : La suffusion érode de manière sélective les fines particules de la matrice du sol. En cours de suffusion, les particules érodées sont déplacées par l'écoulement et peuvent être filtrées par la fraction grossière. Ce phénomène couplé se traduira par des modifications de la vitesse d'infiltration, du gradient hydraulique et du coefficient de perméabilité, etc. Un dispositif de grandes dimensions est utilisé pour étudier le processus de filtration en érosion interne et le mécanisme de suffusion. Grâce aux prises de pression situées le long de la paroi rigide du dispositif, il est possible d'étudier localement le processus de suffusion. Les résultats d'un autre petit appareil sont utilisés pour comparer les résultats du grand appareil afin de rechercher l'effet d'échelle spatial.

L'équation de filtration de base indique l'état final du processus de filtration. Dans le processus de suffusion, le processus de filtration se termine lorsque le pourcentage de fines est proche de la valeur calculée par l'équation de filtration.

Un petit nombre de particules fines peut encore affecter

la réponse hydraulique. La suffusion est un processus hétérogène et la position de la valeur maximale du gradient hydraulique local est transférée d'amont en aval. La taille des grains des particules érodées devient plus grande avec le développement de la suffusion. Le processus d'érosion peut être divisé en trois étapes: l'étape "ajustement du grain", l'étape "stabilité des infiltrations" et l'étape "changement d'infiltration". La taille de l'échantillon a une influence sur le processus d'érosion. Les critères basés sur la taille des particules entraîneront un risque élevé de surestimation de la résistance à la suffusion, mais la méthode énergétique est adaptée à cette estimation. A partir de trois lois d'érosion, trois modèles sont proposés sur la base des équations d'équilibre et en distinguant quatre types de constituants : le squelette solide supposé stable, les particules fines érodables, les particules fluidisées et le fluide pur. La méthode des différences finies est utilisée pour résoudre les équations différentielles de contrôle.

Title: Study of Soil Behavior Subjected to An Internal Erosion Process

Keywords: Suffusion; Filtration; Local process; Scale effect; Simulation

Abstract: Suffusion selective erodes the fine particles from the soil matrix. In the process of suffusion, eroded particles are moved by the seepage and filtered by the coarse fraction. This coupled phenomenon will result in the changes in seepage velocity, hydraulic gradient and permeability coefficient and so on. A large device is selected to study the filtration process in internal erosion and the mechanism of suffusion. Thanks to the pressure measuring ports along the rigid wall of the large device, local process of suffusion can be studied. The results from another small device are used to compare with the results of the large device to research the scale effect of the specimen.

The basic filtration equation indicates the final state of the filtration process. In the suffusion process, the filtration process ends when the fine content is closed to the value computed by the basic filtration equation.

A small number of fine particles can still affect the hydraulic response. Suffusion is a heterogeneous process and the position of the maximum value of the local hydraulic gradient is transferred from upstream to downstream. The grain size of eroded particles becomes huger with the development of the suffusion. And the erosion process can be divided into three stages: "grain adjustment" stage, "seepage stability" stage, and "seepage change" stage. The specimen size has some influence on the erosion process. The criteria based on particle size will lead to a high risk, but energy method is compatible.

Combining three erosion laws, three erosion models were formulated based on the mass balance of four assumed constituents: stable fabric of the solid skeleton, erodible fines, fluidized particles, and pure fluid. The finite difference method is used to solve the governing differential equations.